Universiteit Gent
Faculteit Ingenieurswetenschappen en Architectuur
Vakgroep Toegepaste Fysica

Promotoren: Prof. dr. ir. Christophe Leys
Dr. ir. Anton Nikiforov

Examencommissie:

Prof. František Krčma	Faculty of Chemistry Brno University of Technology, Czech Republic
Prof. Nathalie De Geyter	Department of Applied Physics Ghent University, Belgium
Prof. Stijn W.H. Van Hulle	Department of Industrial Biological Sciences Ghent University, Belgium
Prof. Frédéric Lynen	Department of Organic and Macromolecular Chemistry Ghent University, Belgium
Prof. Karel De Schamphelaere	Department of Applied ecology and environmental biology Ghent University, Belgium

Proefschrift tot het bekomen van de graad van
Doctor in de Ingenieurswetenschappen: Toegepaste natuurkunde
Academiejaar 2015-2016

Non nobis solum nati sumus.
- Marcus Tullius Cicero

Acknowledgements

When I graduated at Ghent University, eight years ago, I could not imagine that I would ever return to the university again. In the meantime, I have learnt the hard way that anything is possible in life. Whether this was fate, I rather keep as an open question, but what I do know is how grateful I am that things turned out this way. In this regard, I want to express my greatest gratitude to my supervisor Prof. Christophe Leys and my co-promotor Dr. Anton Nikiforov, because they are the main reasons why I have loved my job as teaching assistant so much.

Christophe, first of all, provided me with the opportunity to start this job and pursue my PhD studies. More importantly, he always formed the very core of the comfortable working environment and the nice group atmosphere in our research unit. His passion for scientific education is contagious, which made it a true pleasure to assist him in the many exercise lessons, student labs and student projects. I will always remember him as a wise mentor who highly values righteousness as well as the comfort of his group members.

Then there is the man who helped me tremendously with many of my practical scientific challenges. The man who guided me with infinite patience through a maze of experimental obstacles. A man with exceptionally broad hands-on expertise and specialized knowledge. Anton, the Tony Stark of our department. I am actually quite sure that he is able to build real Iron Man's armor. Apart from being a multi-talented scientist, Anton is an excellent mentor. Thanks to him, my research found a clear direction in the early stages and progressed quicker than ever would have been in the later stages. I cannot imagine a better PhD guide than him. His patience, motivation and enthusiasm invoked in me the deepest respect.

During my PhD studies, I had the great pleasure to work closely together with three master thesis students, all of which who delivered work of high quality. Gert Willems was the first one to work with the DBD reactors used in this study, shortly after they were built. Despite the several teething problems we encountered with the setups, he was able to deliver enough experimental data for two peer-reviewed papers, including Chapter 6 and the first part of Chapter 8 in this dissertation. Next, Dries Davister contributed a lot to Chapter 8, with his more hands-on attitude. Although we already had more experience with the DBD reactor, he faced another challenge: performing experiments with α-HCH and PeCB, two compounds that are hard to handle due to their high volatility and low solubility. Nonetheless, Dries

collected a considerable amount of data with high accuracy, in the limited time that he had for his master thesis. Niels Wardenier arrived in our department at the moment that I was supposed to start writing on my dissertation and to distantiate myself more from the experimental work. However, his motivation and focused attitude made me decide otherwise and I do not regret it for a single moment. He proved to be a very hard worker and intelligent student. As he decided to work longer on his thesis than he was supposed to, his work comprised a huge amount of experiments and analysis data. Moreover, the depth of his literature study was beyond anyone's expectations. Stijn and Anton, you have a promising new PhD student! Apart from my three master thesis students, there was also Mario Lessiak, an Austrian student who assisted me in the ICCD measurements that were performed for Chapter 5, in the summer of 2011. Surprisingly, he helped me just for fun, as he could not receive any credits in his studies for this work. Yet, he was motivated to execute the same experiment accurately over and over again for thousands of times. Full-time. During three weeks. In a dark room. Just for fun. Mario, Gert, Dries and Niels, I am very glad to have worked with you! You guys all did an excellent job.

Further, Benoît Tuybens and Henri Van Overmeire helped me with the COMSOL simulations and data processing of Chapter 7, in the frame of their bachelor project. Benoît and Henri, thanks for making my thesis more colorful! My colleague and friend Xiaolong Deng helped me selflessly with making all figures of Chapter 3. Xiaolong, you are awesome! I mean, really! Next, I would like to thank Lucie Němcová for the help with my first conference paper in the earliest phase of my PhD. Also a word of thanks goes to Su Di from Shanghai, who assisted me and Dries for a few weeks during some experiments. Additionally, I feel the need to state that Hiba contributed to this work. The experiments in this thesis were, of course, not possible without the administrative and practical support of the technical staff that our department has known during the past seven years, including Peter, Dries and Joris. I am especially thankful to Danniël, Ivan, Frank and Kjell for their fast and precise assistance.

This thesis has resulted from a collaboration of several research groups: the Department of Industrial Biological Sciences, the Department of Textiles and the Department of Organic and Macromolecular Chemistry from Ghent University, the Research Group Molecular Odor Chemistry from KU Leuven and the Faculty of Chemistry from the Brno University of Technology. I was happy to experience a consistently fast and smooth cooperation with these different groups. First of all, I am very grateful to Prof. Stijn Van Hulle, for providing me with advice, two master thesis students and an accurate GC-MS system that has analyzed over one thousand samples for this work. Stijn, I was very glad to have your advice on one of our papers in the evening right before the deadline of submission and I will remember that moment for a long time. Yannick, thanks for your incredible patience with me, my samples and my master thesis students. You are the best! Also a big thank you for Dr. Nele Daels and Prof. Karen De Clerck for their advice and assistance with the nanofiber membranes. My

gratitude goes as well to Prof. Jim Van Durme and Jeroen Vandamme who took good care of my other GC-MS samples, even in periods when their GC-MS device was overly occupied. The HPLC-MS part of my work, I owe to Prof. Frédéric Lynen and Pieter Surmont. Thank you both for all the analyses and advice. Because of you, analytical chemistry has become one of my new scientific passions. Further, I would like to thank Prof. Karel De Schamphelaere for the several interesting discussions we had and for the toxicity analyses, which have not been included in this work, but which are soon to be published. Last but not least, I would like to express my gratitude to Prof. František Krčma, who has made my stay of seven weeks at the Brno University of Technology in Czech Republic possible. Franta, I appreciate your hospitality a lot and I look back at this scientific visit as a very positive experience. Edita, Michal and your friend with the unpronounceable name, thanks for all the practical help and the nice conversations we had! I gratefully acknowledge the European Cooperation in Science and Technology (COST action TD1208) as the funding source of my stay in Brno through a Short Term Scientific Mission (STSM).

An additional word of thanks goes to all the examination committee members for their interest in my work, their careful review of this thesis and the resulting feedback that has led to an improvement of the manuscript.

Now comes the part where I want to thank all the people that did not directly contribute to my scientific investigations, yet who have influenced them in several ways. I am always cautious about glorifying the past, since I want to maintain this strong feeling that the best is yet to come. Notwithstanding, I can safely say that the last four years were the ones that I have enjoyed most up to now. There are many people that I want to thank for that: colleagues, friends and family.

First of all, a big thank you to Laurine for helping me with improving the English grammar of the manuscript. Also thank you to Aqsa for your advice on the esthetical part. And, of course, thanks to both of you for your emotional support during the writing of this work. You girls know how much that meant to me, but just in case you want to read it in black and white, here we go: a lot!

Daarnaast zou ik mijn ouders willen bedanken voor hun voortdurende steun tijdens mijn doctoraatsstudie. Ik ben erg dankbaar dat jullie vaak op zijn minst al moeite deden om te begrijpen waarover ik het had, telkens wanneer ik een van mijn laatste wetenschappelijke ontdekkingen probeerde uit te leggen.

I would like to thank all my office roomies from the last years for all the good moments and nice conversations. Abi, Leila, Tinneke, Ivan, Aqsa, Xiaolong, Qing, Ranhua, Nathan, you are all burnt in my memory forever. In a good way, obviously! Especially Abi, Tinneke, Aqsa and Xiaolong, you have supported me emotionally on moments that were hard for me. I am very happy with you as friends!

A special word of thanks goes to Fatemeh. Not only does she have a PhD topic very related to mine – which makes her one of the few people who can fluently understand me when I am talking in science –, she has also become a very good friend. Fatemeh, thanks a lot for the many talks and the continuous support you gave me.

Koen, Annick, Toon, Johan, thanks for the fun moments on campus Schoonmeersen! There are many more colleagues who made these seven years such a nice and memorable experience. Iryna, Silvia, Mahtab, Gaelle, Pieter, Ke Vin, Savita, Arne, Li Li, Iuliia, Sharmin, Zhiping, Rim, Stijn, Rouba, Grégoire, Lei Wang, Li Dong, Yan Sun, it was always nice to have you around. Thanks as well for all the candies, cookies, birthday pies and so on that unexpectedly kept appearing in the coffee room! Further, I am thankful to Prof. Rino Morent, Prof. Nathalie De Geyter and Prof. Geert Verdoolaege for the past and ongoing efforts to organize events and lunches for our group as a way of team building.

There are many friends that listened to me, supported me or helped me during my PhD studies. It is hard to list them all here, but I am sure that they know who I mean. Anyhow, there are always a few who really want to read their names here explicitly. So yes, Laurine, I hereby officially acknowledge your contribution to my emotional well-being and the importance of your continuous support. Bart, bro, Kristel, sis, it was always a pleasure to have you as my siblings, what do I need to say more? Francis, Bart, Kristof, Masha, even with the geographical challenges that have appeared, your friendship has always meant a lot to me. All my friends in the salsa group, the Couchsurfing community and beyond, you know that I appreciate you a lot, as well as the many beautiful moments you gave me! You all make this world a wonderful place.

Table of Contents

The secret of getting ahead is getting started.
- Mark Twain

You can't take over the world without a good acronym.
- Caroline Sarah Woolley

List of Acronyms

α-HCH	α-Hexachlorocyclohexane
γ-HCH	γ-Hexachlorocyclohexane
AC	alternating current
AOPs	advanced oxidation processes
CAR/PDMS	carboxen/polydimethylsiloxane
CCS	cross-correlation spectroscopy
CDET	simazine amide
CDIT	atrazine amide
CMFG	confirmation by the molecular formula generator
DAD	diode array detector
DBD	dielectric barrier discharge
DC	direct current
DC (Chapter 8)	duty cycle
DEA	deethylatrazine
DIDEA	didealkylatrazine
DLS	density of least squares
EEDF	electron energy distribution function
EEO	electrical energy per order
ESI	electrospray ionization

EU	European Union
FWHM	full-width at half-maximum
GC-MS	gas chromatography – mass spectrometry
HPLC-HRMS	High performance liquid chromatography – high resolution mass spectrometry
HPLC-MS	high precision liquid chromatography – mass spectrometry
HV	high voltage
ICCD	intensified charge coupled device
IED	interelectrode distance
LIF	laser-induced fluorescence
MS	mass spectrometry
OES	optical emission spectroscopy
PA-6	polyamide 6
pDBD	pulsed dielectric barrier discharge
PDMS	polydimethylsiloxane
PeCB	pentachlorobenzene
PMT	photomultiplier tube
RF	radio frequency
SHA	sample of highest abundance
SIM	selected ion mode
SLM	standard liter per minute
SPME	solid phase microextraction
TOF-MS	time-of-flight mass spectrometer
U.S.	United States
UV	ultraviolet radiation

Waarom zou ik me iets aantrekken van toekomstige generaties?
Wat hebben zij ooit voor mij gedaan?
- Groucho Marx

Nederlandse samenvatting

-Summary in Dutch-

Wereldwijd worden in toenemende mate gevaarlijke microverontreinigingen gedetecteerd in het effluent van afvalwaterzuiveringsinstallaties. Dit geeft aan dat de verwijdering ervan onvoldoende is door middel van de conventionele moderne waterzuiveringstechnieken. In de zoektocht naar kosteneffectieve oplossingen, hebben geavanceerde behandelingstechnieken, waaronder elektrochemische scheiding, actieve kool, nanofiltratie, omgekeerde osmose en geavanceerde oxidatieprocessen, onlangs meer aandacht gekregen, omdat zij de meest effectieve beschikbare technieken zijn om biorecalcitrante organische stoffen te verwijderen. Ze zijn echter geassocieerd met hoge energiekosten en hoge financiële kosten. Bovendien hebben al deze werkwijzen, met uitzondering van geavanceerde oxidatieprocessen, het bijkomend probleem van toxische concentraatverwerking, omdat ze alleen de bestanddelen verwijderen zonder verdere afbraak in minder toxische nevenproducten. Geavanceerde oxidatietechnieken daarentegen, kunnen toxische verbindingen oxideren tot kleinere moleculen, idealiter via volledige mineralisering tot CO_2 en H_2O. Niettemin blijft hun zwakste punt de hoge vraag naar energie. Bovendien kunnen ze schadelijk zijn voor het milieu door de productie van langlevende oxidanten en potentieel toxische oxidatieproducten. Daarom is verder onderzoek nodig die zich richt op het optimaliseren van bestaande systemen om deze problemen te overwinnen.

Plasmaontlading in contact met water neemt een belangrijke plaats in binnen geavanceerde oxidatieprocessen, aangezien het een breed spectrum aan oxidatieve deeltjes genereert in de nabijheid van de vloeistof onder behandeling. Verdere optimalisatie van deze technologie is echter een complexe taak vanwege de grote verschillen in reactorontwerp en materialen, ontladingstypes en operationele parameters. In dit werk wordt een uitgebreid overzicht gegeven van de verschillende soorten plasmareactoren en verder worden de specifieke gevallen van belontlading en diëlektrische barrièreontlading (DBD) reactoren meer in detail onderzocht. Het experimentele gedeelte is opgesplitst in twee delen. Het eerste deel is gericht op de belontladingsreactoren, waarvan bekend is dat deze minder vermogen nodig

hebben dan reactoren waarvan de ontlading rechtstreeks in de vloeistoffase gebeurt, zonder extern toegevoegde bellen. In dit deel worden alleen de plasmafysische eigenschappen van de belontlading onderzocht, met het oog op het verkrijgen van een beter inzicht in de onderliggende mechanismen van plasma-initiatie en -propagatie en de implicaties daarvan op de behandeling van water. Hiertoe worden elektrische en spectroscopische analyses, alsook ICCD-beeldvorming uitgevoerd voor twee reactorconfiguraties. In het tweede deel wordt de focus verlegd naar de plasmafysica en -chemie in DBD-reactoren waar de ontlading in direct contact staat met een bewegende waterfilm. Een dergelijk type reactor wordt verwacht minder energieverlies te vertonen door elektrolytische processen en Joule-opwarming van de vloeistof dan belontladingsreactoren en reactoren met plasmaontlading rechtstreeks in de vloeistoffase. Daarnaast wordt de diëlektrische barrièreontlading over water minder beïnvloed door de vloeistofeigenschappen en kan het eenvoudig worden opgeschaald voor de behandeling van grote hoeveelheden water, waardoor het aantrekkelijker is voor verschillende waterbehandelingstoepassingen.

In de literatuur worden plasmareactoren algemeen ingedeeld in twee of drie categorieën op basis van hun plasma-waterfase distributie, met verdere onderverdeling afhankelijk van de soort ontlading en de spanningsgolfvorm. Niettemin variëren reactorprestaties sterk binnen elk subtype, als gevolg van verschillen in gebruikte materialen en elektrodeconfiguraties. Terwijl het begrijpen van deze invloeden essentieel is voor het slim ontwerp en de optimalisatie van plasmareactoren, ontbreekt een overzicht over dit onderwerp. Om die reden werd een uitgebreide literatuurstudie uitgevoerd in dit werk, om een overzicht te bieden van plasmareactortypes op basis van reactorontwerp en materialen. Zes hoofdklassen van reactoren worden onderscheiden, op basis van hun plasma-waterfase distributies. De mogelijkheden om elk systeem op te schalen naar groter plasmavolume worden besproken en de invloed van het ontwerp, de materialen en de operationele parameters inzake energie-efficiëntie worden onderzocht. In elektrohydraulische ontladingsreactoren, waarbij plasma direct in de vloeistof wordt gegenereerd, kan het elektrodemateriaal grote invloed hebben op de organische afbraak na plasmabehandeling als gevolg van de vorming van erosiedeeltjes in het water. Dergelijke reactoren worden geoptimaliseerd door het verplaatsen van één van de elektroden naar de gasfase en de reactor te transformeren in een hybride, waarbij plasma wordt gegenereerd zowel in de gasfase als in de vloeistoffase. In belontladingsreactoren kan de energie-efficiëntie worden verhoogd door het vermeerderen van het aantal naaldelektroden of, in het geval van opstijgende bellen tussen de elektroden, door gebruik van een dubbele diëlektrische barrière of door het toevoegen van glasparels in de watermassa. Wanneer plasma over een waterfilm of watermassa wordt geproduceerd, kan de energie-efficiëntie worden verhoogd door roeren of door het water te laten stromen langsheen de plasma-actieve zone. In verstuivende ontladingsreactoren, waarbij het water als druppels in de plasmazone wordt gebracht, hangt de behandeling af van de locatie van de druppels. In het specifieke geval van een glijdende boogontlading kan het proces worden geoptimaliseerd door toevoeging van een koppel controle-elektroden of door toevoeging van

een tweede hoogspanningselektrode en daarnaast door de introductie van het water loodrecht op de gasstroom om het contact met plasma te verbeteren. Een laatste reactorklasse, die een sterke concurrent is voor de andere plasmasystemen, genereert plasma op een bepaalde afstand van de vloeistof, waarbij ozonreactoren de meest populaire varianten zijn. Hoe afhankelijk de energie-efficiëntie is van de spanningsparameters is significant verschillend voor verschillende reactortypes. Bijvoorbeeld, positieve pulspolariteit veroorzaakt een hogere efficiëntie in elektrohydraulische en belontladingsreactoren in alle gevallen, terwijl negatieve polariteit betere prestaties geeft in reactoren met ontlading in de gasfase. Zuurstof is het voedingsgas bij voorkeur, aangezien het in het algemeen de energie-efficiëntie verhoogt in vergelijking met alle andere gassen zoals lucht en argon. Om technische redenen betreffende de veiligheid echter, hebben we zuurstof voornamelijk gebruikt in onze meest recente experimenten, waarvan de meerderheid niet is opgenomen in dit werk.

In de eerste belontladingsreactor bestudeerd in dit werk wordt gepulseerde vonkontlading opgewekt in stikstof, helium en argonbellen tussen een pin-tot-plaat elektrodesysteem ondergedompeld in een wateroplossing. Uit elektrische en spectroscopische analyse bleek de vorming van twee soorten belontlading: een directe belontlading, met onmiddellijk begin van de vonkontlading binnen de bel, en een uitgestelde belontlading, waar de vonkontlading optreedt na een vertragingstijd van typisch enkele microseconden. Op basis van onze metingen en eerder gerapporteerde experimenten is een dynamisch model voor belontlading voorgesteld, waarbij de positie van de bel ten opzichte van de elektroden tijdens het aanbrengen van de spanningspuls bepaalt of de belontlading direct of vertraagd is. Dit model bevat een beschrijving van het plasmakanaal en het externe pulscircuit als een RLC serieschakeling met constante weerstand. Dit model is consistent met het effect van de experimentele parameters op de gemeten plasmakarakteristieken. Bijvoorbeeld, de frequentie van de spanningsoscillaties tijdens de ontlading is constant in alle metingen en de dempingstijd van de gedempte trillingen blijkt niet beïnvloed te worden door het belgas, spanningspulsamplitude en geleidbaarheid van de oplossing. De breedte van de H_α Balmerlijn in het uitgestraalde spectrum wordt gedomineerd door Stark-verbreding en impliceert elektronendichtheden in de orde van 10^{24}-10^{25} m^{-3}, wat relatief hoog is in vergelijking met andere koude atmosferische plasma's. De uitgezonden spectra bevatten ook een continuüm, dat afkomstig is van een zwarte straler, namelijk het verhitte belgas. Zwarte stralertemperaturen binnen het bereik van 6000-9000 K werden bepaald door middel van een fittingsalgoritme uit de literatuur dat we hebben aangepast voor dit doel.

De tweede belontladingsreactor bestaat uit een enkelvoudige, stationaire bel bevestigd aan een naar omhoog gerichte naaldelektrode. De bel wordt geproduceerd door middel van een programmeerbare spuitpomp uit de zuivere gassen helium, argon, stikstof, zuurstof of lucht. Nadat de bel tot rust is gekomen, worden hoogspanningspulsen handmatig getriggerd op de naaldelectrode. Dit reproduceerbaar systeem maakt nauwkeurig onderzoek mogelijk van de

plasma-initiatie en -ontwikkeling, die we voornamelijk hebben uitgevoerd met snelle beeldvorming en elektrische analyse. In deze configuratie treedt belontlading consistent verscheidene microseconden na het aanbrengen van de spanningspuls op. De plasmageometrie evolueert in vijf fasen, waarbij plasma eerst snel de bel vult en vervolgens verdwijnt, gevolgd door een donkere fase, waarna het plasma weer geleidelijk de bel vult tot de bovenste rand. De lengte van de donkere fase en de latere belvulfase is sterk afhankelijk van het belgas. In de vijfde fase vertrekken vertakkende streamerachtige structuren vanuit het beloppervlak naar het water toe. De onderzochte kenmerken van de streamers in onze metingen gelijken op de kenmerken van gepulste streamer-ontlading rechtstreeks in water, wat aangeeft dat ze vergelijkbaar zijn in aard. Hun spectrum bevat een sterke H_α lijn en een zwakke of afwezige zuurstoflijn bij 777 nm. De vertragingstijd en vijf stadia worden verklaard door het capacitieve gedrag van de bel. Een eenvoudig model dat de bel als een klassieke plaatcondensator beschouwt, is in relatief goede overeenstemming met de experimentele waarden in onze experimenten. Deze resultaten suggereren sterke aantrekking van waterige ionen naar de bel tijdens de initiële vertragingstijd met een daaropvolgende ontlading die het meest actief is nabij het beloppervlak. Dit maakt het systeem bijzonder aantrekkelijk voor de oxidatie van ionische targetverbindingen en oppervlakte-actieve stoffen.

Met de eerste DBD-reactor in dit werk werd het synergetisch effect tussen plasmaontlading en adsorptie van microverontreiniging onderzocht. Hiertoe werd een polyamide nanovezelmembraan gekozen als adsorbens en atrazine als modelmicropolluent met de aanzienlijk lage initiële concentratie van 30 µg/L. Via H_2O_2 en O_3-metingen en een kinetisch model gevonden in de literatuur werd de bijdrage van oxidatie door directe ozonaanval en het peroxoneproces (O_3/H_2O_2) berekend, wat slechts ongeveer 20% bleek te zijn. Aangezien ozonatie en peroxone in de literatuur worden voorgesteld als de meest dominante oxidatieprocessen in de vloeibare massa, komen de determinerende oxidatiereacties voor in de dunne laag water onder het actieve plasmagebied. Terwijl de H_2O_2 en O_3-productie in de reactor niet worden beïnvloed door de aanwezigheid van het membraan is er een aanzienlijke toename van atrazineverwijdering van 61% tot 85% wanneer het membraan wordt toegevoegd nabij het actieve plasmagebied. Vorming van de oxidatieproducten deethylatrazine en ammelide is meer uitgesproken in aanwezigheid van het membraan, wat de efficiëntere afbraak en synergie tussen plasmaontlading en polluentadsorptie bevestigt. Dit synergetisch effect wordt verklaard met een hogere lokale concentratie aan atrazine nabij het plasma-vloeistof grensvlak, wat de frequentie verhoogt van directe en indirecte oxiderende interacties van de micropolluenten met reactieve deeltjes van het actieve plasmagebied.

Voordat het opschalen van het eerste DBD-reactorconcept tot een krachtiger en duurzamer ontwerp aan bod komt, onderzoeken we eerst de plasmafysische eigenschappen van een enkelevoudige, AC-aangedreven DBD-filament in contact met een stromende waterfilm.

Door middel van elektrische en spectroscopische analyse, simulatie met COMSOL en gegevensverwerking met BOLSIG+ werden meerdere plasmaparameters van het ontladingsfilament bepaald, waaronder de rotatie- en vibratietemperaturen van N_2, het gereduceerde elektrische veld tussen de elektroden, de elektronenmobiliteit en de stroomdichtheid. Uit deze parameters werd een elektronendichtheid berekend van de orde $n_e \approx 10^{14}$ cm^{-3}. Alle verkregen plasmaparameterwaarden zijn in goede overeenstemming met literatuurwaarden voor DBD-microfilamenten in atmosferische lucht tussen vaste elektroden. De ontladingsevolutie is echter opmerkelijk verschillend van de gewoonlijk waargenomen evolutie voor de tegenhanger met vaste elektroden. Terwijl in de negatieve halve cyclus van de spanning een intense lichtpuls wordt gezien zoals in het geval met vaste elektrodes, start de positieve halve cyclus met een minder intense lichtpuls gevolgd door een bult in de fotostroom. De bult is geassocieerd aan een intense kathodevlek aan het wateroppervlak en een opwaarts bewegende gloei-achtige ontladingsgolf op het diëlektrische oppervlak, wat wijst op stapsgewijze ladingsdepositie op de barrière. Dit verschijnsel is kenmerkend voor resistieve barrièreontlading, waarbij één elektrode fungeert als een resistieve barrière, wat in ons geval de waterelektrode is. Vorming van de kathodeval treedt alleen op nabij de waterkathode tijdens de positieve halve cyclus van de spanning, voor het gehele bereik van de stroombron. Deze voorkeur kan vele oorzaken hebben, waaronder lokale veldversterking door vervorming van het wateroppervlak of druppelvorming, lokale ionisatieversterking door het inhomogene profiel van de luchtvochtigheid en effectievere secundaire elektronenemissie door de waterelektrode, in vergelijking met de diëlektrische barrière. Soortgelijke mechanismen kunnen de onderliggende oorzaak verklaren van de gloed-achtige ontladingsvlek die continu aan de waterelektrode wordt waargenomen tijdens de gehele spanningscyclus. Deze kathodevlek duidt op de continue vorming van oxidatieve deeltjes aan de waterlaag, zelfs wanneer plasma is verdwenen in alle andere gebieden tussen de elektrodes. Dit nieuwe inzicht is zeer interessant in de context van waterzuiveringstoepassingen en verdient om grondiger te worden onderzocht in toekomstige studies.

Met de laatste DBD-reactor wordt de combinatie tussen plasma en adsorptie verder onderzocht door toevoeging van een actieve kooltextiel onder de stromende waterfilm. Daarnaast wordt het tijdens de behandeling geproduceerde plasmagas doorheen de oplossing geborreld in een aparte ozonisatiekamer, teneinde een tweede optimalisatie te bereiken. De verhoging in energie-efficiëntie door beide combinaties werd bevestigd met een aantal experimenten. Uit adsorptie en desorptie-experimenten blijkt dat de adsorptiesnelheid op het textiel constant blijft of zelfs verbetert na langdurig plasmacontact. Niet alleen illustreert dit dat het actieve kooltextiel een duurzame technologie vormt in combinatie met plasma, maar het wijst ook het plasma aan als een effectieve regeneratiemethode voor actieve kool. Het optimalisatie-effect van extra borrelen van plasmagas werd bevestigd door het effect te vergelijken tussen atrazinebehandeling met enkel plasma, enkel plasmagas en beide. De resultaten geven aan dat het borrelen van plasmagas bijdraagt tot 40,5% van de

totale atrazineverwijdering. Experimenten met de reactor in single-pass modus, waar water eenmalig doorheen de reactor stroomt, bewijzen ook dat toevoeging van de ozonisatiekamer de reactorprestaties verdubbelt voor het verwijderen van vijf andere stoffen. Desalniettemin is het belangrijk om het invloeiende water eerst doorheen de ozonatiekamer te laten stromen en pas daarna doorheen de plasmakamer, aangezien de omgekeerde cascadeconfiguratie steeds een slechter energierendement geeft. Dit wordt toegelicht met het wegvangen van ozon door NO_2^- ionen, die in de oplossing worden geïntroduceerd tijdens direct plasmacontact in de plasmakamer. Voor de gebruikte experimentele condities verbruikt de reactor 13,6 kWh/m^3 voor 90% atrazineverwijdering. Vergelijking met acht andere plasmareactoren in de literatuur die werden gebruikt voor atrazinebehandeling blijkt dat slechts twee andere reactoren beter presteerden dan de onze. Verdere optimalisatie van onze reactor werd onderzocht met vijf andere micropolluenten. De energie-efficiëntie van hun verwijdering in referentie-omstandigheden varieert meer dan een grootteorde, van 3,9 tot 26 kWh/m^3, met een toenemende waarde in de volgorde diuron < isoproturon < alachloor < PeCB < α-HCH. Onderzoek van het energierendement van het verwijderingsproces in functie van de initiële concentratie aan micropolluent toont een stijgende trend van G_{50} en een lichte stijging van EEO voor hogere concentraties, in overeenstemming met resultaten van andere auteurs. Daarom is het voordeliger oplossingen met hogere dichtheid en concentraten te behandelen, in tegenstelling tot verdunde oplossingen, als het doel is om zoveel mogelijk micropolluentmassa af te breken. Voor waterbehandelingstoepassingen waar de concentratie niet geregeld kan worden betekent dit echter dat verlaging van de concentratie van verontreinigingen met een factor 10 minder energie vereist bij lagere concentraties. Zoals blijkt uit onze experimenten, kan optimalisatie van de reactor worden bereikt door het verlagen van de arbeidscyclus en door het gebruik van zuurstof als voedingsgas. Variatie van vermogen bij constante arbeidscyclus, anderzijds, vertoonde een beperkt effect op de energie-efficiëntie, wat een flexibel gebruik van de plasmareactor mogelijk maakt zonder energieverlies.

Identificatie van de oxidatiebijproducten van alachloor, diuron en isoproturon in HPLC-TOF-MS analyse werd uitgevoerd door het vergelijken van hun dissociatiepatronen tijdens electrosprayionisatie met die van de moedercomponenten. Op basis van literatuurdata hebben we gedetailleerde dissociatietrajecten voorgesteld voor elke herbicide, om inzicht te krijgen in de groepspecifieke fragmentatiemechanismen van hun oxidatieproducten. Met deze methode kan de locatie van gesubstitueerde groepen op een oxidatieproduct worden gespecificeerd en kunnen de voorkeursplaatsen van ozonaanval of aanval door radicalen van de initiële componenten worden bepaald. Voor diuron en isoproturon leidt enkelvoudige demethylering van de dimethylamidefunctie tot een sterk verschillend fragmentatiemechanisme, dat wordt toegelicht aan de hand van een analogie met de bekende fragmentatie van N-methylcarbamaat pesticiden. Op één oxidatieproduct van alachloor na worden alle tussenproducten gevormd door één of meer oxidatiestappen die in 4 types kunnen worden ingedeeld: hydroxylering, substitutie van 2 H-atomen met

dubbelgebonden zuurstof, dealkylering en nitrificatie. Het laatste proces is uniek voor waterbehandeling met plasmaontlading in lucht en werd in het verleden, voor zover wij weten, slechts eenmalig vermeld in een andere studie, voor het specifieke geval van fenol. Aangezien nitrificatie een van de belangrijkste oxidatiestappen is voor diuron en isoproturon, dienen de overeenkomstige oxidatiebijproducten verder geanalyseerd te worden door middel van toxiciteitsproeven, teneinde de toepasbaarheid van luchtplasma voor waterzuivering te bepalen.

I think God's going to come down
and pull civilization over for speeding.
- Steven Wright

English summary

Hazardous micropollutants are increasingly detected worldwide in wastewater treatment plant effluent. As this indicates, their removal is insufficient by means of conventional modern water treatment techniques. In the search for a cost-effective solution, advanced treatment techniques including electrochemical separation, activated carbon, nanofiltration, reverse osmosis and advanced oxidation processes, have recently gained more attention, since they are the most effective available techniques to remove biorecalcitrant organics. However, they are associated with high energy costs and high financial costs. Moreover, all these methods, with the exception of advanced oxidation processes, have the additional problem of toxic concentrated residue disposal, as they only remove the compounds without further decomposition into less toxic by-products. Advanced oxidation techniques, on the other hand, are able to oxidize toxic compounds to smaller molecules, ideally with full mineralization to CO_2 and H_2O. Nevertheless, their weakest point is as well their high energy demand. Additionally, they can be hazardous to the environment, by their production of long-living oxidants and potentially toxic oxidation products. Therefore, research needs to focus on optimizing existing systems in order to overcome these problems.

Plasma discharge in contact with water takes a promising place among advanced oxidation processes, as it generates a wide spectrum of oxidative species in close proximity of the liquid under treatment. Further optimization of this technology, however, is a complex task due to the wide variety in reactor design and materials, discharge types, and operational parameters. In this work, an extended overview is given on plasma reactor types and the specific cases of bubble discharge and dielectric barrier discharge (DBD) reactors are investigated in more detail. The experimental part is split in two parts. In the first part, focus is aimed towards bubble discharge reactors, which are known to require less input power than reactors where discharge is generated directly into the liquid phase without externally applied bubbles. In this part, only the plasma-physical properties of bubble discharge is investigated, in order to gain a deeper understanding of the underlying mechanisms of plasma initiation and propagation and their implications on water treatment. To this end, electrical and spectroscopical analysis as well as ICCD imaging is performed for two reactor configurations. In the second part, focus is shifted to the plasma physics and chemistry in DBD reactors where discharge is in direct contact with a moving water film. Such reactor

type is expected to display less energy losses towards electrolytic processes and Joule heating of the liquid than bubble discharge reactors and reactors with plasma discharge directly into the liquid phase. Additionally, dielectric barrier discharge over water is less affected by solution properties and can easily be scaled up for the treatment of large volumes of water, making it more attractive for applications.

In literature, plasma reactors are classified generally in two or three categories, based on their plasma–water phase distributions, with further subdivision according to the discharge regime and voltage waveform. Nonetheless, reactor performance varies strongly inside each subtype, due to differences in used materials and electrode configurations. While understanding these influences is essential for smart design and optimization of plasma reactors, an overview on this topic is lacking. For that reason, an extended literature review has been performed in this work, in order to provide an overview on plasma reactor types based on reactor design and materials. Six main reactor types are distinguished, according to their plasma–water phase distributions. The possibilities to upscale each system towards larger plasma volume is discussed and influence of design, materials and operational parameters on energy efficiency is investigated. In electrohydraulic discharge reactors, where plasma is generated directly into the liquid, electrode material can have substantial influence on organic decomposition after plasma contact due to formation of erosion particles in water. Such reactors can be optimized by shifting one of the electrodes to the gas phase and transform the reactor into a hybrid type, where plasma is generated in the gas phase as well as in the liquid phase. In bubble discharge reactors, energy efficiency can be enhanced by increasing the amount of nozzle electrodes or, for the case with rising bubbles in the electrode gap, by using a double dielectric barrier or adding glass beads in the water bulk. When plasma is generated over a water film or bulk, energy efficiency can be increased by stirring or making the water flow along the plasma active zone. In spray discharge reactors, which introduce the water as droplets in the plasma zone, treatment is dependent on the droplets location. For the specific case of gliding arc, the process can be optimized by addition of a couple of controlled electrodes or a second high voltage electrode and by introducing the water perpendicular to the gas flow to improve contact with plasma. A last reactor class, which is strong competitive technology to the other plasma systems, generates plasma remotely from the liquid, with ozone reactors as the most popular variants. The dependency of energy efficiency on voltage parameters is significantly different for different reactor types. For example, positive pulse polarity causes higher efficiency in electrohydraulic and bubble discharge reactors in all considered cases, while negative polarity gives better performance in gas phase discharge reactors. Oxygen is the plasma feed gas of preference, as it generally increases energy efficiency as compared to all other gases including air and argon. For technical reasons concerning safety, however, we have used oxygen mainly in our most recent experiments, of which the majority is not included in this work.

In the first bubble discharge reactor studied in this work, pulsed spark discharge is generated in nitrogen, helium and argon bubbles in between a pin-to-plate electrode system submerged in a water solution. Electrical and spectroscopical analysis revealed two types of bubble discharge: a direct bubble discharge, with an immediate onset of a spark discharge inside the bubble, and a delayed bubble discharge, where spark discharge occurs after a delay time of typically several microseconds. Based on our measurements and previously reported experiments, a dynamic model for bubble discharge is proposed, in which the position of the bubble relative to the electrodes during application of the voltage pulse determines whether the bubble discharge is direct or delayed. This model includes the description of the plasma channel and the external pulse circuit as a series RLC circuit with constant resistance. This model is consistent with the effect of the experimental parameters on the measured plasma characteristics. For instance, the frequency of the voltage oscillations during discharge is constant in all measurements and the decay time of the damped oscillations appears to be unaffected by the bubble gas, voltage pulse amplitude and solution conductivity. The width of the H_α Balmer line in the emitted spectra is dominated by Stark broadening and implies electron densities in the order of 10^{24} to 10^{25} m^{-3}, which is relatively high in comparison with other low-temperature atmospheric plasmas. Also, the emitted spectra contain a continuum, originating from black-body radiation of the heated bubble gas. Black-body temperatures are determined to range from 6000 to 9000 K by means of a custom-made fitting algorithm, which we modified for this specific purpose.

The second bubble discharge reactor comprises a single, stationary bubble attached to a high voltage nozzle electrode, which is pointed upwards. The bubble is produced by means of a programmable syringe pump from the pure gases helium, argon, nitrogen, oxygen or air. After the bubble has reached a steady state, voltage pulses are manually triggered on the nozzle electrode. This reproducible system permits accurate investigation of the plasma onset and development, which we mainly performed with fast imaging and electrical measurements. In this configuration, bubble discharge is consistently delayed, several microseconds after the application of the voltage pulse. The plasma geometry evolves in five stages, where plasma rapidly fills the bubble and subsequently decays, followed by a dark stage, after which the plasma fills the bubble again gradually towards the upper bubble edge. The length of the dark phase and the subsequent bubble filling phase depends strongly on the bubble gas. In the fifth stage, branching streamer-like structures start to propagate from the bubble surface into the water. The investigated features of the streamers in our measurements resemble the features of pulsed streamer discharge in water, indicating they are similar in nature. Their spectrum contains a strong H_α line and a weak or absent oxygen line at 777 nm. The delay time and five stages are explained by a capacitive feature of the bubble. A simple model that considers the bubble as a classic plate capacitor is in relatively good agreement with the experimental values in our experiments. These results suggest the strong attraction of aqueous ionic species towards the bubble during the initial delay time

with a subsequent discharge that is most active at the bubble surface. This makes the system especially attractive for oxidation of ionic target compounds and surface-active agents.

With the first DBD reactor in this work, the synergetic effect between plasma discharge and micropollutant adsorption is investigated. For this purpose, a nanofiber polyamide membrane is applied as adsorbent and atrazine is chosen as model micropollutant with a considerably low initial concentration of 30 µg/L. By means of H_2O_2 and O_3 measurements and a kinetic model found in literature, the contribution of oxidation by direct ozone attack and by the peroxone (O_3/H_2O_2) process is calculated to be only about 20%. Since ozonation and peroxone are suggested in literature to be the most dominant oxidation processes in the liquid bulk, the determining oxidation reactions are occurring in the thin water layer near the plasma active region. While the H_2O_2 and O_3 production in the reactor is not influenced by the presence of the membrane, there is a significant increase in atrazine removal from 61% to 85% when the membrane is added near the active plasma region. Formation of the oxidation by-products deethylatrazine and ammelide is more pronounced in presence of the membrane, confirming more efficient decomposition and the synergy between plasma discharge and pollutant adsorption. This synergetic effect is explained with a higher local atrazine concentration near the plasma-liquid interface, which increases the frequency of direct and indirect oxidizing interactions of the micropollutant with reactive species from the active plasma region.

Before scaling up the first DBD reactor concept to a more powerful and sustainable design, plasma-physical properties are investigated of a single AC powered DBD filament in contact with a flowing water film. By means of electrical and spectroscopical analysis, simulation with COMSOL and data processing with BOLSIG+, several plasma parameters of the discharge filament are determined, including the rotational and vibrational N_2 temperatures, the reduced electric field in the middle of the electrode gap, electron mobility and current density. From these parameters, electron density is calculated to be in the order of $n_e \approx 10^{14}$ cm^{-3}. All the obtained plasma parameter values are in good agreement with literature values for DBD microfilaments in atmospheric air in between solid electrodes. Discharge evolution, however, is remarkably different from the one usually observed for the solid electrode counterpart. While in the negative voltage half cycle, one intense light pulse is seen as in the solid electrode case, the positive half cycle starts with a less intense light pulse followed by a hump in the photocurrent. The hump is associated with an intense cathode spot at the water surface and an upwards moving glow-like discharge wave at the dielectric surface, indicating stepwise charge deposition on the barrier. This phenomenon is characteristic for resistive barrier discharge, where one electrode acts as a resistive barrier, which is the water electrode in our case. Cathode fall formation only occurs at the water cathode during the positive voltage half cycle for the entire working range of the power source. This preference can have many causes, including local field enhancement by water surface deformation or droplet formation, local ionization enhancement by the inhomogeneous humidity profile and

more effective secondary electron emission at the water electrode than at the dielectric barrier. Similar mechanisms can be the underlying cause of the glow-like discharge spot which is continuously observed at the water electrode during the entire voltage cycle. This cathode spot indicates the continuous generation of oxidative species at the water layer, even when plasma has decayed in all other parts of the electrode gap. This new insight is very interesting in the light of water treatment applications and deserves to be investigated more thoroughly in future studies.

In the last DBD reactor, the combination of plasma and adsorption is further explored by applying an activated carbon textile underneath the flowing water film. The plasma gas produced during treatment is additionally bubbled through the solution in a separate ozonation chamber, in order to reach a second optimization. Enhancement of energy efficiency by both combinations is confirmed with several experiments. Adsorption and desorption experiments reveal that the adsorption rate on the textile remains constant or even improves after long periods of plasma contact. Not only does this illustrate that the activated carbon textile is a sustainable technology when combined with plasma, it also indicates plasma as an effective regeneration method for activated carbon. The optimization effect of additional plasma gas bubbling has been confirmed by comparing the effect of atrazine treatment with only plasma, only plasma gas bubbling and both. The results indicate that plasma gas bubbling contributes for up to 40.5% to the total atrazine removal. Experiments with the reactor in single-pass mode, where water flows through the reactor only once, prove as well that addition of the ozonation chamber approximately doubles reactor performance for removal of five different compounds. Nonetheless, it is important to let the influent water flow through the ozonation chamber first and only afterwards through the plasma chamber, since the reverse cascade configuration gives consistently worse energy efficiency. This is explained with scavenging of ozone by NO_2^- ions, which are introduced into the solution during direct plasma contact in the plasma chamber. For the used experimental conditions, the reactor consumes 13.6 kWh/m^3 for 90% of atrazine removal. Comparison with 8 other plasma reactors reported in literature for atrazine treatment shows that only two other reactors performed better. Further optimization of our reactor is investigated with five other compounds. Energy efficiency of their removal in reference conditions ranges over one order of magnitude, from 3.9 to 26 kWh/m^3, with increasing value in the order diuron < isoproturon < alachlor < PeCB < α-HCH. Investigation of the removal energy efficiency as a function of the initial micropollutant concentration showed an increasing trend of G_{50} and a slight increase in EEO for higher concentrations, in agreement with results from other authors. Therefore, it is more advantageous to treat dense solutions or concentrates as opposed to dilute solutions if the aim is to decompose as much pollutant mass as possible. For water treatment applications where concentration cannot be controlled, however, this means that reducing the pollutant concentration with a factor 10 will require less energy at lower concentrations. As shown in our experiments, optimization of the reactor can be reached by lowering the duty cycle and by using oxygen as feed gas. Variation

of power at constant duty cycle, on the other hand, displayed a limited effect on the energy efficiency, which allows flexible operation of the plasma reactor without energy loss.

Identification of the oxidation by-products of alachlor, diuron and isoproturon in HPLC-TOF-MS analysis is performed by comparing their dissociation patterns during electrospray ionization with the ones of the mother compounds. Based on data found in literature, detailed dissociation pathways are proposed for each herbicide, in order to gain insight into the group-specific fragmentation mechanisms of their oxidation by-products. Using this technique, the location of substituted groups on the oxidation by-product can be specified and the preferable sites of ozone or radical attack on the initial compounds can be determined. For diuron and isoproturon, single demethylation of the dimethyl amide function gives rise to a significantly different fragmentation mechanism, which is explained with an analogy to the known fragmentation of N-methyl carbamate pesticides. Apart from one by-product from alachlor, all intermediates are explained with one or more oxidation steps that can be classified into 4 types: hydroxylation, substitution of 2 H atoms with double bonded oxygen, dealkylation and nitrification. The latter process is unique for water treatment with plasma discharge in air and has, to our knowledge, only been reported once before, for the specific case of phenol. Since nitrification is one of the major oxidation steps for diuron and isoproturon, the corresponding oxidation by-products require further analysis by means of toxicity tests in order to understand the feasibility of air plasma for water purification.

Everything is theoretically impossible, until it is done.
- Robert A. Heinlein

Chapter 1

Introduction

1.1 Plasma in contact with liquid

As solid substance transforms to liquid and liquid to gas by addition of energy, gas can be further excited to the fourth state of matter, called plasma or gas discharge. Plasma is encountered in many forms, from the low pressure plasma in the interstellar medium to the high pressure and highly energetic fusion processes in the core of the sun. While such astrophysical plasmas have been extensively studied and described in the past and 21st century, a lot of interest has been directed to gas discharges at laboratory scale as well. Among them, atmospheric pressure plasmas in particular are interesting from industrial point of view, since they can operate in ambient air without the use of vacuum pumps or compressors. In many applications, heating up the gas is undesired, which can be avoided by working outside of thermodynamic equilibrium. The resulting non-equilibrium plasma, often termed nonthermal plasma, has the additional advantage of having higher energy efficiency. That is, energy does not need to be spread into all degrees of freedom, such as into the thermal motion, rotation, and vibration of neutral gas molecules, but only into those degrees of freedom that efficiently generate the desired reaction products for the intended application. Accelerating electrons to high velocities is sufficient to excite and ionize molecules by impact while keeping the gas at relatively low temperature. With an appropriate electron energy distribution, some reactions can be triggered very specifically. In this manner, electromagnetically generated plasmas can be turned into a specialized tool. Energy can be channeled into desired excitations and reactions by variation of gas composition, electrode shape, dimensions, circuit characteristics and other operational parameters.

Nowadays, nonthermal plasma is investigated for a variety of intended applications such as sterilization, decontamination, gas cleaning, chemical synthesis and conversion, surface modification of polymeric substrates, coating, and biomedical applications. More specifically, plasma in contact with liquid can be applied in water treatment and industrial waste processing for organic, inorganic and biological decontamination, as well as in high power switching devices, for shock wave production in treatment of kidney stones, for synthesis of nanomaterials and polymers, and for spectroscopical detection of water contaminants. For every application, different plasma sources and reactors can be developed and adapted in order to obtain optimal plasma properties, which can accordingly be investigated with a wide spectrum of diagnostic techniques. Finding the link between plasma properties and the observed effects is essential for further method optimization. Moreover, such interrelationships can provide key information on applications where plasma is brought in contact with biological matter, since biological tissue or organisms are naturally surrounded by a liquid layer. These include biomedical applications, which are often subdivided in three promising research fields: plasma treatment of dental cavities, wounds, and cancer. While the former has not received yet the attention it deserves, the effectiveness of plasma for wound healing and cancer treatment is supported by a quickly growing amount of evidence in recent years. Closely related is the plasma treatment of seeds, which has recently been shown to improve germination and growth of several plant species, thus opening a new field in agricultural biotechnology as well. Apart from the mentioned applications, the science of plasma in contact with liquid can also provide a deeper understanding of a few naturally occurring phenomena, such as ultrasonic and biological sonoluminescence.

Plasma in contact with liquids is generally harder to investigate than their counterparts in the gas phase for multiple reasons:

- They occur in inhomogeneous gas-liquid phase in highly non-equilibrium state.
- Their complex discharge geometry and the surrounding liquid prevent the application of several diagnostic techniques.
- The liquid is acting as one of the electrodes in most cases, giving a deformable and evaporating electrode.
- When plasma is ignited directly in the liquid phase, the submerged electrode also deforms, as it erodes under plasma action. As an effect, the curvature of sharp electrodes changes in time, while metal and oxide nanoparticles accumulate in the liquid.
- Liquid properties such as conductivity and temperature often change under influence of the plasma, impeding reproducibility of experiments. At high conductivity, for example, a shielding effect on the electrical field can occur by free charge. Accordingly, liquid conductivity influences the excitation and radical production efficiency, especially in case of electrical discharge in a bubble or directly into the

liquid phase. Higher temperature, on the other hand, leads to faster cavitation in the liquid and stronger evaporation. Water vapor concentration in the gas phase strongly interferes with ignition and other properties of the plasma, therefore making reproducibility harder to attain.

Due to these complications, many of the fundamental mechanisms behind plasma-liquid interactions are still poorly understood. For electrical discharge in bubbles or directly into the liquid phase, the exact location, timing and underlying processes of plasma onset and propagation are still a topic under discussion. For electrical discharge ignited in the gas phase, plasma behavior in close proximity of the liquid interface remains largely uncomprehended as well. While plasma-liquid interface deformation with or without shockwave generation has been described in detail for a few electrode configurations and discharge regimes, this information is yet lacking in the majority of cases.

Furthermore, in the specific context of water treatment, many research questions remain unanswered on the underlying chemistry and treatment effects. These questions involve plasma chemistry at the water interface, the transfer and transformation of reactive species through the plasma-water barrier, and the resulting chemistry in the water bulk. As discussed in the following chapter, it is very beneficial to combine electrical discharge with other advanced water treatment techniques. The observed synergy of such combination gives rise to an even more complex chemistry. More insight is required in the dominant decontamination mechanisms for removal of organic, inorganic and biological water pollution in order to make the process more efficient and to decide upon the most efficient and versatile reactor types. Besides, reactor optimization can only be achieved when the influence of operational parameters is sufficiently understood. This influence has shown to be characteristic for every reactor type, creating the need for a systematic overview. In light of reactor optimization, an interesting new research topic is devoted to the decontamination chemistry that remains active long after plasma treatment has ended. So called "plasma-activated water" with sterilization effects up to 6 hours after plasma contact has quickly become a hot topic in last years, with many questions still to be answered. In contrast, post-treatment degradation of organic contaminants has received only little attention up to now. Last but not least, it is necessary to investigate more deeply the limitations and possible hazards of the plasma process. Although oxidation by-products are more frequently analyzed in studies on plasma treatment of organic water contamination, only sporadically a toxicity analysis is performed. Nevertheless, accurate information on the global toxicity of the effluent water is essential to bring this technology into practice.

1.2 Scope and methods of the dissertation

This dissertation focuses on most of these questions for one or more electrode configurations and discharge regimes. While most of the applied methods are experimental in nature, significant effort has been put into literature study as well. For the experiments, plasma

reactors are utilized in which electrical discharge is ignited either in a gas bubble or in gas phase over a moving water film. A strong accent is kept on the application of these reactors for micropollution removal. For this application, it is necessary to understand the benefits and drawbacks of each reactor in comparison to other plasma techniques and alternative water treatment methods. Although a few reviews on this topic could be found in literature nowadays, a comprehensive overview was lacking. To overcome this shortage, an extensive review has been made in the next two following chapters, based on more than 300 references.

The experimental measurement methods can mainly be split up into plasma diagnostics and chemical analysis. A variety of plasma diagnostical techniques has been used to gain detailed information on several plasma properties:

- With electrical characterization by means of voltage and current waveforms, it is possible to investigate the timing of plasma phenomena as well as the capacitive behavior of the discharge.
- Spectroscopical characterization is usually performed with optical emission spectroscopy. From the features of spectral peaks or continuous radiation, properties such as electron density and plasma temperature can be deduced, with or without the use of specialized analysis and simulation software. The time dependency of a selected peak and thus of the corresponding excited species can be measured by combining a photomultiplier tube with an appropriate narrow spectral filter.
- Time- and space-resolved characterization is carried out by means of ICCD-imaging with resolution in nanosecond scale. With this technique, the timing and location of plasma evolution can be charted.

Chemical analysis, on the other hand, has been utilized to measure the aqueous contamination before, during and after treatment:

- To transfer the contamination from water solution to mobile state, either a solid phase microextraction (SPME) fiber was used or liquid-liquid extraction from water to dichloromethane.
- With gas chromatography – mass spectrometry (GC-MS), the concentration of the main micropollutant is measured as a function of treatment time. From the resulting oxidation kinetics, quantities such as reaction rate constant, energy yield and electrical energy per order are calculated.
- High performance liquid chromatography – high resolution mass spectrometry (HPLC-HRMS) is carried out for identification of oxidation by-products during plasma treatment.

Apart from these methods, the reactors were also characterized for their H_2O_2 and O_3 production. H_2O_2 concentration was determined with a photometric method using metavanadate ammonium, while O_3 was measured with an ozone monitor. Temperature and

pH were monitored as well, since they are essential in understanding the underlying chemistry.

1.3 Outline

The present dissertation consists of three main parts. In the first part, the potential role and versatility of plasma technology in water treatment is further defined by means of a broad literature study:

- Chapter 2 explains the limitations of conventional water treatment methods for the removal of micropollution and the need for more advanced treatment techniques. The potential and position of plasma technology in this question is discussed thoroughly, including different treatment strategies.
- Chapter 3 presents several plasma technologies that can be applied in water treatment. First, different approaches for reactor classification will be analyzed in detail. Next, an extended overview will be given of different plasma reactor types, where classification is based on reactor design and reactor materials. Afterwards, the influence of multiple working parameters on reactor energy efficiency is discussed. The final section of this chapter gives a summary with future prospects and concluding remarks on the research that is still required in this field.

The second part of this dissertation focuses on the characterization of electrical discharge in gas bubbles in water, as an example of a more fundamental approach in the application of water treatment with plasma:

- Chapter 4 deals with the electrical and spectroscopical characterization of underwater plasma discharge in rising gas bubbles. After description of the used multi-bubble plasma reactor and analysis methods, two types of discharge are deduced from the voltage and current waveforms: direct bubble discharge and indirect bubble discharge. Next, the influence on the discharge of several working parameters and of the observed delay time is investigated. Afterwards, bubble temperature and electron density are calculated from, respectively, the black-body radiation and Stark broadening in the obtained optical emission spectra of the discharge.
- Chapter 5 presents the time-resolved characterization of pulsed discharge in a stationary bubble in contact with a high voltage needle electrode. By means of ICCD imaging, 5 stages in the plasma geometry evolution are observed. The discharge onset and 5 stages are explained with a capacitive model for the bubble. The relevance of this capacitive feature for water treatment purposes is shortly discussed.

The third part of this dissertation deals with the characterization and optimization of dielectric barrier discharge (DBD) over a moving water film:

- In chapter 6, the synergetic effect of DBD and adsorption for micropollutant removal is explored, by adding an adsorptive nanofiber membrane into a pulsed DBD reactor. The influence of the membrane on O_3 and H_2O_2 production and decomposition of atrazine traces in the treated solution is investigated. The contribution of O_3 and H_2O_2 in the degradation process is estimated by means of a kinetic model proposed in literature. Lastly, detected oxidation by-products are compared with atrazine oxidation by-products found in other studies.
- Chapter 7 presents the spectroscopical, electrical and time-resolved characterization of an AC dielectric barrier single micro-discharge filament with a thin water layer as a second electrode. From optical emission spectra, synthesis software and simulation software, rotational and vibrational temperature are determined, as well as reduced electrical field and electron mobility. From ICCD imaging and the current waveform, current density is estimated, finally leading to the calculation of the electron density. Six stages are observed in the plasma evolution, including three dark stages, which are partly explained with glow-like behavior of the discharge.
- Chapter 8 describes the operation of a DBD reactor in which the treated solution flows as a water film over an activated carbon textile along the active plasma. First, the chemistry of this reactor for air plasma is extendedly schematized and discussed, based on literature and on measurement of O_3 and H_2O_2 production. First degradation experiments are performed with atrazine as model micropollutant for determination of decontamination kinetics and oxidation by-products. The reactor is compared in energy efficiency for atrazine removal with other plasma reactors reported in literature. Next, the functionality and sustainability of the activated carbon textile is established by means of adsorption and desorption experiments. In the last part of the chapter, the removal of three other pesticides and two volatile chlorinated compounds is studied in more detail for a slightly different configuration of the reactor. Decontamination kinetics are investigated as a function of several working parameters and conditions in order to make suggestions on further reactor optimization. Detected oxidation by-products of the three pesticides and their kinetics are discussed and compared with literature, with proposal of the oxidation pathway.

Chapter 9 contains the concluding remarks and future prospects of the presented research. Next to a summary of the most important results and their interpretation, suggestions will be made on how to continue this line of research in order to find answers on the most pressing questions.

1.4 Publications and contributions

1.4.1 Publications in international journals

R. Xiong, A. Nikiforov, **P. Vanraes**, C. Leys, Hydrogen peroxide generation by DC and pulsed underwater discharge in air bubbles, Journal of Advanced Oxidation Technologies, 15(1), 197-204, 2012.

P. Vanraes, A. Nikiforov, C. Leys, Electrical and spectroscopic characterization of underwater plasma discharge inside rising gas bubbles, Journal of Physics D: Applied Physics 45.24, 245206, 2012.

R. Xiong, A. Nikiforov, **P. Vanraes**, C. Leys, Characteristics of an underwater direct current discharge in bubbles and the temperature distribution in the bubbles, Physics of Plasmas, 19(2), 023501, 2012.

R. Xiong, Q. Xiong, A. Nikiforov, **P. Vanraes**, C. Leys, Influence of helium mole fraction distribution on the properties of cold atmospheric pressure helium plasma jets, Journal of Applied Physics, 112(3), 033305, 2012.

Q. Xiong, A. Nikiforov, L. Li, **P. Vanraes**, N. Britun, R. Snyders, C. Leys, Absolute OH density determination by laser induced fluorescence spectroscopy in an atmospheric pressure RF plasma jet, The European Physical Journal D, 66(11), 1-8, 2012.

X.L. Deng, A. Nikiforov, **P. Vanraes**, C. Leys, Direct current plasma jet at atmospheric pressure operating in nitrogen and air, Journal of Applied Physics, 113(2), 023305, 2013.

X. Deng, A. Nikiforov, **P. Vanraes**, C. Leys, Deposition of nanosilver-organosilicon composite films using an atmospheric pressure DC plasma jet, Romanian Reports in Physics, 66(4), 1088-1098, 2014.

A. Nikiforov, L. Li, N. Britun, R. Snyders, **P. Vanraes**, C. Leys, Influence of air diffusion on the OH radicals and atomic O distribution in an atmospheric Ar (bio) plasma jet, Plasma Sources Science and Technology, 23(1), 015015, 2014.

H. Ghodbane, O. Hamdaoui, J. Vandamme, J. Van Durme, **P. Vanraes**, C. Leys, A. Nikiforov, Degradation of AB25 dye in liquid medium by atmospheric pressure non-thermal plasma and plasma combination with photocatalyst TiO_2, Open Chemistry, 13(1), 2015.

P. Vanraes, G. Willems, N. Daels, S.W. Van Hulle, K. De Clerck, P. Surmont, F. Lynen, J. Vandamme, J. Van Durme, A. Nikiforov, C. Leys, Decomposition of atrazine traces in water by combination of non-thermal electrical discharge and adsorption on nanofiber membrane, Water Research, 72, 361-371, 2015.

P. Vanraes, G. Willems, A. Nikiforov, P. Surmont, F. Lynen, J. Vandamme, J. Van Durme, Y.P. Verheust, S.W.H. Van Hulle, A. Dumoulin, C. Leys, Removal of atrazine in water by combination of activated carbon and dielectric barrier discharge, Journal of Hazardous Materials, 299, 647–655, 2015.

1.4.2 Chapters in international publications

P. Vanraes, A.Y. Nikiforov, C. Leys, Electrical Discharge in Water Treatment Technology for Micropollutant Decomposition, Plasma Science and Technology, Intech Open, ISBN 978-953-51-4617-9, 2015.

1.4.3 Conference papers and extended abstracts

P. Vanraes, A. Nikiforov, C. Leys, L. Němcová, F. Krčma, Under Water Discharge in Bubbles in Very Low Conductive Solutions, 18th Symposium on Application of Plasma Processes (SAPP XVIII), Workshop on Plasmas as a Planetary Atmosphere Mimics, January 15-20, 2011, Vrátna, Slovakia, Book of Contributed Papers, p. 88-92.

Z. Kozakova, F. Krcma, M. Vasicek, L. Hlavata, L. Hlochova, **P. Vanraes**, Generation of pin-hole discharges in liquids, The XXI Europhysics Conference on Atomic and Molecular Physics of Ionized Gases (ESCAMPIG XXI), July 10-14, 2012, Viana do Castelo, Portugal, Conference Proceedings, ISBN: 2-914771-74-6, 4 pages.

P. Vanraes, A. Nikiforov, M. Lessiak, C. Leys, Time-resolved characterization of a pulsed discharge in a stationary bubble, 12th High-Tech Plasma Processes conference (HTPP-12), June 24-29, 2012, Bologna, Italy, Journal of Physics: Conference Series 406(1), p. 012013, December 2012, 10 pages.

P. Vanraes, A. Nikiforov, E. Vyhnankova, M. Subrt, F. Krčma, M. Vávrová, P. Surmont, F. Lynen, N. Daels, K. De Clerck, S.W.H. Van Hulle, J. Vandamme, J. Van Durme, C. Leys, Plasma-assisted decomposition of atrazine traces in water, International Congress on Water, Waste and Energy Management (EWWM 2014), July 16-18, 2014, Porto, Portugal, ISBN 978-989-95089-5-8, 4 pages.

P. Vanraes, G. Willems, A. Nikiforov, P. Surmont, F. Lynen, N. Daels, K. De Clerck, S.W.H. Van Hulle, J. Vandamme, J. Van Durme, C. Leys, Decomposition of atrazine traces in water by plasma discharge, Hakone XIV, September 21-26, 2014, Zinnowitz, Germany, Book of contributions, 5 pages.

1.4.4 Abstracts and oral presentations in international conferences

P. Vanraes, A. Nikiforov, M. Lessiak, C. Leys, Time-resolved characterization of a pulsed discharge in a stationary bubble, 12th High-Tech Plasma Processes conference (HTPP-12), June 24-29, 2012, Bologna, Italy.

P. Vanraes, A. Nikiforov, C. Leys, A new water treatment technique with plasma and photo-induced catalysis for destruction of traces of persistent organic pollutants, 8th Conference on Sustainable Development of Energy, Water and Environment Systems (SDEWES 2013), September 22-27, 2013, Dubrovnik, Croatia.

P. Vanraes, A. Nikiforov, E. Vyhnankova, M. Subrt, F. Krčma, M. Vávrová, P. Surmont, F. Lynen, N. Daels, K. De Clerck, S.W.H. Van Hulle, J. Vandamme, J. Van Durme, C. Leys, Plasma-assisted decomposition of atrazine traces in water, International Congress on Water, Waste and Energy Management (EWWM 2014), July 16-18, 2014, Porto, Portugal.

1.4.5 Abstracts and poster presentations in international conferences

P. Vanraes, A. Nikiforov, C. Leys, Electrical and spectroscopical characterization of pulsed single bubble discharge in water with a pin-to-plate electrode configuration, 11th High-Tech Plasma Processes Conference (HTPP 11), June 27 to July 2, 2010, Brussels, Belgium.

P. Vanraes, A. Nikiforov, C. Leys, Characterization of bubble discharge in water, Congress Centre 18th International Colloquium on Plasma Processes (CIP-2011), July 4-8, 2011, Nantes, France.

P. Vanraes, G. Willems, A. Nikiforov, N. Daels, K. De Clerck, P. Surmont, F. Lynen, C. Leys, The use of pulsed DBD discharge above water in combination with nanofiber filtration for control of micropollutants in water, The XXII Europhysics Conference on Atomic and Molecular Physics of Ionized Gases (ESCAMPIG XXII), July 15-19, 2014, Greifswald, Germany.

P. Vanraes, G. Willems, A. Nikiforov, P. Surmont, F. Lynen, N. Daels, K. De Clerck, S.W.H. Van Hulle, J. Vandamme, J. Van Durme, C. Leys, Decomposition of atrazine traces in water by plasma discharge, Hakone XIV, September 21-26, 2014, Zinnowitz, Germany.

P. Vanraes, A. Nikiforov, C. Leys, A barrier single micro-discharge with thin water layer as second electrode, 11th Frontiers in Low Temperature Plasma Diagnostics (FLTPD-XI), May 24-28, 2015, Porquerolles Island, Hyères, France.

P. Vanraes, A. Nikiforov, C. Leys, Decomposition of micro-pollutants in water by combination of non-thermal electrical discharge and adsorption on nano-fiber materials, 22nd International Symposium on Plasma Chemistry (ISPC 2015), July 5-10, 2015, Antwerp, Belgium.

P. Vanraes, A. Nikiforov, P. Cools, C. Leys, Micropollutants removing in water treatment processes by combination of a barrier discharge and adsorption on nano-materials, Bioplasmas and Plasmas with liquids - Joint Conference of COST ACTIONS TD1208 "Electrical discharges with liquids for future applications" & MP1101 Biomedical

Applications of Atmospheric Pressure Plasma Technology, September 13-17, 2015, Bertinoro, Italy.

1.4.6 Abstracts and poster presentations in national conferences

P. Vanraes, C. Leys, Characterization of plasma discharge in single gas bubbles in water, The 11th edition of the FirW PhD Symposium, December 1st, 2010, Ghent University, Ghent, Belgium.

In one drop of water are found all the secrets of all the oceans.
- Khalil Gibran

Chapter 2

Micropollution and removal strategies

In this chapter, the current status and limitations of both conventional and advanced water treatment systems are explained in detail, with a focus on their performance on micropollutant removal. This context is necessary to understand the role that plasma technology can play in the future challenges of water purification, which is the main topic of this chapter. Further, it opens a clear perspective on research which still needs to be done in order to turn the plasma treatment of water into a mature technology. This chapter focuses mainly on the possible application of plasma discharge for direct water treatment. It should be kept in mind, however, that plasma technology can also be applied for preparation and recycling of water treatment materials and processing of water treatment residues.

With ongoing improvement of chemical analytical methods, a wide spectrum of compounds and their transformation products are increasingly detected in water bodies and sewage sludge. Many of these compounds occur in low concentrations in the range of microgram to nanogram per liter. They are therefore called micropollutants. Among these are food additives, industrial chemicals, pesticides, pharmaceuticals and personal care products. Even with such low concentrations, various environmental effects have been observed. Continuous release of antibiotics in the environment leads, for example, to increasing resistance of microorganisms [1]. Chronic exposure of aquatic life to endocrine disruptive compounds causes feminization, masculinization, and immunomodulating effects in fish and frogs, which has tremendous effects on the ecosystem [2, 3]. Additionally, there is growing concern for the direct acute and chronic effects of micropollutants on human health and safety [4-8]. Although more insight is gained on the impact of individual micropollutants, their synergistic, additive, and antagonistic effects are still vastly unknown. Some countries

or regions have adopted regulations for a small number of compounds. Nevertheless, effluent limitation guidelines and standards do not exist for most micropollutants.

The primary source of many micropollutants in aquatic systems is the effluent of conventional wastewater treatment plants. An example of such treatment plant is schematically shown in Figure 2.1. The treatment process occurs in sequential steps:

- Primary treatment consists of a series of mechanical and/or physicochemical treatment steps which remove solids, oil and fat. This step is usually common to all wastewater treatment plants [9]. During pretreatment, large debris is eliminated, as it can damage or clog pumps and sewage lines in later steps. Next, abrasive particles are withdrawn, such as grit, sand, oil and fat. As a third step, a primary clarifier removes the last part of solid material before the wastewater is send to the secondary treatment unit. With this solid material, as much as possible biodegradable material is removed as well in order to significantly reduce oxygen demand and therefore costs in the later biological treatment unit. Overall, primary treatment removes almost half of the suspended solids in raw wastewater [10]. Sometimes, pH adjustment for neutralization is added as a last step of primary treatment to make the effluent suitable for secondary treatment [11].
- Secondary treatment usually consists of biological conversion of dissolved and colloidal organic compounds into stabilized, low energy compounds, by means of a diversified group of microorganisms in presence of oxygen. Additionally, new cells of biomass are generated during this biological treatment step. The mixture of microorganisms with inorganic and organic particles contained in the suspended solids is referred to as activated sludge. Secondary treatment can differ substantially between wastewater treatment plants, as it depends on the nature of the activated sludge [9].
- Tertiary treatment, also called water polishing, consists of any additional treatment, which is carried out to make the effluent quality more suitable for discharge in the receiving environment. Chlorination is the most common method of wastewater disinfection due to its low costs. Nevertheless, it can lead to formation of chlorinated organic compounds that may be carcinogenic or harmful to the environment. Therefore, also ultraviolet disinfection is increasingly finding application in wastewater treatment plants [12]. Additional pollutant removal can be achieved with sand filtration, biological nutrient removal, adsorption on activated carbon, membrane processes, and advanced oxidation processes [9, 12]. However, many conventional wastewater treatment plants have no or limited tertiary treatment, due to the high costs associated with most of these methods.

As should be noted, organic pollution that enters a wastewater treatment plant has three outlets: effluent water, excess sludge and exhaust gas in the form of CO_2 or volatile organic compounds. Excess sludge disposal is complex since it contains a high concentration of harmful substances and only a small part of it consists of solid matter. Sludge treatment is required to reduce the water and hazardous organic content and to render the processed

solids suitable for reuse or final disposal. Therefore, sludge is processed in sequential steps of thickening, digestion, and dewatering before disposal [10].

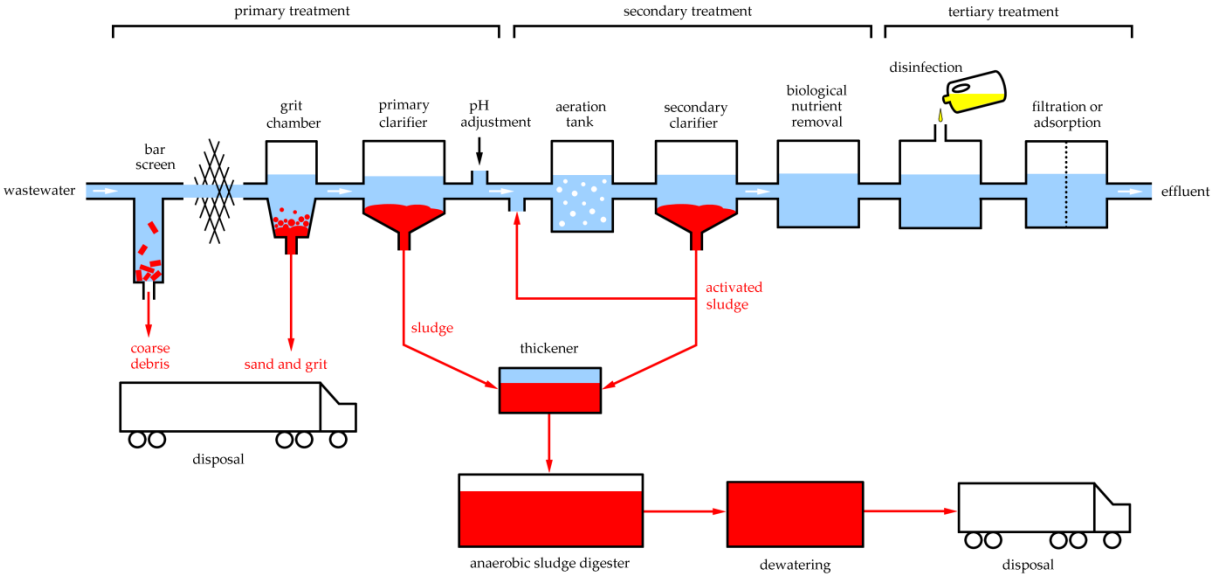

Figure 2.1 Simplified scheme of a conventional wastewater treatment plant, adapted from Flores Alsina and Benedetti et al. [10, 13].

Up to now, conventional treatment plants cannot sufficiently remove micropollutants, as shown by many studies worldwide [13]. Several options are available to improve the elimination of these contaminants, including:

- Prevention by application of products without micropollutants or only with micropollutants that are easily removed
- Reassessment and optimization of current treatment processes
- Pretreatment of hospital and industrial effluents
- End-of-pipe upgrading of wastewater treatment plants

Preventive measures will always be limited by the increased demand for industrial, pharmaceutical, and personal care products. Moreover, highly stable micropollutants such as the pesticide atrazine are detected even several years after the discontinuation of their use. Hence, more effective water treatment processes are required. Existing processes in water treatment plants can be optimized by increased sludge ages and hydraulic retention times in conjunction with nutrient removal stages and the varying redox conditions associated with them. Temperature and pH control can also enhance micropollutant removal. According to the reviews by Jones et al. and Liu et al., this is expected to be the most economically feasible approach to increase overall water treatment plant performance [14, 15]. While such measures indeed lead to more effective removal of micropollution in general, they often have limited or negligible effect on several specific persistent micropollutants, as shown in the extended review by Luo et al. [13].

The removal difference among different compounds can be partly ascribed to micropollutant properties. For example, Henry's law constant as a measure of compound volatility gives an

indication how easily a contaminant will be removed by aeration and convection. In activated sludge processes, the solid–water distribution coefficient K_d has been proposed as a relative accurate indicator of sorption behavior [16, 17]. It is defined as the partition of a compound between the sludge and the water phase and takes into account both hydrophobicity and acidity of the molecule. The biodegradation of micropollutants is more complex to predict, but compound structure is an important indicator. Highly branched side chains and sulfate, halogen, or electron withdrawing functional groups generally make a contaminant less biodegradable. Also, saturated or polycyclic compounds show high resistance to biodegradation [18, 19].

In order to remove such persistent compounds, an additional secondary or tertiary treatment step for wastewater is required. As a cost-effective alternative, the treatment of hospital and industrial effluent can solve the problem at its source. For these purposes, several advanced treatment techniques have been proposed in recent years. Each removal option has its own limitations and benefits in removing trace contaminants. A complete review on this topic was conducted by Luo et al. [13]. Advanced biological treatment techniques are advanced activated sludge (see for instance [20, 21]), membrane bioreactors, and attached growth technology. As in the case of conventional biological treatment, these methods are commonly unable to remove polar persistent micropollutants. Coagulation–flocculation processes yield ineffective elimination of most micropollutants. In contrast, electrochemical separation treatment methods such as electrocoagulation and internal microelectrolysis give very good results, as discussed by Sirés and Brillas [22]. Activated carbon, nanofiltration, and reverse osmosis are generally also very effective for removal of trace contaminants. However, they are associated with high energy costs and high financial costs. Moreover, all these separation methods have the additional problem of toxic concentrated residue disposal, as they only remove the compounds without further decomposition into less toxic by-products. Adsorbed toxic concentrates are also associated with an environmental hazard during disposal, since persistent toxic compounds are not decomposed after adsorption and desorption. For the specific case of activated carbon, adsorbed compounds can be released into the environment during thermal regeneration, the most widely used regeneration technique. This issue is, for instance, discussed in [23] for activated carbon exhausted with siloxanes, which have been assessed for their human and environmental risks, as well as their atmospheric transport pathways and bioaccumulation. Regeneration of activated carbon by means of organic chemical regenerants with solubilizing powers, on the other hand, implies the transfer of adsorbed compounds towards the solvent and therefore also results in a liquid concentrate and the problem of its disposal [24]. Advanced oxidation techniques, on the other hand, are able to oxidize toxic compounds to smaller molecules, ideally with full mineralization to CO_2 and H_2O [25]. Nevertheless, their weakest point is as well their high energy demand. Additionally, they can be hazardous to the environment, by their production of long-living oxidants and potentially toxic oxidation products. Therefore, research needs to focus on optimizing existing systems in order to overcome these problems.

Optimal water treatment schemes will eventually be decided upon, achieving effluent limitations set by national or international environmental regulations at a reasonable cost. In their extended reviews, Jones et al. and Liu et al. conclude that it seems unpractical for activated carbon, nanofiltration, reverse osmosis, and advanced oxidation techniques to be widely used in conventional wastewater treatment [14, 15]. However, with more and more shortages of drinking water all over the world, the recycling of wastewater treatment plant effluents as a drinking water source seems just a question of time. For such purpose, these technologies may be advantageous due to their high removal efficiency. Moreover, with the recent developments in energy harvesting in wastewater treatment [26, 27], one needs to consider the possibility to make wastewater treatment plants self-sustainable in power consumption, even with additional implementation of advanced treatment. As mentioned above, the treatment of hospital and industrial effluent can be a cost-effective approach as well. This last approach has gained a lot of attention over the past several years. For an overview of research done in this field for the case of hospitals, the reader is referred to the reviews of Verlicchi et al. [28, 29].

Comninellis et al. propose in their perspective article a strategy for wastewater treatment, depending on the water's total organic content, biodegradability, toxicity, and other physicochemical requirements, such as transparency [30]. According to this strategy, the use of cost-effective biological treatment is only advised when total organic content is high enough. If such wastewater is not biodegradable, advanced oxidation can be used as pretreatment step, to enhance biodegradability and reduce toxicity. One needs to consider, however, that presence of oxidant scavengers can sabotage the oxidation efficiency. Therefore, the used oxidation technology needs to be geared toward the wastewater under treatment. In the case that total organic content is low, wastewater possesses little metabolic value for the microorganisms. Then, advanced oxidation technology which effectively mineralizes the targeted pollution can be applied as a one-step complete treatment method. Alternatively, separation treatment can be applied prior to advanced oxidation, where pollutants are transferred from the liquid to another phase and subsequently posttreated.

Following this line of thought, advanced oxidation techniques take a promising place in the quest for micropollutant removal, as they appear the most effective methods for the decomposition of biorecalcitrant organics. However, in this time of a growing energy crisis and concerns over global warming, removal efficiency should not be the only objective. Sustainable development on the whole must to be considered. Therefore, the main objective of research on advanced oxidation technology should be optimization in terms of energy cost and effluent toxicity as well as its compatibility with biological treatment.

Examples of advanced oxidation processes are ozonation, hydrogen peroxide addition, chlorination, Fenton process, UV irradiation, radiolysis, microwave treatment, subcritical wet air oxidation, electrochemical oxidation, homogeneous and heterogeneous catalytic oxidation, ultrasonication and combinations thereof, such as peroxonation, photocatalysis, and electro-Fenton process.

One type of oxidation method is typically insufficient for micropollutant removal, while a combination of oxidation methods with each other or other advanced treatment techniques leads to significant improvement up to complete removal, as concluded in many reviews, such as for antibiotics [31], for pharmaceuticals [32], for UV-based processes [33] and for the general case [34, 35]. Subcritical wet air oxidation is not feasible for micropollutant removal [36].

Oturan and Aaron conclude from their review that chemical methods such as Fenton's process and peroxonation perform worse than photochemical, sonochemical, and electrochemical advanced oxidation techniques [35]. For the latter three technologies, they further conclude the following:

- Among the photochemical methods, photo-Fenton process and heterogeneous photocatalysis possessed in most cases a better efficiency than H_2O_2 and O_3 photolysis. Moreover, the solar photo-Fenton process and solar photocatalysis reduce energy consumption even further. The heterogeneous catalyst TiO_2 has many advantages, as it is chemically highly stable, biologically inert, very easy to produce, inexpensive, and possessing an energy gap comparable to that of solar photons.
- The sonochemical combination of Fenton's process with ultrasonication has effective results at lab scale, but application at the industrial level in real time is needed to demonstrate its economic and commercial feasibility.
- Electrochemical methods have the advantage of minimizing or eliminating the use of chemical reagent. Anode oxidation and electro-Fenton have very good performance when a boron-doped diamond anode is used. They can be combined with other advanced oxidation methods for further improvement of efficiency. Examples of such combinations are photoelectro-Fenton, solar photoelectro-Fenton, sonoelectro-Fenton, and peroxyelectrocoagulation. One needs to consider, however, that boron-doped diamond anodes are very expensive [22].

In conclusion, a synergetic combination of multiple oxidants and oxidation mechanisms is recommended for efficient micropollutant decomposition. Therefore, water treatment by means of plasma discharge takes an interesting and promising place among the advanced oxidation techniques, as it can generate a wide spectrum of oxidative species and processes in proximity of the solution under treatment, including shock waves, pyrolysis, and UV radiation. The hydroxyl radical OH is often named as the most important oxidant, due to its high standard oxidation potential of 2.85 V and its unselective nature in organic decomposition. Further, plasma in contact with liquid can generate significant amounts of O_3 and H_2O_2. These two oxidants are frequently used in other advanced oxidation methods and lead together to the peroxone process. Other important reactive oxygen plasma species include the oxygen radical O, the hydroperoxyl radical HO_2, and the superoxide anion O_2^-. When electrical discharge occurs in air, also reactive nitrogen species such as the nitrogen radical, the nitric oxide radical NO, and the peroxynitrite anion $ONOO^-$ will play an important role. Oxidants can either enter the liquid phase through transfer from the gas

phase or be formed directly in the liquid phase at the plasma–water interface by interaction of plasma species with water or dissolved molecules. Radical hydrogen H, a powerful reducing agent, is directly formed in aqueous phase by the electron collision with water molecules. Plasma discharge also leads to aqueous electrons, which even have a stronger reduction potential. A more detailed overview of oxidative plasma species and processes without nitrogen-containing oxidants was conducted by Joshi and Thagard [37]. Recent insights on the chemistry of plasma-generated aqueous peroxynitrite and its importance in water treatment are given by Brisset and Hnatiuc and Lukes et al. [38, 39].

The presence of different oxidants reduces the selectivity of an oxidation method. Direct oxidation of organics by ozone is, for example, very selective. This is illustrated with the reaction rate constants listed by Jin et al., Sudhakaran and Amy, and Von Gunten [40-42], which range from 10^{-5} to 3.8×10^{7} $M^{-1}s^{-1}$. Hydroxyl, on the other hand, is considered unselective in the decomposition of organics, with reaction rate constants from 2.2×10^{7} to 1.8×10^{10} M^{-1} s^{-1}, as listed in the same 3 references and [43]. Hence, organic oxidation by means of plasma is expected to be rather unselective as well. Nevertheless, the chemistry behind plasma treatment is very complex due to the interactions between the various reactive species in the gaseous phase, in the aqueous phase and at their interface. Moreover, this chemistry is strongly dependent on the used electrode configuration and material, discharge regime, applied voltage waveform, water properties and feed gas. Therefore, the optimization of plasma reactors for water treatment in terms of energy costs and effluent toxicity is a complicated task, which still requires more research effort and insight. On the positive side, plasma-based water treatment has already shown itself as a versatile technology, which can find application in the treatment of biological, organic, and inorganic contamination, after sufficient optimization has been reached. As an additional advantage, its flexible design allows it to be easily combined with other advanced treatment techniques. Such combinations can lead to interesting synergetic effects and further optimization.

As pointed out already by Sillanpää et al. [44], no information has been reported in scientific literature on the treatment cost of advanced oxidation processes. To our knowledge, plasma technology has only been compared with other water treatment methods in the review of Sirés and Brillas [22]. According to their review, the main drawback of plasma technology would be its high energy requirement. However, the authors did not validate this claim with quantitative data. Comprehensive quantitative assessment is needed to compare different techniques better from both economic and technical points of view, as Luo et al. conclude in their review [13]. For the specific case of plasma technology for water treatment, only 3 reviews have extensively compared different reactors in their energy efficiency for organic decomposition. Malik was the first to do this for dye degradation [45]. Recently, Bruggeman and Locke and Jiang et al. have made a comparison for mostly phenolic compounds [46, 47]. Their findings will be discussed in next chapter. Nevertheless, the main comparative parameter in these reviews is energy yield G_{50} for 50% pollutant removal, expressed in g/kWh, which is only used in literature on plasma treatment. Moreover, G_{50} is strongly

dependent on the initial pollutant concentration. It is therefore not fit for comparison with other advanced treatment techniques. For this reason, electrical energy per order EEO will be introduced in Chapter 8 as a better alternative.

Conclusion

Removal of hazardous micropollutants is often insufficient by means of modern conventional wastewater treatment plants. Preventive measures and optimization of conventional biological treatment are suggested as most cost-effective solutions. Nevertheless, preventive measures are limited by increasing demand, while optimization of conventional techniques often has negligible effect on many persistent micropollutants. Therefore, advanced treatment techniques such as electrochemical separation, activated carbon, nanofiltration and reverse osmosis have recently received more attention for their effective removal of micropollutants. These techniques, however, are associated with high costs and the additional problem of hazardous concentrate disposal. Advanced oxidation techniques are a promising alternative, as they are the most effective available methods to decompose bio-recalcitrant organics. As a main drawback, their energy costs are high up to now, preventing their implementation on large scale. Alternatively, their application can be limited to treatment of important micropollutant sources, such as hospital and industrial effluent.

Amongst the advanced oxidation techniques, water treatment by means of electrical discharge takes an interesting place, since it is able to generate a wide spectrum of oxidative species, leading to a low selectivity of the degradation process. Further optimization of this technology is complex due to the wide variety in reactor design and materials, discharge types and operational parameters. Yet, its flexible design facilitates synergetic combination with other advanced oxidation processes and opens doors for many applications.

References

[1] L. Rizzo, *et al.*, "Urban wastewater treatment plants as hotspots for antibiotic resistant bacteria and genes spread into the environment: a review," *Science of The Total Environment*, vol. 447, pp. 345-360, 2013.

[2] T. Hayes, *et al.*, "Herbicides: feminization of male frogs in the wild," *Nature*, vol. 419, pp. 895-896, 2002.

[3] S. Milla, *et al.*, "The effects of estrogenic and androgenic endocrine disruptors on the immune system of fish: a review," *Ecotoxicology*, vol. 20, pp. 305-319, 2011.

[4] I. R. Falconer, *et al.*, "Endocrine-disrupting compounds: A review of their challenge to sustainable and safe water supply and water reuse," *Environmental Toxicology*, vol. 21, pp. 181-191, 2006.

[5] R. McKinlay, *et al.*, "Endocrine disrupting pesticides: Implications for risk assessment," *Environment International*, vol. 34, pp. 168-183, 2008.

[6] W. Mnif, *et al.*, "Effect of Endocrine Disruptor Pesticides: A Review," *International Journal of Environmental Research and Public Health*, vol. 8, pp. 2265-2303, 2011.

[7] K. Fent, *et al.*, "Ecotoxicology of human pharmaceuticals," *Aquatic Toxicology,* vol. 76, pp. 122-159, 2006.
[8] A. Pruden, *et al.*, "Antibiotic resistance genes as emerging contaminants: studies in northern Colorado," *Environmental Science & Technology,* vol. 40, pp. 7445-7450, 2006.
[9] A. L. Batt, *et al.*, "Comparison of the occurrence of antibiotics in four full-scale wastewater treatment plants with varying designs and operations," *Chemosphere,* vol. 68, pp. 428-435, 2007.
[10] X. Flores Alsina, "Conceptual design of wastewater treatment plants using multiple objectives," Doctor PhD, Universitat de Girona, Girona, 2008.
[11] Y.-P. Wang and R. Smith, "Design of distributed effluent treatment systems," *Chemical Engineering Science,* vol. 49, pp. 3127-3145, 1994.
[12] I. Michael, *et al.*, "Urban wastewater treatment plants as hotspots for the release of antibiotics in the environment: a review," *Water Research,* vol. 47, pp. 957-995, 2013.
[13] Y. Luo, *et al.*, "A review on the occurrence of micropollutants in the aquatic environment and their fate and removal during wastewater treatment," *Science of The Total Environment,* vol. 473-474, pp. 619-641, 2014.
[14] O. A. Jones, *et al.*, "Questioning the excessive use of advanced treatment to remove organic micropollutants from wastewater," *Environmental Science & Technology,* vol. 41, pp. 5085-5089, 2007.
[15] Z.-h. Liu, *et al.*, "Removal mechanisms for endocrine disrupting compounds (EDCs) in wastewater treatment — physical means, biodegradation, and chemical advanced oxidation: A review," *Science of The Total Environment,* vol. 407, pp. 731-748, 2009.
[16] A. Joss, *et al.*, "Removal of pharmaceuticals and fragrances in biological wastewater treatment," *Water Research,* vol. 39, pp. 3139-3152, 2005.
[17] T. A. Ternes, *et al.*, "Peer reviewed: scrutinizing pharmaceuticals and personal care products in wastewater treatment," *Environmental Science & Technology,* vol. 38, pp. 392A-399A, 2004.
[18] O. H. Jones, *et al.*, "Human pharmaceuticals in wastewater treatment processes," *Critical Reviews in Environmental Science and Technology,* vol. 35, pp. 401-427, 2005.
[19] N. Tadkaew, *et al.*, "Removal of trace organics by MBR treatment: the role of molecular properties," *Water Research,* vol. 45, pp. 2439-2451, 2011.
[20] R. Ileri, *et al.*, "Bioremoval of colour from textile wastewater by sequencing batch reactor and biotechnological methods," *International Journal of Environment and Pollution,* vol. 38, p. 48, 2009.
[21] P. Yan, *et al.*, "Investigation of microbial community structure in an advanced activated sludge side-stream reactor process with alkaline treatment," *International Biodeterioration & Biodegradation,* vol. 104, pp. 356-362, 2015.
[22] I. Sirés and E. Brillas, "Remediation of water pollution caused by pharmaceutical residues based on electrochemical separation and degradation technologies: a review," *Environment International,* vol. 40, pp. 212-229, 2012.
[23] A. Cabrera-Codony, *et al.*, "---Regeneration of siloxane-exhausted activated carbon by advanced oxidation processes," *Journal of Hazardous Materials,* vol. 285, pp. 501-508, 2015.
[24] R. Martin and W. Ng, "Chemical regeneration of exhausted activated carbon—I," *Water Research,* vol. 18, pp. 59-73, 1984.
[25] J. M. Poyatos, *et al.*, "Advanced oxidation processes for wastewater treatment: state of the art," *Water, Air, and Soil Pollution,* vol. 205, pp. 187-204, 2010.

[26] O. Lefebvre, *et al.*, "Microbial fuel cells for energy self-sufficient domestic wastewater treatment—a review and discussion from energetic consideration," *Applied Microbiology and Biotechnology,* vol. 89, pp. 259-270, 2011.

[27] A. Helal, *et al.*, "Feasibility Study for Self-Sustained Wastewater Treatment Plants—Using Biogas CHP Fuel Cell, Micro-Turbine, PV and Wind Turbine Systems," 2013.

[28] P. Verlicchi, *et al.*, "What have we learned from worldwide experiences on the management and treatment of hospital effluent?—An overview and a discussion on perspectives," *Science of The Total Environment,* vol. 514, pp. 467-491, 2015.

[29] P. Verlicchi, *et al.*, "Hospital effluents as a source of emerging pollutants: An overview of micropollutants and sustainable treatment options," *Journal of Hydrology,* vol. 389, pp. 416-428, 2010.

[30] C. Comninellis, *et al.*, "Advanced oxidation processes for water treatment: advances and trends for R&D," *Journal of Chemical Technology and Biotechnology,* vol. 83, pp. 769-776, 2008.

[31] V. Homem and L. Santos, "Degradation and removal methods of antibiotics from aqueous matrices – A review," *Journal of Environmental Management,* vol. 92, pp. 2304-2347, 2011.

[32] J. Rivera-Utrilla, *et al.*, "Pharmaceuticals as emerging contaminants and their removal from water. A review," *Chemosphere,* vol. 93, pp. 1268-1287, 2013.

[33] W. Yang, *et al.*, "Treatment of organic micropollutants in water and wastewater by UV-based processes: a literature review," *Critical Reviews in Environmental Science and Technology,* vol. 44, pp. 1443-1476, 2014.

[34] H. R. Ghatak, "Advanced oxidation processes for the treatment of biorecalcitrant organics in wastewater," *Critical Reviews in Environmental Science and Technology,* vol. 44, pp. 1167-1219, 2014.

[35] M. A. Oturan and J.-J. Aaron, "Advanced oxidation processes in water/wastewater treatment: principles and applications. A review," *Critical Reviews in Environmental Science and Technology,* vol. 44, pp. 2577-2641, 2014.

[36] M. Klavarioti, *et al.*, "Removal of residual pharmaceuticals from aqueous systems by advanced oxidation processes," *Environment International,* vol. 35, pp. 402-417, 2009.

[37] R. P. Joshi and S. M. Thagard, "Streamer-like electrical discharges in water: part II. Environmental applications," *Plasma Chemistry and Plasma Processing,* vol. 33, pp. 17-49, 2013.

[38] J.-L. Brisset and E. Hnatiuc, "Peroxynitrite: a re-examination of the chemical properties of non-thermal discharges burning in air over aqueous solutions," *Plasma Chemistry and Plasma Processing,* vol. 32, pp. 655-674, 2012.

[39] P. Lukes, *et al.*, "Aqueous-phase chemistry and bactericidal effects from an air discharge plasma in contact with water: evidence for the formation of peroxynitrite through a pseudo-second-order post-discharge reaction of H2O2 and HNO2," *Plasma Sources Science and Technology,* vol. 23, p. 015019, 2014.

[40] X. Jin, *et al.*, "Reaction kinetics of selected micropollutants in ozonation and advanced oxidation processes," *Water Research,* vol. 46, pp. 6519-6530, 2012.

[41] S. Sudhakaran and G. L. Amy, "QSAR models for oxidation of organic micropollutants in water based on ozone and hydroxyl radical rate constants and their chemical classification," *Water Research,* vol. 47, pp. 1111-1122, 2013.

[42] U. Von Gunten, "Ozonation of drinking water: Part I. Oxidation kinetics and product formation," *Water Research,* vol. 37, pp. 1443-1467, 2003.

[43] W. R. Haag and C. D. Yao, "Rate constants for reaction of hydroxyl radicals with several drinking water contaminants," *Environmental Science & Technology,* vol. 26, pp. 1005-1013, 1992.

[44] M. E. Sillanpää, *et al.*, "Degradation of chelating agents in aqueous solution using advanced oxidation process (AOP)," *Chemosphere,* vol. 83, pp. 1443-1460, 2011.

[45] M. A. Malik, "Water Purification by Plasmas: Which Reactors are Most Energy Efficient?," *Plasma Chemistry and Plasma Processing,* vol. 30, pp. 21-31, 2010.

[46] P. J. Bruggeman and B. R. Locke, "Assessment of Potential Applications of Plasma with Liquid Water," in *Low Temperature Plasma Technology - Methods and Applications*, P. K. Chu and L. XinPei, Eds., ed Boca Raton, FL 33487-2742: CRC Press, 2014, pp. 367-399.

[47] B. Jiang, *et al.*, "Review on electrical discharge plasma technology for wastewater remediation," *Chemical Engineering Journal,* vol. 236, pp. 348-368, 2014.

If we knew what it was we were doing,
it would not be called research, would it?
- Albert Einstein

Chapter 3

Plasma reactor classification and optimization

In this chapter, several plasma technologies are discussed that can be applied in water treatment. First, different approaches for reactor classification will be analyzed in detail. From section 3.2 to 3.7, an overview will be given of different plasma reactor types, where classification is based on reactor design and reactor materials. The influence of multiple working parameters on reactor energy efficiency is discussed in section 3.8. Section 3.9 gives a summary with future prospects and concluding remarks on the research that is still required in this field.

3.1 Approaches for reactor classification

Plasma reactors for water treatment can be classified in many ways, depending on several criteria. Such classifications have already been made in a few reviews. One popular approach starts from 2 or 3 main plasma–water phase distributions and subdivides reactors further based on their electrode configuration, as in Bruggeman and Leys and Locke et al. [1, 2]. Here, we will adapt this approach with 6 plasma–water phase distributions, where electrical discharge is generated

1. directly in the water bulk,
2. directly in the water bulk with externally applied bubbles (bubble discharge reactors),
3. in gas phase over water bulk or film,
4. in gas phase with water drops or mist,
5. as a combination of the previous types, or

6. not in direct contact with the solution under treatment.

Accordingly, these reactor types are called (1) electrohydraulic discharge, (2) bubble discharge, (3) gas phase discharge, (4) spray discharge, (5) hybrid, and (6) remote discharge reactors. The basic idea behind this classification is that the total plasma–water interface surface is an important, determining parameter for a reactor's energy efficiency. A larger interface surface is expected to cause higher pollutant degradation efficiency, in agreement with the reviews of Malik, Jiang et al., and Bruggeman and Locke [3-5]. Interface surface can be enlarged by generating plasma in bubbles by spraying the solution through the active plasma zone and by making the solution flow as a thin film along the discharge. It can be further enlarged by extending the plasma volume, which has led to many possible choices of electrode configurations and geometries. Additionally, dielectric barriers and porous layers are often introduced in the setup to avoid unwanted energy losses to Joule heating of water and spark formation, while enhancing the local electric field for easier breakdown. From section 3.2 to 3.7, this approach for reactor classification will be studied in more detail.

Another popular approach classifies reactors based on the used discharge regime and applied voltage waveform. The following discharge regimes should be considered:

a. corona and streamer discharge
b. glow discharge
c. dielectric barrier discharge (DBD)
d. arc discharge

Townsend discharge and non-DBD micro-discharge are not included in this list, as they are not used for water treatment plasma reactors to our knowledge, except in ozone generation. Spark discharge is to be understood as a transient form of arc discharge and therefore falls in the fourth category. All four discharge regimes can be formed in the gas phase or the liquid phase, although we only found one very short and recent report on submerged DBD discharge without bubbles for water disinfection [6]. In the gas phase, corona discharge needs lowest power input and arc discharge the highest. Underwater discharge requires additional energy for plasma onset by cavitation, but it has the advantage of a large plasma–liquid contact surface. Locke et al. and Jiang et al. suggested in their reviews to apply low-energy plasma such as corona and glow discharge for the treatment of water with low contaminant concentration. On the other hand, high-energetic arc discharge might be more effective for high pollutant concentration [2, 4].

Depending on the voltage waveform used, the following types of discharge can be distinguished:

i. DC discharge
ii. AC (low frequency) discharge
iii. Radio frequency discharge
iv. Microwave discharge
v. Monopolar pulsed discharge

vi. Bipolar pulsed discharge

Variations are possible, such as periodically interrupted AC discharge to avoid excessive heating of the plasma gas [7]. Multiple voltage-related parameters can influence reactor energy efficiency, such as voltage amplitude and polarity, sinusoidal or pulse frequency, and pulse rise time and width. Their influence will be discussed in more detail in section 3.8. By combining different voltage waveforms with the different discharge regimes in either the liquid or the gas phase, a list of discharge types can be obtained. Malik, for example, identified 27 distinct reactor types in his literature study, using this approach [5]. Locke et al. made a classification into 7 types [2]:

- pulsed corona and corona-like electrohydraulic discharge
- pulsed spark electrohydraulic discharge
- pulsed arc electrohydraulic discharge
- pulsed power electrohydraulic discharge
- gas phase glow discharge
- gas phase pulsed corona discharge
- hybrid gas–liquid electrical discharge

This classification partly overlaps with the 6 types of plasma–water phase distribution mentioned above, where bubble discharge is included in hybrid gas–liquid discharge. Jiang et al. add 4 more types [4]:

- DC pulseless corona electrohydraulic discharge
- dielectric barrier discharge
- gas phase gliding arc discharge
- DC arc discharge torch

While the first 3 types generate plasma in or in contact with the liquid, the last type introduces the water under treatment directly in the torch, where it subsequently gets vaporized and becomes the plasma forming gas. It can therefore be classified as a subtype of spray discharge reactors. For more summarized information on the basic chemistry and physics of the discharge types in this list, the reader is referred to [2, 3].

The list illustrates how the 6 reactor types based on plasma–water phase distribution can be further split into subtypes. This has been done in a more extensive way by Locke and Shih, who identified more than 30 subtypes during their comparative study for the reactor energy efficiency of H_2O_2 production [8]. While this method has proven to be useful for their purpose, it disregards the influence of reactor design, materials and working parameters. As Locke and Shih point out, studying this influence is a challenging task, but it will reveal valuable information on reactor optimization.

A small number of reviews have been made on plasma reactor energy efficiency for organic decomposition, which mostly focused on the influence of plasma–water phase distribution, discharge type, and a few working parameters. Nevertheless, no comprehensive overview is

found in literature up to now on reactor design and reactor materials. Section 3.2 to 3.7 will deal with this topic. While these sections are not meant to be fully comprehensive, we want to give a broader overview of reactor types reported in literature than has been done in prior reviews. Such overview is not only useful to get easier and faster understanding of reactor operation and development but also serves as source of inspiration for future reactor designs. Moreover, it reveals the close relationship between electrode configuration and discharge type. Both popular and more exotic, unique designs will be discussed, with extra focus on several general working parameters in section 3.8. This review also includes plasma reactors that have been used for inorganic removal or biological treatment, as these reactors are also valuable candidates for aqueous organic decomposition.

3.2 Electrohydraulic discharge reactors

Electrohydraulic discharge reactors have been studied for many years due to their importance in electrical transmission processes and their potential for water treatment. From theoretical point of view, they are attractive for water treatment due to the relatively high ratio of plasma–water contact surface to plasma volume and proximity of plasma to the water surface. Moreover, they generate shock waves that can aid in organic decomposition. Nevertheless, electrohydraulic discharge reactors are usually less efficient than other reactor types for water decontamination [5, 9]. This is likely due to the additional input energy required for cavitation, i.e., gas phase formation during discharge onset.

Most commonly reported types of electrohydraulic discharge are pulsed arc and pulsed corona discharge. To our knowledge, all arc electrohydraulic discharge reactors reported in literature have pulsed input power. Mostly, a rod-to-rod electrode configuration is used (Figure 3.1a), but there are also reports on a reactor with a grounded L-shaped stationary electrode and a vibrating rod electrode (Figure 3.1b) [10, 11]. As learned from personal communication with Dr. Naum Parkansky, the vibrating electrode has the purpose to facilitate electrical breakdown and mix the treated solution. Apart from organic degradation, pulsed arc electrohydraulic discharge is also gaining more recent attention for biological treatment [12, 13]. Often, refractory metal such as tantalum, titanium, tungsten, or a corresponding alloy is selected as electrode material, as it needs to be sufficiently resistant to corrosion and shock waves. Tungsten has proven to be less corrosive than titanium and titanium alloy [12]. Particles that eroded from titanium electrodes enhanced methylene blue decomposition during aging in one study. The authors explained this enhancement with titanium peroxide formation from interaction of H_2O_2 with the particle surface [14]. In contrast, particles that eroded from low carbon steel electrodes diminished the decomposition of the same pollutant, possibly through the catalytic decomposition of H_2O_2 and scavenging of OH radicals [11]. While an increasing energy efficiency is reported for the decomposition of 2,4,6-trinitrotoluene [15] and methyl-tert-butyl ether [16] when the electrode gap is reduced, the opposite effect has been observed for atrazine degradation in

another study [17]. Further investigation is needed to understand this apparent contradiction. In a small comparative study, Hoang et al. found the energy efficiency of 4-

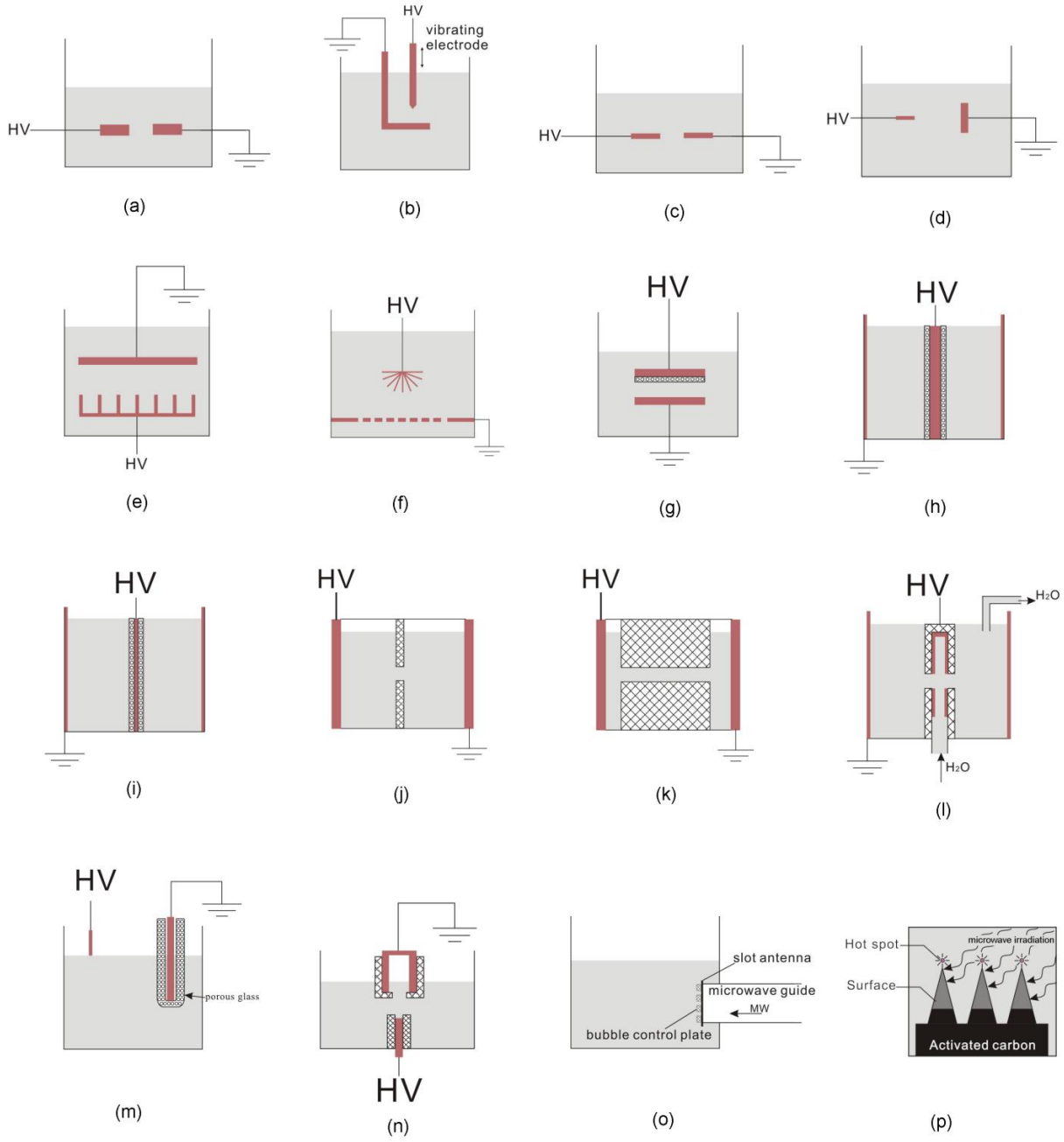

Figure 3.1 Types of electrohydraulic discharge reactors: (a) pulsed arc, (b) pulsed arc with vibrating electrode, (c) pin-to-pin, (d) pin-to-plate, (e) multi-pin-to-plate, (f) brush-to-plate, (g) plate-to-plate with porous ceramic coating, (h) coaxial rod-to-cylinder with ceramic coating on rod, (i) coaxial wire-to-cylinder with ceramic coating on wire, (j) diaphragm discharge, (k) capillary discharge, (l) coaxial diaphragm discharge reactor from Šunka et al. [19] with perforations in tubular electrode covered by polyethylene layer, (m) contact glow discharge electrolysis, (n) RF-discharge in cavitation bubble on electrode, (o) microwave bubble plasma from waveguide with antenna slot, and (p) "hot spot" plasma formation on activated carbon surface under influence of microwave irradiation.

chlorophenol decomposition of this type of reactor to be one order of magnitude lower than degradation efficiency with UV, UV/H_2O_2, and O_3 systems [18].

Submerged pin-to-pin electrode configuration, as in Figure 3.1c, is uncommon in scientific literature. Such reactor has been used with high frequency bipolar pulsed power with reduced voltage and low pulse energy by Potocký et al. [20], to lower temperature loading of the electrodes and to clean both electrode tips continuously from any possible adjacent products. With addition of a high inductance in series with the discharge, transition from glow type to arc type discharge can be suppressed [21]. For sufficiently large interelectrode distance and low voltage amplitude, unbridged nonarc discharge was observed. For closer electrodes and higher voltage, bridged arc discharge was obtained, which, according to the authors, was initiated with spark formation at both electrodes [22].

A pin-to-plate electrode configuration (Figure 3.1d) is often used in electrohydraulic discharge reactors, either for DC glow [23, 24] or pulsed corona [25-27] discharge with positive polarity. The pin curvature radius determines the local electric field strength and is therefore an important parameter that influences discharge initiation [28]. For pulsed corona discharge, the anode pin material has been reported to lead to catalytic effects for organic decomposition. Platinum enhances pollutant degradation as compared to a NiCr, but only in combination with certain electrolytes. In the case of ferrous salts, this is due to reduction of Fe^{3+} to Fe^{2+} by erosion particles from the platinum electrode [25, 26]. Erosion of tungsten, on the other hand, causes catalysis of oxidation by plasma generated H_2O_2 [29].

To achieve a higher plasma volume, the pin electrode can be replaced by a multi-pin electrode [30], a brush electrode [31] or a plate electrode coated with a thin ceramic layer [32], respectively shown in Figure 3.1e, 3.1f and 3.1g. Concentration of pre-discharge in pores of the ceramic layer enhance the electric field strength on the electrode surface [27]. Due to inhomogeneities such as entrapped microbubbles inside the ceramic layer, the electric field can be locally even higher. As a result, a large number of streamers can be generated with lower input voltage as compared to uncoated electrode systems. Moreover, a ceramic coating does not only facilitate an upscale of the system, it can also serve as a support for a suitable catalyst of the plasma chemical reactions. Also, certain ceramic materials can enhance organic decomposition by catalytic effects [33]. Usually, positive high voltage pulses are applied to the coated electrode. In some cases, negative high voltage is used to avoid arc formation, as this can damage the coating [32]. However, bipolar pulses are advised, since monopolar pulses cause a polarized charge buildup on the ceramic which can quench the electrical discharge [34].

To enlarge the plasma volume even further, coaxial geometry has been used, where either a coated rod [34] or wire [27, 33] high voltage electrode is located at the symmetry axis of the grounded cylindrical electrode (Figure 3.1h-i). Analogue to the curvature of pin electrodes, the diameter of the inner electrode is an important system parameter.

When a submerged anode and cathode are separated from each other with a perforated dielectric barrier, electrohydraulic discharge will occur through cavitation at the perforation. For larger ratio of perforation diameter to thickness, this type of discharge is called diaphragm discharge (Figure 3.1j), while for lower values the term capillary discharge is used (Figure 3.1k). DC glow discharge [35, 36] and pulsed corona discharge [37] are commonly used for this reactor, but also AC power input is possible. The strongly inhomogeneous electric field during plasma onset has a similar structure to the one in pin-to-plate geometry. Therefore, similar plasma features can be expected. Energy efficiency for dye and phenol degradation with a single diaphragm is the same as in the case of a pin-to-plate electrode system [2]. Also, similarities with contact glow discharge electrolysis are reported [36]. As an important difference, diaphragm discharge is not in direct contact with the electrodes, which prevents electrode erosion [35]. Sunka et al. developed a coaxial reactor where a polyethylene covered tubular anode with perforations was placed inside a cylindrical cathode (Figure 3.1l) [19]. The generated plasma was reported to be similar as well.

Another common type of electrohydraulic discharge is contact glow discharge electrolysis. As depicted in Figure 3.1m, a pointed anode is placed with its tip in the water surface. It is separated from the submerged cathode by means of a sintered glass barrier. In such reactor, glow discharge is generated at the anode tip in a vapour layer surrounded by water. Plasma volume can be increased by increasing the anode number. Stainless steel performed better as anode material than platinum for Acid Orange 7 decoloration [38].

Electrohydraulic discharge can also be generated with RF or microwave power, but such reactor types are less common. Figure 3.1n shows a reactor where plasma is generated in a cavitation bubble on the tip of a RF electrode [39]. Producing cavitation bubbles by means of microwave power is more complicated. Therefore, a slot antenna can be placed in between the liquid and a microwave guide, as illustrated in Figure 3.1o. The electric field intensity can be enhanced by installing a quartz plate with holes, a so called bubble control plate, on the slot antenna. Ishijima et al. reported an increase of methylene blue decomposition efficiency with a factor of 20 after installation of the bubble control plate and tripling the amount of slot antennas [40]. Another way to produce underwater plasma with microwave power is by adding a microwave-absorbing material with high surface area, such as activated carbon, to the solution under treatment. Under influence of microwave irradiation, delocalized π-electrons on the activated carbon surface gain enough energy to jump out of the surface and generate confined plasmas (Figure 3.1p), also called hot-spots, which are known to increase organic decomposition efficiency [41].

3.3 Bubble discharge reactors

Since electrohydraulic discharge generally has low energy efficiency due to the difficulty of initiating discharge directly in the water phase, a lot of attention has gone to enhancing

efficiency by discharge formation in externally applied bubbles. Bubbling has the additional advantage of mixing the solution. Moreover, discharge initiation in the gas phase minimizes electrode erosion, which lengthens life time of the system. Bubbling gas through the discharge region greatly increases radical density in the plasma, as for example observed in [28] for O_2 and Ar bubbles. Obviously, feed gas plays a determining role. Yasuoka et al. measured highest efficiency for Ar bubbles, in which plasma spread extensively along the inner surface, while lowest efficiency was obtained with He plasma, which has smallest plasma-water contact surface [42]. The importance of the working gas in plasma reactors in general will be further discussed in section 3.8.

A common method is to pump gas upwards through a nozzle anode, located underneath a grounded electrode [28], as shown in Figure 3.2a. Often, the nozzle electrode is placed inside a dielectric tube up to its tip, to avoid any energy leakage towards the water. Alternatively, a pin anode is sometimes placed inside a dielectric nozzle which transports the feed gas (Figure 3.2b) [45]. The pin tip can be placed below or above the nozzle extremity. Many variations can be encountered in literature, such as a pin anode inside a perforation in a dielectric plate (Figure 3.2c) [46] and different nozzle orientations (Figure 3.2d-e) [47, 48]. All choices in nozzle or perforation material, shape, dimensions and orientation determine the bubble shape during formation and its position after detachment, which significantly influences the electric field in the inter-electrode region and therefore the plasma characteristics. This complicates comparison of different reactors. Another option is to place the high voltage electrode underneath the perforated dielectric plate, as in [42, 49, 50] (Figure 3.2f-h), where the ring-shaped grounded electrode is located around the bubble. Also here, electrode geometry and position influence the electric field. Yasuoka et al. found their single hole reactor (Figure 3.2h) to be more energy efficient than advanced oxidation with photochemical persulfate, photocatalyst heteropoly acid, photodegradation and ultrasonic cavitation for decomposition of 2 surface active compounds [42]. By increasing the number of nozzles or holes, energy efficiency can be enhanced. In [49], a reactor with a single hole (Figure 3.2f) was compared to a reactor with 9 holes (Figure 3.2g). Discharge power deposited per hole was lower in the reactor with 9 holes, which seemed to minimize self-quenching of OH radicals, resulting in higher efficiency. Following this line of thought, a multi-bubble system as in Figure 3.2i with a high voltage mesh in the gas phase attached to a porous ceramic seems a promising alternative [51]. Similarly, bubbling gas through a porous ceramic tube containing a high voltage wire electrode [52] (Figure 3.2j) give a large plasma-water contact surface as well. Increasing gas flow rate had no influence in this reactor on decomposition efficiency of phenol, while energy efficiency was enhanced for Acid Orange II removal.

Another situation is found when bubbles are formed on the grounded electrode, as in [50, 53] (Figure 3.2k). Reactor from Figure 3.2h has more aggressive reaction with water and improved durability of electrode in comparison to the reactor from Figure 3.2k, as concluded by Yamatake et al. in [50]. Nevertheless, one needs to take into account the applied voltage

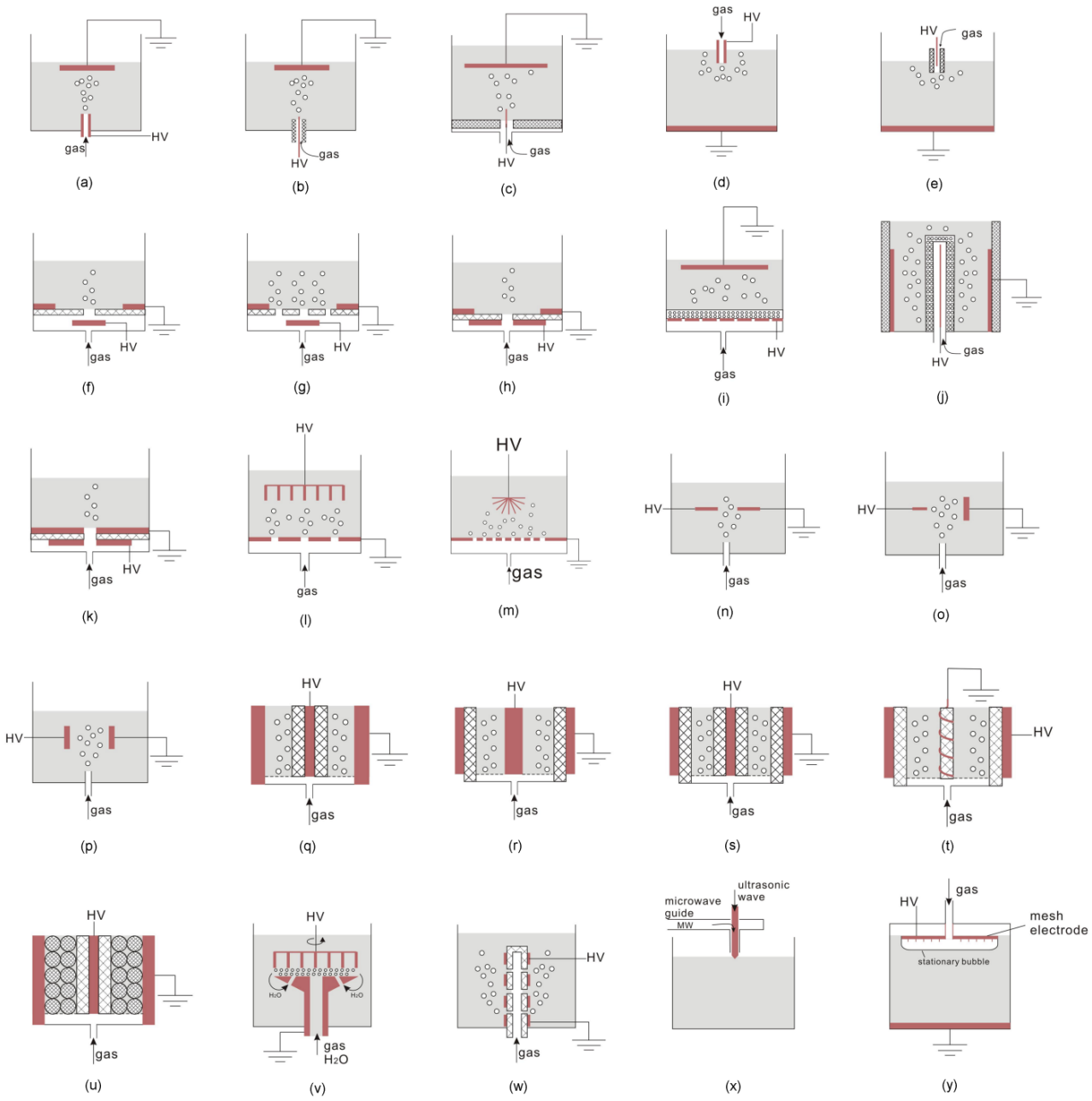

Figure 3.2 Types of bubble discharge reactors: (a) upward nozzle electrode-to-plate, (b) upward nozzle containing needle electrode-to-plate, (c) hole containing needle electrode-to-plate, (d) downward nozzle electrode-to-plate, (e) downward nozzle containing needle electrode-to-plate, (f-h) hole above electrode and inside circular ground electrode, (i) multi-bubble discharge on porous ceramic with high voltage mesh, (j) multi-bubble discharge on porous ceramic tube surrounding a high voltage wire electrode, (k) bubble discharge on hole in grounded electrode, (l-m) bubbles rising towards high voltage electrode, (n-p) bubbles rising in between electrodes, (q) DBD reactor with inner barrier, (r) DBD reactor with outer barrier, (s) DBD reactor with double barrier, (t) DBD reactor with spiral electrode from [43], (u) glass bead packed-bed DBD reactor, (v) coaxial arc discharge reactor with rotating multi-pin electrode from [44], (w) multi-electrode slipping surface discharge reactor, (x) microwave discharge in ultrasonic cavitation bubble and (y) stationary bubble under high voltage mesh.

type. While for most of the reactors above positive pulsed corona discharge is used, less commonly AC voltage [53] or positive DC voltage [48, 50] is applied, leading to significantly different phenomena. As Yamatake has shown, plasma can be stably generated in the reactor from Figure 3.2h even without gas flow, since O_2 gas is generated from electrolysis by application of positive DC voltage, while this is not the case for the reactor from Figure 3.2k. The micro-discharge channel makes plasma more stable than in [48], where the same phenomenon has been studied. Therefore, the system of Figure 3.2k requires higher gas flow due to the short life time of the oxygen radical, while in the reactor of Figure 3.2h decomposition did not depend on flow rate due to direct reaction with water.

Gas can also be bubbled from the ground electrode towards a multi-pin or brush high voltage electrode, as in [31, 54] (Figures 3.2l-m) or in between 2 sideways positioned electrodes, as in [55-57] (Figures 3.2n-p). The discharge systems are often very similar to the ones described in section 3.2 without bubbles. For a plate-to-plate configuration, pulsed streamer discharge mostly occurred inside bubbles adjacent to the electrodes [56].

A last common type of bubble discharge reactor has a coaxial DBD geometry. The cylindrical dielectric barrier can either be placed at the inner [58] or at the outer electrode [50], or at both [50] (Figures 3.2q-s). For a single barrier, a reticulate electrode can be placed in contact with the water in order to enhance the local electric field [58]. With double barrier, unwanted erosion of the electrodes can be avoided. In [50], a double barrier reactor was found to have higher decomposition efficiency of acetic acid in comparison to a single barrier reactor with similar dimensions, which is most likely caused by a difference in energy density. Monopolar pulsed, bipolar pulsed and AC high voltage are most commonly applied to the inner electrode. In [43], however, the reactor from Figure 3.2t was used to generate RF glow-like plasma in bubbles. The grounded spiral electrode impeded the motion of the bubbles in the small gap between the electrodes, which increases the probability of discharge in the bubbles. Nevertheless, most of the input energy seems to be dissipated as heat in this system, resulting in low energy efficiency. Bubble movement can also be impeded by adding obstacles in the water bulk. For the single barrier reactor of [59] (Figure 3.2u), addition of spherical glass beads significantly enhanced energy efficiency of indigo carmine decomposition. Porous ceramic sphere gave worse performance than glass beads, but better one than inert conductive fragments. As an interesting research question, it is still unclear whether bubbles in contact with the electrodes in these DBD systems give rise to a better efficiency than freely rising bubbles or not.

A more exotic and patented reactor design is investigated in [44] (Figure 3.2v). In this reactor, the high voltage electrode is a pin array that can rotate at speeds up to 2500 rpm. Oxygen is pumped through the stationary electrode and nebulized to form a bubble mist between the electrodes. DC voltage is applied to the system, generating arc discharge. Rotating the electrode distributes erosion particles evenly on the stationary electrode, preventing pitting and unwanted changes in the relative distance between the electrodes. Moreover, it reduces mass transfer limitations that are apparent in pin-to-plate reactors. Additionally, it lowers

the inception voltage by abating the effective distance between the pin electrodes and the stationary electrode. Energy efficiency for methyl tert-butyl ether decomposition increased with an increase in spin rate. The system was found to be more energy efficient than many corona-based technologies, but still requires further optimization.

Anpilov et al. developed the multi-electrode slipping surface spark discharge system depicted in Figure 3.2w [60]. A series of cylindrical electrodes are mounted on the outside of a dielectric tube. One of the extreme electrodes is grounded and high voltage pulses are applied to the other extreme electrode. All other electrodes are on floating potential. To increase system efficiency, the outer surface of the electrodes is coated with a thin insulating layer. Gas is pumped into the electrode gaps through drilled holes in the dielectric tube. When a high voltage pulse is applied, plasma discharge occurs initially in the first inter-electrode gap adjoining the high voltage electrode. Breakdown of this gap quickly transports the high voltage potential to the next electrode, which leads to breakdown of the second gap. The process repeats itself until the grounded electrode has been reached. This way, the discharge load on each electrode can be kept low, enhancing erosion resistance and increasing the system life time. Effectiveness of the system has been demonstrated for disinfection of biological wastewater, methane conversion and aqueous organic waste decomposition [61].

Apart from bubble cavitation by electrical discharge, the classical gas pumping method and gas formation by electrolysis, bubbles can also be generated with ultrasonic cavitation. Since microwave power cannot easily generate cavitation bubbles, a combination of ultrasound and microwave discharge can be an attractive method. An example is given in [62] (Figure 3.2x). Stationary bubbles, however, are not commonly used in bubble discharge reactors, unless for diagnostic purposes. An example is given in [63], with the reactor of Figure 3.2y. This reactor was used to investigate plasma formation and propagation along the gas-water interface, which is a common feature for bubble discharge reactors and makes it therefore different in nature than most gas phase discharge reactors.

3.4 Gas phase discharge reactors

Electrical discharge in the gas phase is usually more energy efficient for organic degradation than discharge in the liquid phase [3, 5, 9]. In this section, we will distinguish 4 subgroups of gas phase discharge reactors: corona and glow discharge over a horizontal water surface (Figure 3.3), DBD over a horizontal water surface (Figure 3.4), falling water film reactors (Figure 3.5) and arc discharge over a water surface (Figure 3.6).

3.4.1 Corona and glow discharge over water surface

The most standard version of a discharge over water surface has a pin-to-water configuration with a grounded water electrode, as depicted in Figure 3.3a. The type of

discharge produced in this reactor, corona, glow or transient glow-to-spark, depends on the applied voltage, pin curvature, inter-electrode distance and voltage polarity [64, 65]. For the application of water treatment, both positive and negative DC and monopolar pulsed voltage has been reported. AC input power is less common, but has been used as well [66]. Plasma volume can be increased by replacing the high voltage pin electrode with a multi-pin [67], a brush [31] or a horizontal wire [68] (Figures 3.3b-d). In [67] with a multi-pin electrode, the energy efficiency for a certain amount of phenol decomposition was independent of the type of discharge, the voltage amplitude, the polarity of the applied voltage and the amount of pin electrodes.

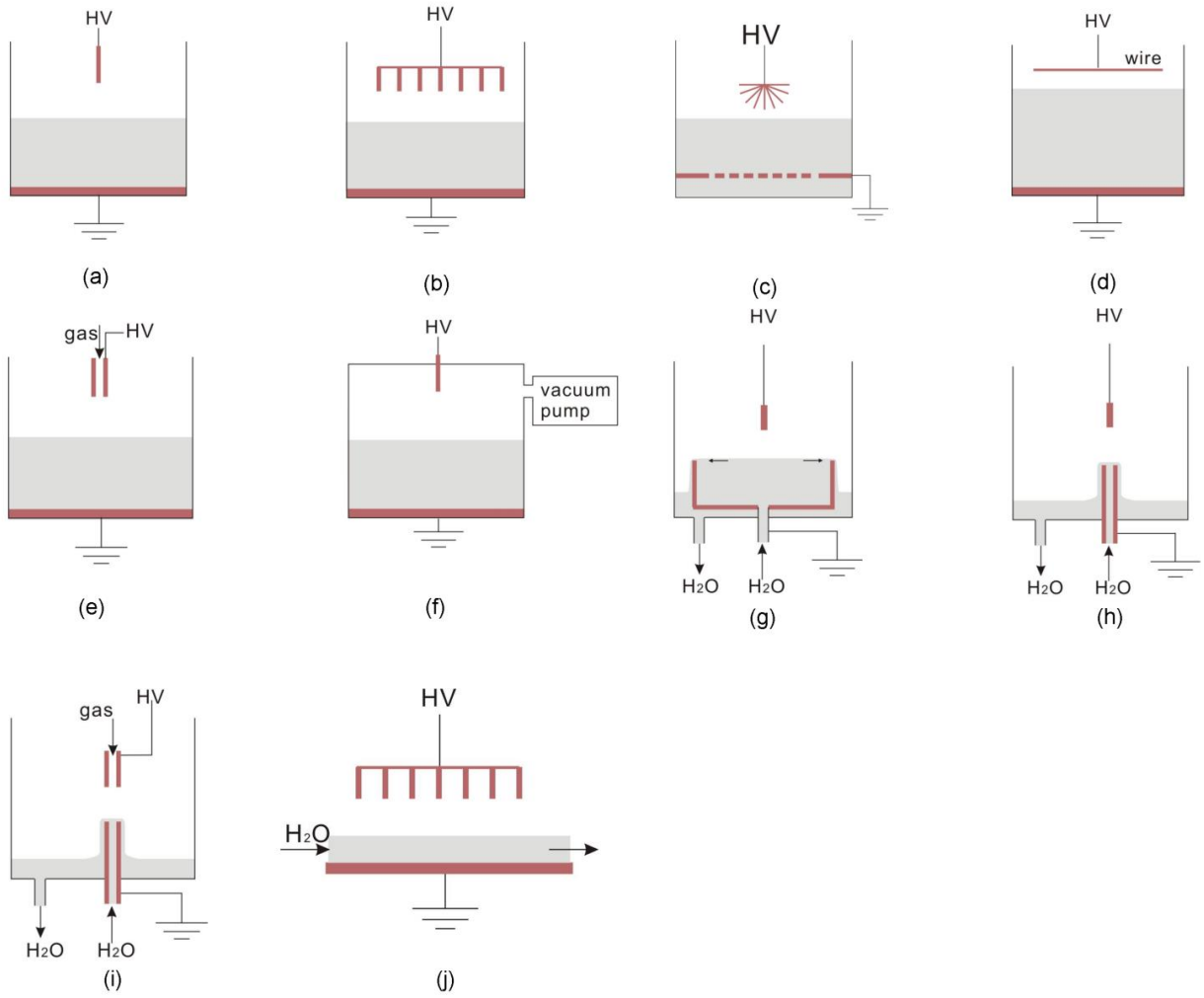

Figure 3.3 Types of reactors with corona or glow discharge over water surface: (a) pin-to-water, (b) multi-pin-to-water, (c) brush-to-water, (d) wire-to-water, (e) nozzle electrode-to-water, (f) low-pressure pin-to-water glow discharge reactor, (g) pin above radial water flow, (h) pin above flowing liquid electrode, (i) miniature microjet above flowing liquid electrode and (j) multi-pin above water flow.

According to Dors et al., atmospheric pressure glow discharge in air produces gaseous nitrogen oxides, leading to formation of undesirable aqueous nitrates and nitrites, while DC positive corona produces ozone in air without any traces of nitrogen oxides [69]. Energy

efficiency of phenol oxidation in their system, depicted in Figure 3.3e, was comparable to the results obtained in pulsed corona discharge systems. Sharma et al., however, compared their low pressure negative DC glow discharge reactor (Figure 3.3f) with bench scale data of atmospheric pressure corona discharge and concluded that the power cost for pentachlorophenol decomposition was lower for their system [70]. Additionally, the operating cost of their reactor was found to be comparable with power cost of UV based advanced oxidation technologies. Yet, it is unclear how feasible such low pressure system for applications with large water volume or continuous water flow.

It is important to note that dimensions and movement of the water phase in this type of reactors can influence energy efficiency significantly. In the system of Sharma et al., for example, stirring rate increased the rate of pentachlorophenol removal [70]. Water movement also plays an important role in radial flow reactors (Figure 3.3g). In the reactors from [71] with small sized flowing liquid cathode (Figures 3.3h-i), degradation efficiency depended strongly on the water flow rate, while the Ar flow rate from the miniature flow Ar microjet (Figure 3.3i) gave negligible effect on methyl red decomposition. The importance of water and gas flow rates will be further discussed in section 3.8. As mentioned above, making the solution flow as a thin film along the discharge is another way to enhance the oxidation process. Promising results from a pilot-scale system with negative pulsed corona from multiple carbon fiber cathodes above a flowing water film (Figure 3.3j) have been published in [72-74]. The system was similar or more efficient than a pilot-scale UV/H_2O_2 advanced oxidation process and achieved similar energy efficiency to those reported in the literature for other advanced oxidation processes [72, 73]. Moreover, the plasma pilot system with additional ozone injection was more cost-effective than three other commercialized advanced oxidation systems (O_3/H_2O_2, O_3/UV, O_3/H_2O_2/UV) [74]. However, the total capital costs and reliability of large-scale gas discharge reactors for water treatment are still relatively unclear.

3.4.2 DBD over water surface

DBD over horizontal water surface is most commonly powered with AC voltage, but occasionally pulsed high voltage has been used as well. Often, glass is used as dielectric barrier, especially quartz glass, while Al_2O_3 ceramic barriers have also been reported less frequently. Interestingly, reactors with DBD over water often have energy efficiency for organic decomposition which increases with input power [75-77]. The most standard reactor design for DBD in the gas phase over a water surface is shown in Figure 3.4a. In [75], energy efficiency in such reactor was found to increase by decreasing the distance between the dielectric barrier electrode and the water surface. This can be explained with a decrease in plasma volume and thus in unused plasma reactions far from the water surface. A water batch can also be placed in between two dielectric barriers to avoid erosion of one of the electrodes, as in [78] (Figure 3.4b). A more exotic way of bringing DBD over a water surface, is shown in Figure 3.4c, where water is kept on floating potential. This device has, however,

not been applied for organic degradation and is instead used for biomedical applications [79]. In another less common design, the water can be located above the dielectric barrier, with an uncovered high voltage electrode positioned above the water surface, as in the wire-to-water reactor in [80] (Figure 3.4d). In this reactor, energy efficiency of phenol decomposition was 3.2 times higher with stainless steel wires as compared to Ni/Cr wires. However, it is unclear whether this effect should be attributed to the larger diameter of the Ni/Cr wires or their possible inhibiting effect on ozone or other oxidants. Material of the ground electrode in contact with water in many DBD reactors is, on the other hand, clearly important. In [81], the use of a stainless steel substrate resulted in a better decomposition efficiency in comparison to the use of brass. This is explained with corrosion of the brass substrate under influence of nitrate, leading to formation of aqueous nitrite, which scavenges OH radicals and thus inhibits the degradation process. Stainless steel, as a more inert metal, does not have this effect.

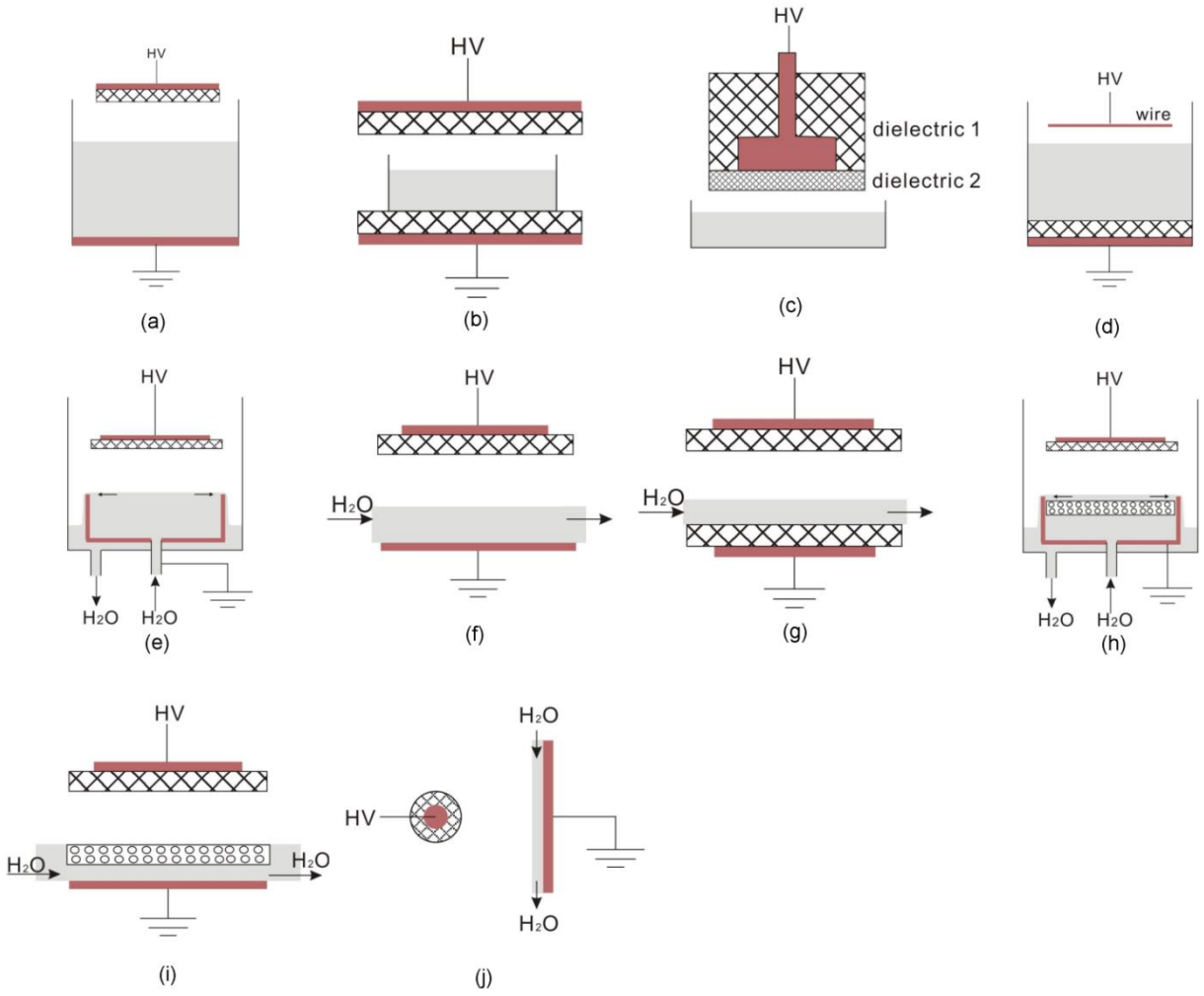

Figure 3.4 Types of reactors with DBD over water surface: (a) DBD-to-water, (b) water batch in between DBD, (c) DBD above floating electrode, (d) wire-to-water DBD, (e) DBD above radial water flow, (f) DBD above water flow, (g) water flow in between DBD, (h) DBD over radial water flow on porous ceramic, (i) DBD over water flow on porous ceramic and (j) DBD rod to falling water film.

Also for DBD-based systems, the movement of water influences the degradation efficiency. Reactors with radial flow [76] or flowing water films [77, 82] are investigated in literature for organic decomposition (Figures 3.4e-g). Both situations have also been reported with incorporation of a porous ceramic segment in the zone between electrodes (Figures 3.4h-i) [83, 84]. This porous segment serves as guide for the flowing water. It allows the water to remain undisturbed by the electrical discharge due to hydrophilic force. This enables a reduction of the discharge gap and subsequently an increase in the intensity, stability, homogeneity and efficiency of the discharge. Under such a configuration, a transition from filamentary mode to semi-homogeneous mode of the plasma discharge can be realized [84]. Moreover, such ceramic can be effectively used as substrate for photocatalysts, where both substrate and catalyst remain unchanged after use [83].

An exotic reactor type where a rod high voltage electrode with dielectric cover is placed next to a falling water film has been investigated in [81, 82] (Figure 3.4j). The reactor was found to be significantly more efficient than a gliding arc (see section 3.4.4) over the same falling water film, partly due to less corrosion of the brass substrate in contact with the water.

3.4.3 Coaxial reactors with falling water film

A relatively common falling water film reactor that does not use DBD is shown in Figures 3.5a-b and is often referred to with the term wetted-wall reactor. Either a rod [85] or more commonly a wire [86-89] high voltage electrode is placed along the axis of a grounded cylindrical electrode. The falling water film flows along the inner wall of the cylinder electrode where it comes in contact with streamer or corona discharge. Mostly, positive pulsed power is applied on the inner electrode, but also negative DC [86] has been reported. Usually, corona discharge is formed in such reactors for all voltage waveforms, while spark discharge is undesired due to excessive energy dissipation to Joule heating. To prevent spark formation, it is necessary to have the entire inner wall area covered by the water flow [89]. The choice of gas flow direction is important, as concluded in [90] for negative DC corona. Experiments showed a downward air flow to be more effective than upward air flow for acetaldehyde degradation. In [86], energy efficiency of a wetted-wall reactor with negative DC voltage applied to the inner wire was calculated to be 3 to 4 times higher than in a wire-to-water corona reactor (Figure 3.3d) over flowing water with negative DC voltage. For the same reactor, energy efficiency was found to be highest for conditions of a smooth water surface, i.e. for a minimal water flow rate where the flow entirely covers the anode inner wall and for an optimal current which does not disturb the flow by strong ion wind. There is an optimal wall radius, where decomposition efficiency is maximal. For higher radius, many plasma generated short-lived radicals cannot reach the water film in time, while for smaller radius, the plasma-water contact surface decreases [86]. Sato et al. compared four kinds of coaxial reactors with falling water film and positive pulsed power. They found phenol most

energy efficiently removed with the configuration of Figure 3.5b [87]. Sealing such reactor seems beneficial for energy efficiency, due to better confinement of the produced ozone [88].

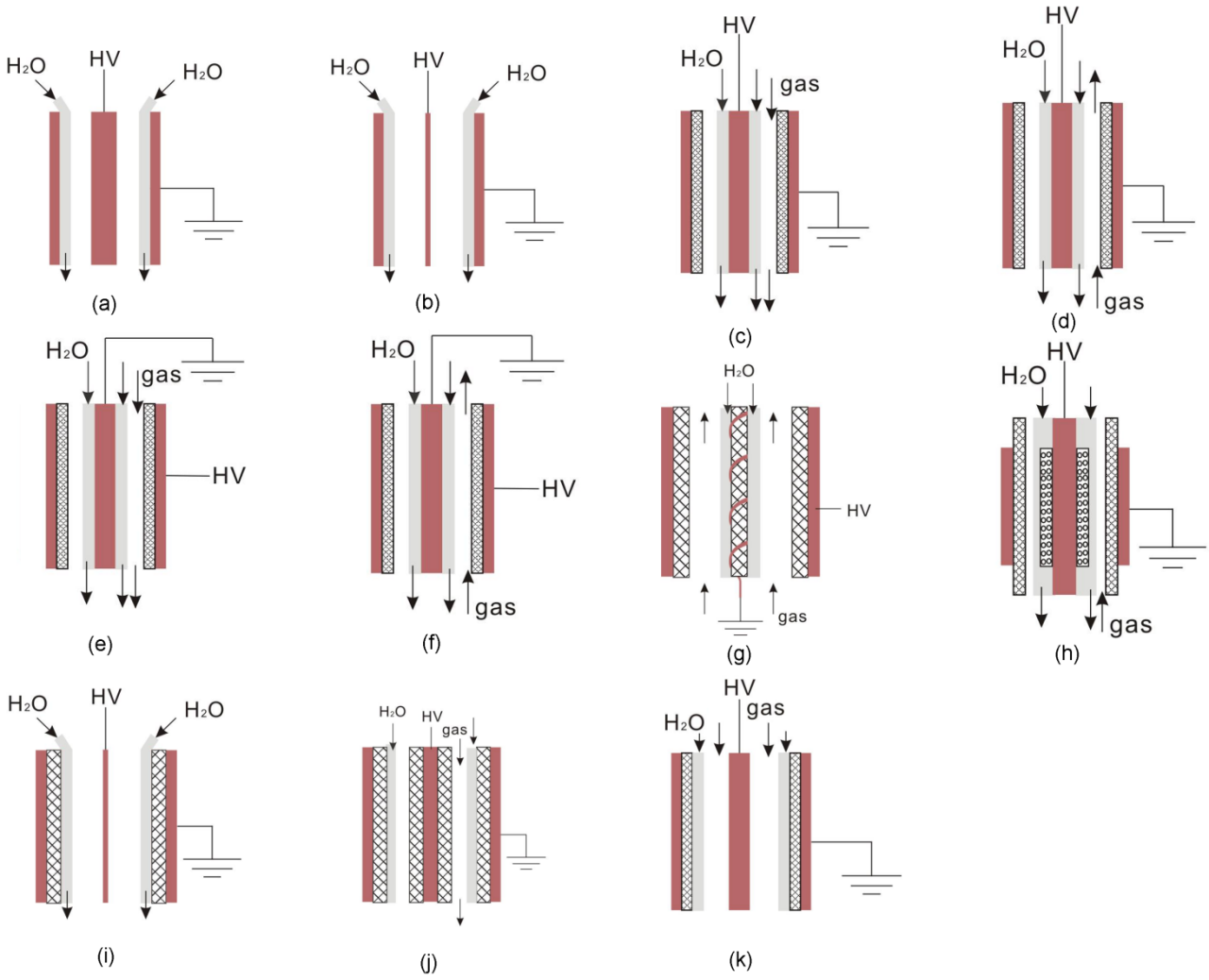

Figure 3.5 Types of coaxial reactors with falling water film: (a) wetted-wall reactor with rod electrode, (b) wetted-wall reactor with wire electrode, (c-f) 4 variations of falling water film DBD reactor with outer barrier, (g) falling water film DBD reactor with inner spiral electrode, (h) falling water film on glass fiber fabric in DBD reactor with outer barrier, (i) wetted-wall DBD reactor with wire electrode, (j) wetted-wall DBD reactor with double barrier and (k) configuration of coaxial whirlpool reactor of [91].

Most falling water film reactors generate plasma by DBD, either with AC or monopolar pulsed high voltage. Pulsed DBD in coaxial configuration using O_2 is considered as one of the most efficient electrical discharge systems evaluated, because of the large surface area and small electrode distance [9]. Several configurations are possible, but in the most common design, the water film flows over the surface of an inner stainless steel rod electrode placed inside a glass cylindrical vessel which acts as dielectric barrier. The outer electrode can be a metal mesh or a metal painted layer which is located around the vessel. Four versions of this reactor design are found in literature, where the inner electrode is either grounded or

connected to the high voltage and with an upward or downward gas flow (Figures 3.5c-f). With the reactor of Figure 3.5f, energy efficiencies of micropollutant decomposition are about one order of magnitude higher than for a water batch in between a DBD reactor (Figure 3.4b) [78]. A slightly different configuration was used in [92], where a tungsten wire that was rolled around a dielectric rod served as inner grounded electrode (Figure 3.5g). In this study, volatile aqueous compounds were treated. The more volatile the compound was, as expressed with the Henry's law constant, the more efficiently it was removed. Therefore, degradation processes of pollutants in the gas phase should be considered in plasma reactors, depending on the volatility of the compound. In [93], the inner electrode of a coaxial DBD reactor was covered with a 1 mm thick porous hydrophilic glass-fiber fabric (Figure 3.5h). This fabric allows a more homogeneous water flow and higher water retention time. Moreover, it can function as substrate for catalysts, such as Cu and Ni compounds which enhanced decomposition efficiency in [93].

Less frequently, the water film is chosen to flow along the inner wall of the dielectric barrier. Morimoto et al., for example, investigated the effect of placing a dielectric barrier inside the wetted-wall reactor of Figure 3.5b, as shown in Figure 3.5i. Addition of the barrier allows to decrease the inter-electrode gap without formation of spark discharge, which is expected to increase energy efficiency. With the application of positive nanosecond pulsed high voltage on the inner wire, the treatment efficiency of the DBD system was found to be, surprisingly, less energy efficient for indigo carmine decomposition as compared to the normal wetted-wall reactor. Another type of wetted-wall DBD reactor with falling water film is investigated in [94], for a reactor with double dielectric barrier (Figure 3.5j). A more exotic type of DBD reactor with modified water-gas mixing is reported in [91]. The system is powered with high frequency bipolar tailored voltage pulses. It has a configuration as shown in Figure 3.5k, but water and air are introduced in the reactor with high flow rate of respectively 5 L/min and 100 to 200 L/min, causing a whirlpool. For this reactor, gas flow rate was shown to have negligible effect on decomposition efficiency of methyl orange.

3.4.4 Arc discharge over water surface

Gliding arc discharge above a water surface (Figure 3.6a) is a popular approach for water treatment with plasma. In this reactor type, two diverging electrodes are placed above a water solution. An electric arc forms at the shortest electrode gap and glides along the electrode's axis under influence of a gas flow directed towards the water surface. The arc length increases on moving and its temperature decreases, turning the arc from thermal plasma into quenched plasma while breaking into a plume. A new arc then forms at the narrowest gap and the cycle continues. Unfortunately, many publications on this type of reactor are unclear about the use of AC or DC voltage, but AC power is definitely a common choice. Important research in this field has focussed on enlarging the plasma treated water surface with adjustments in design. One possibility is to use a couple of controlled electrodes in between the electrode gap to facilitate breakdown, increasing current intensity and

allowing a larger inter-electrode distance [95]. Another option is to use three main electrodes supplied by two power sources, as proposed in [96] (Figure 3.6b). Both approaches have shown to increase reactor efficiency. Gliding arc discharge can also be used for treatment of falling water films, as in [82] (Figure 3.6c). Arc discharge with an active water electrode is less commonly researched (Figure 3.6d). In [97], energy efficiency of such system was found to be strongly dependent on the type of discharge produced, such as arc or gliding arc. For more detailed information on water treatment by means of gliding arc, the reader is referred to the review in [95].

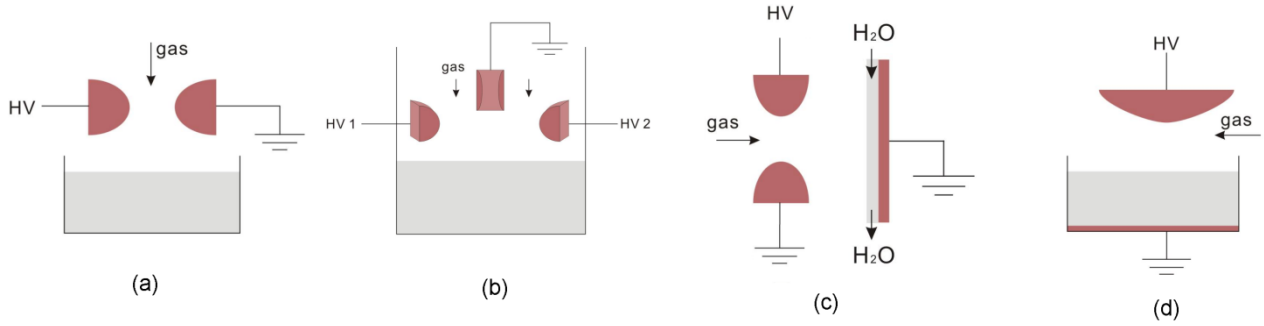

Figure 3.6 Types of gliding arc discharge reactors over water surface: (a) standard configuration, (b) configuration with extra main electrode, (c) gliding arc discharge to falling water film and (d) gliding arc discharge with active water electrode.

3.5 Spray discharge reactors

3.5.1 Low-energy spray discharge reactors

Although spray discharge reactors have received more attention in recent years due to their high reported energy efficiencies [3-5], still more research is required to characterize and optimize them. One of the most common spray reactors has a wire-to-cylinder geometry (Figure 3.7a), similar to wetted-wall reactors. This reactor type is always operating with positive pulsed corona or streamer discharge, according to our literature review. In [98], different spraying nozzles were used to investigate the influence of water location on energy efficiency of indigo carmine decomposition. As the results showed, spraying water as droplets into the discharge area is more effective than making it flow as a water film on the inner reactor wall. Moreover, droplets that were sprayed close to the reactor wall underwent 1.5 times faster decolorization than droplets near the wire electrode. Energy efficiency was found to be independent of droplet size for same water flow rate [99].

Sugai et al. adjusted this reactor by addition of packed-bed of pellets (Figure 3.7b) or fluorocarbon wires (Figure 3.7c) in order to increase the droplet retention time in the discharge space [100]. The packed pellets were hollow polyethylene balls with 14 holes per ball to increase discharge. The fluorocarbon wires were woven as insulation grids in the outer cylindrical electrode. Addition of the pellets decreased the energy efficiency

significantly, due to the narrowing of the discharge space. The fluorocarbon wires, however, kept the discharge space unaltered and increase the energy efficiency with 2 to 10%.

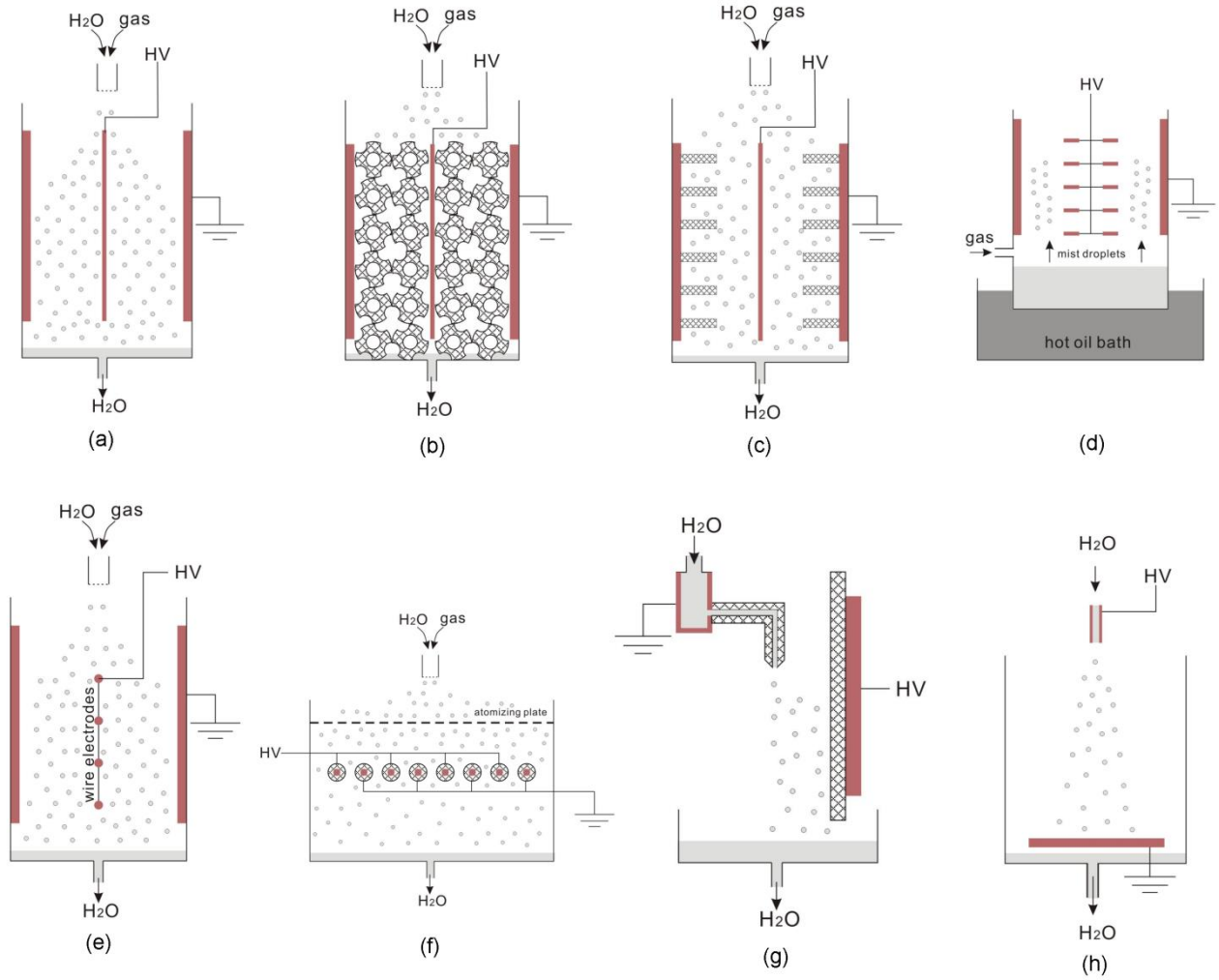

Figure 3.7 Types of low-energy spray discharge reactors: (a-c) wire-to-cylinder corona or streamer reactor without or with packed-bed of pellets or fluorocarbon wires for increased droplet retention, (d) mist droplets in tooth wheel-to-cylinder corona reactor, (e) multi-wire-to-plate corona reactor, (f) spray through DBD rods, (g) spray from grounded electrode to DBD plate and (h) electrospray reactor.

In [101], a similar electrode configuration was used as in Figure 3.7a, but with tooth wheels assembled on the inner electrode (Figure 3.7d). Here, droplets were not created by spraying, but due to condensation of steam under influence of up-flowing air. Alternatively, positive pulsed corona can also be generated in a spray reactor around wire anodes in parallel with two grounded plate cathodes [102], as depicted in Figure 3.7e. In another approach, water is sprayed in between rod electrodes that are each surrounded with a dielectric barrier (Figure 3.7f). Monopolar pulsed voltage of both polarities is reported in literature [103, 104]. In [105], grounded water was sprayed from dielectric nozzles in proximity of a high voltage dielectric barrier plate electrode (Figure 3.7g). When AC high voltage was applied to the plate, the by electrostatic induction generated electrostatic force pulled the water droplets to the glass

dielectric layer. Energy efficiency of indigo carmine decomposition depended on both voltage amplitude and air gap distance, for which optimal values were found. Another interesting reactor type is based on the electrospray process to simultaneously generate and treat water spray under influence of high voltage, as shown in Figure 3.7h. In [106], water is treated that way with positive pulsed corona electrospray.

3.5.2 Spray arc reactors

Water spray can also be introduced in gliding arc discharge for treatment, as depicted in Figure 3.8a. This method is found to be more energy efficient than gliding arc discharge over a water surface as discussed in section 3.4.4 [95, 96]. Decomposition of 4-chlorophenol in such spray reactor became more energy efficient with increasing gas-water mixing rate [107]. Efficiency is higher with electrodes from stainless steel than for aluminium or brass electrodes. Also here, extending the plasma volume by the use of a controlled electrode couple or an extra main electrode enhances energy efficiency (Figure 3.8b) [96]. The process can also be optimized by introducing the water with a flat spraying nozzle perpendicular to the gas flow to improve the contact with the plasma (Figure 3.8c) [108]. For more detailed information on water treatment by means of gliding arc spray reactors, the reader is referred to the review in [95]. Water can be treated as well with a DC plasma torch, where it is usually directly introduced into the torch as plasma forming gas. A discussion on this treatment method can be found in [4].

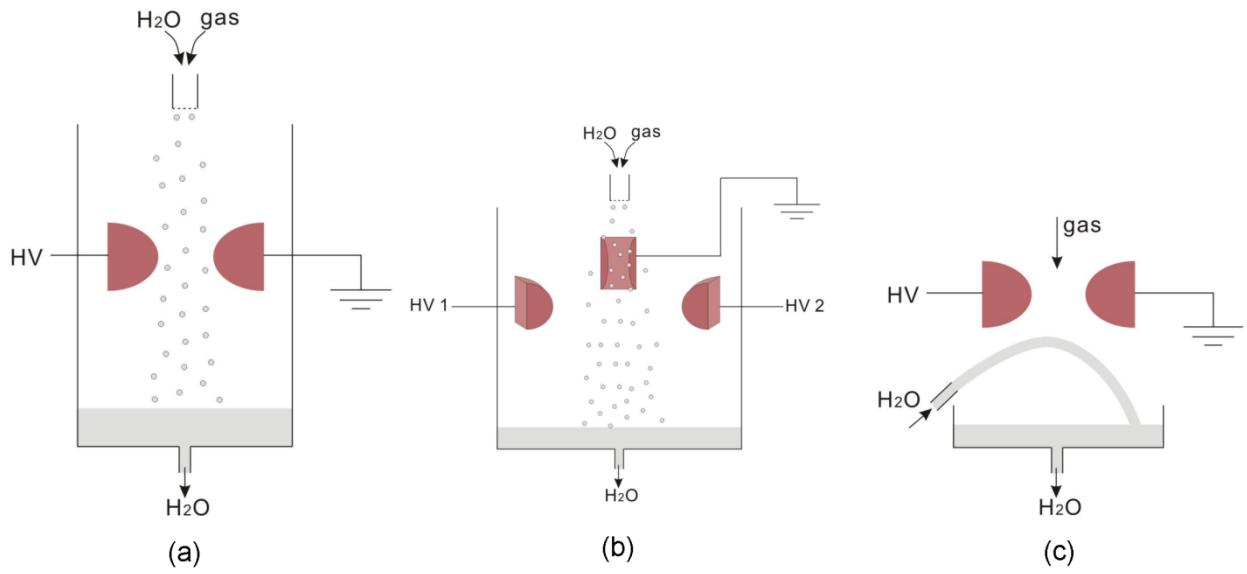

Figure 3.8 Types of spray gliding arc reactors: (a) standard configuration, (b) configuration with extra main electrode and (c) water jet under angle through gliding arc discharge.

3.6 Hybrid reactors

Electrohydraulic discharge and gas phase discharge can simultaneously be generated when a high voltage electrode is placed in the water phase with a grounded electrode above the water surface in the gas phase. Mostly, positive pulsed corona is generated in these systems reported in literature. Several electrode configurations are possible, such as an underwater pin to plate in gas [109] (Figure 3.9a) and an underwater pin to multi-pin in gas [110] (Figure 3.9b). In some reactors, a second high voltage electrode is placed in the gas phase, either powered by the same high voltage source [110] (Figure 3.9c) or by a second one [111] (Figure 3.9d). Also here, energy efficiency can be enhanced by discharge formation in externally applied bubbles, leading to hybrid reactors that combine bubble discharge with gas phase discharge. One example is given in [112], where bubbles are formed on high voltage nozzle electrodes located underneath a plate electrode in the gas phase (Figure 3.9e). Hybrid reactors with discharge in both water and gas phase are sometimes proposed for treatment of gaseous and aqueous pollutants simultaneously, as in the case of volatile pollutants [2, 4]. Their energy efficiency for organic decomposition is moderately higher than the one of electrohydraulic discharge reactors [3, 5].

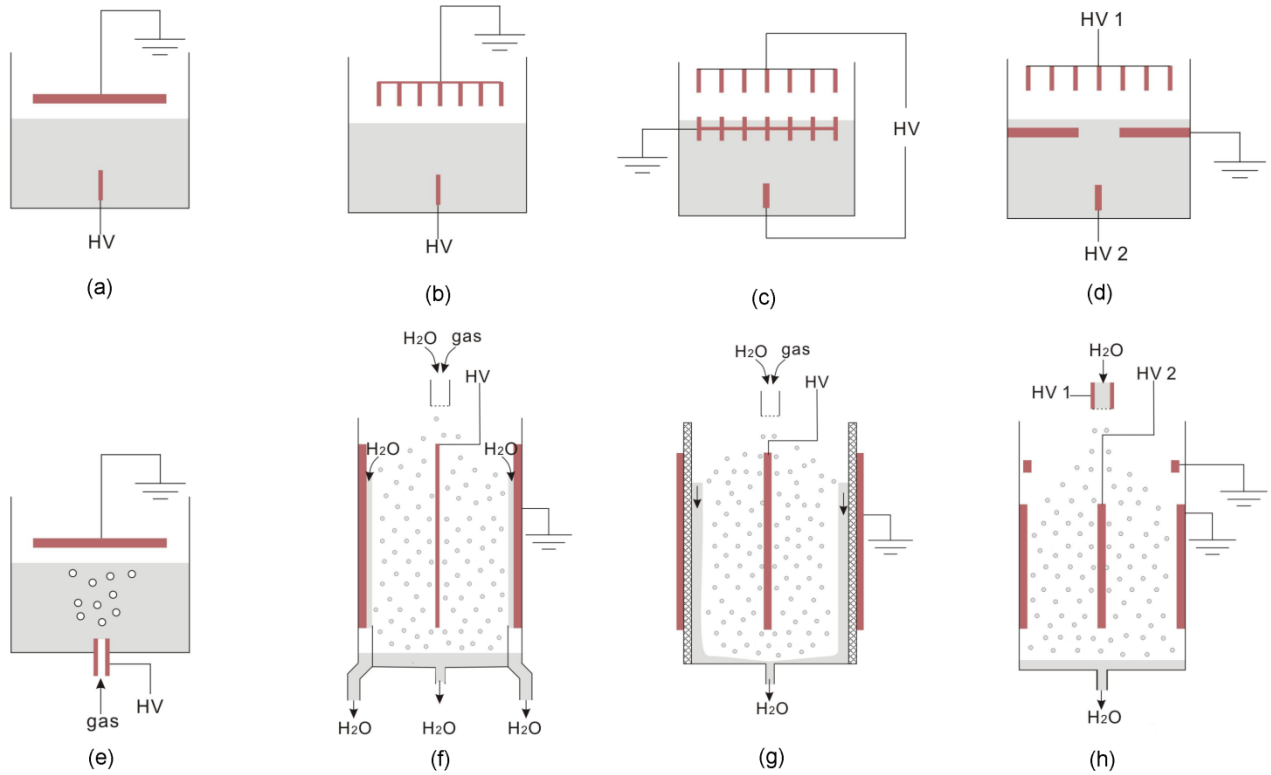

Figure 3.9 Types of hybrid reactors: (a-b) underwater high voltage pin to plate or multi-pin in gas, (c) reactor from [110], (d) reactor from [111], (e) bubble discharge on underwater nozzle electrode to plate in gas, (f) wetted-wall spray corona reactor with inner wire electrode, (g) wetted-wall spray DBD reactor with outer barrier and (h) electrospray through wire-to-mesh corona reactor.

Another type of hybrid reactor combines treatment of a falling water film and droplets. This situation naturally occurs by spraying water from a shower nozzle at an angle. In [98], a wetted-wall hybrid reactor with inner wire anode was used, where water solutions from the falling film and from the droplets were collected separately (Figure 3.9f). Indigo carmine was decomposed 0.57 times faster in the droplets than in the water film, as could be expected from the higher energy efficiency of spray discharge reactors as compared to falling water film reactors. In [113], the water film was formed on the dielectric barrier which separated the inner rod anode and the grounded mesh surrounding the barrier (Figure 3.9g). For low water flow rate, energy efficiency of rhodamine B decomposition was similar for 3 of such reactors with different inner diameter and barrier thickness. For higher flow rates, however, one reactor performed significantly better. This reactor had larger inner diameter and equal barrier thickness compared to one of the other reactors.

A special case is found when droplets from an electrospray are treated a second time with plasma discharge. In [114], electrostatically atomized droplets passed through pulsed corona discharge in between a wire-to-mesh electrode configuration (Figure 3.9h). In both parts of the reactor, positive polarity performed better than negative one for decomposition of Chicago sky blue dye. In the electrospray, positive DC voltage produced a larger number of finer droplets with a wider spray angle than in the case of negative voltage.

3.7 Remote discharge reactors

The concept of remote discharge reactors for water treatment is not new. An early example is ozonation, where ozone is generated by means of plasma discharge in gas phase and subsequently transported towards the solution under treatment. More recently, electrical discharge reactors have been developed where remotely generated plasma gas is bubbled through the solution. As main difference, the plasma gas does not only contain ozone, but also other reactive species, such as H_2O_2 and OH. In [115], this is accomplished by using humid air as feed gas of a DBD gas phase reactor (Figure 3.10a). With corona discharge in dry air, positive and negative ions can be generated in addition to ozone for water treatment, as in the air ionization device reported in [116]. Yamatake et al. compared the bubble discharge reactor from Figure 3.2k with ground electrode in contact with water to a reactor where plasma is generated separately from the water and subsequently bubbled through the solution (Figure 3.10b) [117]. Both reactors had identical electrode configuration, used oxygen as feed gas and were powered by the same positive DC voltage source. Acetic acid was not decomposed in the remote discharge reactor, while decomposition was significant in the bubble discharge reactor. This difference was explained with the production of oxygen radicals, which acted as main oxidant during bubble discharge, but had too short life time to reach the water in the remote discharge reactor.

Plasma gas bubbling can be combined with UV irradiation by generating plasma inside a quartz tube submerged in the solution. Several variations are reported in literature, where

the high voltage electrode inside the tube is a screw [121], a spiral wire [122], a rod covered by dielectric barrier [123] or a glass tube filled with NaCl solution [124]. A metal mesh surrounding the tube [121] or a metal rod in contact with the water [124] serves as ground electrode (Figure 3.10c-d). DBD plasma is usually generated inside the tube with AC power. The working gas is pumped in the tube and subsequently bubbled through the solution by means of a gas diffuser or a series of air distribution needles (Figure 3.10e) [123]. Comparison with other oxidation techniques has indicated that such reactors may be competitive technology to other plasma systems such as the hybrid reactor in [113] (Figure 3.9g) and to photocatalytic oxidation [124, 125].

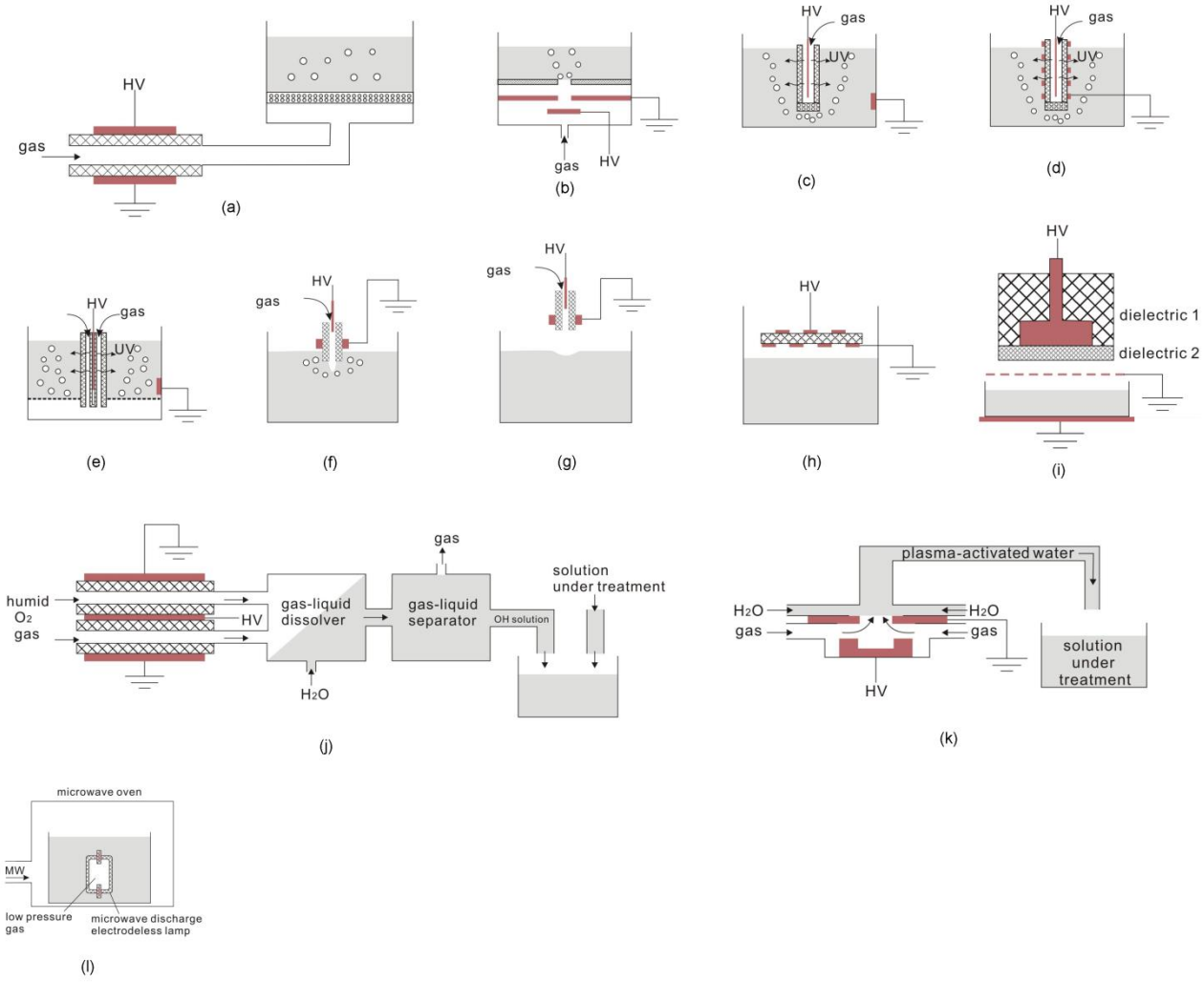

Figure 3.10 Types of remote discharge reactors: (a-b) plasma gas bubbling reactors, (c-e) plasma gas bubbling reactors with UV irradiation through quartz barrier, (f) underwater DBD plasma jet, (g) DBD plasma jet over water surface, (h) metal strips on quartz disc for DBD above water surface, (i) setup from [118] with removable grounded mesh, (j) reactor from [119] for production of hydroxyl radical solution, (k) gliding arc reactor from [120] for plasma-activated water production and (l) reactor with tungsten-triggered microwave discharge electrodeless lamp.

A system closely related to these plasma gas bubbling reactors is a submerged DBD plasma jet for water treatment. In [126], a nanosecond pulsed DBD plasma jet is investigated for oxidation of aqueous organic pollutants (Figure 3.10f). Its decomposition efficiency was higher than the one reported in literature for glow discharge and pulsed corona discharge [126]. Energy efficiency of methylene blue decomposition significantly dropped with increasing treatment time. As the results suggest, using multiple plasma jets powered in parallel can improve the process significantly. The plasma jet can also be placed above the water surface (Figure 3.10g), as is done for the production of plasma-activated water in [127]. Nevertheless, application of non-thermal plasma jets for water treatment is relatively uncommon for now.

A few systems are reported in literature where plasma is generated above a water surface without direct contact with the solution. In [128], copper strips adhered to both sides of a quartz disc were used as electrode configuration for methyl orange decomposition with AC DBD plasma (Figure 10h). In [118], inactivation of spores was investigated by means of the DBD electrode system of Figure 3.4c above a removable mesh for reference experiments (Figure 3.10i). Experiments with and without the mesh were compared to reveal the role of UV irradiation.

Recently, a new approach is gaining popularity in which water treated with plasma, often termed plasma-activated water, is added to the solution under treatment. Plasma-activated water contains several long-living oxidants that are able to inactivate biological organisms. According to Zhang et al., long-living aqueous hydroxyl radicals were produced in their setup by mixing DBD-treated humid O_2 gas with water (Figure 3.10j) [119]. This hydroxyl radical solution was sprayed in a sea enclosure to effectively inactivate red tide organisms. Plasma-activated water can be produced by means of any of the reactors mentioned above, but gliding arc discharge is most commonly used. Figure 3.10k depicts the gliding arc reactor used in [120] for plasma-activated water generation utilizing a vortex flow with two circular disk electrodes. Introducing the produced water-air mixture in the solution under treatment through microbubble generators significantly enhanced the process. Up to now, plasma-activated water is used for disinfection of water, while its effects on organic contamination are still largely unknown.

In principle, plasma technology is also frequently used in water treatment technology solely as UV source in plasma lamps or excimer lamps. An upcoming new technology is the microwave discharge electrodeless lamp, which self-ignites under influence of microwave power. As an example, Figure 3.10l schematically shows a tungsten-triggered microwave discharge electrodeless lamp proposed in [129] for low microwave power levels. The tungsten wire was embedded in a synthetic quartz tube attached to the lamp system to act as a trigger. In that manner, the high microwave power usually required for self-ignition in aqueous medium is avoided.

3.8 Influence of working parameters on energy efficiency

In addition to reactor design and materials, there are several other factors that influence reactor energy efficiency which need to be considered for reactor optimization. Roughly, these factors can be split into two groups: working parameters determining reactor operation and solution parameters. Since solution parameters, such as water temperature, pH, conductivity and water matrix are hard to control, especially for large volume of influent water, they are not discussed in this chapter. For a discussion on their influence, the reader is referred to [4]. In contrast, operational parameters such as applied voltage characteristics, working gas and flow rates of gas and solution are easier to adjust. Therefore, they deserve additional attention for further reactor optimization. As should be noted, impedance matching is important for both high frequency AC power sources and pulse forming networks, in order to enhance power transfer and energy efficiency. In this section, we will shortly review the importance of voltage waveform, working gas and gas and water flow rates. Their influence on reactor efficiency for organic decomposition will be illustrated with examples from literature.

For a given reactor, energy efficiency depends on voltage-related parameters. In the pulsed bubble discharge reactor of [51] and the positive pulsed streamer discharge in wetted-wall reactor of [88], energy efficiency increased for rising voltage amplitude. In a negative pulsed DBD falling water film reactor [130] and a positive pulsed corona electrospray reactor [106], however, increasing voltage amplitude reduced the energy efficiency. In the gas phase DBD reactor of [128], the interruption period of pulse-modulated AC voltage had no effect on methyl orange degradation, while lowering its duty cycle from 100% to 25% increased energy efficiency 2.11 times. The authors explained the latter effect with additional dye degradation during plasma off time under influence of long living reactive species such as O_3 and H_2O_2. Sinusoidal voltage frequency is an important parameter, as it can lead to different plasma phenomena, which explains the distinction of AC, radio frequency and microwave discharge. Nevertheless, very limited information is available in literature on the dependence of energy efficiency of the sinusoidal frequency for a given reactor design. In [81], no change in energy efficiency was observed for 4-chlorobenzoic acid decomposition with voltage frequency increase of from 500 Hz to 2000 Hz for AC powered DBD over moving water film. Increasing AC frequency from 1.5 kHz to 15.6 kHz, kept energy efficiency of a coaxial falling water film DBD reactor in the same order of magnitude as well, in spite of the additional heating that resulted from the higher frequency [131]. In the case of pulsed discharge, pulse properties such as rise time and width are expected to be important. For pulsed positive corona discharge in humid O_2/N_2 atmosphere, energy efficiency of radical and excited species production increases with decreasing pulse width [132]. This is in agreement with the higher efficiency of indigo carmine decomposition for shorter pulse width observed in [133] for a positive pulsed streamer discharge spray reactor. A faster pulse rise rate generated thicker streamers and a higher energy efficiency in the same reactor [134]. Positive pulsed arc

electrohydraulic discharge was reported to have increased energy efficiency of sulfadimethoxine when pulse duration was brought back from 100 μs to 20 μs [10]. Remarkably, also pulse frequency can influence reactor efficiency. In a bubble reactor with positive pulsed corona, energy efficiency of 2,4-DCP degradation increased with increasing pulse frequency [135]. In contrast, energy efficiency of indigo carmine reduction dropped for increasing pulse frequency in a positive pulsed streamer wetted-wall reactor [88], in a negative pulsed DBD spray reactor [103] and in a positive pulsed DBD hybrid film and spray reactor [113]. In a negative pulsed DBD falling water film reactor [136] and a positive pulsed corona spray reactor [102], no influence of the frequency was observed. In bipolar pulsed electrohydraulic reactors, breakdown voltage decreases with frequency [21, 55]. Reversing voltage polarity can also cause significant changes in plasma properties and thus treatment efficiency. In [55], positive polarity of pulsed corona in electrohydraulic discharge greatly enhanced energy efficiency of methyl orange decomposition in pin-to-plate electrode configuration in comparison with negative polarity. The authors explain this observation with the space charge effect, which causes positive corona streamers to be faster and longer, hence increasing radical production and plasma-water contact surface. In [137], higher efficiency was observed as well for positive polarity in a DC bubble discharge reactor. For phenol decomposition in gas phase discharge reactors with a 20% O_2 and 80% N_2 atmosphere, negative DC was found to be more efficient than positive one in [138], while in [67], no significant difference was seen for both polarities with pulsed power. In a pulsed DBD falling water film reactor, better results were obtained with negative polarity as compared to positive one [130]. In the bubble discharge reactor of Figure 3.2h with O_2, He, Ar or Ne bubbles, positive DC voltage performed better than negative one for decomposition of interfacial active agents [42]. For negative polarity, electrolysis occurred with formation of hydrogen and oxygen gases. For positive polarity, the interfacial anion agents were more concentrated at the bubble surface due to electrostatic attraction. Positive plasma species collided with the water surface, where a cathode drop is formed. These unknown species likely enhanced decomposition of the agents.

The working gas determines many plasma features for a given input voltage waveform, such as breakdown voltage, electron density and temperature, plasma homogeneity and intensity, generated reactive species, etc. Air is the most frequently used working gas for water treatment plasma reactors, due to its wide availability. Pure oxygen gas, however, is often found to give more efficient organic degradation, while nitrogen gas leads to lower efficiency [4, 5, 9]. This can be partly explained with formation of OH radicals and O_3 in oxygen. In N_2 containing gases, however, toxic aqueous nitric products are generated which decrease solution pH and act as scavengers of oxidants such as OH radicals [9]. Noble gases like helium and argon are sometimes used, especially in bubble discharge reactors. Often, argon leads to faster decomposition of phenols but performs worse than oxygen for other compounds [9]. In a wetted-wall reactor (Figure 3.5b) with argon, streamer discharge has been observed which had slightly better phenol decomposition energy efficiency than corona

in oxygen [87]. Noble gases, however, are expected to be less economically feasible for use on larger scale due to their high price. Interestingly, treatment efficiency of electrohydraulic discharge reactors can also be altered by bubbling different gases through the solution under treatment, where bubbles are kept away from the discharge zone. Sahni and Locke observed a decrease in nitroform anion decomposition by pulsed underwater corona when the solution was oxygenated with O_2 gas or deoxygenated with N_2, He or Ar gas as compared to discharge without prior bubbling, but the authors could not explain this effect [139]. Also water content of the working gas should be taken into account, as it influences formation of important oxidants such as OH and H_2O_2.

Gas flow rate is another factor that needs to be taken into consideration. In three bubble discharge reactors, increasing bubble flow rate enhanced the decomposition process [117, 140, 141], while in [142] no significant effect was observed. In the hybrid reactor with bubbles from Figure 3.9e, oxidation rate first increased and then reached a stationary value with rising gas flow rate [112]. Also in the remote discharge reactor with bubbling from [143], increasing gas flow enhanced decomposition. For gas phase discharge reactors, the influence of gas flow rate seems less pronounced. In a positive pulsed corona-like discharge over water, phenol decomposition was slower with increasing oxygen flow and slightly dropped with increasing air flow, while argon flow rate had no influence [144, 145]. In a pulsed DBD falling water film reactor, the effect of the oxygen flow rate on methylene blue degradation was not significant [130].

In reactors with moving solution, the water flow rate often influences the decomposition process. In coaxial falling water film reactors with corona discharge, phenol degradation rate was unchanged with faster water flow for positive pulsed voltage [87], while it dropped in case of negative DC, which was attributed to higher roughness of the water surface [86]. In a pulsed DBD falling water film reactor, energy efficiency of methylene blue degradation decreased with increasing water flow rate [130]. In contrast, 4-chlorobenzoic acid was decomposed faster with increasing water flow for AC gliding arc discharge over falling water film [82]. Measurements in spray discharge reactors indicate the existence of an optimal water flow rate. In a positive pulsed streamer spray reactor, energy efficiency of indigo carmine decomposition initially increased and then stabilized with increasing water flow rate due to saturation of aqueous ozone [99]. Moreover, the efficiency was independent of droplet size. In a similar corona reactor, energy efficiency of oxalic acid decomposition first increased with rising water flow rate, reached a maximal value and subsequently dropped again [146]. The optimal water flow rate increased with applied pulse frequency. Rising water flow rate decreased breakdown voltage in a positive pulsed DBD spray reactor [104]. For the hybrid positive pulsed DBD spray and falling water film reactor of Figure 3.9g, energy efficiency of rhodamine B decomposition enhanced with increasing water flow [113].

3.9 Summary and concluding remarks

In this chapter, plasma reactors for liquid treatment are comprehensively classified based on their design and materials, in contrast to other reviews where focus lies more on applied voltage and discharge type. Although our focus lies mostly on aqueous micropollutant decomposition, this overview also applies to other applications, such as to oxidation of dyes and organic compounds in higher concentration and to treatment of liquids in general. Six main reactor types are distinguished. In electrohydraulic discharge reactors and bubble discharge reactors, plasma is generated directly in the liquid bulk, respectively without and with external application of bubbles. In gas phase discharge reactors and spray discharge reactors, plasma is generated in het gas phase, respectively over a water bulk or film and in contact with water drops or mist. Reactors that use a combination of these types simultaneously are classified as hybrid reactors. In the last type of reactors, referred to as remote discharge reactors, plasma is not generated in direct contact with the solution under treatment. All reactor types are summarized in Table 3.1.

Table 3.1 Overview of all plasma reactor types reported for water treatment with some of their most important features. IED stands for interelectrode distance.

Reactor type		Important features
Electrohydraulic discharge		Pulsed arc or corona; erosion particles; HV pin curvature; IED
Bubble discharge		Easier plasma onset; bubble gas; attached or free bubbles
Gas discharge	Corona and glow discharge	DC or pulsed power; water movement and dimensions
	DBD	Often AC, sometimes pulsed power; electrode material; IED
	Coaxial falling water film	Corona or DBD; gas flow rate and direction; IED
	Arc discharge	Gliding arc or active water electrode; addition of extra electrodes
Spray	Low-energy spray discharge	Efficient; corona, DBD or electrospray; droplet retention time
	Spray arc discharge	Addition of extra electrodes; spray direction
Hybrid reactor		Increased flexibility in design; possible synergetic effects
Remote discharge		Plasma gas bubbling and/or UV irradiation

Most commonly, electrohydraulic discharge reactors use pulsed arc or positively pulsed corona discharge, where electrode material can have substantial influence on organic decomposition after plasma contact due to formation of erosion particles in water. For the case of arc discharge, energy efficiency is reported to be dependent on inter-electrode distance. For pulsed corona, high voltage pin curvature radius is an important parameter as well. The corona plasma volume can be enlarged by replacing the high voltage pin with a multi-pin electrode or a high voltage electrode covered with a thin porous ceramic layer. Diaphragm and capillary discharge are expected to have similar plasma features to corona

discharge in pin-to-plate electrode configuration, which is in agreement with the similar energy efficiency. Contact glow discharge electrolysis is another common type of electrohydraulic discharge, where electrode material also plays an important role. In more exotic types of electrohydraulic discharge reactors, plasma formation is preceded by cavitation under application of RF or microwave power.

Adding external bubbles in the water bulk has the advantages of easier plasma onset, immediate mixing of the solution, minimizing electrode erosion and increasing radical density. Most commonly, bubbles are generated by pumping gas through a dielectric or an electrode, which is shaped as a nozzle, perforated plate or porous ceramic. Choices in bubble gas, nozzle or perforation material, shape, dimensions and orientation strongly influence plasma properties, which complicates reactor comparison. Often, the high voltage electrode is positioned directly in contact with the bubble or in de gas phase in contact with the bubble. In that case, energy efficiency can be enhanced by increasing the number of nozzles or holes. Alternatively, bubbles can be positioned in between submerged electrodes. Some common bubble discharge reactors use a coaxial DBD configuration, where the gas is bubbled in axial direction. Energy efficiency in these systems can be increased by using a double barrier or adding glass beads in the water bulk. More exotic types of bubble discharge reactors have been reported in literature, with promising first results.

Corona and glow discharge in gas phase over grounded water bulk or film is mostly generated with pulsed power. Negative pulsed corona over flowing water film in a pilot system has been shown to have better or comparable energy efficiency than other advanced oxidation processes. Based on one report, energy efficiency of organic decomposition seems to be independent of the type of discharge, voltage amplitude, polarity of the applied voltage and amount of pin electrodes. In contrast, DBD over water bulk or film has an energy efficiency which is reported to increase with increasing voltage amplitude and decreasing inter-electrode distance. Inter-electrode distance can be decreased substantially by adding a porous ceramic segment at the water surface. Movement of the water phase by stirring or by making it flow as a film along the discharge increases energy efficiency substantially, making water flow rate an important parameter for optimization. Based on this principle, coaxial reactors with falling water film are gaining more popularity. Such reactors can be further optimized by adjusting gas flow direction and electrode and barrier dimensions. A last common gas phase discharge reactor uses arc discharge over the water bulk or film. Larger arc treated water surface and energy efficiency can be reached by using a couple of controlled electrodes or a second high voltage electrode.

Spray discharge reactors have received more attention in recent years due to their high reported energy efficiencies. In the case of positive pulsed corona, treatment is more efficient for droplets near the inner reactor wall, while droplet size has no influence on energy efficiency. Such reactors can be further optimized by adding fluorocarbon wires along the inner reactor wall for larger droplet retention time. Other spray discharge reactors treat droplets with DBD, electrospray or arc discharge. In the case of gliding arc, the process can

be optimized by addition of a couple of controlled electrodes or a second high voltage electrode and by introducing the water perpendicular to the gas flow to improve contact with plasma. Also DC plasma torches can be used for water treatment by injecting the solution into the torch as plasma forming gas.

One type of hybrid reactors is designed by placing a high voltage electrode in the water phase and a ground electrode or second high voltage electrode in the gas phase above the water surface, without or with the addition of bubbles. Their energy efficiency for organic decomposition is moderately higher than the one of electrohydraulic discharge reactors. Another hybrid reactor type naturally occurs by spraying water from a shower nozzle at an angle, causing a falling water film in combination with spray. In such case, organic decomposition in droplets is more efficient than in the water film. A more exotic hybrid reactor that deserves more attention consists of a spray discharge reactor where droplets are formed by electrospray.

Remote discharge reactors can be encountered in many configurations. In the most standard design, plasma gas is remotely generated and sequentially bubbled through the solution, as in the well-known example of ozonation. Plasma gas bubbling can be combined with UV irradiation by generating plasma inside a quartz tube submerged in the solution. Research has indicated that such reactors may be competitive technology to systems with direct plasma treatment. Plasma can also be used solely for UV irradiation, as in plasma lamps, excimer lamps and microwave discharge electrodeless lamps. Recently, generation and application of plasma-activated water for water disinfection is gaining popularity, while its effects on organic contamination are still largely unknown.

Additionally, the importance of voltage waveform, working gas and flow rates of gas and water for further optimization are shortly reviewed in this chapter. Energy efficiency has different dependency for different reactor types on voltage parameters, such as voltage type, amplitude, polarity, sinusoidal frequency, pulse rise time, pulse duration and pulse frequency. For example, positive polarity causes higher efficiency of electrohydraulic and bubble discharge reactors in all considered cases, explained with the space charge effect. On the other hand, negative polarity gives better performance in gas phase discharge reactors. The choice of working gas can significantly alter plasma chemistry and therefore treatment efficiency and by-product formation. While atmospheric air is often chosen due to its wide availability, oxygen generally enhances the process. Argon often performs better for phenol degradation, but is expected to be less economically feasible for use on large scale. Increasing gas flow rate typically enhances decomposition in bubble discharge and remote discharge reactors, whereas its effect is less pronounced in gas phase discharge reactors. Also adjustment of water flow can significantly increase energy efficiency. Measurements in spray discharge reactors, for instance, indicate the existence of an optimal water flow rate. While dependency of a few of these parameters on energy efficiency seems adequately established for a limited number of reactor types, a deeper literature study and more experimental investigation are required for additional confirmation and a better understanding in most of

the cases. Due to the wide variety in plasma reactors and the distinct, unique features of every reactor, researchers are motivated to report new results in this field, including clear descriptions of reactor design and materials.

One needs to keep a few additional influences in mind when interpreting energy efficiencies reported in literature. First of all, initial concentration of the considered compound can influence the exact value of energy efficiency. Therefore, researchers are advised to use representative concentrations in their experiments, as this is commonly not done for micropollutant removal. Also, solution parameters such as water temperature, pH, conductivity and water matrix can have significant effect on plasma chemistry and reactions in the water bulk. Often, deionized water at room temperature is used as solvent in plasma reactors. In other cases, however, deviations in energy efficiency can be caused by a difference in solution parameters. Also, it should be remarked that micropollutant measurement is generally performed a certain time after plasma treatment with analytical chemistry methods, such as gas chromatography-mass spectrometry and liquid chromatography-mass spectrometry. During this time, post-reactions with long-living oxidants can occur, decomposing the micropollutant to a greater extent. This effect is usually neglected by researchers, complicating accurate comparison between reported energy efficiencies. On the positive side, this aging effect can be beneficial in applications where sufficiently long hydraulic retention time is possible after plasma treatment. Last but not least, most of the reported electrical discharge reactors only treat small water volumes in batch mode without or with recirculation of water. As a result, the determined energy efficiency can be significantly different for the same reactor type in single-pass mode, where water is flowing through the system only once. The latter case is more representative for industrial application and thus deserves more attention.

In this chapter, only improvement of the plasma process in terms of reactor design, materials and working parameters is discussed. Further optimization can be achieved by combining plasma discharge with other advanced treatment methods, such as adsorption, Fenton's reagent, photocatalysis and ultrasonication. Such combinations have been reported before, but require additional attention and further exploration. As should be noted, plasma technology can also be used for synthesis, pre-treatment, regeneration and post-treatment of materials and matter involved in water treatment processes, such as nanotubes, membranes, activated carbon, excess sludge and organic concentrate from filtration. In-line application of these methods during the water treatment process needs to be considered as a possible alternative to direct water treatment with advanced oxidation processes, since energy demand and overall costs can be pressed significantly this way. However, more experimental investigation and thorough cost analysis is necessary to confirm this claim.

Future application of plasma discharge for water treatment will largely depend on its effectiveness and energy efficiency as compared to other advanced oxidation processes and treatment methods in general, but additional criteria need to be taken into consideration as well. Sustainability, ease of operation, capital costs and costs related to maintenance, gas

input and additional energy for pumps will also determine whether a system will be adopted on a large scale. Moreover, an extensive study of generated oxidation by-products and long-living oxidants in treated water is necessary to assure that overall toxicity is consistently and sufficiently decreased after plasma treatment. Up to now, reports on these topics are largely lacking in literature or limited to only a few specific cases.

Considering the insights gained from this literature study, five reactors have been developed and used in this work. Each of the following chapters deals with one of these reactors. For reasons of clarity and comprehensibility, these reactors are summarized in Table 3.2, with a short motivation.

Table 3.2 Short description of the reactors used in each chapter of this work, including a motivation for their study and application.

Chapter 4	reactor	Multiple rising bubbles in between pin-to-plate electrodes with pulsed power
	motivation	Bubbles allow less energy input and larger plasma-liquid interface
Chapter 5	reactor	Single, stationary bubble on HV needle electrode with pulsed power
	motivation	Reproducible bubble discharge allows time and space resolved measurement
Chapter 6	reactor	Pulsed DBD in air over flowing water film on nanofiber membrane
	motivation	Easily upscalable and possible synergy with adsorption and catalysis
Chapter 7	reactor	Single, stable AC powered DBD micro-discharge filament over water film
	motivation	Reproducible micro-discharge allows time and space resolved measurement
Chapter 8	reactor	AC DBD in air over falling water film on 100% activated carbon textile
	motivation	Upscalability and possible synergy with adsorption and plasma gas bubbling

References

[1] P. Bruggeman and C. Leys, "Non-thermal plasmas in and in contact with liquids," *Journal of Physics D: Applied Physics,* vol. 42, p. 053001, 2009.

[2] B. Locke*, et al.*, "Electrohydraulic discharge and nonthermal plasma for water treatment," *Industrial & Engineering Chemistry Research,* vol. 45, pp. 882-905, 2006.

[3] P. J. Bruggeman and B. R. Locke, "Assessment of Potential Applications of Plasma with Liquid Water," in *Low Temperature Plasma Technology - Methods and Applications*, P. K. Chu and L. XinPei, Eds., ed Boca Raton, FL 33487-2742: CRC Press, 2014, pp. 367-399.

[4] B. Jiang*, et al.*, "Review on electrical discharge plasma technology for wastewater remediation," *Chemical Engineering Journal,* vol. 236, pp. 348-368, 2014.

[5] M. A. Malik, "Water Purification by Plasmas: Which Reactors are Most Energy Efficient?," *Plasma Chemistry and Plasma Processing,* vol. 30, pp. 21-31, 2010.

[6] E.-J. Lee, *et al.*, "Application of underwater elctric barrier discharfe as a washing system to inactivate salmonella typhimurium on perillar leaves," in *Plasma Sciences (ICOPS), 2015 IEEE International Conference on*, 2015, pp. 1-1.

[7] P. Vanraes, *et al.*, "Removal of atrazine in water by combination of activated carbon and dielectric barrier discharge," *Journal of Hazardous Materials,* vol. 299, pp. 647–655, 2015.

[8] B. R. Locke and K.-Y. Shih, "Review of the methods to form hydrogen peroxide in electrical discharge plasma with liquid water," *Plasma Sources Science and Technology,* vol. 20, p. 034006, 2011.

[9] M. Hijosa-Valsero, *et al.*, "Decontamination of waterborne chemical pollutants by using atmospheric pressure nonthermal plasma: a review," *Environmental Technology Reviews,* vol. 3, pp. 71-91, 2014.

[10] N. Parkansky, *et al.*, "Submerged Arc Breakdown of Sulfadimethoxine (SDM) in Aqueous Solutions," *Plasma Chemistry and Plasma Processing,* vol. 28, pp. 583-592, 2008.

[11] N. Parkansky, *et al.*, "Submerged Arc Breakdown of Methylene Blue in Aqueous Solutions," *Plasma Chemistry and Plasma Processing,* vol. 32, pp. 933-947, 2012.

[12] Q.-X. Lin, *et al.*, "The Research on Pulsed Arc Electrohydraulic Discharge With Discharge Electrode and Its Application to Removal of Bacteria," *Plasma Science, IEEE Transactions on,* vol. 43, pp. 1029-1039, 2015.

[13] L. Zhu, *et al.*, "The research on the pulsed arc electrohydraulic discharge and its application in treatment of the ballast water," *Journal of Electrostatics,* vol. 71, pp. 728-733, 2013.

[14] N. Parkansky, *et al.*, "Decomposition of Dissolved Methylene Blue in Water Using a Submerged Arc Between Titanium Electrodes," *Plasma Chemistry and Plasma Processing,* vol. 33, pp. 907-919, 2013.

[15] P. Lang, *et al.*, "Oxidative degradation of 2, 4, 6-trinitrotoluene by ozone in an electrohydraulic discharge reactor," *Environmental Science & Technology,* vol. 32, pp. 3142-3148, 1998.

[16] D. M. Angeloni, *et al.*, "Removal of Methyl-tert-butyl Ether from Water by a Pulsed Arc Electrohydraulic Discharge System," *Japanese Journal of Applied Physics,* vol. 45, pp. 8290-8293, 2006.

[17] N. Karpel Vel Leitner, *et al.*, "Generation of active entities by the pulsed arc electrohydraulic discharge system and application to removal of atrazine," *Water Research,* vol. 39, pp. 4705-4714, 2005.

[18] L. V. Hoang and B. Legube, "Degradation of 4-chlorophenol by pulsed arc discharge in water-estimation of the energy consumption," *IEEE Transactions on Dielectrics and Electrical Insulation,* vol. 16, pp. 1604-1608, 2009.

[19] P. Šunka, *et al.*, "Potential applications of pulse electrical discharges in water," *Acta Physica Slovaca,* vol. 54, pp. 135-145, 2004.

[20] Š. Potocký, *et al.*, "Needle electrode erosion in water plasma discharge," *Thin Solid Films,* vol. 518, pp. 918-923, 2009.

[21] P. Baroch, *et al.*, "Generation of plasmas in water: utilization of a high-frequency, low-voltage bipolar pulse power supply with impedance control," *Plasma Sources Science and Technology,* vol. 20, p. 034017, 2011.

[22] T. Takeda, *et al.*, "Morphology of high-frequency electrohydraulic discharge for liquid-solution plasmas," *Plasma Science, IEEE Transactions on,* vol. 36, pp. 1158-1159, 2008.

[23] Q. Lu, *et al.*, "Degradation of 2,4-dichlorophenol by using glow discharge electrolysis," *Journal of Hazardous Materials,* vol. 136, pp. 526-531, 2006.

[24] Q. Lu, *et al.*, "Glow discharge induced hydroxyl radical degradation of 2-naphthylamine," *Plasma Science and Technology,* vol. 7, p. 2856, 2005.

[25] S. Mededovic, *et al.*, "Aqueous-phase mineralization of s-triazine using pulsed electrical discharge," *IJPEST,* vol. 1, pp. 82-90, 2007.

[26] S. Mededovic and B. R. Locke, "Side-chain degradation of atrazine by pulsed electrical discharge in water," *Industrial & Engineering Chemistry Research,* vol. 46, pp. 2702-2709, 2007.

[27] P. Sunka, *et al.*, "Generation of chemically active species by electrical discharges in water," *Plasma Sources Science and Technology,* vol. 8, p. 258, 1999.

[28] B. Sun, *et al.*, "Optical study of active species produced by a pulsed streamer corona discharge in water," *Journal of Electrostatics,* vol. 39, pp. 189-202, 1997.

[29] P. Lukes, *et al.*, "The catalytic role of tungsten electrode material in the plasmachemical activity of a pulsed corona discharge in water," *Plasma Sources Science and Technology,* vol. 20, p. 034011, 2011.

[30] H. Zheng, *et al.*, "p-Nitrophenol Enhanced Degradation in High-Voltage Pulsed Corona Discharges Combined with Ozone System," *Plasma Chemistry and Plasma Processing,* vol. 33, pp. 1053-1062, 2013.

[31] C. W. Chen, *et al.*, "Ultrasound-assisted plasma: a novel technique for inactivation of aquatic microorganisms," *Environmental Science & Technology,* vol. 43, pp. 4493-4497, 2009.

[32] M. M. Sein, *et al.*, "Studies on a non-thermal pulsed corona plasma between two parallel-plate electrodes in water," *Journal of Physics D: Applied Physics,* vol. 45, p. 225203, 2012.

[33] P. Lukes, *et al.*, "Effect of ceramic composition on pulse discharge induced processes in water using ceramic-coated wire to cylinder electrode system," *Czech. J. Phys,* vol. 52, pp. D800-D806, 2002.

[34] P. Lukes, *et al.*, "The Role of Surface Chemistry at Ceramic/Electrolyte Interfaces in the Generation of Pulsed Corona Discharges in Water Using Porous Ceramic-Coated Rod Electrodes," *Plasma Processes and Polymers,* vol. 6, pp. 719-728, 2009.

[35] Y. J. Liu and X. Z. Jiang, "Phenol degradation by a nonpulsed diaphragm glow discharge in an aqueous solution," *Environmental Science & Technology,* vol. 39, pp. 8512-8517, 2005.

[36] L. Wang, "4-Chlorophenol degradation and hydrogen peroxide formation induced by DC diaphragm glow discharge in an aqueous solution," *Plasma Chemistry and Plasma Processing,* vol. 29, pp. 241-250, 2009.

[37] V. Goncharuk, *et al.*, "The diaphragm discharge and its use for water treatment," *Journal of Water Chemistry and Technology,* vol. 30, pp. 261-268, 2008.

[38] X. Jin, *et al.*, "An improved multi-anode contact glow discharge electrolysis reactor for dye discoloration," *Electrochimica Acta,* vol. 59, pp. 474-478, 2012.

[39] T. Maehara, *et al.*, "Influence of conductivity on the generation of a radio frequency plasma surrounded by bubbles in water," *Plasma Sources Science and Technology,* vol. 20, p. 034016, 2011.

[40] T. Ishijima, *et al.*, "Efficient production of microwave bubble plasma in water for plasma processing in liquid," *Plasma Sources Science and Technology,* vol. 19, p. 015010, 2010.

[41] N. Remya and J.-G. Lin, "Current status of microwave application in wastewater treatment—a review," *Chemical Engineering Journal,* vol. 166, pp. 797-813, 2011.

[42] K. Yasuoka, *et al.*, "An energy-efficient process for decomposing perfluorooctanoic and perfluorooctane sulfonic acids using dc plasmas generated within gas bubbles," *Plasma Sources Science and Technology,* vol. 20, p. 034009, 2011.

[43] H. Aoki, *et al.*, "Plasma generation inside externally supplied Ar bubbles in water," *Plasma Sources Science and Technology,* vol. 17, p. 025006, 2008.

[44] D. C. Johnson, *et al.*, "Treatment of methyl tert-butyl ether contaminated water using a dense medium plasma reactor: a mechanistic and kinetic investigation," *Environmental Science & Technology,* vol. 37, pp. 4804-4810, 2003.

[45] W. Bian, *et al.*, "Enhanced degradation of p-chlorophenol in a novel pulsed high voltage discharge reactor," *Journal of Hazardous Materials,* vol. 162, pp. 906-912, 2009.

[46] Y. Zhang, *et al.*, "Methyl orange degradation by pulsed discharge in the presence of activated carbon fibers," *Chemical Engineering Journal,* vol. 159, pp. 47-52, 2010.

[47] N. Lu, *et al.*, "Electrical Characteristics of Pulsed Corona Discharge Plasmas in Chitosan Solution," *Plasma Science and Technology,* vol. 16, pp. 128-133, 2014.

[48] M. Kurahashi, *et al.*, "Radical formation due to discharge inside bubble in liquid," *Journal of Electrostatics,* vol. 42, pp. 93-105, 1997.

[49] K. Sato, *et al.*, "Water treatment with pulsed discharges generated inside bubbles," *Electrical Engineering in Japan,* vol. 170, pp. 1-7, 2010.

[50] A. Yamatake, *et al.*, "Water purification by atmospheric DC/pulsed plasmas inside bubbles in water," *Int. J. Plasma Environ. Sci. Technol,* vol. 1, pp. 91-95, 2007.

[51] J. Li, *et al.*, "Degradation of phenol in water using a gas–liquid phase pulsed discharge plasma reactor," *Thin Solid Films,* vol. 515, pp. 4283-4288, 2007.

[52] N. Lu, *et al.*, "Treatment of Dye Wastewater by Using a Hybrid Gas/Liquid Pulsed Discharge Plasma Reactor," *Plasma Science and Technology,* vol. 14, pp. 162-166, 2012.

[53] A. Y. Nikiforov, "An application of AC glow discharge stabilized by fast air flow for water treatment," *Plasma Science, IEEE Transactions on,* vol. 37, pp. 872-876, 2009.

[54] H. Wang, *et al.*, "Enhanced generation of oxidative species and phenol degradation in a discharge plasma system coupled with TiO2 photocatalysis," *Applied Catalysis B: Environmental,* vol. 83, pp. 72-77, 2008.

[55] H. Lee, *et al.*, "The Effect of Liquid Phase Plasma for Photocatalytic Degradation of Bromothymol Blue," *Science of Advanced Materials,* vol. 6, pp. 1627-1631, 2014.

[56] T. Miichi, *et al.*, "Generation of radicals using discharge inside bubbles in water for water treatment," *Ozone: Science & Engineering,* vol. 24, pp. 471-477, 2002.

[57] P. Vanraes, *et al.*, "Electrical and spectroscopic characterization of underwater plasma discharge inside rising gas bubbles," *Journal of Physics D: Applied Physics,* vol. 45, p. 245206, 2012.

[58] R. Zhang, *et al.*, "Plasma induced degradation of Indigo Carmine by bipolar pulsed dielectric barrier discharge (DBD) in the water-air mixture," *Journal of environmental sciences (China),* vol. 16, pp. 808-812, 2004.

[59] R.-b. Zhang, *et al.*, "Enhancement of the plasma chemistry process in a three-phase discharge reactor," *Plasma Sources Science and Technology,* vol. 14, pp. 308-313, 2005.

[60] A. Anpilov, *et al.*, "Electric discharge in water as a source of UV radiation, ozone and hydrogen peroxide," *Journal of Physics D: Applied Physics,* vol. 34, p. 993, 2001.

[61] E. M. Barkhudarov, *et al.*, "Multispark Discharge in Water as a Method of Environmental Sustainability Problems Solution," *Journal of Atomic and Molecular Physics,* vol. 2013, pp. 1-12, 2013.

[62] S. Horikoshi, *et al.*, "A novel liquid plasma AOP device integrating microwaves and ultrasounds and its evaluation in defluorinating perfluorooctanoic acid in aqueous media," *Ultrasonics Sonochemistry,* vol. 18, pp. 938-942, 2011.

[63] C. Yamabe, *et al.*, "Water treatment using discharge on the surface of a bubble in water," *Plasma Processes and Polymers,* vol. 2, pp. 246-251, 2005.

[64] P. Bruggeman, *et al.*, "Water surface deformation in strong electrical fields and its influence on electrical breakdown in a metal pin–water electrode system," *Journal of Physics D: Applied Physics,* vol. 40, p. 4779, 2007.

[65] P. Bruggeman, *et al.*, "Influence of the water surface on the glow-to-spark transition in a metal-pin-to-water electrode system," *Plasma Sources Science and Technology,* vol. 17, p. 045014, 2008.

[66] L. O. d. B. Benetoli, *et al.*, "Effect of temperature on methylene blue decolorization in aqueous medium in electrical discharge plasma reactor," *Journal of the Brazilian Chemical Society,* vol. 22, pp. 1669-1678, 2011.

[67] Y. Miyazaki, *et al.*, "Pulsed discharge purification of water containing nondegradable hazardous substances," *Electrical Engineering in Japan,* vol. 174, pp. 1-8, 2011.

[68] M. Magureanu, *et al.*, "Pulsed Corona Discharge for Degradation of Methylene Blue in Water," *Plasma Chemistry and Plasma Processing,* vol. 33, pp. 51-64, 2013.

[69] M. Dors, *et al.*, "Phenol oxidation in aqueous solution by gas phase corona discharge," *Journal of Advanced Oxidation Technologies,* vol. 9, pp. 139-143, 2006.

[70] A. Sharma, *et al.*, "Destruction of pentachlorophenol using glow discharge plasma process," *Environmental Science & Technology,* vol. 34, pp. 2267-2272, 2000.

[71] P. Jamróz, *et al.*, "Atmospheric Pressure Glow Discharges Generated in Contact with Flowing Liquid Cathode: Production of Active Species and Application in Wastewater Purification Processes," *Plasma Chemistry and Plasma Processing,* vol. 34, pp. 25-37, 2014.

[72] I. Even-Ezra, *et al.*, "Application of a novel plasma-based advanced oxidation process for efficient and cost-effective destruction of refractory organics in tertiary effluents and contaminated groundwater," *Desalination and Water Treatment,* vol. 11, pp. 236-244, 2009.

[73] D. Gerrity, *et al.*, "An evaluation of a pilot-scale nonthermal plasma advanced oxidation process for trace organic compound degradation," *Water Research,* vol. 44, pp. 493-504, 2010.

[74] A. Mizrahi and I. M. Litaor, "The kinetics of the removal of organic pollutants from drinking water by a novel plasma-based advanced oxidation technology," *Desalination and Water Treatment,* vol. 52, pp. 5264-5275, 2013.

[75] Y. Hu, *et al.*, "Application of dielectric barrier discharge plasma for degradation and pathways of dimethoate in aqueous solution," *Separation and Purification Technology,* vol. 120, pp. 191-197, 2013.

[76] S. P. Li, *et al.*, "Degradation of nitenpyram pesticide in aqueous solution by low-temperature plasma," *Environmental Technology,* vol. 34, pp. 1609-1616, 2013.

[77] J. Feng, *et al.*, "Degradation of aqueous 3,4-dichloroaniline by a novel dielectric barrier discharge plasma reactor," *Environmental Science and Pollution Research,* vol. 22, pp. 4447-4459, 2015.

[78] M. Hijosa-Valsero, *et al.*, "Removal of priority pollutants from water by means of dielectric barrier discharge atmospheric plasma," *Journal of Hazardous Materials,* vol. 262, pp. 664-673, 2013.

[79] G. Fridman, *et al.*, "Floating electrode dielectric barrier discharge plasma in air promoting apoptotic behavior in melanoma skin cancer cell lines," *Plasma Chemistry and Plasma Processing,* vol. 27, pp. 163-176, 2007.

[80] E. Marotta, *et al.*, "Advanced Oxidation Process for Degradation of Aqueous Phenol in a Dielectric Barrier Discharge Reactor," *Plasma Processes and Polymers,* vol. 8, pp. 867-875, 2011.

[81] O. Lesage, *et al.*, "Degradation of 4-Chlorobenzoïc Acid in a Thin Falling Film Dielectric Barrier Discharge Reactor," *Industrial & Engineering Chemistry Research,* vol. 53, pp. 10387-10396, 2014.

[82] O. Lesage, *et al.*, "Treatment of 4-chlorobenzoic acid by plasma-based advanced oxidation processes," *Chemical Engineering and Processing: Process Intensification,* vol. 72, pp. 82-89, 2013.

[83] S. Li, *et al.*, "Degradation of thiamethoxam in water by the synergy effect between the plasma discharge and the TiO2photocatalysis," *Desalination and Water Treatment,* vol. 53, pp. 3018-3025, 2014.

[84] P. Baroch, *et al.*, "Special type of plasma dielectric barrier discharge reactor for direct ozonization of water and degradation of organic pollution," *Journal of Physics D: Applied Physics,* vol. 41, p. 085207, 2008.

[85] S. Rong and Y. Sun, "Wetted-wall corona discharge induced degradation of sulfadiazine antibiotics in aqueous solution," *Journal of Chemical Technology & Biotechnology,* vol. 89, pp. 1351-1359, 2013.

[86] N. Sano, *et al.*, "Decomposition of Phenol in Water by a Cylindrical Wetted-Wall Reactor Using Direct Contact of Gas Corona Discharge," *Industrial & Engineering Chemistry Research,* vol. 42, pp. 5423-5428, 2003.

[87] M. Sato, *et al.*, "Decomposition of phenol in water using water surface plasma in wetted-wall reactor," *International Journal of Plasma Environmental Science & Technology,* vol. 1, pp. 71-75, 2007.

[88] T. Yano, *et al.*, "Decolorization of indigo carmine solution using nanosecond pulsed power," *Dielectrics and Electrical Insulation, IEEE Transactions on,* vol. 16, pp. 1081-1087, 2009.

[89] M. Morimoto, *et al.*, "Indigo carmine solution treatment by nanosecond pulsed power with a dielectric barrier electrode," *Dielectrics and Electrical Insulation, IEEE Transactions on,* vol. 22, pp. 1872-1878, 2015.

[90] K. Faungnawakij, *et al.*, "Removal of acetaldehyde in air using a wetted-wall corona discharge reactor," *Chemical Engineering Journal,* vol. 103, pp. 115-122, 2004.

[91] Y. Chen, *et al.*, "A Discharge Reactor with Water-Gas Mixing for Methyl Orange Removal," *International Journal of Plasma Environmental Science and Technology,* 2008.

[92] S. Ognier, *et al.*, "Analysis of Mechanisms at the Plasma–Liquid Interface in a Gas–Liquid Discharge Reactor Used for Treatment of Polluted Water," *Plasma Chemistry and Plasma Processing,* vol. 29, pp. 261-273, 2009.

[93] A. G. Bubnov, *et al.*, "Plasma-Catalytic Decomposition of Phenols in Atmospheric Pressure Dielectric Barrier Discharge," *Plasma Chemistry and Plasma Processing,* vol. 26, pp. 19-30, 2006.

[94] S.-P. Rong, *et al.*, "Degradation of sulfadiazine antibiotics by water falling film dielectric barrier discharge," *Chinese Chemical Letters,* vol. 25, pp. 187-192, 2014.

[95] J.-L. Brisset, *et al.*, "Chemical reactivity of discharges and temporal post-discharges in plasma treatment of aqueous media: examples of gliding discharge treated solutions," *Industrial & Engineering Chemistry Research,* vol. 47, pp. 5761-5781, 2008.

[96] R. Burlica, *et al.*, "Organic dye removal from aqueous solution by glidarc discharges," *Journal of Electrostatics,* vol. 62, pp. 309-321, 2004.

[97] J. Janca, *et al.*, "Investigation of the chemical action of the gliding and "point" arcs between the metallic electrode and aqueous solution," *Plasma Chemistry and Plasma Processing,* vol. 19, pp. 53-67, 1999.

[98] T. Kobayashi, *et al.*, "The effect of spraying of water droplets and location of water droplets on the water treatment by pulsed discharge in air," *Plasma Science, IEEE Transactions on,* vol. 38, pp. 2675-2680, 2010.

[99] T. Sugai, *et al.*, "The Effect of Flow Rate and Size of Water Droplets on the Water Treatment by Pulsed Discharge in Air," *IEEE Transactions on Plasma Science,* vol. PP, p. 1, 2015.

[100] T. Sugai, *et al.*, "Improvement of efficiency for decomposition of organic compound in water using pulsed streamer discharge in air with water droplets by increasing of residence time," in *Pulsed Power Conference, 2009. PPC'09. IEEE*, 2009, pp. 1056-1060.

[101] G. An, *et al.*, "Degradation of phenol in mists by a non-thermal plasma reactor," *Chemosphere,* vol. 84, pp. 1296-1300, 2011.

[102] S. Preis, *et al.*, "Formation of Nitrates in Aqueous Solutions Treated with Pulsed Corona Discharge: The Impact of Organic Pollutants," *Ozone: Science & Engineering,* vol. 36, pp. 94-99, 2014.

[103] S. Jiang, *et al.*, "Investigation of pulsed dielectric barrier discharge system on water treatment by liquid droplets in air," *Dielectrics and Electrical Insulation, IEEE Transactions on,* vol. 22, pp. 1866-1871, 2015.

[104] J. Kornev, *et al.*, "Generation of Active Oxidant Species by Pulsed Dielectric Barrier Discharge in Water-Air Mixtures," *Ozone: Science & Engineering,* vol. 28, pp. 207-215, 2006.

[105] Z. Wang, *et al.*, "Plasma decoloration of dye using dielectric barrier discharges with earthed spraying water electrodes," *Journal of Electrostatics,* vol. 66, pp. 476-481, 2008.

[106] M. Elsawah, *et al.*, "Corona discharge with electrospraying system for phenol removal from water," *Plasma Science, IEEE Transactions on,* vol. 40, pp. 29-34, 2012.

[107] C. M. Du, *et al.*, "Degradation of 4-Chlorophenol using a Gas–Liquid Gliding Arc Discharge Plasma Reactor," *Plasma Chemistry and Plasma Processing,* vol. 27, pp. 635-646, 2007.

[108] D. Moussa, *et al.*, "Plasma-chemical destruction of trilaurylamine issued from nuclear laboratories of reprocessing plants," *Industrial & Engineering Chemistry Research,* vol. 45, pp. 30-33, 2006.

[109] D. R. Grymonpré, *et al.*, "Hybrid gas-liquid electrical discharge reactors for organic compound degradation," *Industrial & Engineering Chemistry Research,* vol. 43, pp. 1975-1989, 2004.

[110] P. Lukes, *et al.*, "Hydrogen peroxide and ozone formation in hybrid gas-liquid electrical discharge reactors," *Industry Applications, IEEE Transactions on,* vol. 40, pp. 60-67, 2004.

[111] P. Lukes, *et al.*, "Generation of ozone by pulsed corona discharge over water surface in hybrid gas–liquid electrical discharge reactor," *Journal of Physics D: Applied Physics,* vol. 38, pp. 409-416, 2005.

[112] H. Ren, *et al.*, "Oxidation of ammonium sulfite by a multi-needle-to-plate gas phase pulsed corona discharge reactor," *Journal of Physics: Conference Series,* vol. 418, p. 012128, 2013.

[113] Y. Nakagawa, *et al.*, "Decolorization of Rhodamine B in Water by Pulsed High-Voltage Gas Discharge," *Japanese Journal of Applied Physics,* vol. 42, pp. 1422-1428, 2003.

[114] E. Njatawidjaja, *et al.*, "Decoloration of electrostatically atomized organic dye by the pulsed streamer corona discharge," *Journal of Electrostatics,* vol. 63, pp. 353-359, 2005.

[115] Q. Tang, *et al.*, "Gas phase dielectric barrier discharge induced reactive species degradation of 2,4-dinitrophenol," *Chemical Engineering Journal,* vol. 153, pp. 94-100, 2009.

[116] J. Wohlers, *et al.*, "Application of an Air Ionization Device Using an Atmospheric Pressure Corona Discharge Process for Water Purification," *Water, Air, and Soil Pollution,* vol. 196, pp. 101-113, 2008.

[117] A. Yamatake, *et al.*, "Water treatment by fast oxygen radical flow with DC-driven microhollow cathode discharge," *Plasma Science, IEEE Transactions on,* vol. 34, pp. 1375-1381, 2006.

[118] D. Dobrynin, *et al.*, "Cold plasma inactivation of Bacillus cereus and Bacillus anthracis (anthrax) spores," *Plasma Science, IEEE Transactions on,* vol. 38, pp. 1878-1884, 2010.

[119] Z. Zhang, *et al.*, "Killing of red tide organisms in sea enclosure using hydroxyl radical-based micro-gap discharge," *Plasma Science, IEEE Transactions on,* vol. 34, pp. 2618-2623, 2006.

[120] H. S. Kim, *et al.*, "Use of plasma gliding arc discharges on the inactivation of E. Coli in water," *Separation and Purification Technology,* vol. 120, pp. 423-428, 2013.

[121] L. Jie, *et al.*, "Degradation of organic compounds by active species sprayed in a dielectric barrier corona discharge system," *Plasma Science and Technology,* vol. 11, p. 211, 2009.

[122] T. C. Wang, *et al.*, "Multi-tube parallel surface discharge plasma reactor for wastewater treatment," *Separation and Purification Technology,* vol. 100, pp. 9-14, 2012.

[123] D. Zhu, *et al.*, "Wire–cylinder dielectric barrier discharge induced degradation of aqueous atrazine," *Chemosphere,* vol. 117, pp. 506-514, 2014.

[124] M. Tichonovas, *et al.*, "Degradation of various textile dyes as wastewater pollutants under dielectric barrier discharge plasma treatment," *Chemical Engineering Journal,* vol. 229, pp. 9-19, 2013.

[125] Y. S. Mok, *et al.*, "Application of Dielectric Barrier Discharge Reactor Immersed in Wastewater to the Oxidative Degradation of Organic Contaminant," *Plasma Chemistry and Plasma Processing,* vol. 27, pp. 51-64, 2007.

[126] J. E. Foster, *et al.*, "A comparative study of the time-resolved decomposition of methylene blue dye under the action of a nanosecond repetitively pulsed DBD plasma jet using liquid chromatography and spectrophotometry," *Plasma Science, IEEE Transactions on,* vol. 41, pp. 503-512, 2013.

[127] R. Ma, *et al.*, "Non-thermal plasma-activated water inactivation of food-borne pathogen on fresh produce," *Journal of Hazardous Materials,* vol. 300, pp. 643-651, 2015.

[128] P. Olszewski, *et al.*, "Optimizing the electrical excitation of an atmospheric pressure plasma advanced oxidation process," *Journal of Hazardous Materials,* vol. 279, pp. 60-66, 2014.

[129] S. Horikoshi, *et al.*, "Microwave discharge electrodeless lamps (MDEL). III. A novel tungsten-triggered MDEL device emitting VUV and UVC radiation for use in wastewater treatment," *Photochemical & Photobiological Sciences,* vol. 7, p. 303, 2008.

[130] M. Magureanu, *et al.*, "Decomposition of methylene blue in water using a dielectric barrier discharge: Optimization of the operating parameters," *Journal of Applied Physics,* vol. 104, p. 103306, 2008.

[131] B. Jaramillo-Sierra, *et al.*, "Phenol degradation in aqueous solution by a gas-liquid phase DBD reactor," *The European Physical Journal Applied Physics,* vol. 56, p. 24026, 2011.

[132] R. Ono, *et al.*, "Effect of pulse width on the production of radicals and excited species in a pulsed positive corona discharge," *Journal of Physics D: Applied Physics,* vol. 44, p. 485201, 2011.

[133] T. Sugai, *et al.*, "Investigation of optimum pulse width of appled voltage for water treatment by pulsed streamer discharge in air spraying water droplets," in *Power Modulator and High Voltage Conference (IPMHVC), 2010 IEEE International*, 2010, pp. 213-216.

[134] T. Sugai and Y. Minamitani, "Influence of rise rate of applied voltage for water treatment by pulsed streamer discharge in air-sprayed droplets," *Plasma Science, IEEE Transactions on,* vol. 41, pp. 2327-2334, 2013.

[135] J. Zhang, *et al.*, "Degradation of 2,4-dichorophenol by pulsed high voltage discharge in water," *Desalination,* vol. 304, pp. 49-56, 2012.

[136] M. Magureanu, *et al.*, "Degradation of pharmaceutical compound pentoxifylline in water by non-thermal plasma treatment," *Water Research,* vol. 44, pp. 3445-3453, 2010.

[137] K. Yasuoka, *et al.*, "Degradation of perfluoro compounds and F-recovery in water using discharge plasmas generated within gas bubbles," *Int. J. Plasma Environ. Sci. Technol,* vol. 4, pp. 113-117, 2010.

[138] N. Sano, *et al.*, "Decomposition of organic compounds in water by direct contact of gas corona discharge: influence of discharge conditions," *Industrial & Engineering Chemistry Research,* vol. 41, pp. 5906-5911, 2002.

[139] M. Sahni and B. R. Locke, "Quantification of Reductive Species Produced by High Voltage Electrical Discharges in Water," *Plasma Processes and Polymers,* vol. 3, pp. 342-354, 2006.

[140] Y. Jin, *et al.*, "Optimizing decolorization of methylene blue and methyl orange dye by pulsed discharged plasma in water using response surface methodology," *Journal of the Taiwan Institute of Chemical Engineers,* vol. 45, pp. 589-595, 2014.

[141] R. Zhang, *et al.*, "Kinetics of decolorization of azo dye by bipolar pulsed barrier discharge in a three-phase discharge plasma reactor," *Journal of Hazardous Materials,* vol. 142, pp. 105-110, 2007.

[142] P. M. K. Reddy, *et al.*, "Degradation and mineralization of methylene blue by dielectric barrier discharge non-thermal plasma reactor," *Chemical Engineering Journal,* vol. 217, pp. 41-47, 2013.

[143] X. Chen, *et al.*, "Degradation of 4-chlorophenol in a dielectric barrier discharge system," *Separation and Purification Technology,* vol. 120, pp. 102-109, 2013.

[144] M. Sato, *et al.*, "Aqueous phenol decomposition by pulsed discharges on the water surface," *Industry Applications, IEEE Transactions on,* vol. 44, pp. 1397-1402, 2008.

[145] Z. He, *et al.*, "The Formation, Role and Removal of No3-N During Corona Discharge in Air for Phenol Removal," *Environmental Technology,* vol. 26, pp. 285-292, 2005.

[146] P. Ajo, *et al.*, "Pulsed Corona Discharge in Water Treatment: The Effect of Hydrodynamic Conditions on Oxidation Energy Efficiency," *Industrial & Engineering Chemistry Research,* vol. 54, pp. 7452-7458, 2015.

Look within. Within is the fountain of good,
and it will ever bubble up, if thou wilt ever dig.
- Marcus Aurelius

Chapter 4

Electrical and spectroscopic characterization of underwater plasma discharge inside rising gas bubbles

One of the most common generation methods encountered in the literature is a pulsed HV applied to a pin-to-plate electrode configuration submerged in water. The introduction of externally generated gas bubbles in between these electrodes may be preferable for several reasons. Electrical breakdown in water requires more energy and a higher electrical field than in gas. Therefore, the presence of bubbles in between submerged electrodes strongly reduces needed electrical power. Moreover, plasma discharge in bubbles is an attractive alternative for applications where the plasma–liquid interface is desired to be as large as possible in order to make chemical processes at the plasma–liquid interface more efficient. This efficiency is expected to be strongly dependent on bubble size and gas flow rate [1].

This chapter deals with pulsed plasma discharge in rising gas bubbles in between a pin-to-plate electrode system. Measurements of plasma properties in bubble gases helium, argon and nitrogen in water with different conductivities are carried out and compared. Also, these results are compared with measurements in the absence of bubbles. The emission spectra are analyzed by fitting the observed continuum in the spectrum to Planck's radiation law with a modified version of the fitting algorithm proposed by Bukvic et al. [2]. The number density of electrons in the plasma has been evaluated from Stark broadening of the hydrogen H_α Balmer line.

4.1 Experimental setup and procedure

The electrical bubble discharge is generated inside a cylindrical chamber made of stainless steel. The chamber has inside and outside diameter of, respectively, 21.6 cm and 22.0 cm, thickness of 10 mm at the bottom and top and an inside height of 20.1 cm. It is filled with solution up to 12 cm from the bottom. The discharge is observed through a circular quartz window of 30 mm diameter with its center at 6.2 cm from the bottom. The pin-to-plate electrode system is submerged in the water with its symmetrical axis horizontally at the same height. Both stainless steel electrodes were mounted on 1.0 cm thick PVC holders which insulated the electrical connections from the water. The plate electrode with diameter of 30 mm was fixed into its holder up to its surface. To prevent breakdown at its edges, they were grounded and covered with insulating glue. The pin electrode was 4.8 mm long and 1.6 mm thick. Its tip had the shape of a right circular cone with an aperture of 10°. It was pointing towards the center of the plate electrode with an interelectrode distance of 6.1 mm. The plate electrode is grounded in all experiments.

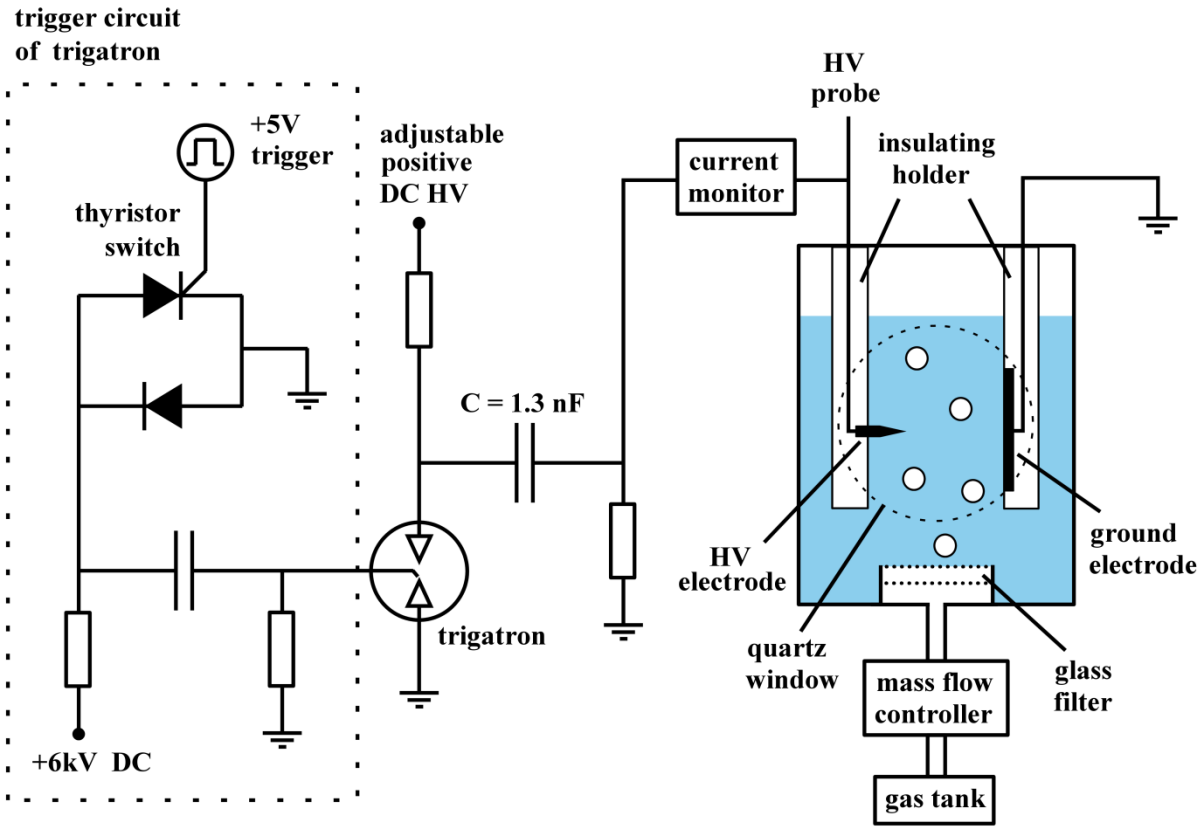

Figure 4.1 The setup consists of a negative HV pulse generator connected to a pin-to-plate electrode system submerged in distilled water or a salt solution inside a stainless steel chamber. Rising bubbles in between the electrodes are produced by pumping a gas through a porous glass filter disc.

A triggered HV power supply with an output capacitance of C = 1.3 nF was adjusted to generate negative HV pulses with a rise time of 3.8 ns kV^{-1}. The schematic of the used power supply and chamber is presented in figure 4.1. The trigger circuit of the trigatron is controlled by a HTS thyristor switch (Behlke, model 300-100-SCR). In this way, HV pulses in between the submerged electrodes with amplitudes up to 20 kV at a rate of about one pulse per four seconds are produced. Multiple gas bubbles are generated by flowing a gas through a glass filter disc made by ROBU (a standard filter with a diameter of 40 mm, a thickness of 4.5 mm and porosity class 3) positioned 3.2 cm underneath the symmetrical axis of the submerged electrodes. The gas flow is regulated with a mass flow control system (MKS 4000). Unless mentioned otherwise, a gas flow of 1.4 SLM is used in the measurements. A bubble diameter of 2.0 ± 0.3 mm is determined from photographs. The photographs confirm that at least one bubble is closer than 2 mm from the symmetrical axis of the electrodes at every moment of breakdown and that the bubbles never stick to the electrodes. Assuming a bubble velocity of 30 cm s^{-1} [3], a bubble number density of 26 cm^{-3} is calculated.

Voltage and current waveforms are measured with a Tektronix HV probe (model P6015A) and a Pearson current monitor (model 2877) connected to a Tektronix oscilloscope (model DTS 1002). In order to record the emitted spectrum of the plasma, an optical fiber with collimating lens is attached in front of the quartz glass window. The fiber is connected to an Ocean Optics spectrometer (model S2000) with integration time of 4 s, which corresponds to one plasma pulse. Also, the time-dependent light emission intensity is measured by connecting a PMT with a response time of 20 ns to the optical fiber afterwards.

With this experimental setup, we studied plasma discharge inside helium, argon and nitrogen bubbles rising in distilled water or a solution of $NaH_2PO_4 \bullet H_2O$ in distilled water. The used salt solution had a conductivity of 5.0 mS cm^{-1}, while distilled water had, due to contamination inside the reactor, a conductivity of 25 μS cm^{-1}. In all these conditions, we applied voltage pulses with amplitudes of 10, 15 or 20 kV. Also, we carried out measurements without bubbles in both liquids for the same voltage amplitudes.

4.2 Analysis

Prior to analysis, all obtained spectra of the discharge have been corrected for spectral sensitivity of the spectrometer by an ORIEL calibration lamp (model 63355). The spectra are characterized by an obvious continuum beneath the spectral lines in the measured range 250–900 nm. To work out whether this continuous radiation originated from a black-body source, Planck's radiation law is fitted to the spectrum. In this simulation, the used model function therefore has the form

$$I(\lambda;T) = \frac{c_1}{\lambda^5} \times \frac{1}{exp\left(\frac{hc}{\lambda k_B T}\right)-1} \tag{4.1}$$

where I (λ; T) is the intensity of the light emitted by a black-body source with temperature T in the wavelength interval [λ, λ + dλ] and c_1 is a scaling factor. Both c_1 and T are fitting parameters. In the fitting procedure, the influence of the spectral lines is minimized using a modified version of the algorithm proposed by Bukvic et al [2]. In short, the original algorithm fits a user-defined model function multiple times to measured data points by sequentially removing the most deviating data points from the fitting procedure. The amount of data points removed at once depends on the removal parameter r. During every iteration, the algorithm uses the ordinary least squares method. After the last data points are removed, it chooses the fitted curve over subset s of data points with the highest density of least squares (DLS) $D_k(s)$ as the most optimal one, where

$$D_k(s) = \frac{\sum_s d_i^2}{d_{max}^k(s)} \tag{4.2}$$

In this equation, Σ_s represents summation over all data points of subset s, d_i is the vertical deviation of data point i from the best-fitted model function, $d_{max}(s) = \max\{d_i\}$ and k is a user-defined real number wherefore $2 \leq k < 3$.

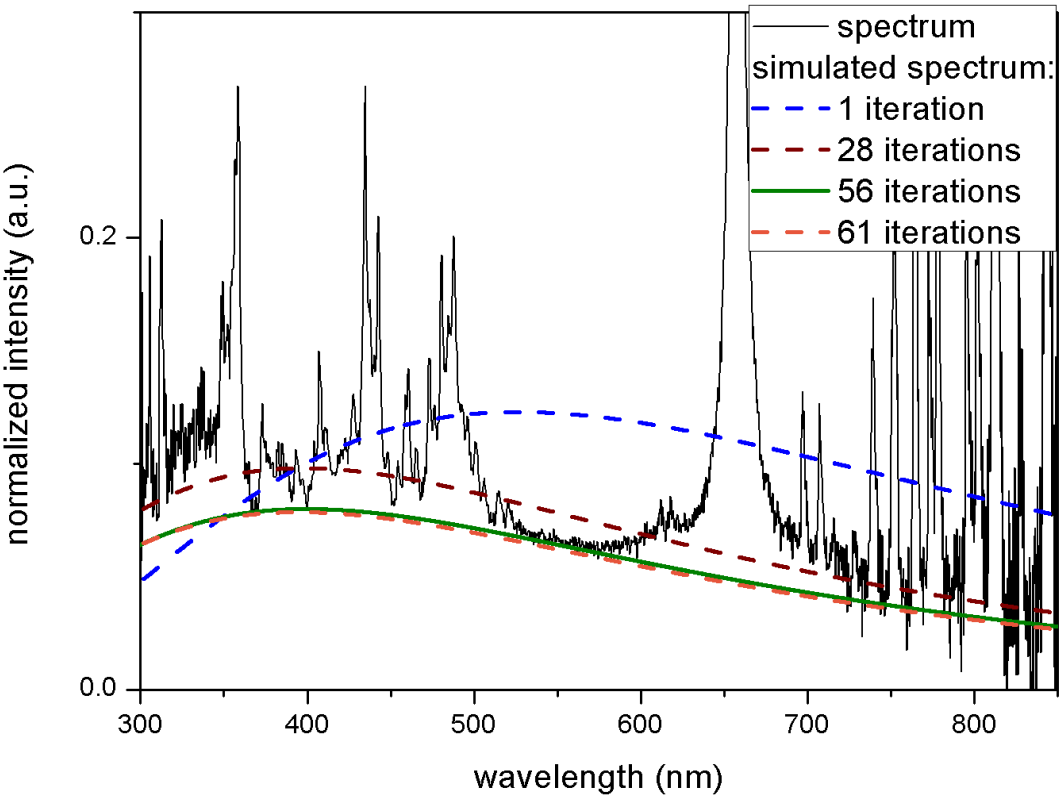

Figure 4.2 Fitting procedure for a spectrum of a plasma discharge inside an argon bubble (direct bubble discharge, as described in section 4.3.1) in distilled water, 15 kV. The shown fitting curves are derived during different iterations. For example, iteration 28 represents the fitting result over subset 28, containing 723 of the 1012 initial data points. According to the algorithm, fitting curve 56 (over 54 remaining data points) is the most optimal one, as it has the highest $D_k(s)$ (see equation (2)).

This procedure works well for spectra with sharp, thin spectral lines and weak vibrational and rotational bands that do not overlap. For our spectra, however, it constantly overestimated the continuum, due to the presence of several overlapping bands and peaks in between 300 and 500 nm and the wide H_α Balmer line, which all dominated the spectrum. In our modified version of the algorithm, only data points above the fitted curve are removed to prevent the removal of data points belonging to the continuum. We fitted the measured spectra over the interval from 350 to 700 nm, given that in this range the continuum contained the least noise. The best results were achieved with values for the removal parameter and the DLS exponent of, respectively, r = 0.9 and k = 2.9. Figure 4.2 shows the evolution of the fitting curve during the progress of the modified algorithm.

Subtracting the obtained fitted continuum curve from the corresponding spectrum enabled us to measure the full-width at half-maximum (FWHM) $\Delta\lambda$ of the H_α Balmer line. The electron density N_e is calculated in the plasma, using the formula for Stark broadening

$$N_e = C(N_e; T)\Delta\lambda^{3/2} \tag{4.3}$$

where the factor $C(N_e, T)$ was determined from the plasma diagnostics tables of Gigosos and Cardenoso [4].

4.3 Results

4.3.1 Electrical characterization

For identical experimental conditions two types of voltage and current waveforms during bubble discharge in distilled water are observed. An example is shown in figure 4.3 for helium bubbles and applied voltage pulse amplitudes of U = 15 kV. The first type of waveform is an exponentially damped sinusoid immediately after breakdown. In the second type, two well- defined phases occur. The first phase had a variable length Δt, with typical values in the order of tens of microseconds. During this phase, voltage and current evolved in the same way as during discharge in water without bubbles. The absolute value of voltage, for instance, decreased exponentially with a time constant of 0.28 ms. During the second phase, the waveforms displayed an exponentially damped sinusoidal behavior very similar to the first type of bubble discharge. For convenience, the first type of discharge is henceforth called *direct bubble discharge* and the second type *delayed bubble discharge*. In both types of discharges, sinusoidal oscillations had a frequency f of 2.1 MHz for all bubble gases and voltage pulse amplitudes (figure 4.4(a)–(c)). In direct bubble discharge, exponential damping of the oscillations had a time constant τ ranging from 0.8 to 1.3 μs. In delayed bubble discharge, τ typically decreased for increasing delay time Δt to be halved after some tens of microseconds, as can be seen in figure 4.4(c).

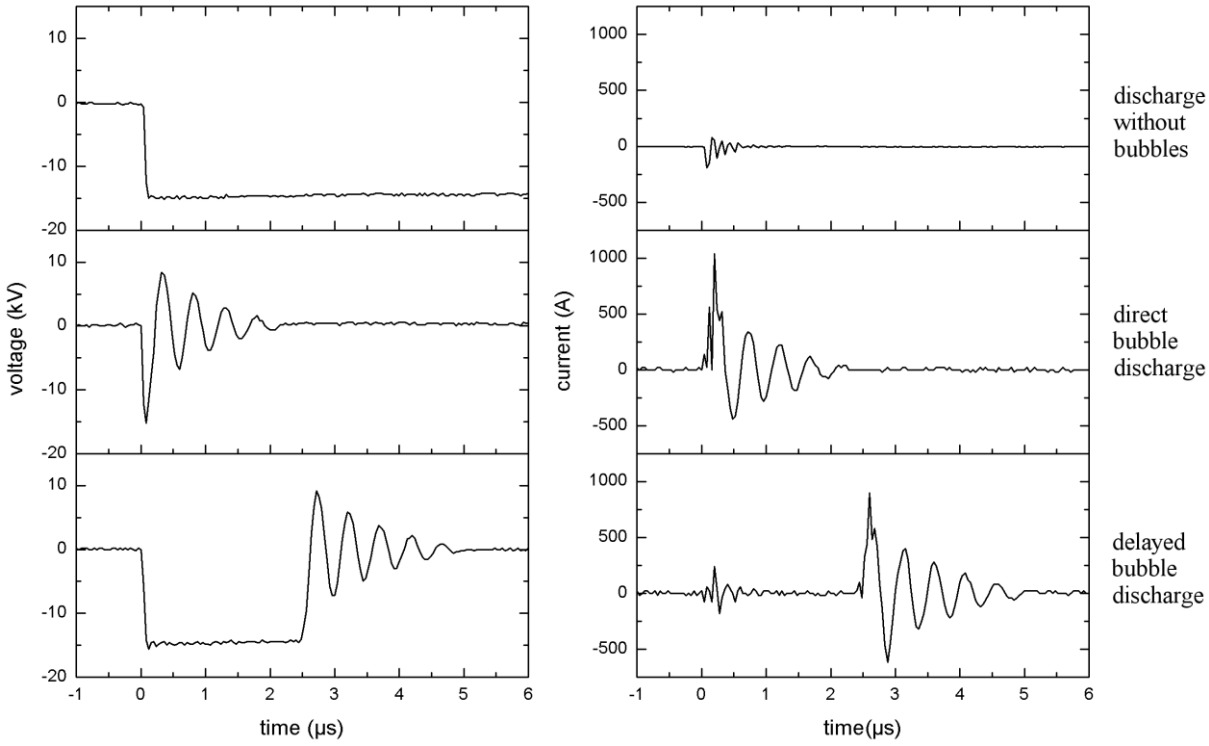

Figure 4.3 Voltage and current waveforms are measured with U = 15 kV with distilled water, without bubbles (top graph) or with helium bubbles (middle and bottom graphs). The experimental conditions for the so-called direct bubble discharge and delayed bubble discharge are identical.

Small delay times around 100 ns are measured, which means that Δt displays a continuum down to zero. Considering the rise time of the HV pulse, we define direct bubble discharge as the discharge where the exponentially damped sinusoidal behavior starts in the first 50 ns after the onset of the voltage rise, i.e. when $\Delta t < 50$ ns. The probability of direct bubble discharge depends on the bubble gas and is, respectively, 49%, 38% and 29% for argon, helium and nitrogen bubbles, independent of the voltage pulse amplitude. Because of these high probabilities, two fundamentally different mechanisms are expected for direct and delayed bubble discharge. When direct bubble discharge is not taken into account, the measured values of Δt have, respectively, average values of 18.1 μs, 25.7 μs and 22.0 μs and maximal values of 74.7 μs, 84.1 μs and 88.3 μs for argon, helium and nitrogen bubbles.

Bubble discharge in solution of $NaH_2PO_4 \bullet H_2O$ in water with conductivity of 5.0 mS cm^{-1} generated similar voltage and current waveforms, although the delay time Δt was negligible in this case. All voltage and current waveforms displayed an exponentially damped sinusoidal behavior immediately after breakdown, without a gaugeable delay time (figure 4.4(d)).

Discharge in liquid without bubbles has a decreasing voltage that is fitted as an exponential decay for voltage pulse amplitudes up to 19 kV, with a time constant of 0.28 ms for distilled water and 0.27 μs for the $NaH_2PO_4 \bullet H_2O$ solution. For distilled water, however, the

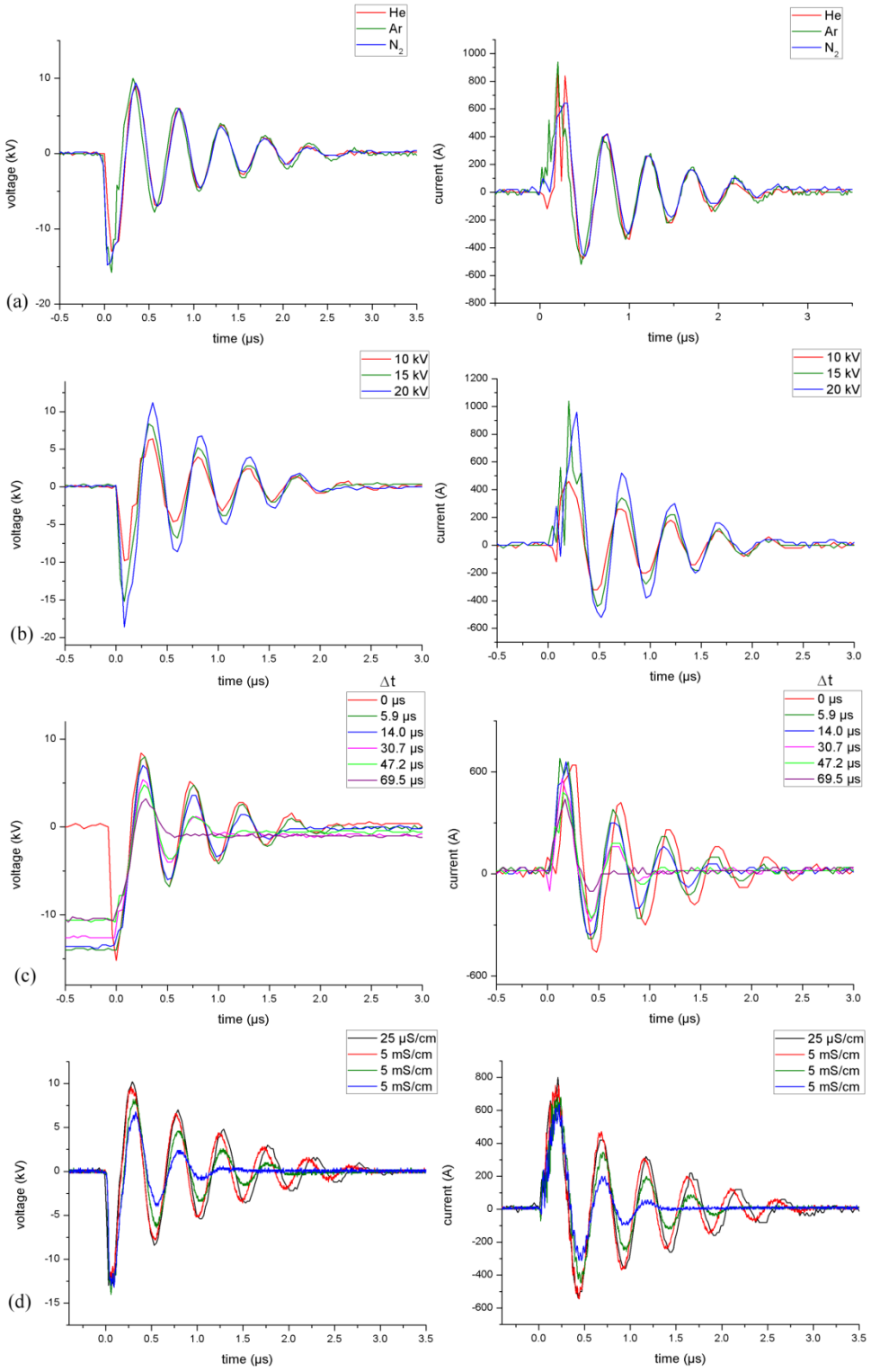

Figure 4.4 (a) *V/I* waveforms for different bubble gases in direct bubble discharge in distilled water. All waveforms are measured for voltage pulse amplitudes of 15 kV. (b) In these measurements, voltage pulses with amplitudes of 10, 15 and 20 kV are applied to helium bubbles in distilled water, resulting in direct bubble discharge. (c) Discharge in N_2 bubbles, U = 15 kV. The zero on the time axis represents the beginning of the second phase where the actual discharge inside the bubble occurs, a time Δt after the application of the voltage pulse. (d) Influence of conductivity on *V/I* waveform.

discharge characteristics change substantially when a voltage pulse with an amplitude of 20 kV is applied. Under these circumstances, a sharp voltage drop with a characteristic time of 0.6 µs or less is observed on the voltage waveform after a variable delay time, as shown in figure 4.5. Probably, this effect can be explained with the formation of a spark in between the electrodes whereas only streamer discharge occurs for lower voltage amplitude.

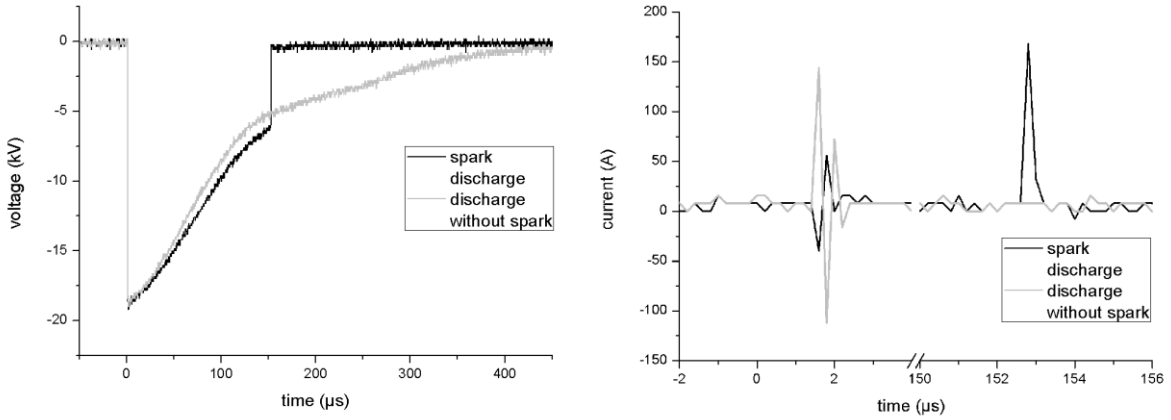

Figure 4.5 *V*/*I* waveforms measured for discharge in distilled water without bubbles, *U* = 20 kV. No spark is observed in the absence of the voltage drop.

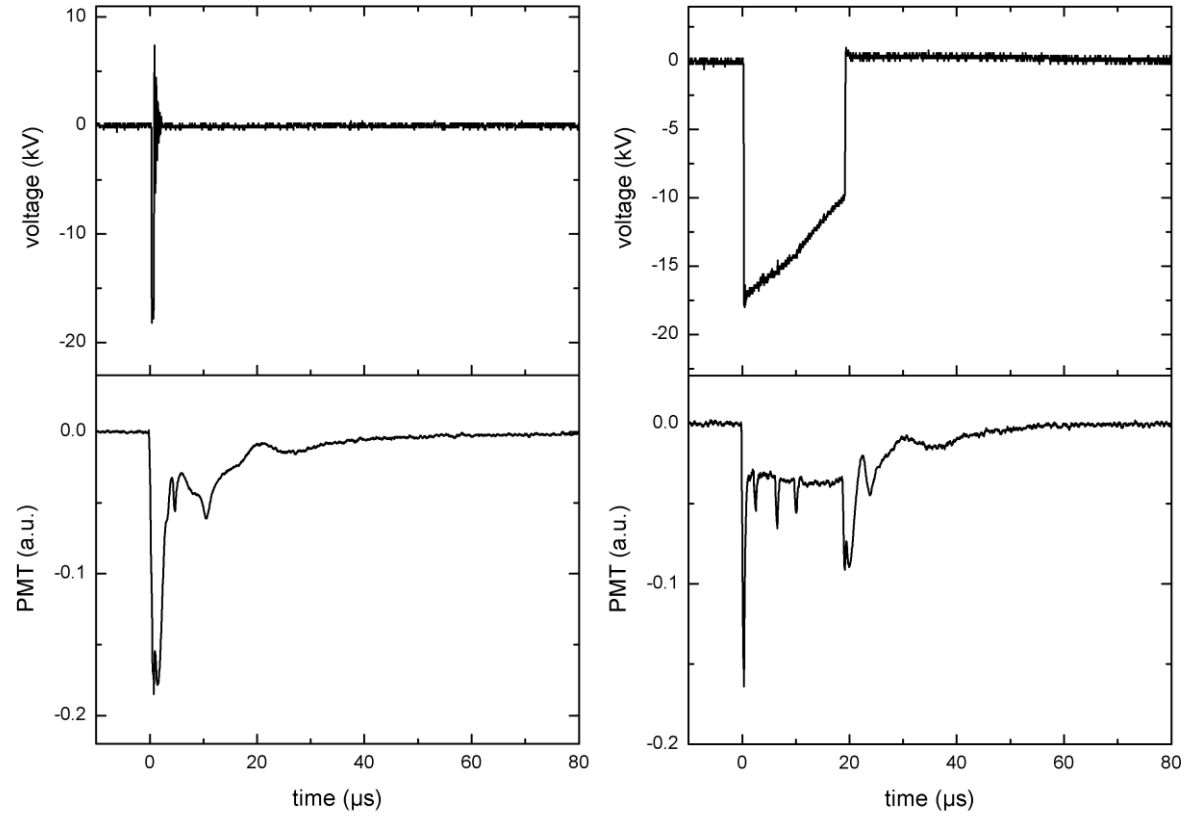

Figure 4.6 Time-dependent emitted light intensity and voltage waveform for direct (left) and delayed (right) bubble discharge for argon bubbles in distilled water.

4.3.2 Spectroscopic characterization

As can be seen in figure 4.6, intense light is emitted by the discharge immediately after the application of the voltage pulse for both direct and delayed bubble discharge, with FWHM in the range 0.5–2.3 μs which rapidly decreases after 0.5 to 2.0 μs. During the delay time Δt, less intense light is emitted continuously with sharp superposed peaks with FWHM of 0.5 μs, which can be attributed to branching of the streamer channel (see section 4.4). After the delay time, the intensity peaks sharply.

Figure 4.7 shows the spectra of direct bubble discharge in a nitrogen, argon or helium bubble. An example of the spectrum of discharge without bubbles is presented for comparison as well. For all bubbling gases, the spectrum is dominated by atomic lines of the neutral and singly ionized gas element and lines occurring in the spectrum of discharge without bubbling. No OH-band was found around 309 nm in the spectrum of discharge in water without bubbles, unlike the results of many other authors on discharge in water. For argon bubbles, lines of doubly ionized argon are also present. In all spectra, an obvious continuum is measured that matches Planck's radiation law.

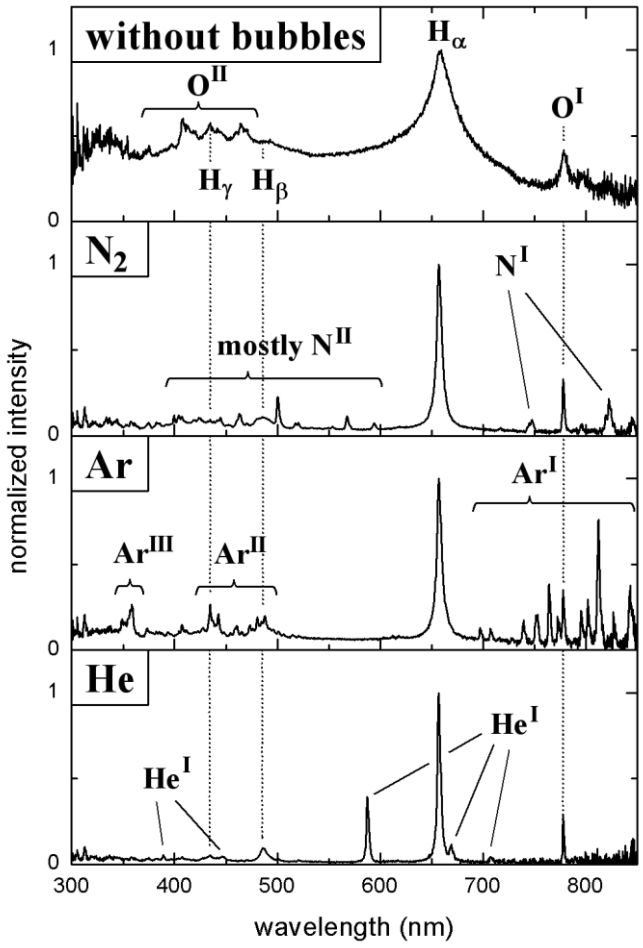

Figure 4.7 Direct bubble discharge spectra with HV-pulses of 15 kV for the different bubble gases and a HV-pulse of 20 kV without bubbles.

The corresponding black-body temperature is determined with the fitting procedure described in section 4.2. For nitrogen, argon and helium bubbles, the value of this temperature ranges, respectively, from 6300 to 8500 K, from 6500 to 7300 K and from 6600 to 9400 K. Without bubbles, it ranges from 6000 to 7800 K, depending on the experimental conditions. The voltage amplitude has no obvious effect on the black-body temperature. The solution conductivity has a negligible effect on spectral properties of the discharge.

Table 4.1 Peak width measurements.

Spectral line	Bubble gas	Discharge type	FWHM (nm)	$\Delta\lambda_S$ (nm)	N_e (10^{24} m^{-3})
H_α	no bubbles		9.7 to 43.6	9.6 to 43.6	2.5 to 24.2
	N_2	direct	5.7 ± 0.2	5.6 ± 0.2	1.11 ± 0.06
		delayed	7.8	7.7	1.8
	Ar	direct	5.0 ± 0.3	4.9 ± 0.3	0.91 ± 0.08
		delayed	7.4	7.3	1.7
	He	direct	3.6 ± 0.2	3.5 ± 0.2	0.55 ± 0.05
		delayed	20.9	20.9	8.0
H_β	He	direct	7.2 ± 0.8	7.1 ± 0.8	0.18 ± 0.03

Spectra of the discharge have been used to estimate the average electron density from Stark broadening. In order to avoid overestimation of spectral line width, the black-body continuum is first subtracted from the total spectrum. The measured FWHM of H_α for all bubble gases and of H_β for direct bubble discharge in helium bubbles has a value of several nanometers, as shown in table 4.1. Theoretically, the FWHM can be written as [5, 6]

$$\text{FWHM} = \sqrt{0.25\Delta\lambda_L^2 + \Delta\lambda_G^2} + \Delta\lambda_L/2 \tag{4.4}$$

where $\Delta\lambda_L$ is the Lorentzian contribution to the FWHM and $\Delta\lambda_G$ is the Gaussian one. Van der Waals, resonance, natural and Stark broadening mechanisms lead to the Lorentzian component, while the Gaussian one is caused by Doppler and instrumental broadening. The van der Waals broadening FWHM in nm is given by $\Delta\lambda_{vdW} = ApT_{gas}^{-0.7}$, where p is the pressure in bar, T_{gas} is the gas temperature in K and A is a coefficient smaller than 6 for H_α and H_β in case of a He, Ar, N_2 or water vapor plasma, [6–9]. The resonance broadening FWHM in nm for both hydrogen lines can be written as $\Delta\lambda_{res} = B\chi_H pT_{gas}^{-1}$, with χ_H the mole fraction of hydrogen atoms and B a coefficient smaller than 60 for both hydrogen lines. The natural broadening FWHM of H_α and H_β are both smaller than 10^{-4} nm and are therefore negligible [8, 10]. The FWHM in nm caused by Doppler broadening can be written as $\Delta\lambda_D = C \times 10^{-4}\sqrt{T_{gas}}$, where the coefficient C is, respectively, 4.70 and 3.1 for H_α and H_β [8, 11]. Assuming a pressure p of maximally 30 bar in the bubble, a hydrogen mole fraction χ_H of at most 0.1 and a gas temperature T_{gas} equal to the determined black-body temperatures, the above formulae give negligible values for the contributions of the van der Waals, resonance and Doppler broadening to the FWHM. Therefore, only instrumental and Stark broadening

have to be taken into consideration. This conclusion has been made by several authors for hydrogen Balmer lines with similar FWHM of discharges in water [12–14].

The Lorentzian Stark broadening FWHM $\Delta\lambda_S$ is determined by eliminating the contribution of the Gaussian instrumental broadening FWHM, which is measured to be $\Delta\lambda_I = 0.7$ nm. The resulting values are listed in table 4.1 for different bubble gases when voltage pulses of 15 kV were applied or without bubbles with voltage pulses of 20 kV. The corresponding electron densities N_e from equation (3) are given as well. For delayed bubble discharge, the FWHM and electron density are larger. The values of the measured FWHM for delayed bubble discharge in table 4.1 are the maximal ones, while for discharge without bubbles, the minimal and maximal values are given. The largest value occurred in the spectrum of helium bubble discharge with Δt = 80.0 µs which qualitatively resembled the spectra of discharge without bubbles, as shown in figure 4.8. The FWHM, and therefore the electron density, slightly increases for increasing voltage pulse amplitude in the case of direct bubble discharge. In the solution with conductivity of 5.0 mS cm^{-1}, the H_α peak width is slightly smaller than for direct bubble discharge in distilled water.

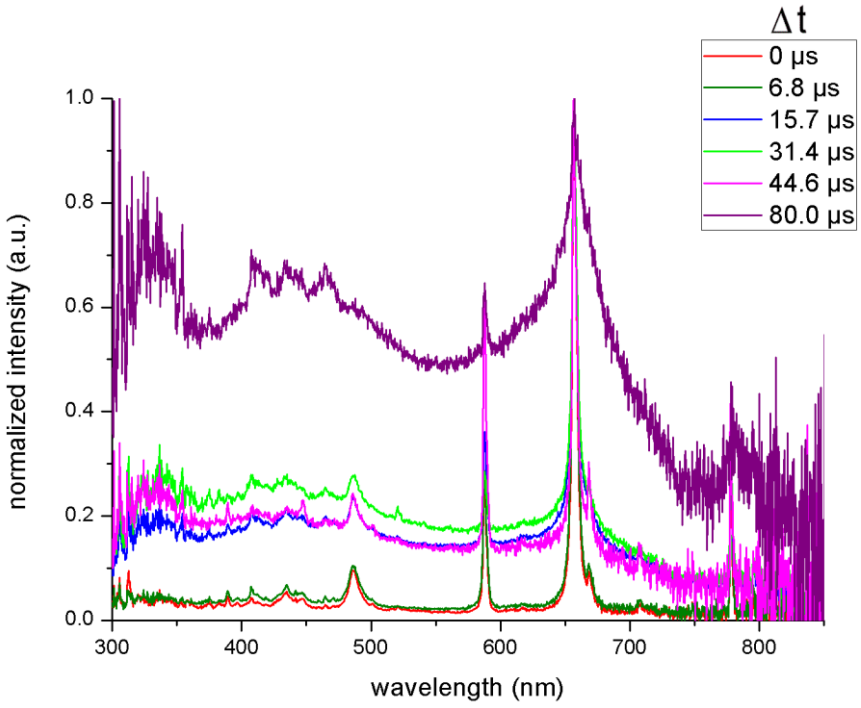

Figure 4.8 Spectra of discharge in helium bubbles with HV-pulses of 15 kV in distilled water for different delay times Δt.

4.4 Discussion

Discharge in between a pin-to-plate electrode system in liquid starts with the formation and propagation of a streamer from the pin electrode towards the plate electrode [15–17]. The same authors distinguished consecutive phases in this propagation process, where speed and structure of the streamer change in a stepwise manner. The amount of modes, the velocities

and the structure depend strongly on characteristics of the experimental setup as well as the applied voltage waveform [15]. While propagating, the streamer splits up several times into daughter streamers. When one of the branches reaches the plate electrode, a conductive path is formed in between the electrodes and arc or spark discharge begins. Since the voltage and current waveforms in the first phase of plasma formation in delayed bubble discharge are similar to the ones in discharge without bubbles, the assumption can be made that streamer formation and propagation are similar as well.

With this assumption, one can explain the difference between direct and delayed bubble discharge as follows. In delayed bubble discharge, no bubble is present in the immediate vicinity of the pin electrode at the moment of discharge. Therefore, the breakdown occurs through solution only. However, if a bubble is not very distant from the pin electrode, one or more branches of the streamer will make contact with the bubble surface during streamer propagation. Depending on the conductivity of the liquid medium and the nature of the gas, this streamer branch will propagate inside the bubble or along the bubble surface. After a delay time Δt of several microseconds, the branch reaches the plate electrode. Since this new conductive path in between the electrodes has a lower electrical resistance after its expansion, a second breakdown occurs, i.e. delayed bubble discharge. In direct bubble discharge, on the other hand, a bubble is located close to the pin electrode at the moment a voltage pulse is applied on the electrodes. Therefore, no delay (or a very short delay in the range of ns) up to the moment of breakdown is observed.

Sun et al. reported a time delay as well between a voltage pulse onset and spark discharge in a similar setup with an aqueous solution without bubbles, but proposed a different explanation [18]. They suggest the streamer propagates from the pin towards the plate with a significantly lower velocity, connecting both electrodes only after the delay time, followed by spark discharge. This requires an average streamer velocity of the order of 1 km s^{-1}, which is roughly one thousand times smaller than the streamer velocity in gases [19]. This is disputable, since the accelerated electrons in the streamer head lose their kinetic energy by elastic collisions with a decay time several orders of magnitude smaller than the time which is necessary for the sustainment of such slow streamer head. Moreover, the immediate onset of direct bubble discharge cannot be explained by such slow streamers. Streamer velocities in water ranging from 10^2 to 10^6 m s^{-1} are mentioned in the literature, observed with interferometry, shadowgraph or Schlieren photography [15–17, 20]. Nevertheless, it is unclear whether these velocities have to be attributed to streamer dynamics or rather to hydrodynamical processes.

If we consider the discharge channel and the external pulse circuit as a series RLC circuit with constant resistance, the voltage over the channel is given by the formula for underdamped oscillations:

$$V(t) = \mathrm{V}_0 exp\left(-\frac{t}{\tau}\right) \sin(2\pi f t) \tag{4.5}$$

where V_0 is the amplitude of the voltage pulse, and the time constant τ and the frequency f are parameters dependent on the pulse circuit, given by

$$\tau = \frac{2L}{R}, \qquad 2\pi f = \left(\frac{1}{LC} - \frac{1}{\tau^2}\right)^{1/2} \tag{4.6}$$

C and L denote the capacitance and the inductance of the pulse circuit, while R is the sum of the resistance R_{pl} of the plasma channel and the resistance R_{ext} of the external circuit. Since $\tau^{-1} \ll 2\pi f$, the frequency f can be approximated as $f \cong \frac{1}{2\pi}(LC)^{1/2}$. This is in agreement with our measurements, where f is independent of the bubbling gas, the type of bubble discharge, the solution and the amplitude of the applied voltage pulse. On the other hand, τ is variable in our measurements, which implies that R_{pl} is at least of the same order of magnitude as R_{ext}. Although R_{ext} is not constant, we expect R_{pl} to increase as a function of R, analogue to the calculated results from Timoshkin et al. [21]. Eliminating L from the formulae of τ and f gives $R = (2\pi^2 C\tau f^2)^{-1}$. For C = 1.3 nF, f = 2.1 MHz and τ = 1.3 μs, we find that R = 6.8 Ω. This is in good agreement with the model of Timoshkin et al., developed for a similar electrode configuration in tap water without bubbles. According to our measurements, R_{pl} is independent of the bubble gas and the water solution. Therefore, the variation of R_{pl} can be explained by the variable length of the plasma channel. For relatively small HV amplitudes, the propagating streamer head is attracted towards the plate electrode with a weaker force than for larger amplitudes. This allows bigger deviations of the streamer propagation direction from the symmetrical axis of the electrodes, resulting in a longer conductive zigzag path and thus a larger R_{pl}. This corresponds to our measurements. The typically higher resistance R_{pl} in delayed bubble discharge compared with direct bubble discharge for the same experimental settings is in agreement with our models for both discharge types described above. Indeed, the discharge channel in delayed bubble discharge should be longer, since the bubble is further off the electrodes. Moreover, the discharge energy remaining after the delay time Δt, i.e. the energy left for the discharge in the bubble, is obviously smaller than in direct bubble discharge. This leads to a smaller plasma channel resistance as well, conformable to the results of Timoshkin et al. [21].

The spectrum of streamer discharge consists of only lines and relatively narrow bands, while a broad spectrum occurs during spark discharge, which can be attributed to black-body radiation [18, 22]. The black-body radiation most likely originates from Joule heating of the plasma channel during spark discharge. To our knowledge, black- body temperatures of spark discharge in liquids have not been reported before in the literature. However, Sun et al. mention a strong broadband spectrum for similar conditions without bubbles, which resembles the spectral distribution of sunlight, in agreement with our black-body temperatures [18]. The influence of the solution conductivity on the black-body temperature, however small, can be attributed to a stronger leakage current towards the surrounding solution, rather than to less Joule heating due to a smaller electrical resistance of the channel. The difference in range of black-body temperature for the three bubble gases can be

explained by different electrical conductivities and specific heat ratios of the ionized gases as well as by different geometries of the discharge in the bubble [23, 24].

The recorded spectra are assumed to belong to the liquid channel spark, since the emitted light during streamer formation and propagation, in the case of discharge without bubbles, is too weak to be measured in our setup. Nevertheless, the PMT signal shows intense light is emitted during the delay time Δt (figure 4.6). According to our model above for delayed bubble discharge, this light originates from breakdown through solution only. After the delay time, light is emitted from spark discharge in the bubble. Plasma light is measured up to several microseconds after the voltage pulse, indicating a recombination mode of the discharge, in agreement with Sun et al. [18]. Therefore, the time-integrated spectrum of delayed bubble discharge is a superposition of the spectrum from a narrow plasma channel through water and the spectrum from plasma inside the bubble. This explains why it tends towards the spectrum of discharge without bubbles for large delay times, but still contains strong lines of the bubble gas element. It also results in a wider H_α line for increasing delay time. In contrast to our measurements, Sunka et al observed a time delay for streamer discharge in water during which no light was emitted. The time delay is explained by thermal effects and electrolysis which could play a role in the discharge initiation [12]. With this explanation, however, the question remains why no such time delay occurs in our as well as some of their measurements.

Based on the presented data, N_e refers to the time-averaged electron density in the spark channel. The electron density in direct bubble discharge in helium bubbles derived from H_β is three times lower than the value derived from H_α, which can have several causes. Firstly, self-absorption of H_α is not taken into account, that can lead to an overestimation of N_e. Secondly, absolute values of N_e with an order of magnitude of at least 10^{24} m^{-3} determined from Stark broadening of H_α can strongly deviate from experimental values [25].

The calculated values of N_e are of the order of 10^{24} to 10^{25} m^{-3} (table 4.1), i.e. the same order of magnitude as typically determined for corona discharge in water with high conductivity [12, 26–30]. Where N_e is almost independent of the conductivity in our measurements, it decreases in streamers for lower conductivity [12]. This decrease is explained by a lower discharge current and the generation of longer plasma channels due to a slower compensation of the space charge electric field on the streamer tip [26]. In spark discharge, however, the electron density can increase after breakdown by a mechanism of electron avalanches in the gaseous discharge channel, similar to breakdown in gaseous media. Therefore, the maximal electron density does not depend strongly on the conductivity in spark discharge. Nevertheless, a significantly lower pulse power is expected to result in a lower plasma density, even in spark discharge, which can explain the lower electron densities down to 1.1×10^{22} m^{-3} for sparks in water determined by Burakov et al [31]. According to the spark model by Lu et al, transitional electron densities of 4×10^{26} m^{-3} are theoretically possible in sparks [22]. Electron densities reported for corona discharge in

bubbles on a HV electrode in water are typically in the order of 10^{20} to 10^{21} m^{-3} [7, 8, 32–34], significantly lower than for direct liquid discharge. This difference is explained by a smaller amount of vaporized and dissociated water molecules, since the discharge occurs mainly in the gas phase and along the gas–liquid interface [35].

4.5. Conclusion

In this chapter, underwater discharge with bubbling is investigated. It is shown that spark discharge with a high density can be generated in bubbles in water with relatively low input voltage. This is attractive compared with spark discharges in water without bubbles that require higher voltage amplitudes. From a technological point of view, different bubble gases are supposed to give a different treatment effect in terms of excited species production, since the plasma properties are obviously influenced by the type of gas.

The electrical measurements imply the occurrence of two types of bubble discharges. In direct bubble discharge, spark discharge inside the bubble develops immediately after the application of the high-voltage pulse. Delayed bubble discharge, on the other hand, leads to spark discharge after a delay time Δt, up to microseconds. The frequency f of the voltage oscillations during discharge is constant in all measurements. The bubble gas, voltage pulse amplitude and solution have no obvious effect on the decay time of the damped oscillations.

We proposed a chronological model for both types of discharge, in which the position of the bubble relative to the electrodes during application of the voltage pulse determines whether the bubble discharge is direct or delayed. Accordingly, the length of the discharge channel through the bubble is assumed to be longer in delayed bubble discharge compared with direct bubble discharge. Considering the channel and the external pulse circuit as a series RLC circuit with constant resistance, the electrical measurements are consistent with our model. Our results show that the hydrodynamical model of Timoshkin et al. for discharge in water without bubbles can be extended to discharge in water with bubbles.

For all bubble gases, the emitted spectrum of bubble discharge consists of a continuum that fits Planck's radiation law and spectral lines of the neutral and singly ionized gas element. We suggest that the spectrum of delayed bubble discharge is a superposition of the spectrum of the discharge channel through water only and the spectrum of direct bubble discharge. The black-body radiation most likely originates from Joule heating of the plasma channel during spark discharge. The black-body temperature corresponding to the continuous radiation ranges from 6000 up to 9000 K. The electron density, corresponding to the Stark broadening of H_α, is of the order of 10^{24} m^{-3}. It increases slightly with increasing voltage pulse amplitude and is slightly smaller for the solution with conductivity of 5.0 mS cm^{-1} than for distilled water.

References

[1] Aoki H, Kitano K and Hamaguchi S 2008 *Plasma Sources Sci. Technol.* 17 025006

[2] Bukvic S, Spasojevic D and Zigman V 2008 *Astron. Astrophys.* 477 967–77

[3] Zun I and Groselj J 1996 *Nucl. Eng. Des.* 163 99–115

[4] Gigosos M A and Cardenoso V 1996 *J. Phys. B: At. Mol. Opt. Phys.* 29 4795–838

[5] Griem H R 1997 Principal of Plasma Spectroscopy (Cambridge Monographs on Plasma Physics vol 2) (Cambridge: Cambridge University Press)

[6] Ionascut-Nedelcescu A, Carlone C, Kogelschatz U, Gravelle D V and Boulos M I 2008 *J. Appl. Phys.* 103 063305

[7] Bruggeman P and Leys C 2009 *J. Phys. D: Appl. Phys.* 42 53001

[8] Nikiforov A Y, Leys C, Li L, Nemcova L and Krcma F 2011 *Plasma Sources Sci. Technol.* 20 034008

[9] Dong L F, Qi Y Y, Liu W Y and Fan W L 2009 *J. Appl. Phys.* 106 013301

[10] Stehle´ C, Mazure A, Nollez G and Feautrier N 1983 *Astron. Astrophys.* 127 263–6

[11] Sismanoglu B N, Amorim J, Souza-Correa J A, Oliveira C and Gomes M P 2009 *Spectrochim. Acta B* 64 1287–93

[12] Sunka P, Babicky V, Clupek M, Lukes P, Simek M, Schmidt J and Cernak M 1999 *Plasma Sources Sci. Technol.* 8 258–65

[13] Barmann P, Kroll S and Sunesson A 1996 *J. Phys. D: Appl. Phys.* 29 1188–96

[14] Bruggeman P, Verreycken T, Gonzalez M A, Walsh J L, Kong M G, Leys C and Schram D C 2010 *J. Phys. D: Appl. Phys.* 43 124005

[15] Akiyama H 2000 *IEEE Trans. Dielectr. Electr. Insul.* 7 646–53

[16] van Veldhuizen E and Rutgers W 2001 *15th Int. Symp. on Plasma Chem.* (Orleans, France) 3245–50

[17] An W, Baumung K and Bluhm H 2007 *J. Appl. Phys.* 101 053302

[18] Sun B, Sato M, Harano A and Clements J S 1998 *J. Electrostat.* 43 115–26

[19] Lagarkov A N and Rutkevich I M 1994 Ionization Waves in Electrical Breakdown of Gases (Berlin: Springer)

[20] Beroual A, Zahn M, Badent A, Kist K, Schwabe A J, Yamashita H, Yamazawa K, Danikas M, Chadband W G and Torshin Y 1998 *IEEE Electr. Insul. Mag.* 14 6–17

[21] Timoshkin I V, Fouracre R A, Given M J and MacGregor S J 2006 *J. Phys. D: Appl. Phys.* 39 4808–17

[22] Lu X P, Pan Y, Liu K F, Liu M H and Zhang H J 2002 *J. Appl. Phys.* 91 24–31

[23] Sato K and Yasuoka K 2008 *IEEE Trans. on Plasma Sci.* 36 1144–5

[24] Tachibana K, Takekata Y, Mizumoto Y, Motomura H and Jinno M 2011 *Plasma Sources Sci. Technol.* 20 034005

[25] Griem H R 2000 *Contrib. Plasma Phys.* 40 46–56

[26] Locke B R, Sato M, Sunka P, Hoffmann M R and Chang J S 2006 *Indust. Eng. Chem. Res.* 45 882–905

[27] Namihira T, Sakai S, Yamaguchi T, Yamamoto K, Yamada C, Kiyan T, Sakugawa T, Katsuki S and Akiyama H 2007 *IEEE Trans. on Plasma Sci.* 35 614–8

[28] Yoshinaga K, Yamamoto K, Namihira T, Sakugawa T, Katsuki S and Akiyama H 2007 *16th IEEE Pulsed Power Conf.* (Albuquerque, New Mexico) vols 1–4 pp 1227–30

[29] Gupta S B and Bluhm H 2008 *IEEE Trans. on Plasma Sci.* 36 1621–32

[30] Staack D, Gutsol A, Friedman G and Fridman A 2008 Plasma assisted decontamination of biological and chemical agents Conf. NATO-Advanced-Study-Institute on Plasma Assisted Decontamination of Biological and Chemical Agents (Cesme-Izmir, Turkey, Sept. 2007) ed S Guceri and A Fridman pp 79–86

[31] Burakov V S, Nevar E A, Nedel'ko M I, SavastenkoNA and Tarasenko N V 2009 *J. Appl. Spectrosc.* 76 856–63

[32] Babaeva N Y and Kushner M J 2009 *Plasma Sources Sci. Technol.* 18 035009

[33] Gershman S and Belkind A 2010 *Eur. Phys. J. D* 60 661–72

[34] Sommers B S, Foster J E, Babaeva N Y and Kushner M J 2011 *J. Phys. D: Appl. Phys.* 44 082001

[35] Shih K Y and Locke B R 2010 *Plasma Chem. Plasma Process.* 30 1–20

This life of separateness may be compared to a dream,
a phantasm, a bubble, a shadow, a drop of dew, a flash of lightning.
- Buddha

Chapter 5

Time-resolved characterization of pulsed discharge in a stationary bubble

Time-resolved characterization of the bubble discharge described in previous chapter by means of ICCD imaging was not possible due to mainly three reasons:

- Presence of multiple bubbles nearby the discharging bubble leads to obstruction as well as reflection of the emitted plasma light.
- The bubble generation method of pumping a constant gas flow through a glass filter disc produced a bubble diameter of 2.0 ± 0.3 mm. The relatively large standard deviation in this bubble size distribution hinders reproducibility of the experiment and complicates interpretation of the results.
- Even when the bubble generation method is optimized to generate a single rising bubble with consistent size, hydrodynamic features of the bubble prevent a reproducible bubble location at the moment of discharge. Namely, free bubbles no longer rise rectilinearly above a certain size, for instance above an equivalent radius of 0.81 mm in clean water [1]. Instead, they move in a zigzag or spiral path that has an unpredictable onset direction and which is, moreover, strongly influenced by the wake of preceding bubbles. Bubbles below the critical size, on the other hand, are very hard to generate in clean water due to the relatively high surface tension.

Therefore, the bubble reactor was modified to study pulsed plasma discharge inside a single, reproducible, stationary bubble on a metal tube electrode submerged in grounded water. Electrical characterization and fast-imaging of discharge in helium, argon, nitrogen, oxygen and air bubbles with two different sizes are carried out and compared, in order to gain a deeper insight in the spatial evolution of the plasma discharge.

5.1 Experimental setup and procedure

The electrical bubble discharge is generated inside a grounded cylindrical chamber made of stainless steel with a quartz window of 30 mm diameter, described in previous chapter. It is filled with distilled water with a conductivity of 22 μS/cm up to 12 cm from the bottom. The stainless steel tube electrode with inner diameter of 0.8 mm and outer diameter of 1.2 mm is submerged vertically in the water with its flattened orifice at the same height as the center of the quartz window. To insulate the tube below its orifice from the water and the chamber, it is placed in a glass tube.

A gas bubble is generated by pumping a gas through the tube electrode with a programmable syringe pump (New Era, model NE-1000). From photographs, the volume of the introduced bubble of 45 μl or 100 μl is determined (corresponding to prolate spheroidal bubbles with a horizontal minor axes length of 2.2 mm or 2.7 mm and a vertical major axis length of 2.3 mm or 3.3 mm respectively). Unless mentioned otherwise, the larger bubble size is used, with helium, argon, nitrogen, oxygen or air as bubble gas.

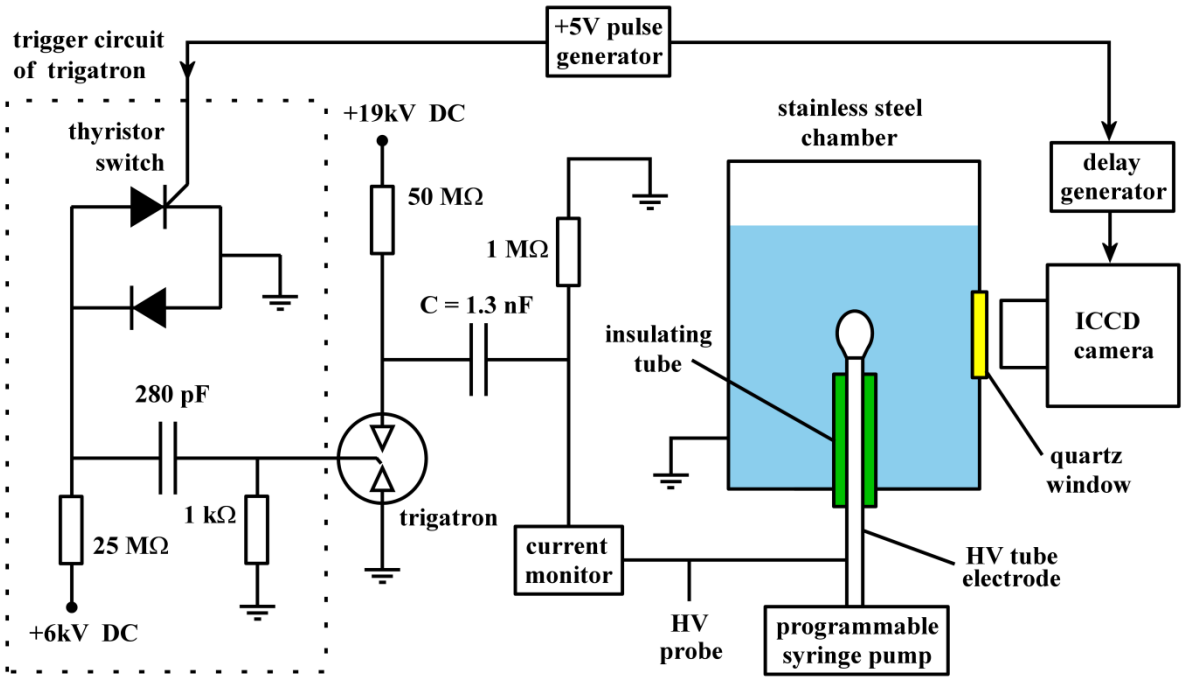

Figure 5.1 The setup consists of a negative HV pulse generator connected to a metal tube electrode submerged in distilled water inside a stainless steel chamber. A stationary bubble on the metal tube is produced by pumping a gas through the tube with a programmable syringe pump.

Table 5.1 Spectral filters

filter name	$\lambda line$ (nm)	λ_L (nm)	λ_U (nm)
H_α filter	656	652.5	662.5
O filter	777	770.4	791.0
He filter	588	585.4	595.1
Ar filter	751	747.8	758.2

A triggered HV power supply with an output capacitance of C = 1.3 nF was adjusted to generate negative high voltage (HV) pulses with a rise time of 72 ns, an amplitude of 19 kV and a repetition rate of 0.1 Hz. The schematic of the used power supply and chamber is presented on figure 5.1. The trigger circuit of the trigatron is controlled by a HTS thyristor switch (Behlke, model 300-100-SCR). The water is grounded in all experiments. Voltage and current waveforms are measured with a Tektronix high voltage probe (model P6015A) and a Pearson current monitor (model 2877) connected to a Tektronix oscilloscope (model DTS 1002).

The discharge is photographed through the circular quartz window with a Hamamatsu ICCD camera (model C8484), with camera exposure times of 50 ns or 5 μs. The camera is triggered with adjustable delay time, using the same trigger signal as the trigger circuit of the trigatron. In some measurements, spectral filters were placed in front of the camera. The lower and upper cutoff wavelengths λ_L and λ_U of the filters are mentioned in table 5.1, as well as the wavelength λ_{line} of the atomic line the filters were used for.

5.2 Results

5.2.1 Electrical characterization

Figure 5.2 shows the voltage and current waveforms of discharge in an air bubble on two different time scales. The voltage decays exponentially with a time constant of 312 μs. A delay time Δt after the voltage pulse application is determined as the time between the onset of two current pulses. No light emission is observed during this delay time, up to about 100 ns before the second current pulse oscillations start. Therefore, the oscillations indicate the moment of plasma discharge. During one series of experiments, Δt varied with a standard deviation of 0.5 μs. The average value of Δt has an order of magnitude of 10 μs. It is independent of the bubble gas, but decreases with decreasing bubble size. For unprocessed distilled water, for example, Δt has an average value of 12.3 μs and 15.4 μs for bubble volumes of respectively 45 μl and 100 μl.

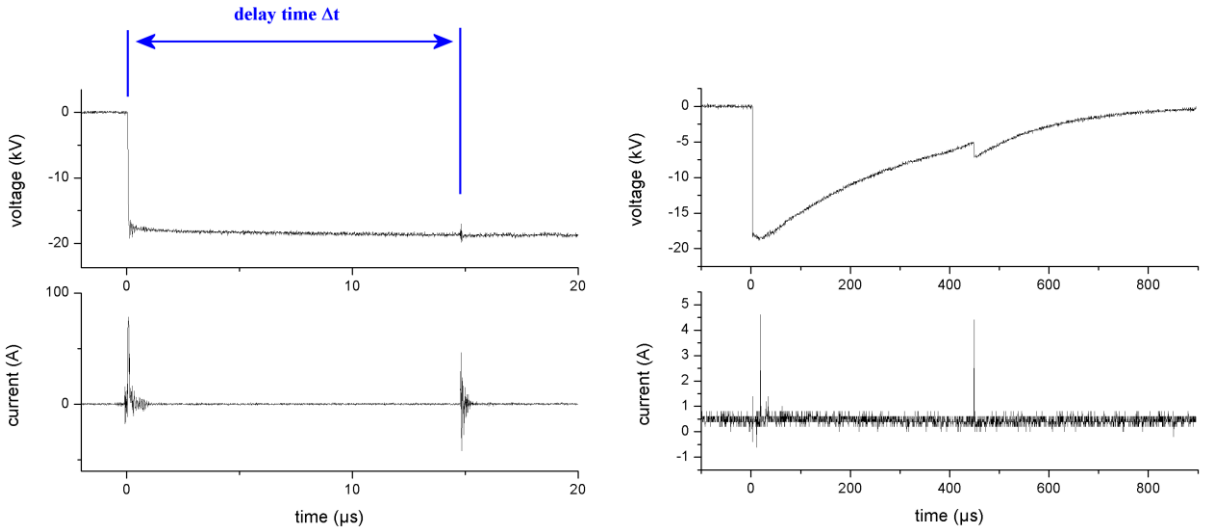

Figure 5.2 Voltage and current waveforms during discharge in a 100 µl air bubble in distilled water. Oscillations in the waveforms occur a delay time Δt = 14.8 µs after the application of the HV pulse. During the delay time, there was no plasma light emission.

5.2.2 Time-resolved characterization

An example of the evolution of plasma geometry in the first two microseconds after the delay time Δt is depicted in figure 5.3. The times indicated on the figure are relative to the point in time where the oscillations on the waveforms begin. Until 100 ns before these oscillations, no plasma light is emitted. Five phases in the development of the plasma geometry are seen. In a time interval of the order of 10 ns or less, 72 ± 18 ns before the voltage oscillations start, intense discharge occurs inside the whole bubble. In a second phase up to 72 ± 30 ns after the start of the oscillations, the plasma diminishes towards the electrode. The third phase is called the *dark phase*, since no emitted light from the bubble bulk is observed during this period of time. Still, plasma remains in proximity of the metal tube. During the fourth phase, the *bubble filling phase*, plasma extends towards the bubble top, either homogeneously for helium bubbles or in filamentary structures along the bubble surface for the other bubble gases. For convenience, these structures are called in short *filaments* henceforth.

The length of the dark phase and the bubble field phase depends strongly on the bubble gas (table 5.2) and is independent of the bubble size within the accuracy of the measurements. The length of the other phases is independent on the bubble gas and size.

From 12.5 ± 2.5 µs after voltage pulse application, the bubble surface blurs due to evaporation of the surrounding water (figure 5.4). At 22.5 ± 2.5 µs after voltage application, streamer-like structures start to form at the bubble surface, some of which are relatively intense. In order not to confuse these structures with the filaments inside the bubble, they are

called henceforth *streamers* in short. The longest streamers that are observed have a branched shape and an estimated velocity with an order of magnitude of 10^2 m/s or more. Although the plasma intensity and homogeneity is strongly influenced by the bubble gas, the process of bubble deformation is independent of bubble gas. In bubbles with a volume of 45 µl, streamers are formed at 17.5 ± 2.5 µs after voltage application and they are more intense in comparison to 100 µl bubbles, as seen in figure 5.5.

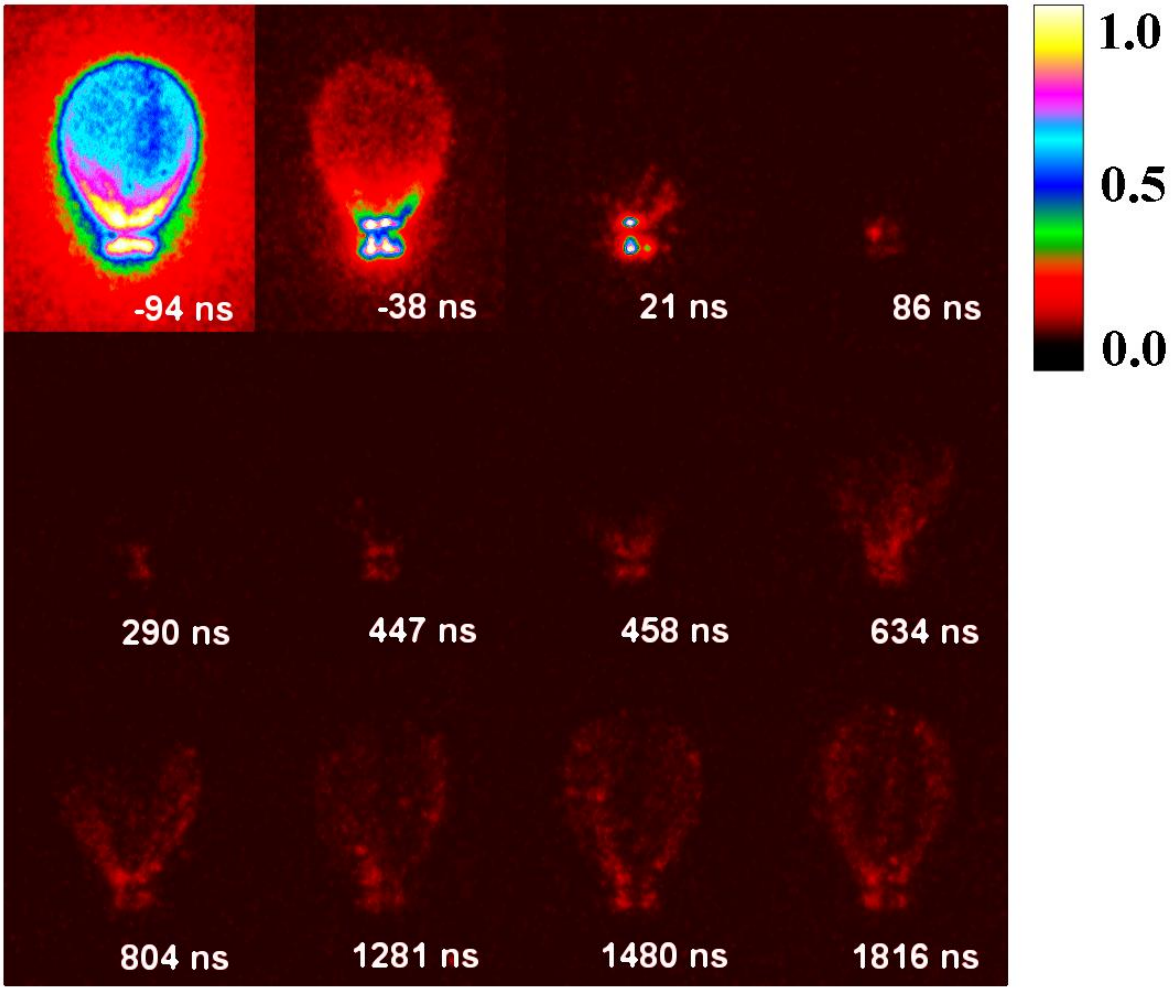

Figure 5.3 Images of the discharge in a 100 µl air bubble captured by the ICCD camera with an exposure time of 50 ns. Every indicated time is the start time of the camera subtracted from the start time of the voltage oscillations.

Table 5.2 Phase length

bubble gas	dark phase length (ns)	bubble filling phase length (ns)
helium	176 ± 5	81 ± 21
argon	116 ± 29	80 ± 5
nitrogen	25 ± 17	711 ± 30
oxygen	194 ± 8	196 ± 10
air	394 ± 40	1008 ± 78

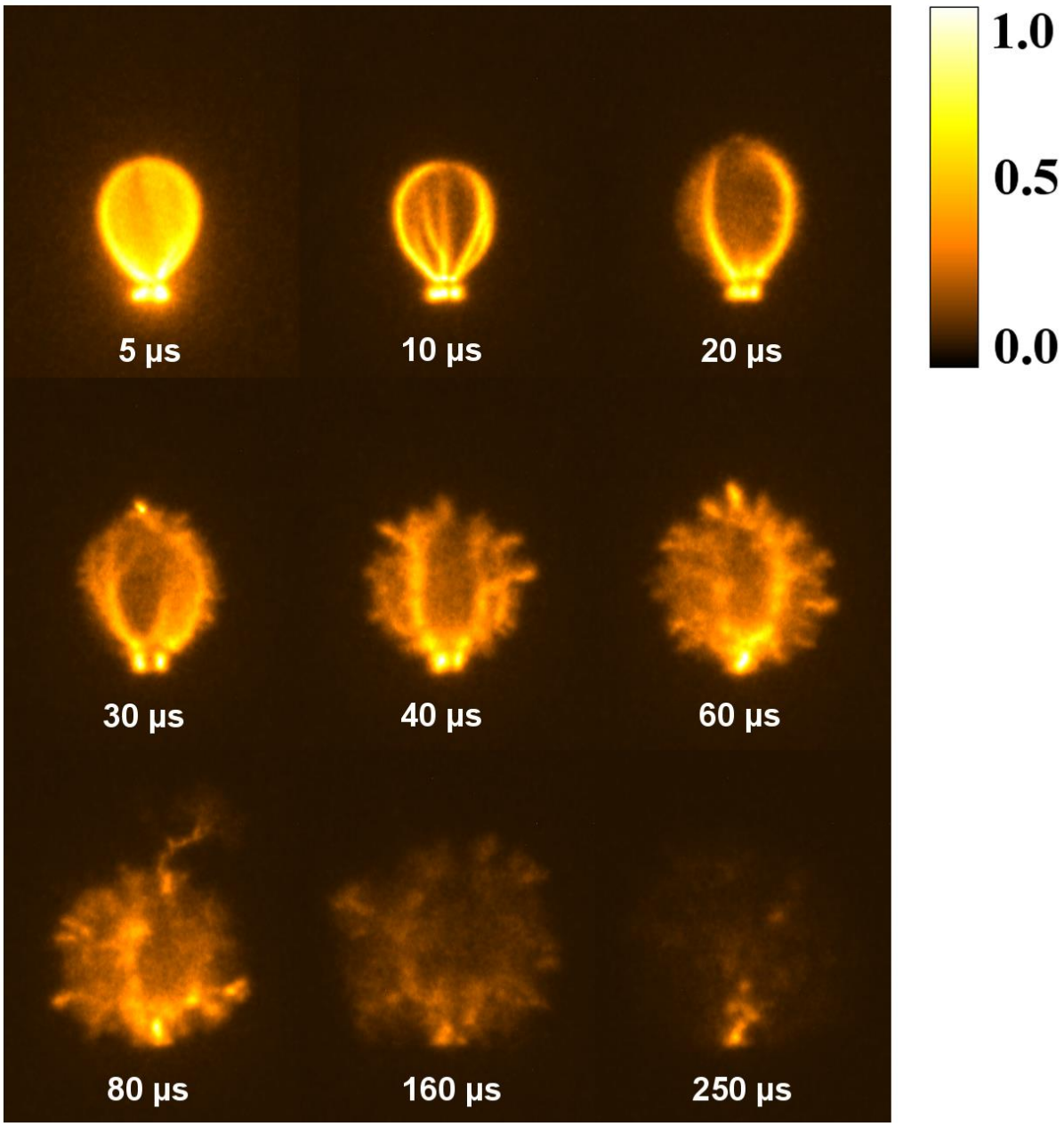

Figure 5.4 Images of the discharge in a 100 µl air bubble captured by the ICCD camera with an exposure time of 5 µs. The delay time of the camera relative to the time of voltage pulse application is indicated in every image.

The filaments in the bubble emit a spectrum that contains the H_α line, the oxygen line at 777 nm and, for helium and argon bubbles, the corresponding bubble gas element line at 588 nm or 751 nm respectively (figure 5.6). The filaments in an oxygen bubble are an exception, since H_α is absent or very dim in their spectrum. Relatively far from the bubble surface, H_α is dominant in the streamer spectrum, while the oxygen line and bubble gas element line are absent or very dim.

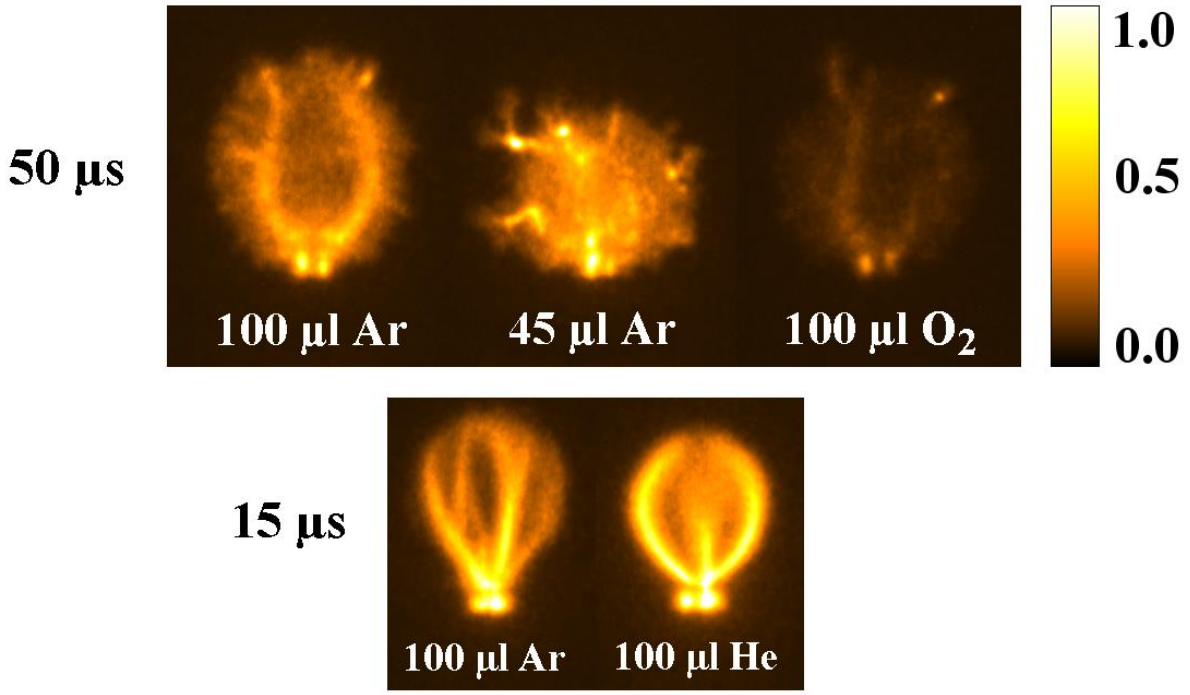

Figure 5.5 Images of the discharge in a bubble captured by the ICCD camera with an exposure time of 5 µs and a delay time of 50 µs (top) or 15 µs (bottom) relative to the time of voltage pulse application. The bubble gas and size are indicated in every image.

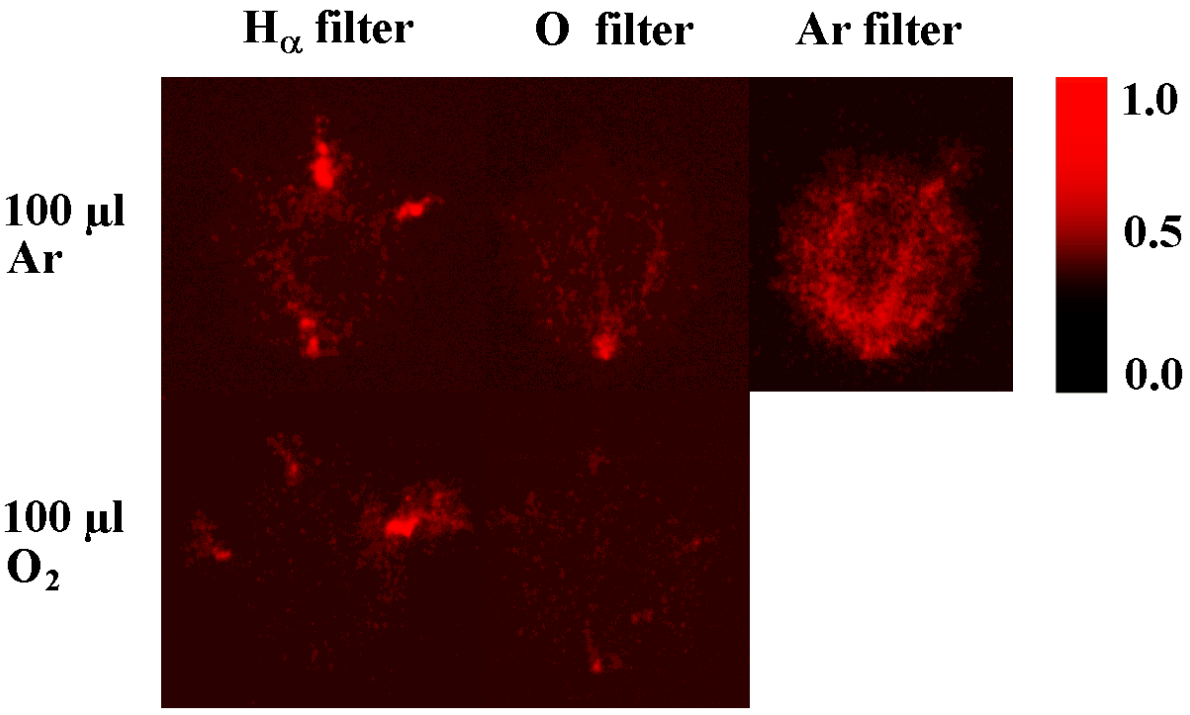

Figure 5.6 Images of the discharge in a 100 µl argon (top) or oxygen (bottom) bubble captured by the ICCD camera with an exposure time of 5 µs and a delay time of 60 µs relative to the time of voltage pulse application when a spectral filter was placed in front of the camera. The type of spectral filter is indicated above the image.

5.3 Discussion

The first current peak at the moment of voltage application is caused mostly by displacement current. Also, Joule heating by current from electrolysis contributes to this peak, but this contribution is expected to be very low due to the low water conductivity. Due to the closing of the HTS thyristor switch, a third current peak that corresponds to a negative bump in the voltage waveform is seen more than 400 μs after the voltage pulse application. Light emission is no longer observed when this peak occurs, indicating that it is not related to plasma discharge in water.

Plasma light is observed only after a delay time Δt of the order of 10 μs, which indicates that the electric field in the bubble is too small for discharge to occur during this period. The delay time is long enough for ions and dipolar molecules in the water in proximity of the bubble to reorganize. Under the influence of the electric field, a positive net charge accumulates on the bubble surface, enhancing the electric field in the bubble. The capacitive effect is caused by accumulation of aqueous positive charge at the upper bubble surface. Since the Coulomb force is directed towards the needle cathode, charge at the bubble flanks is not obstructed by the liquid interface and will not contribute to the capacitive effect. Once the electric field reaches the critical value necessary for breakdown in the bubble, the first phase of plasma development begins. During the first phase, the bubble is filled with plasma in a time of the order of 10 ns or less, which is too short for atomic and molecular species to travel distances of the order of millimeters. Therefore, the mechanism behind plasma onset is explained by electron avalanches.

The charge accumulation on the bubble surface points out that a capacitive feature of the bubble has to be taken into account. This can also explain the next phases in the development of the plasma geometry. In the first phase, electrons from the HV electrode reach the bubble surface, which leads to the neutralization of the positive net charge and, subsequently, the accumulation of a negative net charge. The electric field in the bulk of the bubble drops rapidly, by which the plasma diminishes towards the electrode. During the dark phase, the negative ions at the bubble surface travel away from the bubble by the repulsive Lorentz force caused by the negative high voltage electrode. The electric field inside the bubble increases, leading to the bubble filling phase.

If we consider the bubble, the surrounding water and the external pulse circuit as a series RC circuit with constant resistance, the difference in average delay time Δt for bubbles of 45 μl and 100 μl can be explained. On the assumption that a prolate spherical bubble with horizontal axes length r and vertical axis length d can be modeled as a classic capacitor that consists of two parallel conductive plates with surface $A \propto r^2$ separated by a distance d by the bubble gas with permittivity $\varepsilon \approx \varepsilon_0$, its capacitance can be written as

$$C = \epsilon \frac{A}{d} \propto \frac{r^2}{d} \tag{5.1}$$

Therefore, the time constant $\tau = RC$ is directly proportional to

$$\tau = \frac{r^2}{d} \tag{5.2}$$

Breakdown in the bubble occurs when the electric field E in the bubble gas reaches a critical value E_c. For a charging plate capacitor in a RC circuit, the critical electric field is given by

$$E_c = \frac{V_c}{d} = \frac{V_0\left(1-e^{-t/\tau}\right)}{d} \tag{5.3}$$

where V_c is the critical voltage over the capacitor, V_0 is the constant voltage over the RC circuit and t is the time needed to charge the capacitor up to the critical voltage. Denoting the parameters of a 45 µl and 100 µl bubble respectively with an index 1 and 2 and equating the critical electric field for both bubble sizes leads to

$$-\frac{t_2}{\tau_2} = \ln\left(1 - \frac{d_2}{d_1}\left(1 - e^{-t_1/\tau_1}\right)\right) \tag{5.4}$$

On the assumption that $t_1 \ll \tau_1$ and applying the approximations $\ln(1-x) \approx -x$ and $1 - exp(-x) \approx x$ for $x \ll 1$, equation 5.4 is reduced to

$$\frac{t_2}{t_1} = \frac{d_2\tau_2}{d_1\tau_1} = \frac{r_2^2}{r_1^2} \tag{5.5}$$

where equation 5.2 was used. Substituting the average experimental values of Δt in t_1 and t_2, we find that $t_2/t_1 = 1.25$, which deviates 17.2% from $r_2^2/r_1^2 = 1.51$. Considering the simplicity of the model, this is a good agreement.

The branched structure and the estimated velocity of the streamers in our measurements are in agreement with the lower values mentioned in literature for pulsed streamers in water without externally generated bubbles [2–5]. Also, typical spectra of pulsed streamer discharge in water contain a strong H_α line and a weak oxygen line at 777 nm, which indicates that the streamers in our measurements are similar in nature [3, 5].

The capacitive behavior of the bubble suggests strong attraction of aqueous ionic species towards the bubble during the initial delay time with a subsequent discharge that is most active at the bubble surface. This makes the system especially attractive for oxidation of ionic target compounds and surface-active agents.

5.4 Conclusion

Plasma light emission is recorded only a delay time Δt of the order of 10 µs after the HV pulse application. The plasma geometry evolves in five phases. First, plasma rapidly fills the whole bubble. Next, the plasma decays in 144 ± 35 ns and a dark phase follows. Subsequently, during the bubble filling phase, the plasma extends again towards the top of the bubble. The length of the dark phase and the bubble filling phase depends strongly on

the bubble gas. After 22.5 ± 2.5 μs, branching streamer-like structures start to propagate from the bubble surface into the water. Their spectrum contains a strong Hα line and a weak or absent oxygen line at 777 nm.

The delay time Δt and the five phases in the plasma geometry evolution are explained by a capacitive feature of the bubble. A simple model that considers the bubble as a classic plate capacitor is in relatively good agreement with the experimental values in our experiments. This capacitive behavior in combination with the subsequent strong plasma activity at the bubble surface makes bubble discharge attractive for oxidation of ionic target compounds and surface-active agents.

The investigated features of the streamers in our measurements resemble the features of pulsed streamer discharge in water, indicating they are similar in nature. In future research, the electron density and temperature and the plasma chemistry need to be investigated with time-resolved spectroscopy, in order to gain better insight in the time-resolved characterization of a pulsed discharge in a bubble.

References

[1] De Vries A W G, Biesheuvel A, Van Wijngaarden L 2002 *International journal of multiphase flow* 28.11 1823-1835

[2] Beroual A, Zahn M, Badent A, Kist K, Schwabe A J, Yamashita H, Yamazawa K, Danikas M, Chadband W G and Torshin Y 1998 *IEEE Electrical Insulation Magazine* 14 6–17

[3] Akiyama H 2000 *Ieee Transactions on Dielectrics and Electrical Insulation* 7 646–653

[4] van Veldhuizen E and Rutgers W 2001 *15th International Symposium on Plasma Chemistry* 3245– 3250

[5] An W, Baumung K and Bluhm H 2007 *Journal of Applied Physics* 101

Thunder is good, thunder is impressive;
but it is lightning that does the work.
- Mark Twain

Chapter 6

Combination of dielectric barrier discharge and adsorption on nanofiber membrane for atrazine decomposition

Despite the interesting features of bubble discharge as advanced oxidation process, it has a few limitations that complicate its implementation on large scale for aqueous micropollutant decomposition:

- Treatment of large water volumes requires high, continuous gas flow, in order to sustain a sufficient plasma-liquid interface size. Storage or generation of the supplied gas is associated with additional costs, which makes it less attractive for extensive application.
- In order to optimize an advanced oxidation process, it is recommended to search for synergetic effects with other advanced oxidation techniques or advanced treatment methods, as discussed in Chapter 2. Combinations with heterogeneous catalytic systems such as photocatalysis with TiO_2 or adsorption on activated carbon are mostly effective when the oxidation process is localized at the catalyst. For discharge in rising bubbles, however, this localization is hard to attain due to the irregular and unpredictable path of the rising bubbles. When bubble discharge occurs at the nozzle where the bubble is generated, on the other hand, heterogeneous catalysis of the plasma is mostly effective at the nozzle tip, where catalyst, plasma and solution meet, but this contact area is limited in size.

For these reasons, we opted to investigate such synergy with dielectric barrier discharge, which does not display the same limitations. As seen in Chapter 2, DBD can be easily scaled up to a larger plasma-liquid interface by forming a thin layer of liquid on one of the electrodes. The idea within this chapter is to further improve the latter concept with an additional step of adsorption of micropollutants on a nanofiber membrane placed on the electrode surface. The extremely high surface area of the nanofiber membrane, as described in section 6.1.2, allows to reach higher micropollutant concentration at its surface, close to the active plasma region [1]. There, reaction with active plasma species can take place and remove the micropollutants. This explains the expected synergy of plasma combined with pollutant adsorption.

In spite of the growing amount of studies on organic decomposition by means of plasma discharge, several important research questions remain to be answered to more deeply understand and optimize the oxidation mechanisms. First of all, plasma initiated decomposition has been studied in detail mostly for a few compound types that are easily analysed, e.g. phenol [2], sulfonol [3] and textile dyes [4]. Moreover, when decomposition of common micropollutants in a plasma reactor is investigated, high concentrations in mg/L range are used for simplicity in many cases. Since their concentration in wastewater and natural water typically ranges up to μg/L only, more research is required that focusses on micropollutant removal in this more realistic lower range.

In the present chapter, the pesticide atrazine is used as model micropollutant, since it is a good representative of persistent micropollution in water and stated in EU protocol as a dangerous pollutant. The applied concentration (30 μg/L) is one order of magnitude higher than the maximally allowed concentration in drinking water as defined by the United States Environmental Protection Agency [5], and the World Health Organization [6] and two orders of magnitude higher than the limit defined by the European Parliament and the Council [7]. In the first part of this chapter, the kinetics of H_2O_2 and O_3 production under plasma action is investigated, as they are well known to be responsible for atrazine oxidation in AOPs. The second part of the chapter deals with investigation of atrazine removal by the combination of non-thermal plasma and adsorption on nanofiber membrane and investigation of the by-products of atrazine oxidation.

6.1 Materials and methods

6.1.1 DBD reactor for water treatment

The atrazine solution was treated in pulsed dielectric barrier discharge (pDBD) generated above the solution. The scheme of the setup is presented on figure 6.1. The discharge was generated in between the high voltage electrode (HV) covered by a layer of dielectric material with thickness of about 360 μm and a 0.3 mm thick water film formed on the surface of nanofiber membrane. The membrane was placed on the support made from porous Robu

glass which was used to distribute water uniformly on the membrane surface. The distance between the HV electrode and water surface can be controlled with micro-screw. The radius of HV electrode is 11 mm and the radius of Robu porous glass is 20 mm. In the present study we used HV pulse duration of 400 ns in order to generate the discharge. The pulsed system was based on solid state switch technology from Behlke. The HV switch was connected to positive output of DC high voltage power supply IO BRANDENBURG. The main parameters of the system are presented in Table 6.1.

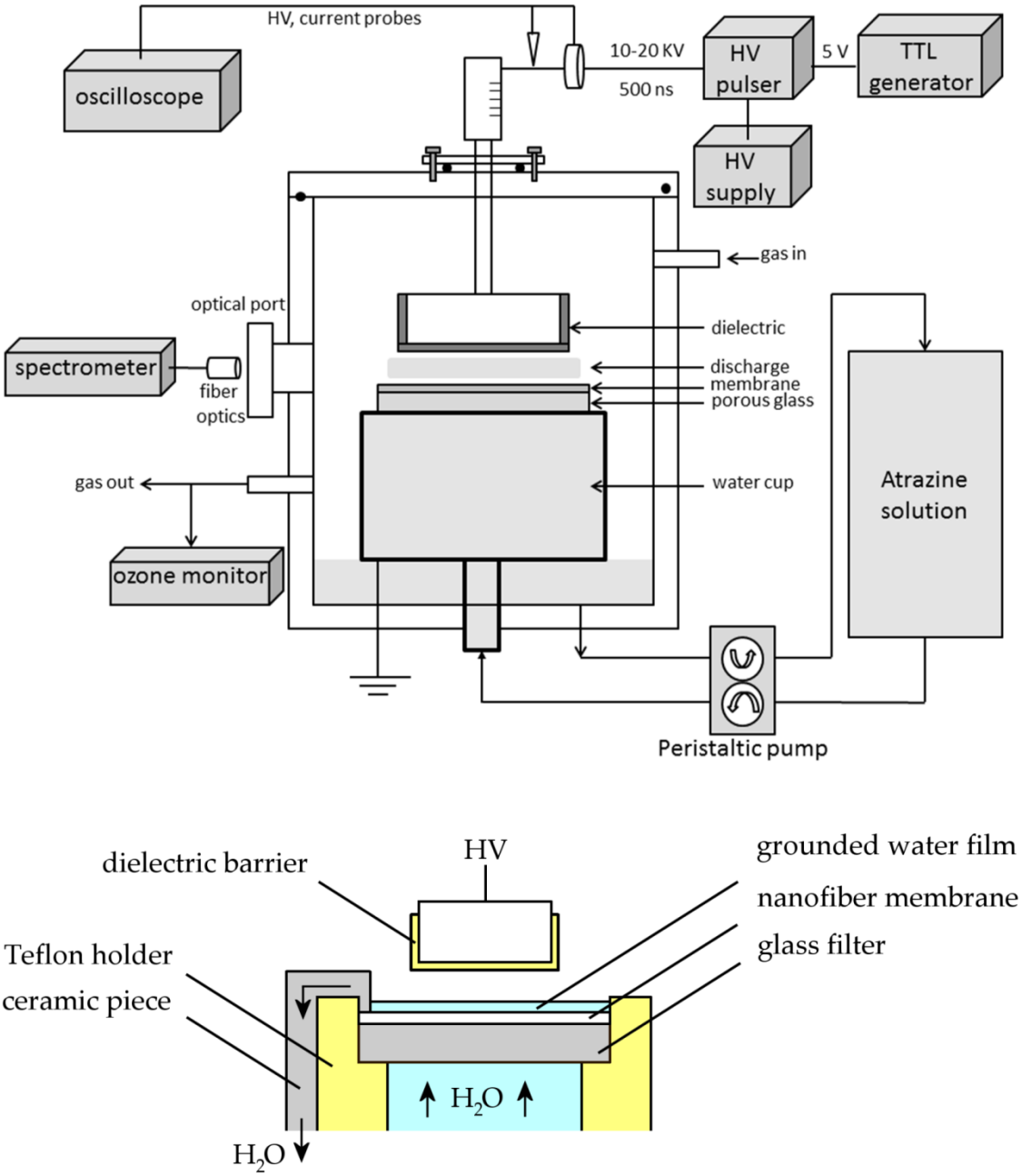

Figure 6.1 (top) The scheme of the pDBD reactor and diagnostics used to control the performance of the process. Meniscus formation of the water film on the nanofiber membrane is avoided by addition of ceramic pieces, as shown in the detailed electrode configuration (bottom).

The voltage was measured with a Tektronix P6015 HV probe and the current was measured with a Pearson model 2877 current probe. The short duration of HV pulses is favourable to generate a uniform discharge and to keep the gas temperature low. In all our experiments the water temperature never exceeded 35 ^{0}C which means that the pDBD plasma has a low gas temperature and can be used for water treatment. The discharge was generated in dry air which is continuously pumped through the system at a flow rate of 0.5 SLM (Standard Liter per Minute). The gas outlet was connected to the ozone monitor. The water solution was pumped in a closed circuit through the polyamide membrane, on which a thin water layer is formed. Atrazine, a persistent and hazardous pesticide, was chosen as a model micropollutant in our experiments, with an initial concentration of 30 μg/L. Initial conductivity was set by addition of $NaH_2PO_4 \cdot 2H_2O$. The solution was pumped through the system with a 2-channel peristaltic pump at a flow rate of 18 mL/min and 2 mL of solution is taken during the experiments for analysis by means of GC-MS, HPLC-MS and to measure H_2O_2 production. Additionally, emission spectra of the discharge are measured with OceanOptics spectrometer S1000 in the range of 250-900 nm in order to identify the main active species produced in the pDBD.

Table 6.1 The experimental parameters used in this work

Experimental parameter	Value/Description
Discharge voltage	23 kV
HV Polarity	positive
Discharge power	1.7 W
Inter-electrode distance	2.75 mm
Pulsed frequency	300 Hz
Robu glass porosity	0.42
Porous glass thickness	3 mm
Treated volume	100 mL
Initial atrazine concentration	30 μg/L
Initial conductivity	350 μS/cm
Initial pH	5.06
Treatment time	45 min

6.1.2 Nanofiber membrane

The membrane is made on the setup with a scaled up multi nozzle system, developed at Ghent University, which is described in details by Decostere et al. [8] and Daels et al. [9]. Polyamide 6 (PA-6) proves to be most suitable for electrospinning, since it can be electrospun

under steady state conditions. In the membrane production process, formic acid and acetic acid in 1:1 concentration ratio is used as solvent with 16 wt% PA-6 concentration. The injection flow rate during the electrospinning process is 2 ml/h, the applied voltage is 20 kV and the distance between needle and collector is 10 cm. The resulting membrane consists of nanofibres with an average diameter of 140 nm. It has a thickness of 120 μm, a mean pore size of 0.4 μm and a density of 10 g/m^2. PA-6 mass density is 1.14 g/cm^3 [10, 11], which gives a surface area of 25 m^2/g, about one order of magnitude less than surface area of activated carbon. In previous research, the membrane was shown to have adsorptive properties towards water pollution, where slightly more adsorption occurs for thinner membranes [12]. A typical SEM image is presented in Figure 6.2. Recently, tensile properties of the membrane were evaluated, resulting in strain to failure of 36.6 ± 5.7 %, stress at failure of 31.3 ± 3.8 MPa and Young's modulus of 111.4 ± 5.9 MPa [13].

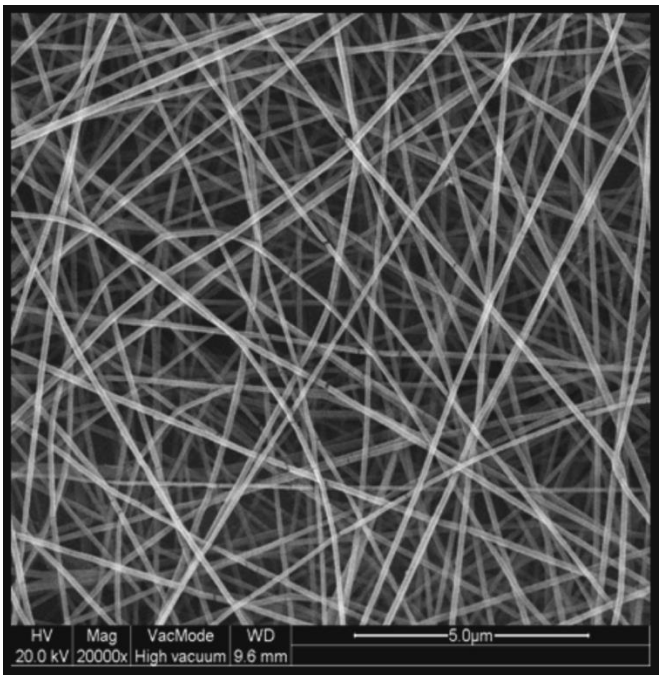

Figure 6.2. SEM image of nanofiber membrane of polyamide deposited on aluminium foil.

6.1.3 Ozone and H_2O_2 measurements

Ozone in gas phase is measured with ozone monitor Envitec model 450. The detection principle is based on absorption of light at 253.6 nm (Hg I line) in the absorption cell of the instrument. The monitor's limit of detection is 2 ppm or 4.3 μg/L with error of O_3 measurements not higher than 5 %. The concentration of hydrogen peroxide is determined by photometric method with metavanadate ammonium, as described by Nogueira et al. [14]. After adding 2.0 mL of sample to 0.8 mL of vanadate solution in acid medium, red-orange peroxovanadium cation is formed:

$$VO_3^- + 4H^+ + H_2O_2 \rightarrow VO_2^{3+} + 3H_2O \quad (6.1)$$

The product of reaction (6.1) has an absorption maximum at 450 nm. Hydrogen peroxide concentration can be estimated as:

$$C_{H_2O_2} = -\log_{10}\left(\frac{I^{sample}}{I^{test}}\right)\frac{V_2}{283V_1}\ [mol/L] \quad (6.2)$$

where I^{sample} and I^{test} are the light intensities at a wavelength of 450 nm passing through the solution of metavanadate ammonium with and without adding the plasma-treated sample respectively. V_1 is the volume of the aliquot used for analysis (mL) and V_2 is the final volume to which the aliquot V_1 is diluted (mL) before the absorbance measurement. The statistic error of measurements is estimated about 5% for H_2O_2 concentration higher than 5 mmol/L and 10% for lower concentration range.

6.1.4 GC-MS technique

Atrazine was extracted with a MPS-2 XYZ autosampler equipped with a headspace-solid phase microextraction unit (multi-PurposeSampler® or MPS®, Gerstel®, Mülheim and der Ruhr, Germany). For extraction, 19.00 g of the analyzed solution was hermetically sealed in 20 mL vials and incubated for 1 minute at 50 °C using agitation. Extraction of dissolved atrazine from the water matrix was done for 60 minutes at 50°C using a SPME fiber (100 μm Polydimethylsiloxane (PDMS), fused silica fiber core, Supelco, USA). Organic molecules that adsorbed onto the fiber were separated and identified using an Agilent GC-MS (HP 6890 Series GC System, 5973 Mass Selective Detector) equipped with a cross-linked methyl silicone column (HP-PONA, 50 m x 0.20 mm, 0.5 μm film thickness; Agilent Technology). For qualitative and quantitative measurements, the compounds were separated using Helium as the carrier gas (flow rate 1 mL min^{-1}). The temperature gradient was 60 °C (6 min) to 280 °C at 15 °C min^{-1}, held 11 minutes. The injector and transfer lines were maintained isothermally at 250 °C and 280 °C, respectively. The total ion current (70 eV) was recorded in the mass range from 40-250 amu (scan mode) and an analysis time of 60 min. Volatile compounds were identified by comparing the mass spectra obtained with the Wiley 275 library. Calibration of the detector was made with atrazine solutions of know concentration, from 1 to 100 μg/L. The integrated atrazine peak was found to be linear with atrazine concentration in this range. All samples were measured in duplicate.

6.1.5 HPLC-MS technique

In order to determine the by-products of atrazine decomposition, solution samples before and after plasma treatment of 45 minutes were also analyzed with high-performance liquid chromatography-coupled to diode array UV detection and time of flight mass spectrometry (HPLC-MS). Before analysis, liquid-liquid extraction of 50 mL water samples was made in 5 mL CH_2Cl_2 solvent with addition of 5 mL acetone and 1.2 g NaCl in a similar way as described by Gong et al. [15]. Separation of 3.2 mL was followed by evaporation to end volume of 1 mL. For analysis, the procedure is similar to the one used by Boelaert et al. [16]

with an Agilent HPLC 1290 system consisting of a binary pump (Agilent Technologies, Waldbronn, Germany), a diode array detector (DAD) with a micro flow cell (volume: 1 µL, path length: 10 mm) and a 6230 time-of-flight mass spectrometer (TOF-MS) equipped with a Jetstream Electrospray Ionization source (ESI). Separations were performed on a Zorbax C18 HPLC column (15 cm x 2.1 mm x 5 µm) equipped with a 2 mm C18 pre-column (SecurityGuard cartridge, Phenomenex). The mobile phase composition has been prepared as follows: A: H_2O + 0.1% formic acid and B: Acetonitrile + 0.1% formic acid. A flow rate of 200 µL/min was used whereby initial conditions containing 2% B were held constant during 5 min, followed by a gradient up to 100% B in 50 min, a plateau of 100% during 10 min and back to initial in 2 min. In between analyses, the column was conditioned during 15 min.

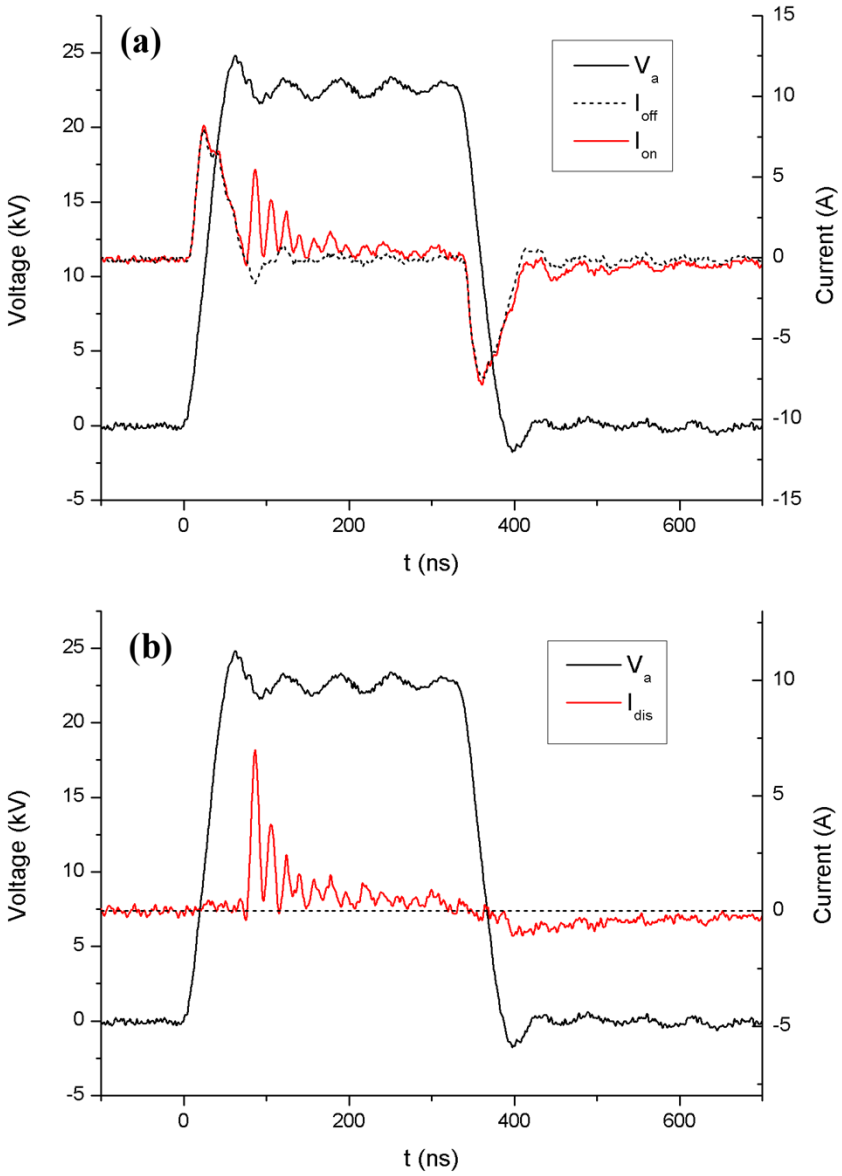

Figure 6.3. a) Waveform of the applied voltage V_a and current I_{on} in the case of plasma generation and displacement current I_{off} in the case without plasma generation. b) Waveform of the applied voltage and discharge current I_{dis} after substracting the displacement current.

The system was operated with the Agilent Masshunter software for instrument control and data acquisition. UV absorbance values were measured at 254 nm with a data acquisition rate of 20 Hz. The injection volume was 5 μL and all experiments were conducted at a temperature of 20 °C. TOF-MS detection was performed in the positive ionization mode. Mass ranges from 50-1000 amu were scanned. All tests were carried out in duplicate with a regular blank solvent analysis to ensure absence of cross contamination.

6.2 Experimental results and discussion

6.2.1 Power calculation

Typical waveforms of the applied voltage and current of the pulsed DBD plasma are shown in figure 6.3. The applied voltage V_a and current I_{on} in figure 6.3 are measured during plasma generation. The displacement current I_{off} is obtained at the same applied voltage when plasma is off. It does not represent a current of moving charges, as it is only caused by a time-varying electric field. Since the displacement current does not contribute to the part of the energy dissipated in the discharge, the actual discharge current I_{dis} in the plasma is obtained by subtracting the displacement current I_{off} from the total current I_{on}. In figure 6.3, a discharge current pulse of 7 A with duration of 20 ns occurs 20 ns after rise of the voltage to its maximum. Discharge power is calculated as $\int_t V_a(t)I_{dis}(t)dt$ whereas total input power of the pulsed generator is given by $\int_t V_a(t)I_{on}(t)dt$. This way, applied power and discharged power are determined to be 2.0 ± 0.1 W and 1.7 ± 0.1 W respectively.

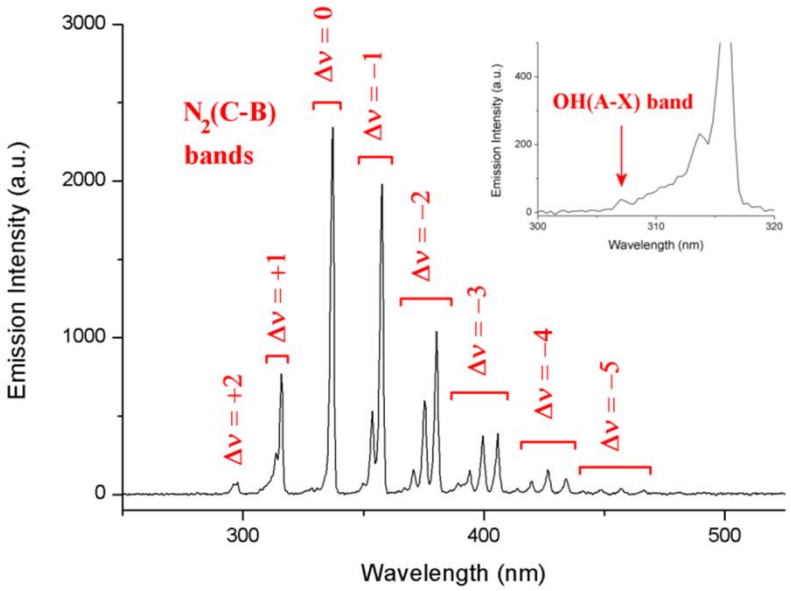

Figure 6.4 Space and time averaged emission spectrum of the discharge measured with resolution of 1.3 nm. Δν represents the change in quantum number ν of each radiative transition in the N_2(C-B) band system. This band system indicates the presence of metastable N_2 molecules.

6.2.2 Spectral analysis

As seen in figure 6.4, the emission spectrum of the discharge is dominated by radiative relaxation of excited vibrational states of the N_2 molecule, indicating the presence of metastable N_2 molecules. As pointed out by Choi et al. [17], metastable states of N_2 formed in air plasma are involved in formation of O and O_3. First, oxygen atoms are formed through the following reactions:

$$N_2 + e \rightarrow N_2^* + e \quad (6.3)$$

$$N_2^* + O_2 \rightarrow N_2 + 2O \quad (6.4)$$

$$N_2^* + O_2 \rightarrow N_2O + O \quad (6.5)$$

Next, ozone is generated from a three body reaction as:

$$O + O_2 + M \rightarrow O_3 + M \quad (6.6)$$

where M = O_2 or N_2 is a third collision partner. Atomic oxygen can also be generated by electron impact on an oxygen molecule:

$$O_2 + e^* \rightarrow O + O + e \quad (6.7)$$

Despite the presence of atomic oxygen in the plasma, emission lines of excited oxygen atoms are very small, such as the O^I triplet at 777.5 nm for example. The OH(A-X) (0,0) Q-band head around 309 nm and the OH(A-X) (1,1) band around 315 nm are overlapped with the N_2^* bands and are therefore not observed in the spectrum. Nevertheless, the small OH(A-X) (0,0) R-band head around 307 nm indicates the presence of excited OH radicals. OH radicals can be formed in plasma through many reactions, which typically require the presence of water molecules, as discussed in two recent excellent reviews by Locke and Shih [18] and Jiang et al. [19]. Dissociation of water by electron impact is the primary example:

$$H_2O + e \rightarrow OH + H + e \quad (6.8)$$

Also, vibrational and rotational excitation of a water molecule can lead to OH radical formation:

$$H_2O + e \rightarrow H_2O^* + e \quad (6.9)$$

$$H_2O^* + H_2O \rightarrow H_2O + H + OH \quad (6.10)$$

$$H_2O^* + H \rightarrow H_2 + OH \quad (6.11)$$

The presence of atomic oxygen boosts OH radical formation as well:

$$O + H_2O \rightarrow 2OH \quad (6.12)$$

It has to be noted that OH radicals have a lifetime in the order of 10 – 100 μs in gas phase [18]. Therefore, only OH radicals that are generated near the water surface can diffuse from the plasma zone into the surrounding water. Their lifetime in the liquid phase is in the nanosecond range, since they will react immediately with a surrounding molecule due to their high reactivity. This way, they can recombine to a long-lived hydrogen peroxide molecule through following reactions:

$$OH + H_2O^* \rightarrow H_2O_2 + H \quad (6.13)$$

$$OH + OH \rightarrow H_2O_2 \quad (6.14)$$

The latter two reactions can also occur in the gas phase, after which the hydrogen peroxide molecules can diffuse into the surrounding water. Generation of UV photons, N_2 metastables, atomic O, OH radicals and O_3 in gas phase indicates that pDBD is indeed an effective source of active species for advanced oxidation of micropollutants in water.

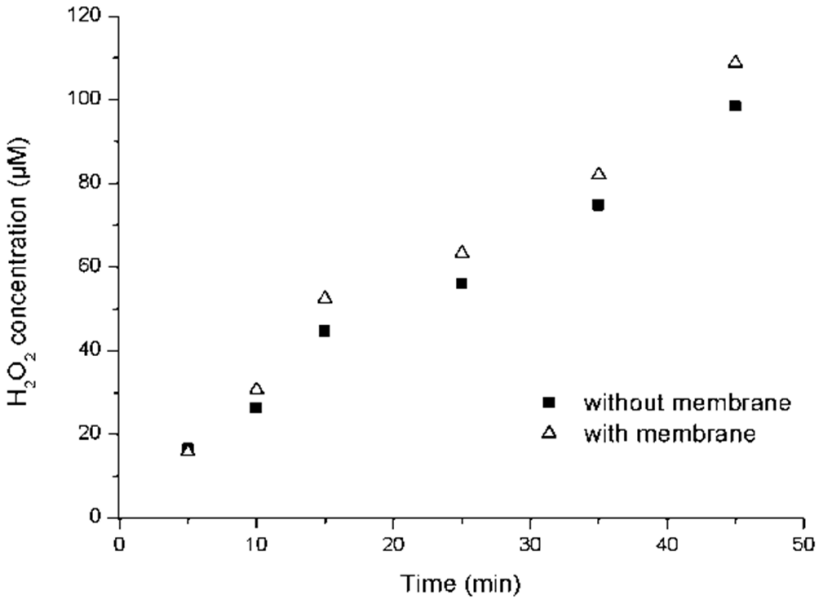

Figure 6.5 Hydrogen peroxide production in the liquid phase as a function of time with and without presence of the nanofiber membrane.

6.2.3 Ozone and H_2O_2 production

O_3 concentration in gas phase is about 153 ppm or 327 μg/L with nanofiber membrane in the setup and 163 ppm or 349 μg/L without membrane. Taking into account the accuracy of the ozone monitor, ozone production is thus independent of the presence of the membrane. This agrees with our expectations, since ozone formation through reactions (6.3) – (6.7) occurs in the gas phase, which is screened off from the membrane by the water film under treatment.

H_2O_2 concentration in the liquid phase is shown as a function of treatment time in figure 6.5. H_2O_2 production is about 5% higher when the nanofiber membrane is added into the setup. This difference is in the range of experimental error in measurements of the discharge power which is about 5 %. Therefore, H_2O_2 production is considered to be independent of the presence of the membrane as well, for similar reasons as those for ozone production. From these results, an energy yield for ozone generation of 5.07 g/kWh and for hydrogen peroxide generation of 0.23 g/kWh is calculated, from 2.0 W applied power, 0.5 SLM gas flow rate and 100 mL total solution volume. According to the review of Locke and Shih [18], reactors based on discharge over a liquid surface have reported H_2O_2 yields ranging from 0.04 to 5.0 g/kWh, with most data falling below 1 g/ kWh. The H_2O_2 yield for plasma systems is limited by mass transfer and the size of the plasma-liquid interface, where a larger plasma-liquid interface is an advantage in pDBD.

6.2.4 Energy efficiency for atrazine removal

Efficiency of atrazine removal is measured by GC-MS method with SPME extraction. According to GC-MS analysis, 45 min of plasma treatment reduces the initial atrazine concentration from 30.0 μg/L to 11.7 μg/L and 4.6 μg/L, respectively in absence and in presence of the nanofiber membrane. The increase of atrazine removal in the reactor with nanofiber membrane can be partly explained by adsorption of atrazine on the membrane. This is confirmed by a drop from 30 μg/L atrazine to 17.7 μg/L after recirculating the solution through the reactor with membrane without plasma discharge. Hijosa-Valsero et al. investigated atrazine decomposition by DBD discharge at much higher initial concentration (5 mg/L) [20]. The authors observed an exponential decay of atrazine concentration during treatment. This allows to determine a first order reaction rate constant k_A for atrazine removal in our reactor from the equation

$$\ln\left(\frac{C_0}{C_t}\right) = k_A t \tag{6.15}$$

where C_0 and C_t are the atrazine concentration of the initial solution and end solution respectively and t = 2700 s (= 45min) is the total treatment time. Energy yield G_{50} in g/kWh for 50% atrazine removal is determined from k_A as [20]

$$G_{50} = \frac{1}{2}\frac{k_A C_0 V}{P \ln 2} 3.6 \times 10^6 \text{ J/kWh} \tag{6.16}$$

where V is the solution volume, P = 2.0 W is the input power and initial concentration C_0 is given in g/L. Resulting values for k_A and G_{50} are found in Table 6.2.

In order to find a synergy between plasma treatment and micropollutant adsorption, a 2 × 2 factorial design should be performed, where the levels should be understood as the absence or presence of the membrane (first factor) and the absence or presence of plasma discharge (second factor). This gives the following four experiments:

1. Atrazine removal without membrane and without plasma treatment
2. Atrazine removal by adsorption on the membrane, without plasma treatment
3. Atrazine removal by plasma treatment, without membrane
4. Atrazine removal by adsorption on the membrane combined with plasma treatment

The first experiment is not performed, as it is considered trivial with atrazine removal of 0%. Without synergy, adsorption with plasma would result in a reaction rate constant $k_A = 2.0 \times 10^{-4}\ s^{-1} + 3.5 \times 10^{-4}\ s^{-1} = (5.5 \pm 0.2) \times 10^{-4}\ s^{-1}$, based on the second and third experiment. In the fourth experiment, however, a reaction rate of $(6.94 \pm 0.02) \times 10^{-4}\ s^{-1}$ is measured, which is 25% higher. Here, the standard errors are calculated using the maximal error of 5% on the concentration measurements. Assuming a null-hypothesis of no synergy, taking a significance level of 0.05 and considering a minimum of 1 degree of freedom, a one-tailed Welch's t-test gives a statistic t = 6.8 and a p-value of 0.047. As the p-value is below 0.05 and is overestimated by means of the maximal measurement error and the minimal degrees of freedom, these results suggest that the null-hypothesis can be rejected, so plasma treatment combined with micropollutant adsorption leads to synergy.

This synergy is explained with a higher local concentration in the water film on the nanofiber membrane. That is, adsorption increases the local concentration of the pollutant near the plasma-liquid interface [1], leading to more effective reaction of active plasma species with pollutant in the plasma-liquid interface. Since this effect only enhances atrazine decomposition in the thin water film near the active plasma region (about 0.1% of the total solution volume), the dominating decomposition processes are taking place at the plasma-liquid interface.

Table 6.2 Final atrazine concentration $c_{A,45min}$, atrazine removal yield y_{-A} and first order reaction rate constant k_A for atrazine removal with initial concentration of 30 μg/L. Energy yield is presented as G_{50} value corresponding to 50% atrazine removal. Experimental data (in bold) without plasma but with nanofiber membrane, with plasma but without nanofiber membrane and with both are retrieved from GC-MS measurements. Data for direct oxidation by O_3, for oxidation by peroxone process and the theoretical limit of the reactor are results of simulation based on formulas (6.17), (6.24) (6.25) and (6.26).

parameter	without plasma	without membrane	membrane + plasma	direct oxidation by O_3	oxidation by peroxone	theoretical limit
$c_{A,45min}$ (μg/L)	**17.7**	**11.7**	**4.6**	29.0	26.9	7.6×10^{-3}
y_{-A} (%)	**41.2**	**61.0**	**84.7**	3.4	10.4	99.97
k_A (s^{-1})	**2.0×10^{-4}**	**3.5×10^{-4}**	**6.9×10^{-4}**	1.3×10^{-5}	4.1×10^{-5}	3.1×10^{-3}
G_{50} (g/kWh)	**-**	**1.4×10^{-3}**	**2.7×10^{-3}**	5.1×10^{-5}	1.6×10^{-4}	1.2×10^{-2}

In order to confirm that atrazine decomposition is taking place mostly at the plasma-liquid interface, the effect of the dominant degradation processes in the water bulk is estimated. According to the general view in literature, direct oxidation by ozone and oxidation by the dark peroxone process are the most dominant oxidation processes in the water bulk in absence of UV light [21]. Atrazine degradation due to direct oxidation by ozone can be determined with the formula

$$-\frac{d[A]}{dt} = k_{A,O_3}[A][O_3] \quad (6.17)$$

where [A] and [O_3] is the molar concentration of atrazine and ozone respectively and $k_{A,O3}$ = 6.0 M^{-1} s^{-1} is the reaction rate constant of direct oxidation of atrazine by O_3. Maximal O_3 concentration in water is reached in thermodynamic equilibrium according to Henry's law. Henry's law constant H_0 for ozone in water at 20°C is reviewed by Kuosa as a function of pH, using several values in literature and from simulation [22]. Based on this review, the constant is taken as $H_0 = 7.9\times10^3$ kPa M^{-1} at pH = 5 and $H_0 = 7.3\times10^3$ kPa M^{-1} at pH = 4, with a linear dependence on pH. For our experiments with initial pH = 5.06 and final pH = 3.99, this gives an initial and final dissolved ozone concentration [O_3] of 2.03 µM and 2.19 µM respectively. This way, atrazine concentration [A] is calculated based on equation (6.17) where pH (and thus also [O_3]) changes linearly in time.

A second process responsible for atrazine decomposition in the bulk is oxidation by peroxone. This process occurs when hydrogen peroxide is added to ozonated water. In that case, OH radicals are formed in liquid phase through the reactions (6.18) to (6.21)

$$H_2O_2 \rightleftharpoons H^+ + HO_2^- \quad (6.18)$$

$$O_3 + HO_2^- \rightarrow O_3^- + HO_2 \quad (6.19)$$

$$O_3^- \rightleftharpoons O_2 + O^- \quad (6.20)$$

$$O^- + H_2O \rightarrow OH^- + OH \quad (6.21)$$

Since the reaction of O_3 is much faster with the perhydroxyl anion HO_2^- than with the conjugate acid H_2O_2, reactions (6.18) to (6.21) become the dominant source of OH radicals during the peroxone process in the absence of UV light [21]. As should be noted, the overall production rate of OH radicals is influenced by scavenging reactions (6.22) and (6.23).

$$OH + O_3 \rightarrow HO_2 + O_2 \quad (6.22)$$

$$OH + H_2O_2 \rightarrow HO_2 + H_2O \quad (6.23)$$

Similarly to equation (6.17), atrazine degradation due to the peroxone process is given by

$$-\frac{d[A]}{dt} = k_{A,OH}[A][0H] \quad (6.24)$$

where [OH] is the molar concentration of OH radicals and $k_{A,OH}$ = 3 × 10^9 M^{-1} s^{-1} is the reaction rate constant of atrazine oxidation by OH radicals [23]. For peroxone process, the pseudo-steady-state concentration of [OH] can be calculated with the kinetic model of Hong et al. [21] as

$$[OH]_{ss} = \frac{1.2k_{19}[O_3][H_2O_2]_T K_{18}[H^+]^{-1}}{k_{22}[O_3]+k_{23}[H_2O_2]_T+k_{A,OH}[A]} \quad (6.25)$$

where k_{19} = 2.8 × 10^6 M^{-1} s^{-1}, k_{22} = 1.1 × 10^8 M^{-1} s^{-1} and k_{23} = 2.7 × 10^7 M^{-1} s^{-1} are reaction rate constants from reactions (6.19), (6.22) and (6.23) respectively, K_{18} = 2.4 × 10^{-12} is the equilibrium constant of reaction (6.18) and $[H_2O_2]_T$ and $[H^+]$ are the molar concentration of hydrogen peroxide and the hydrogen cation. In formula (6.25), the OH radical formation yield reduction of 40% as suggested by Fischenbacher et al. [23] is taken into account. Scavengers of the OH radical, other than O_3, H_2O_2 and atrazine, are disregarded, since the goal is to estimate the maximal degradation of atrazine by the peroxone process. Kinetics of atrazine decomposition due to direct oxidation by O_3 in combination with peroxone process is presented in figure 6.6.

Simulation gives an atrazine degradation of 3.4%, 10.4% and 13.5% after 45 min of treatment, respectively by direct oxidation with ozone, by the peroxone process and by the combination of both. Figure 6.6 shows concentration of atrazine and [OH] as a function of treatment time as simulated for the different processes. Initially, OH radical formation by the peroxone process increases strongly, to reach its peak value of 2.13 × 10^{-14} M after 9.8 min. After the peak, scavenging of OH radicals by H_2O_2 becomes dominant and decreases the efficiency of the peroxone process. This is a well-known phenomenon, since the most optimal $[H_2O_2]$ to $[O_3]$ ratio value for peroxone mentioned in literature is typically ranging from 0.3 to 1.0 [24-28].

Table 6.2 presents a summary of data on atrazine decomposition in the reactor, obtained from experiments and from formulas (6.17), (6.24) and (6.25). Also, a theoretical limit of the reactor efficiency was calculated from the equation (6.26). This formula is based on the assumptions of complete atrazine decomposition at the outlet of the reactor chamber during pumping and of ideal mixing of the solution at the inlet.

$$-\frac{d[A]}{dt} = \frac{Q}{V}[A] \quad (6.26)$$

where Q = 0.3 mL/s (= 18mL/min) is the water flow and V = 100 mL is the total solution volume. To be complete, atrazine degradation by peroxone and ozone in the solution bulk is taken into account in this theoretical limit.

The atrazine removal energy yield in the experiments and in the red curves in figure 6.6 is one order of magnitude lower than the theoretical limit. More specifically, 10% and 21% of atrazine concentration that passes along the active plasma zone and leaves the reactor chamber during pumping is removed without membrane and with membrane respectively,

as determined by our simulations. As discussed before, this effect of the membrane indicates the importance of degradation processes in the proximity of the plasma-liquid interface. Direct oxidation by ozone and oxidation by the peroxone process can only explain about 20% of the observed atrazine decomposition without membrane. This is a further indication that oxidative processes in the thin water film play an important role. Atrazine decomposition at the plasma-liquid interface is caused by multiple reactive plasma species from the active plasma zone, such as UV photons, radicals, ions and long-living metastables like HO_2^*. When these species reach the water surface and interact with atrazine, oxidation takes place. Increasing the local concentration of atrazine near the plasma-liquid interface will increase the chance on such collisions and thus the overall atrazine degradation yield, which is a strong advantage of the suggested method.

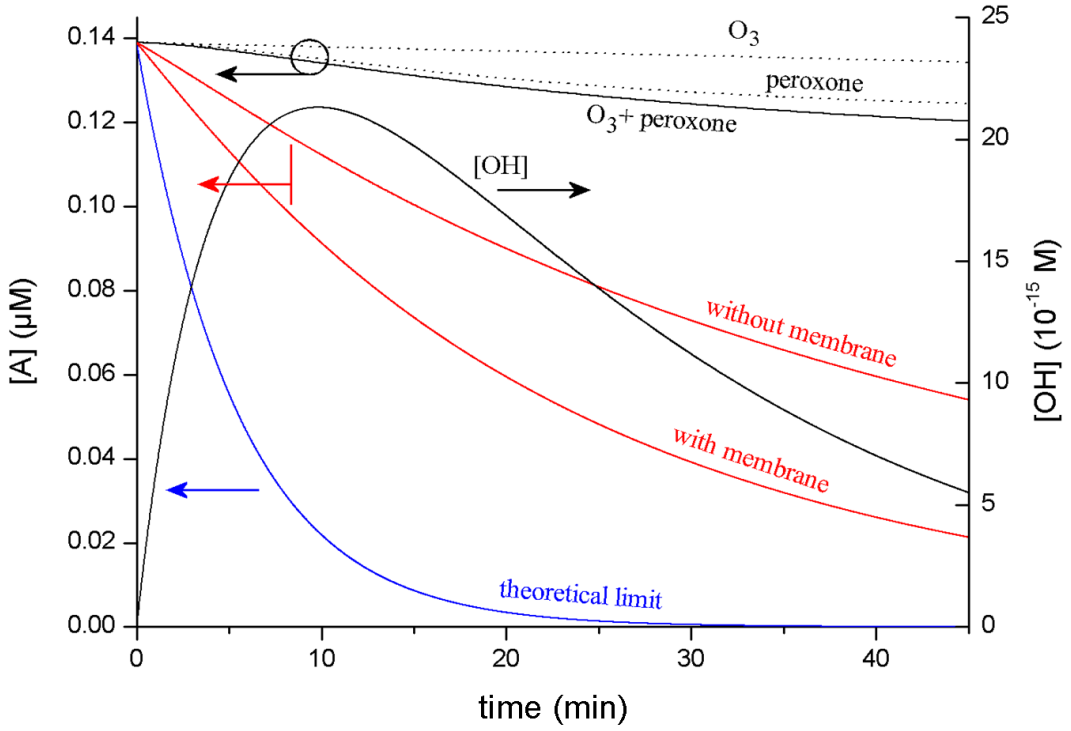

Figure 6.6. Atrazine and OH radical concentration as a function of treatment time for direct oxidation with ozone (O_3), for dark peroxone process and for combination of both, as calculated with the kinetic model of Hong et al. [21] from formulas (6.17), (6.24) and (6.25). The theoretical limit is calculated from formula (6.26), while taking into account the peroxone process with direct ozonation in the bulk solution. The red curves are calculated from 10% and 21% of atrazine removal at the outlet in combination with the bulk processes and correspond with the experiments without and with membrane respectively. Since the red curves are much lower than the combined ozone and peroxone curve, oxidation by ozone and peroxone only contributes to a small part of total atrazine removal.

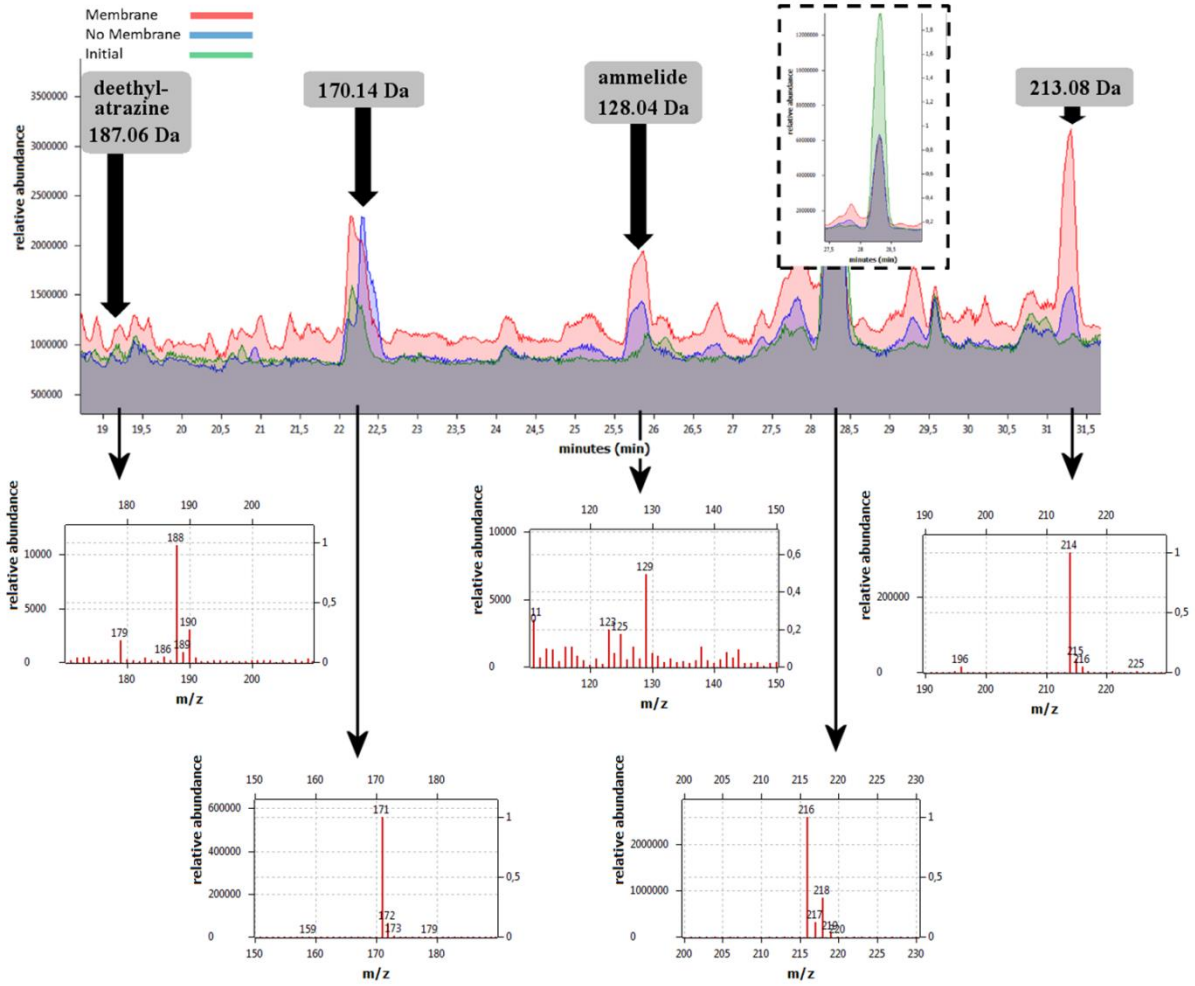

Figure 6.7. Detail (from 18.7 min to 31.7 min) of HPLC-MS chromatogram of initial atrazine solution and of treated samples with and without the presence of the nanofiber membrane. For each considered peak belonging to an oxidation by-product, the mass spectrum is shown.

6.2.5 By-products

HPLC-MS chromatograms of the initial solution and the solution after 45 min of plasma treatment are shown in figure 6.7. In agreement with the GC-MS results, a stronger decrease of the atrazine peak is observed after treatment when the nanofiber membrane is added in the setup. Due to the low initial atrazine concentration, however, accurate detection of most by-products by HPLC-MS is not possible. At least 4 oxidation products have been found with monoisotopic mass 128.04 Da, 170.14 Da, 187.06 Da and 213.08 Da, which all have higher abundance when the membrane is added in the setup. Only two of them are tentatively identified as deethylatrazine and ammelide (figure 6.8). Both are commonly found amongst atrazine by-products in advanced oxidation processes [29, 30]. Deethylatrazine is one of the first generation intermediates in several atrazine degradation pathways proposed in literature. Moreover, it is considered to be more stable than other

intermediates from the first generation, due to its persistence in natural waters and due to the higher reactivity of the ethyl group [29, 31]. Ammelide is one of the final stable products in the atrazine oxidation pathway and is considered to be less toxic than atrazine and its earlier intermediates [30-34]. The relative stability of both intermediates explains why they are detected in the present study despite the low initial atrazine concentration.

To our knowledge, atrazine degradation by-products from treatment with DBD plasma have only been reported by Hijosa-Valsero et al. [20]. The authors used a DBD reactor very similar to the one used in this study, but powered by AC high voltage and with much higher initial atrazine concentration of 5 mg/L. Hijosa-Valsero et al. identified 3 common atrazine oxidation products, deethylatrazine, deisopropylatrazine and atrazine amide, and one less common intermediate 4-chloro-6-(ethenylamino)-1,3,5-triazin-2-yl [20]. After 84% of atrazine decomposition, the deethylatrazine to atrazine relative abundance in the mass spectra was roughly 0.5, while it is 0.02 in the present study in presence of the nanofiber membrane. Hoeben investigated degradation of a 25 mg/L atrazine solution by corona discharge above water and detected at least 7 oxidation products, but could not identify them [35]. As this suggests, the degradation pathway of atrazine under plasma treatment is sensitive to different experimental parameters.

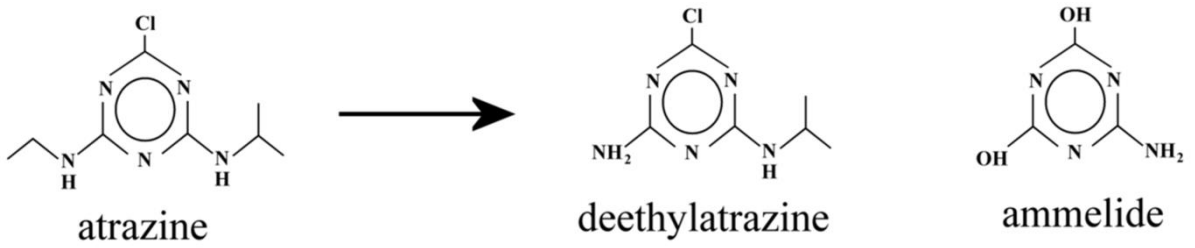

Figure 6.8. Proposed oxidation by-products of atrazine treatment with pulsed DBD.

The HPLC-MS results of the present study illustrate the high potential of pDBD plasma to decompose persistent micropollutants. Moreover, as can be seen from the different peaks in figure 6.7, adding the nanofiber membrane in the setup enhances by-product generation. Cleavage of the s-triazine ring has not yet been reported in any advanced oxidation process [36]. Pelizzetti et al. have concluded from detailed GC-MS analysis that photocatalytic oxidation of aqueous atrazine cannot destroy the triazine ring and that the final oxidation product is cyanuric acid [37].

6.3 Conclusion

In this work, a new water treatment reactor based on atmospheric pulsed dielectric barrier discharge above water is investigated. In order to increase decomposition efficiency and to limit unwanted by-product formation, combination of pDBD plasma with adsorption on nanofiber membrane was proposed. Atrazine is chosen as model micropollutant with an initial concentration of 30 µg/l, which is one order of magnitude higher than the maximally

allowed concentration in drinking water. In the pDBD reactor, the measured energy yield of H_2O_2 production in liquid phase is about 0.23 g/kWh and concentration of H_2O_2 is linearly dependent on treatment time. The energy yield of O_3 production is measured to be 5.07 g/kWh. While the H_2O_2 and O_3 production in the reactor is not influenced by the presence of the nanofiber membrane, there is a significant increase in atrazine decomposition when the membrane is added to the setup. An atrazine removal yield of 85% can be obtained with nanofiber membrane at 45 minutes of treatment where only about 61% removal is reached with plasma alone. The observed effect is caused by atrazine adsorption on the membrane close to the plasma active region, leading to a higher local atrazine concentration near the plasma-liquid interface. The higher local concentration increases the frequency of direct and indirect oxidizing interactions of the micropollutant with reactive species from the active plasma region. To reinforce this explanation, the contribution of the dominant atrazine degradation processes in the water bulk has been estimated. According to literature, direct oxidation by ozone and oxidation by peroxone are the dominant processes in the water bulk in absence of UV light. Using the kinetic model of Hong et al. [21], the contribution of these bulk processes to the overall atrazine degradation is calculated to be only about 14%. Therefore, the determining oxidation reactions are occurring in the thin water layer near the plasma active region. The main by-products of atrazine decomposition measured by HPLC-MS are the first generation intermediate deethylatrazine and the deep oxidation by-product ammelide. System efficiency is almost doubled when the nanofiber membrane is placed in the plasma reactor with deeper degradation of atrazine to the by-products. These results show the benefits of combining non-thermal plasma with pollutant adsorption for degradation of micropollution, a synergetic effect that yet has to receive more attention.

References

[1] J. Toth, *Adsorption: theory, modeling, and analysis*, 1st edition ed.: Marcel Dekker AG, Basel, Switzerland, 2002.

[2] L. R. Grabowski, *et al.*, "Corona Above Water Reactor for Systematic Study of Aqueous Phenol Degradation," *Plasma Chemistry and Plasma Processing*, vol. 26, pp. 3-17, 2006.

[3] E. S. Bobkova, *et al.*, "A Study of Sulfonol Decomposition in Water Solutions Under the Action of Dielectric Barrier Discharge in the Presence of Different Heterogeneous Catalysts," *Plasma Chemistry and Plasma Processing*, vol. 32, pp. 97-107, 2012.

[4] L. O. d. B. Benetoli, *et al.*, "Pyrite-enhanced methylene blue degradation in non-thermal plasma water treatment reactor," *Journal of Hazardous Materials*, vol. 237-238, pp. 55-62, 2012.

[5] "Atrazine," Last revised April 24th 2007 ed, 2007, p. 6.

[6] W. H. Organization, *Guidelines for drinking-water quality: recommendations* vol. 1: World Health Organization, 2004.

[7] "Directive 2006/118/EC of the European Parliament and of the Council of 12 December 2006 on the protection of groundwater against pollution and deterioration," ed, p. 26.

[8] B. Decostere, *et al.*, "Performance assessment of electrospun nanofibers for filter applications," *Desalination,* vol. 249, pp. 942-948, 2009.

[9] N. Daels, *et al.*, "The use of electrospun flat sheet nanofibre membranes in MBR applications," *Desalination,* vol. 257, pp. 170-176, 2010.

[10] S. Pashaei, *et al.*, "Thermal degradation kinetics of nylon6/GF/crysnano nanoclay nanocomposites by TGA," *Chemical Industry and Chemical Engineering Quarterly/CICEQ,* vol. 17, pp. 141-151, 2011.

[11] F. Van De Velde and P. De Baets, "The friction and wear behaviour of polyamide 6 sliding against steel at low velocity under very high contact pressures," *Wear,* vol. 209, pp. 106-114, 1997.

[12] N. Daels, *et al.*, "Functionalisation of electrospun polymer nanofibre membranes with TiO 2 nanoparticles in view of dissolved organic matter photodegradation," *Separation and Purification Technology,* vol. 133, pp. 282-290, 2014.

[13] B. De Schoenmaker, "Electrospinning and characterisation of polyamide nanofibres for composite applications," Doctor Doctoral Thesis, Department of Textiles, Ghent University, Ghent, 2013.

[14] R. Nogueira, *et al.*, "Simple and fast spectrophotometric determination of H2O2 in photo-Fenton reactions using metavanadate," *Talanta,* vol. 66, pp. 86-91, 2005.

[15] A. Gong and C. Ye, "Analysis of trace atrazine and simazine in environmental samples by liquid chromatography–fluorescence detection with pre-column derivatization reaction," *Journal of Chromatography A,* vol. 827, pp. 57-63, 1998.

[16] J. Boelaert, *et al.*, "State-of-the-art non-targeted metabolomics in the study of chronic kidney disease," *Metabolomics,* vol. 10, pp. 425-442, 2014.

[17] J. H. Choi, *et al.*, "Analysis of sterilization effect by pulsed dielectric barrier discharge," *Journal of Electrostatics,* vol. 64, pp. 17-22, 2006.

[18] B. R. Locke and K.-Y. Shih, "Review of the methods to form hydrogen peroxide in electrical discharge plasma with liquid water," *Plasma Sources Science and Technology,* vol. 20, p. 034006, 2011.

[19] B. Jiang, *et al.*, "Review on electrical discharge plasma technology for wastewater remediation," *Chemical Engineering Journal,* vol. 236, pp. 348-368, 2014.

[20] M. Hijosa-Valsero, *et al.*, "Removal of priority pollutants from water by means of dielectric barrier discharge atmospheric plasma," *Journal of Hazardous Materials,* vol. 262, pp. 664-673, 2013.

[21] A. Hong, *et al.*, "Modeling kinetics of illuminated and dark advanced oxidation processes," *Journal of Environmental Engineering,* vol. 122, pp. 58-62, 1996.

[22] M. Kuosa, *Modeling reaction kinetics and mass transfer in ozonation in water solutions*: Lappeenranta University of Technology, 2008.

[23] A. Fischbacher, *et al.*, "The• OH radical yield in the H2O2+ O3 (peroxone) reaction," *Environmental Science & Technology,* vol. 47, pp. 9959-9964, 2013.

[24] B. De Witte, *et al.*, "Ozonation and advanced oxidation by the peroxone process of ciprofloxacin in water," *Journal of Hazardous Materials,* vol. 161, pp. 701-708, 2009.

[25] W. H. Glaze, *et al.*, "The chemistry of water treatment processes involving ozone, hydrogen peroxide and ultraviolet radiation," 1987.

[26] Y.-C. Hsu, *et al.*, "Peroxone Process for RO-16 and RB-19 Dye Solutions Treatment," *Journal of Environmental Science and Health, Part A,* vol. 38, pp. 1361-1376, 2003.

[27] S. S. Kalra, *et al.*, "Advanced oxidation processes for treatment of textile and dye wastewater: a review," in *2nd International conference on environmental science and development*, 2011, pp. 271-5.

[28] R. Munter, "Advanced oxidation processes–current status and prospects," *Proc. Estonian Acad. Sci. Chem,* vol. 50, pp. 59-80, 2001.

[29] C. D. Adams and S. J. Randtke, "Ozonation byproducts of atrazine in synthetic and natural waters," *Environmental Science & Technology,* vol. 26, pp. 2218-2227, 1992.

[30] M. Gonzalez, *et al.*, "Vacuum-ultraviolet (VUV) photolysis of water: mineralization of atrazine," *Chemosphere,* vol. 28, pp. 2121-2127, 1994.

[31] F. J. Beltrán, *et al.*, "Aqueous UV radiation and UV/H2O2 oxidation of atrazine first degradation products: deethylatrazine and deisopropylatrazine," *Environmental toxicology and chemistry,* vol. 15, pp. 868-872, 1996.

[32] C. Y. Chan, *et al.*, "Treatment of atrazine by integrating photocatalytic and biological processes," *Environmental Pollution,* vol. 131, pp. 45-54, 2004.

[33] J. A. Khan, *et al.*, "Kinetic and mechanism investigation on the photochemical degradation of atrazine with activated H 2 O 2, S 2 O 8 2− and HSO 5−," *Chemical Engineering Journal,* vol. 252, pp. 393-403, 2014.

[34] L. Xu, *et al.*, "Atrazine degradation using chemical-free process of USUV: Analysis of the micro-heterogeneous environments and the degradation mechanisms," *Journal of Hazardous Materials,* vol. 275, pp. 166-174, 2014.

[35] W. F. L. M. Hoeben, *Pulsed corona-iduced degradation of organic materials in water*: Technische Universiteit Eindhoven, 2000.

[36] S. Mededovic and B. R. Locke, "Side-chain degradation of atrazine by pulsed electrical discharge in water," *Industrial & Engineering Chemistry Research,* vol. 46, pp. 2702-2709, 2007.

[37] E. Pelizzetti, *et al.*, "Photocatalytic degradation of atrazine and other s-triazine herbicides," *Environmental Science & Technology,* vol. 24, pp. 1559-1565, 1990.

A physicist is just an atom's way of looking at itself.
- Niels Bohr

Chapter 7

Characterization of an AC dielectric barrier single micro-discharge filament over a water film

As discussed in section 3.4.2, dielectric barrier discharge over horizontal water surface is most commonly powered with AC voltage. Moreover, AC high voltage is a popular choice as well for coaxial DBD reactors with falling water film (cfr. section 3.4.3). In the majority of the studies, glass is used as a dielectric barrier, especially quartz glass, and the plasma is operated in air. Chapter 8 deals with organic degradation in a reactor of this kind. A preceding fundamental investigation on this discharge type is therefore interesting, as it can provide better understanding of the process and lead to recommendations for optimized application. Nonetheless, diagnostics of DBD plasma in air are not straightforward, due to its dynamic and inhomogeneous nature. For parallel planar or coaxial configuration, DBD plasma consists of numerous filaments, termed micro-discharges, which move unpredictably in time and space in between the electrodes. This complicates accurate investigation of plasma characteristics, such as discharge shape, dimensions, temporal behavior and electron density.

To this end, we have developed a DBD reactor where a single, stable micro-discharge filament is generated in between a water film and a quartz glass barrier. From spectroscopical analysis, rotational and vibrational temperature T_{rot} and T_{vib} are determined, as well as reduced electrical field strength E/N and electron mobility μ_e. Temporal and spatial features of the discharge are investigated by means of ICCD imaging, a photomultiplier tube (PMT) and electrical characterization. The discharge evolution is

extensively discussed and similarities and differences with observations performed by other authors are pointed out. Finally, after estimation of current density j, an estimation of electron density n_e is determined and compared with other DBD plasmas.

7.1 Insights from literature

Surprisingly, reports on diagnostical investigation of DBD plasma with a liquid electrode in atmospheric air have not been found in scientific literature. Notwithstanding, this discharge type has direct similarities with DBD in air with solid planar parallel electrodes, such as the occurrence of micro-discharges. Moreover, a water electrode behaves as a dielectric on time scales smaller than the Maxwellian relaxation time τ of the solution, which is given by [1]

$$\tau = \varepsilon_r \varepsilon_0 / \sigma \tag{7.1}$$

Here is ε_r the relative dielectric constant of water, with a value of ε_r = 80, ε_0 is vacuum permittivity and σ is solution conductivity. For example, τ = 1 μs for a conductivity of σ = 7.8 μS/cm and drops to 78 ns for a conductivity of σ = 100 μS/cm. The actual conductivity can be significantly different from the initial conductivity, since plasma treatment of the solution raises the conductivity to a few hundreds of μS/cm. This makes the water electrode act as a dielectric on nanosecond scale, a range in which breakdown occurs for DBD with solid electrodes. Therefore, the onset mechanism of dielectric barrier discharge over a water surface is expected to be similar to DBD discharge with a double dielectric barrier. This section gives a concise overview of known micro-discharge properties and mechanisms for the case of solid electrodes, which serves as reference material for micro-discharges in contact with a water electrode, as investigated in the rest of this chapter.

DBD discharge can exhibit filamentary behavior, regular self-organized patterns, or entirely diffuse appearance, even in air, depending on gas properties, electrical parameters, and boundary conditions. At atmospheric pressure, development of a filamentary micro-discharge can be subdivided into three stages [2, 3]:

1. During the pre-breakdown stage, negative charge is accumulated in front of the anode until the local electric field strength reaches a critical level. This stage lasts for at least 0.5 μs.
2. Next, an ionization wave propagates towards the cathode. This stage is called the propagation stage and lasts for 1 to 2 ns. As should be noted, cathode-directed positive streamers are characteristic for AC dielectric barrier discharge between solid planar electrodes, independently of voltage polarity during each sine half cycle [2]. Negative streamers, on the other hand, only occur for specific electrode configurations, such as the multipoint-to-plane geometry in [4].
3. After the discharge filament has bridged the electrode gap, a cathode layer is formed and a bright plasma channel is formed. As a result, charge is accumulated on the dielectric surface, compensating the external electric field. This stage is called the

decay stage, since it is characterized by the decay of light emission and current pulses.

While the development of a micro-discharge channel occurs in the nanosecond range, plasma chemical reactions by atoms and excited species typically starts within the microsecond scale. Production of such plasma species is determined by the reduced local electric field strength E/N and electron density n_e [3]. Hence, these plasma parameters are essential for understanding and optimizing the overall process.

For filamentary discharge at atmospheric pressure, the early breakdown stages are similar to those without dielectric barrier. Therefore, the concepts of streamer onset and propagation, as between metal electrodes, are helpful for a better insight. During streamer onset, an electron avalanche can produce substantial charge density after traveling a short distance, because of the high collision rates at atmospheric pressure. For a positive streamer, the propagation mechanisms are generally believed to be a combination of collisional ionization in the region at the streamer head and ultraviolet photoionization of the gas ahead of it. When the streamer is generated in air in strong uniform external fields, photoionization is essential only during the early stage of streamer formation. Collisional multiplication of the generated seed photoelectrons becomes, however, dominant in the later propagation stages [5]. In atmospheric air, the propagating ionizing region at the streamer head has a thickness of 200 μm [6]. In this region, the initial level of electron density of about 10^{12} cm^{-3} is rapidly increased up to the density in the streamer channel of the order of 10^{14} cm^{-3}, according to the modeling results in [5]. The reduced field E/N at the streamer head can reach 500 to 800 Td and its velocity ranges from 10^7 to 10^8 cm/s [7]. When it reaches the opposite electrode, the plasma channel connects both electrodes and becomes more intense. Both the radius of the streamer head and the width of the resulting plasma channel range from 0.1 to 1 mm [7]. At breakdown, electron density in the filament core remains around 10^{14} to 10^{15} cm^{-3} and the reduced electric field drops to a range from 100 to 200 Td [2, 3, 7]. From that moment on, electron generation at the cathode from photoemission processes is widely substituted with secondary electron emission via positive ion impact. In case of a cathode covered by a dielectric, one should keep in mind the difference between desorption of adsorbed electrons accumulated on the surface and emission of electrons from intrinsic surface levels of the dielectric. Adsorbed electrons have a low binding energy of about 1 eV and small surface density from 10^{10} to 10^{11} cm^{-2}, while intrinsic electrons have a high work function of several eV and large surface density exceeding 10^{16} cm^{-2} [8]. As a result of secondary electron emission, cathode layer formation is associated with a current pulse of about 0.1 A. For electronegative gases such as air and oxygen, shape and amplitude of the current pulse of a single micro-discharge are independent of the applied voltage waveform, as long as the voltage increase rate is slower than about 0.5 kV ns^{-1} [2]. As a result, the total charge transferred in one micro-discharge filament is from the order of 0.1 to 1 nC. Current density reaches a value of 10^6 to 10^7 A m^{-2}. While mean electron energy can reach 1 to 10 eV, gas

temperature of the micro-discharge remains low. Although the local gas temperature elevation inside the micro-discharge channel is theoretically expected to be negligible (ΔT = 5 to 10 K) [3, 7, 9, 10], experimental values up to 230 K are reported in literature. This temperature increase is found to be independent of input power, while it increases with voltage frequency [11]. However, as long as the mean gas temperature is kept low, this temperature rise is sufficiently small for various applications.

In parallel planar or coaxial electrode configuration, individual adjacent micro-discharges compete for the accessible surface area of the dielectric to deposit their charge. Residual charge from previous discharge stages influences the local electric field and accordingly determines the onset location of new micro-discharges. When the residual charge is deposited during the same half cycle of AC high voltage, the electric field is reduced and additional micro-discharges are initiated at new locations. On voltage reversal, the deposited charge enhances the field and new micro-discharges occur at the same location. Due to this memory effect, low-frequency high voltage spreads all micro-discharges over the accessible dielectric surface, while high-frequency low voltage reignites old micro-discharge channels every half cycle. The number density of micro-discharges increases with power density, but does not depend on the form of the applied voltage [7].

Multiple micro-discharges generated by means of AC power can occur simultaneously or at different moments in a voltage half cycle, depending on factors such as voltage amplitude, micro-discharge location and the memory effect caused by deposited charge [12-14]. Light emission of an individual micro-discharge filament as measured with a photomultiplier tube (PMT) is usually observed as a short and sharp peak [15-19]. In this case, light emission of the filament is more intense at the anode than at the cathode. However, a few exceptional cases were reported where the peak is followed by a long hump of several microseconds, as will be further discussed in section 7.5.

In [20, 21], a single DBD micro-discharge filament has been experimentally investigated with cross-correlation spectroscopy by means of a sphere-to-sphere electrode configuration in air atmosphere. In the asymmetric case where only one of the metal electrodes is covered by a dielectric glass barrier, the B(0-0) band at 391.5 nm of the 0-0 transition of the first negative system of N_2^+ has highest intensity at the instantaneous cathode, independent of the voltage polarity. The same is true for the case of a glass barrier on both electrodes. In contrast, the opposite has been observed for diffuse dielectric barrier discharge in pure N_2 between a plate-to-plate configuration [22]. For the sphere-to-sphere arrangement with a double glass barrier in air, following results were reported as well in [20, 21]. The C(0-0) band at 337.2 nm and the C(3-3) band at 328.5 nm of the second positive system of N_2 are brighter at both electrodes and dimmer halfway the electrode gap. Electric field and thus electron energy are highest at the cathode, while electron density is highest at the anode. Nonetheless, it is unclear how representative those results are for multiple micro-discharges in a plate-to-plate or coaxial electrode system.

In the last decades, a lot of research has been done on the plasma chemistry in DBD, either with simulations, with direct quantitative measurement of specific oxidative species including ozone and nitric oxides and with plasma diagnostical techniques such as optical emission spectroscopy (OES), laser-induced fluorescence (LIF) and cross-correlation spectroscopy (CCS). Kozlov et al. used a semi-empirical method to calculate the oxygen and ozone profiles in their sphere-to-sphere electrode system with double glass barrier [21]. According to their results, the concentrations of atomic oxygen and ozone in air are comparable at both electrodes, although slightly higher at the anode, and minimal in the middle of the discharge gap. This is in good agreement with the ozone profile measured in [23] for micro-discharges in a plate-to-plate configuration with double glass barrier. In contrast, the older simulation in [24] predicted a maximal atomic oxygen concentration in the middle of the gap. In an $Ar/O_2/H_2O$ gas mixture, OH radicals are detected with LIF only within the transient micro-discharge channels [25]. Yet, the time-averaged OH distribution is uniform over the whole discharge gap due to the relocation of successive micro-discharges [26].

The effect of air humidity in the case of solid electrodes can provide a better understanding of the processes in the case where water acts as one of the electrodes. Humidity has a strong influence on the physics and chemistry of DBD micro-discharges. First of all, it is well-known that breakdown voltage in air increases with water vapor content. Although this effect is often ascribed to electron scavenging due to the electronegative nature of water vapor, it has been shown in [27] that electron detachment and ion conversion processes need to be taken into account as well. While the critical electric field for breakdown is unchanged with addition of water vapor, the influence of the humidity is caused by the formation of nondetaching cluster ions by collisions of negative ions with H_2O molecules. For instance, H_2O clusters with O_2^- through the cascade reactions [28]:

$$O_2^- + H_2O + M \leftrightarrow O_2^-(H_2O) + M \tag{7.2}$$

$$O_2^-(H_2O) + H_2O + M \leftrightarrow O_2^-(H_2O)_2 + M \tag{7.3}$$

$$O_2^-(H_2O)_2 + H_2O + M \leftrightarrow O_2^-(H_2O)_3 + M \tag{7.4}$$

with M = N_2 or O_2 and where the energy required for electron detachment increases with cluster size. In atmospheric air, $O_2^-(H_2O)_3$ is the most probable cluster from the three reactions (see [28] for corresponding direct and reverse reaction rates). Larger clusters, on the other hand, are improbable. This clustering behavior of water is caused by the dipolar nature of H_2O molecules. It occurs for both positive and negatively charged ions, but is more pronounced for the negative ones [29].

It has to be noted, however, that when water droplets are dispersed in air, the breakdown voltage is reduced due to an enhanced electric field in the close vicinity of the droplets [30]. Next to that, water has the ability to be adsorbed on the dielectric surface of a DBD, reducing

the surface resistance and increasing the effective dielectric capacity [31]. This way, surface charge decay rate is enhanced and the local electric field is reduced. Each micro-discharge filament will therefore require more charge than in the absence of water [32]. As a result, the presence of water will cause more intense, but fewer micro-discharges [32-34]. This effect is considered to be more dominant than the electron scavenging in terms of radical production [32, 33]. Ozone concentration falls and OH concentration rises with increasing H_2O content [35, 36]. Similarly, N_2 has an inhibitory effect on O_3 generation, while it enhances OH production. Accordingly, O_3 is the main reactive species in pure oxygen. For saturated humid air, on the other hand, OH concentration was found to be 12 times higher than O_3 concentration. In dry and humid air, gaseous H_2O_2 was undetectable, while in humid oxygen atmosphere, its concentration increased with increasing humidity. Dissolution of plasma-generated nitric oxides leads to the formation of NO_3^- in the solution, with a corresponding drop in pH. The NO_3^- formation rate decreases with increasing humidity [36].

For a more extensive literature overview and discussion on the different dielectric barrier discharge types, their properties and applications, the reader is referred to the reviews of Xu [10], Kogelschatz [7] and Wagner et al. [3].

7.2 Experimental arrangement and diagnostic methods

In order to produce a stable DBD micro-discharge filament with fixed location, a sphere-to-sphere electrode geometry was used in our study. An additional advantage of such geometry is the possibility to observe not only the filamentary discharge channel, but the surface discharges as well. The setup and its dimensions are shown in Figure 7.1. The upper electrode consists of a 0.75 mm thick sharpened high voltage pin electrode in a quartz tube. The downside of the tube is closed and has a spherical shape with a 1.2 mm radius, which acts as dielectric barrier. It is positioned over a grounded spherical metal mesh. Deionized water is slowly pumped upwards through the mesh, covering the electrode with a thin water layer. Interelectrode distance is kept on 1.0 mm, unless mentioned otherwise. The micro-discharge filament is generated in surrounding air atmosphere by applying an AC high voltage with amplitude of 7.5 kV, 8.5 kV or 9.5 kV and frequency of 36.9 kHz on the upper pin electrode by means of a custom-made power source. Voltage waveforms are measured with a Tektronix P6015 HV probe and current waveforms with a Pearson model 2877 current probe. Both probes are connected to a Tektronix S1200 oscilloscope. Output signals of the ICCD camera and the PMT are monitored with the same oscilloscope. Optical emission spectra are obtained by means of an Ocean Optics spectrometer S1000 in the range of 250 nm to 900 nm with instrumental full-width at half maximum of 1.3 nm. For higher resolution in the range of 300.0 nm to 355.0 nm, spectra are measured with an Avantes spectrometer (AvaSpec-3048) with instrumental full-width at half maximum of 0.05 nm. ICCD imaging is performed with a Hamamatsu ICCD camera (model C8484) connected to a delay generator, for which the voltage waveform was used as trigger signal. To investigate the space-resolved evolution of light emission of the excited OH(A) states, a filter with central wavelength of

309 nm and bandwidth of 10 nm is fixed in front of the camera. The ICCD images are averaged over 100 accumulations without filter and over 325 accumulations with OH filter. Afterwards, they are processed by means of the program ImageJ for a clearer presentation of the discharge light emission. For this purpose, brightness and contrast are adjusted and the Lookup Tables *Magenta Hot* and *royal* are used respectively for unfiltered images and images with OH filter. Space-averaged time-resolved light emission at specific wavelengths of the OH(A) band and two N_2 (C-B) bands is obtained by means of a photomultiplier tube (PMT) with decay/response time of 50 ns connected to a monochromator. Bandwidth of the monochromator is determined with a low pressure Hg spectral calibration lamp to be 1.5 nm.

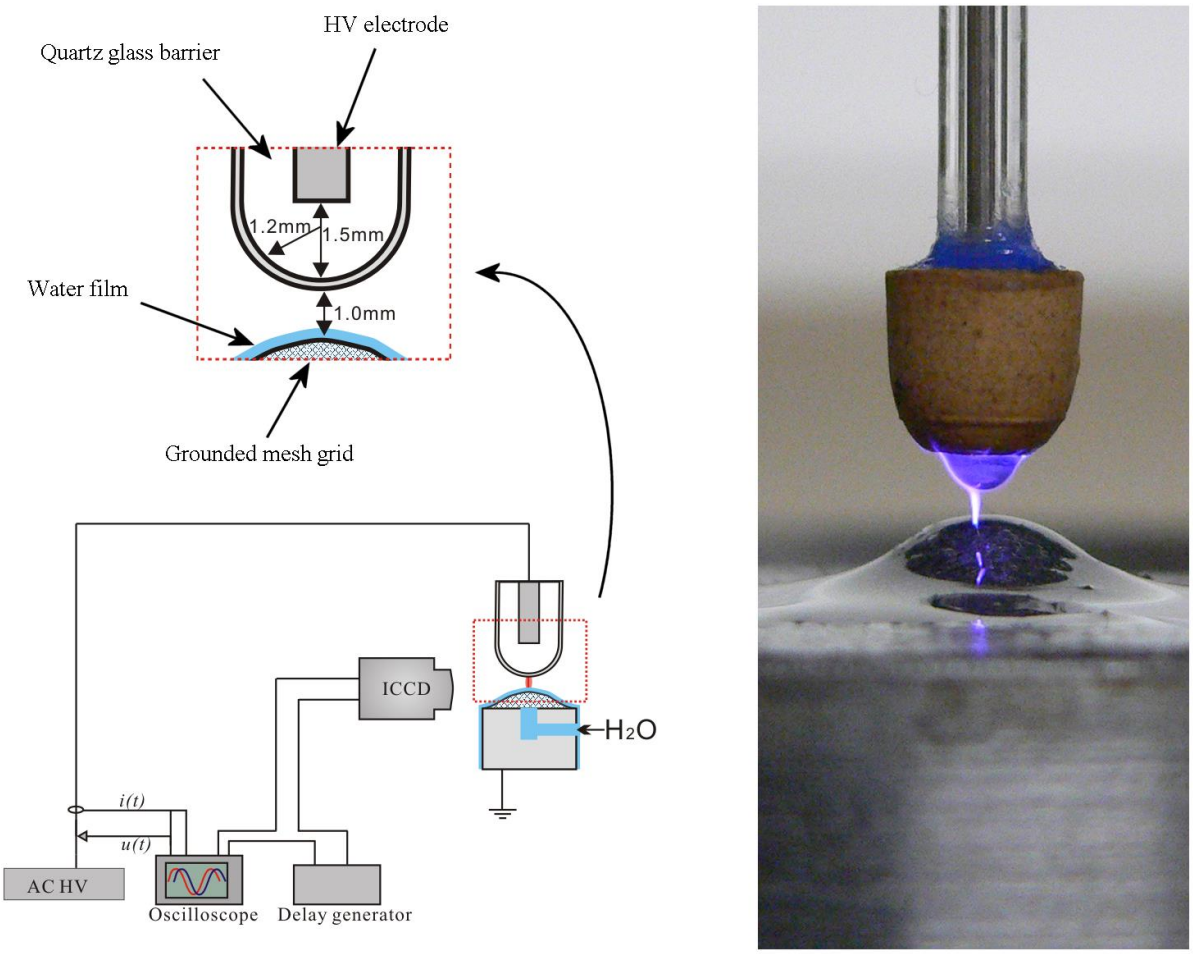

Figure 7.1 (left) Reactor schematic with dimensions. The ICCD camera also indicates the position of the optical fiber leading towards the PMT. (right) Photo of the electrode system with discharge.

7.3 Spectra fitting

The normalized emission spectrum of the discharge, shown in Figure 7.2a, is found to be independent of input voltage. The global spectrum is dominated by vibrational bands of the N_2 second positive band system $C\ ^3\Pi_u(v') \rightarrow B\ ^3\Pi_g(v'')$. The high-resolution spectra obtained

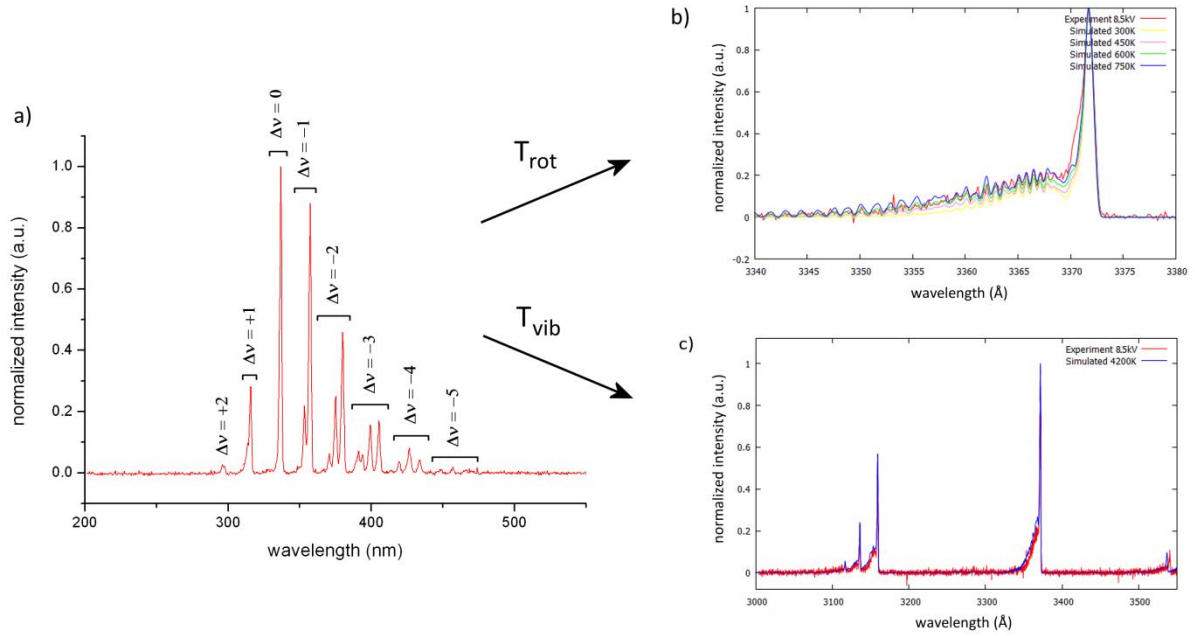

Figure 7.2 a) Normalized space and time averaged emission spectrum of the micro-discharge for 8.5 kV measured with resolution of 1.3 nm, where Δν represents the change in quantum number ν of each radiative transition in the N_2(C-B) band system. b) Determination of rotational temperature T_{rot} by means of slope fitting of the experimental N_2 (C-B) band at 338.0 nm for T_{vib} = 1000 K. c) Determination of vibrational temperature T_{vib} by means fitting the peak size of the experimental N_2 (C-B) bands at 315 nm and 338 nm for T_{rot} = 750 K.

with the Avantes spectrometer are processed with the custom-made synthesis software for N_2 (C-B) transition spectra simulation in order to obtain rotational and vibrational temperature of the filament. Rotational temperature T_{rot} can be considered to be equal to the gas temperature inside the micro-discharge channel. It is found by fitting the experimental slope of the N_2 (C-B) band at 338.0 nm to the simulated one at constant value of vibrational temperature T_{vib} = 1000 K. As can be seen from Fig. 7.2b, the best fitting for 8.5 kV is obtained for a value of T_{rot} = 750 ± 150 K. This is in good agreement with the values of 650 K to 850 K obtained in [11] for filamentary DBD discharge in a 1 mm electrode gap in air. However, these values were measured for a higher frequency of 60 kHz and the same authors found T_{rot} to be dependent on frequency. Dong et al. determined rotational temperatures in air atmosphere ranging from 520 to 680 K for an electrode gap from 0.1 to 0.3 mm and voltage amplitude from 4.8 to 6.2 kV at an AC frequency of 40 kHz [13]. In contrast, a value near room temperature was found for a 0.3 mm gap micro-discharge in atmospheric air between cylindrical electrodes with a nanoporous alumina dielectric, driven by 20 kHz AC power at low voltage around 1.7 kV [37]. The reason for this low temperature is the formation of glow plasma instead of filamentary discharge. In [38], T_{rot} is obtained for a pulsed DBD source with interchangeable opposite electrode. When a grounded aluminum plate is used as opposite electrode at 1 mm distance, T_{rot} = 400 ± 20 K. On the other hand, T_{rot} = 320 K for

phosphate-buffered saline solution or glass as opposite electrode. The significantly lower temperature of this discharge is probably due to its pulsed nature and low duty cycle.

T_{vib} is determined by fitting the amplitude of the N_2 bands for the resulting value of T_{rot} = 750 K. As shown in Fig. 7.2c, the best fit is given for T_{vib} = 4200 ± 500 K. This is significantly higher than values found in literature from 2600 to 2800 K for 0.1 to 0.3 mm short filaments between glass tube electrodes filled with tap water [13]. As should be noted, the values of T_{rot} and T_{vib} in our experiments are independent of the applied voltage amplitude in the used range of 7.6 to 9.5 kV, taking into account the accuracy of the measurements and fitting procedures.

Table 7.1 Rotational and vibrational temperature T_{rot} and T_{vib}, reduced electric field E/N in the middle of the electrode gap, current pulse size ΔI, mean channel diameter D and current density j of the micro-discharge filament during the brightest stage for different values of voltage amplitude V.

V (kV)	T_{rot} (K)	T_{vib} (K)	E/n (Td)	ΔI (mA)	D (µm)	j (10^6 A m^{-2})
7.5			128 ± 3		156 ± 10	3.1 ± 0.4
8.5	750 ± 150	4200 ± 500	144 ± 3	60 ± 2	173 ± 11	2.6 ± 0.3
9.5			164 ± 3		190 ± 12	2.1 ± 0.3

7.4 Simulation results

Electric field E and charge density in a vertical plane of symmetry through the electrode system are calculated with the simulation software Comsol Multiphysics. The electrode configuration is simulated by simplifying the grounded mesh electrode with water layer as a flat solid metal. This is supposed to give a limited error in the results, due to the small dimensions of the water layer and due to the large curvature of the mesh electrode in comparison to the micro-discharge radius and the dielectric barrier's curvature. The metal parts of the electrode system are simulated with the standard material *Armco Iron* from the material library of Comsol. Simulation results of the spatial distribution of electric field and charge density for 8.5 kV input voltage are shown in Fig. 7.3a-b. In order to study the electric field E on the symmetry axis in the electrode gap, a vertical cutline is applied in the simulation. Fig. 7.3c shows the resulting graph of E along the filament core as a function of distance to the grounded mesh electrode. Reduced electric field E/N is calculated using the air density $N = 2.5 \times 10^{25}$ m^{-3} at standard conditions. E/N increases from 132 Td at the mesh electrode to 208 Td at the dielectric barrier, in good agreement with the values during breakdown mentioned in section 7.1 (100 Td to 200 Td). For the pulsed DBD source with interchangeable opposite electrode described in section 7.3, higher values ranging from 300 to 380 Td are found [38]. This higher range is probably due to the higher voltage amplitude of 12 kV. For further calculations, the value of E/N in the middle of the electrode gap is used. The error on this value is deduced from the experimental error of 2% on the voltage

amplitude, by entering the voltage values ±2% as input of the simulation with Comsol. The results for different voltage amplitudes are presented in Table 7.1.

Electron energy distribution function (EEDF) and electron mobility μ_e are determined by means of the BOLSIG+ electron Boltzmann equation solver. Required input parameters are the above values of T_{rot} and E/N as well as the gas composition. For the gas composition, two situations are distinguished: dry air (75% N_2 and 25% O_2) and 100% water vapor. The results are given in Figure 7.3d and Table 7.2. The error on the electron mobility is calculated by taking into account the error on E/N and using the corresponding values ± error as input in BOLSIG+.

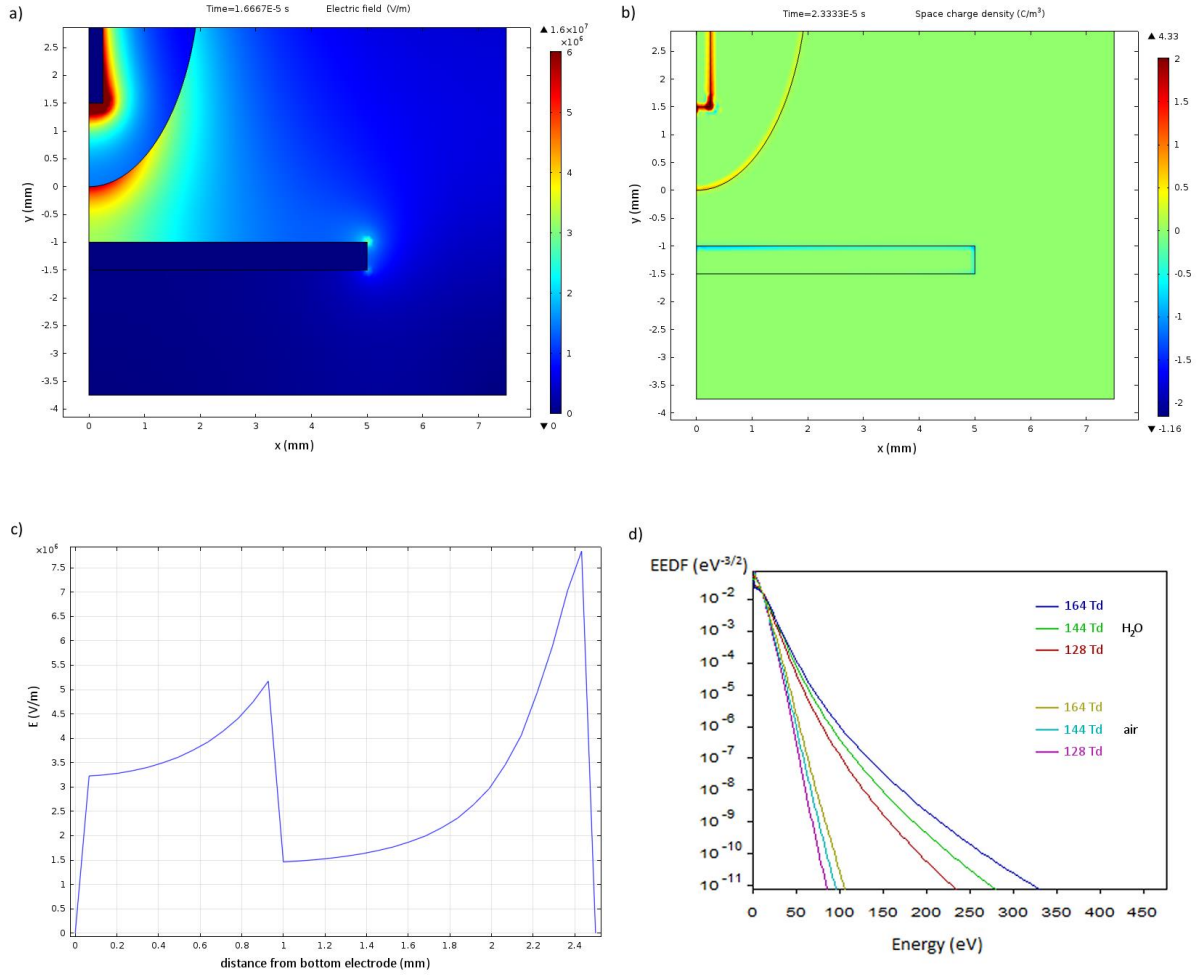

Figure 7.3 Simulation results from COMSOL and BOLSIG+. a) Electric field distribution in the electrode gap. b) Spatial distribution of charge density. c) Electric field along the symmetrical axis of the electrode system. d) Electron energy distribution function determined with BOLSIG+ for pure H_2O gas and dry air for different electric field values, corresponding to the field in the middle of the gap for the considered voltages of 7.5 kV, 8.5 kV and 9.5 kV.

Table 7.2 Product of electron mobility μ_e and air density n, and electron density of the micro-discharge filament for different values of voltage amplitude V in dry air or pure water vapor.

V (kV)	gas	$\mu_e \times n$ (10^{23} $V^{-1}m^{-1}s^{-1}$)	n_e (10^{14} cm^{-3})
7.5	air	9.051 ± 0.005	1.68 ± 0.22
8.5		8.763 ± 0.006	1.26 ± 0.17
9.5		8.504 ± 0.005	0.95 ± 0.13
7.5	H_2O	12.260 ± 0.002	1.24 ± 0.16
8.5		12.200 ± 0.001	0.91 ± 0.12
9.5		12.180 ± 0.001	0.66 ± 0.09

7.5 Temporal discharge properties

Figure 7.4 shows the temporal behavior of the discharge. As could be expected for a capacitive system, the current waveform leads the voltage waveform by 90°. Without plasma discharge, fast oscillations occur on the current waveform due to electromagnetic noise from the power source. When there is plasma, an extra current peak is formed in the most intense plasma stage during the negative half cycle of the voltage. Three bright discharge stages are observed during every voltage cycle, mostly followed by a dark stage. ICCD images and measured PMT signal at 309.0 nm and 357.4 nm for a voltage of 8.5 kV are shown in Figure 7.4. The PMT signal for the N_2 (C-B) band at 336.9 nm is identical to the signal for the N_2 (C-B) band at 357.4 nm and therefore it is not included in the figure. Discharge evolution can be described as follows.

a) During the negative half cycle, only one short bright stage of 1.0 μs is seen at the moment of the current pulse, i.e. when the negative voltage reaches a threshold value of a few kilovolt in absolute value. This stage has similar characteristics to micro-discharge between 2 solid electrodes, as described in section 7.1. After the formation of a conductive channel between the electrodes (t = 2.7 μs in Figure 7.5), breakdown occurs and positive charge is deposited on the dielectric surface. During this process, the plasma appears stationary on the timescale of 0.5 μs. This is the only stage where the PMT signal shows emission from the OH(A) band at 309.0 nm. ICCD images with the filter with central wavelength of 309 nm clearly indicate that OH(A) states are mostly localized in the discharge channel, while dim emission can be seen at the dielectric surface (Figure 7.5).
b) At a voltage of -0.7 kV right before the positive half cycle (see dashed lines in Figure 7.4), a short bright stage occurs with duration of 1.3 μs, which is associated with the formation of a bright plasma channel (t = 13.7 μs in Figure 7.6). For voltage amplitude lower than 8.5 kV, it is immediately followed by a long bright stage. For voltage amplitude from 8.5 kV, a short dark stage takes place in between the short and long bright stage, as seen in Figures 7.4 and 7.6. The long stage manifests itself as a hump with duration of 7.0 μs in the PMT signal for the N_2(C-B) wavelengths, very similar to

the photocurrent humps reported in [39] and [40]. In the ICCD images during the hump, a glow-like discharge wave is seen, which starts at the upper end of the discharge channel and moves upwards along the dielectric surface. At the same time, a cathode spot at the water surface becomes more intense. OH(A) emission is strongly localized in the cathode spot at the water surface.

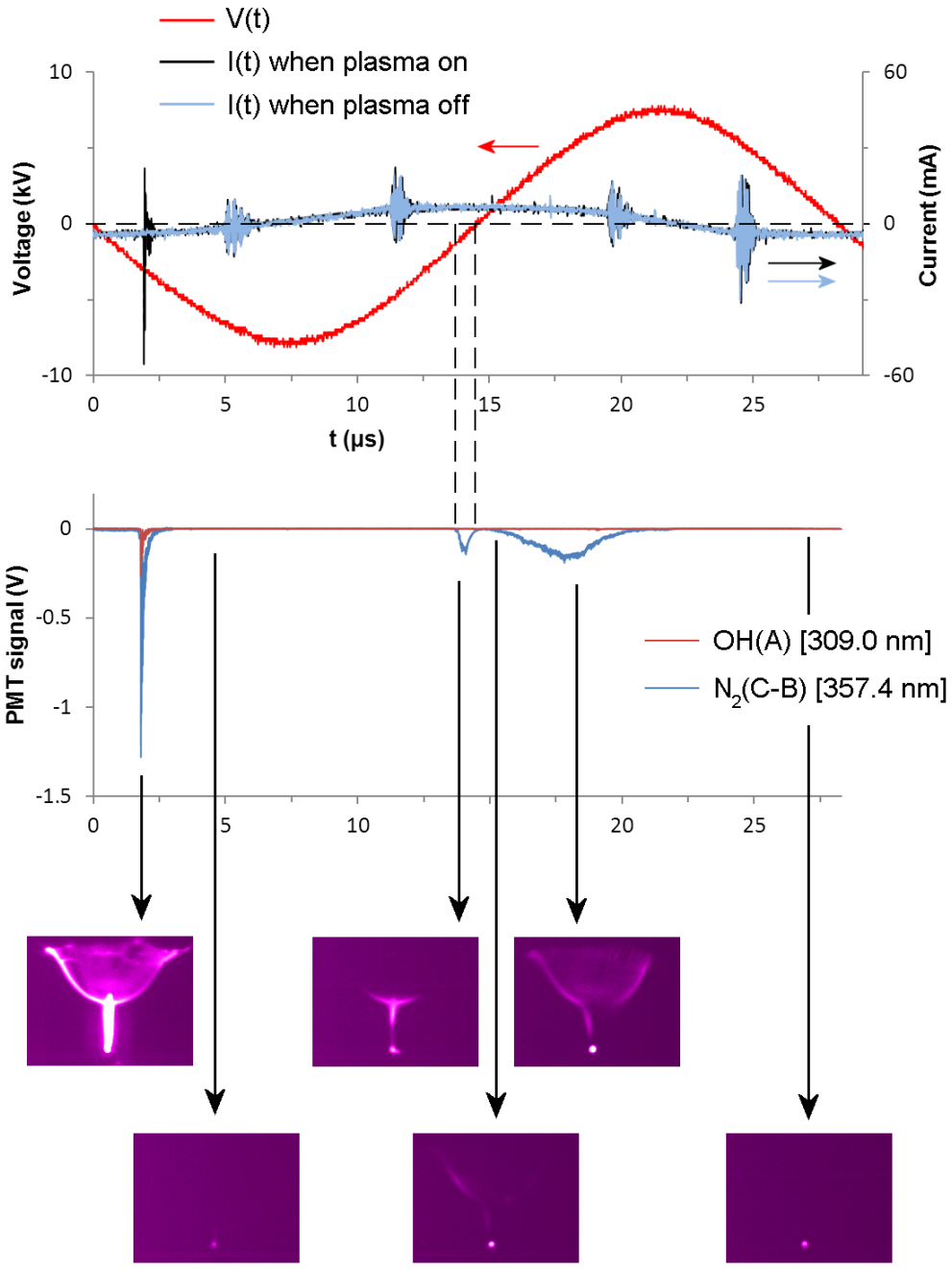

Figure 7.4 Overview of the micro-discharge evolution for voltage amplitude of 8.5 kV, measured by means of voltage and current waveforms (up), by means of PMT signal at wavelengths 309.0 nm and 357.4 nm and by means of ICCD imaging with 1.0 µs exposure time (down). Three bright stages and three dark stages are observed.

Remarkably, glow-like light emission is observed on every moment during each dark stage at the location where the micro-discharge channel hits the water surface during breakdown. This indicates that plasma discharge remains present at all times at the water electrode, although no micro-discharge channel is visible during the dark stages. Within the accuracy of our measurements, OH(A) emission on this location is only observed during the bright stages.

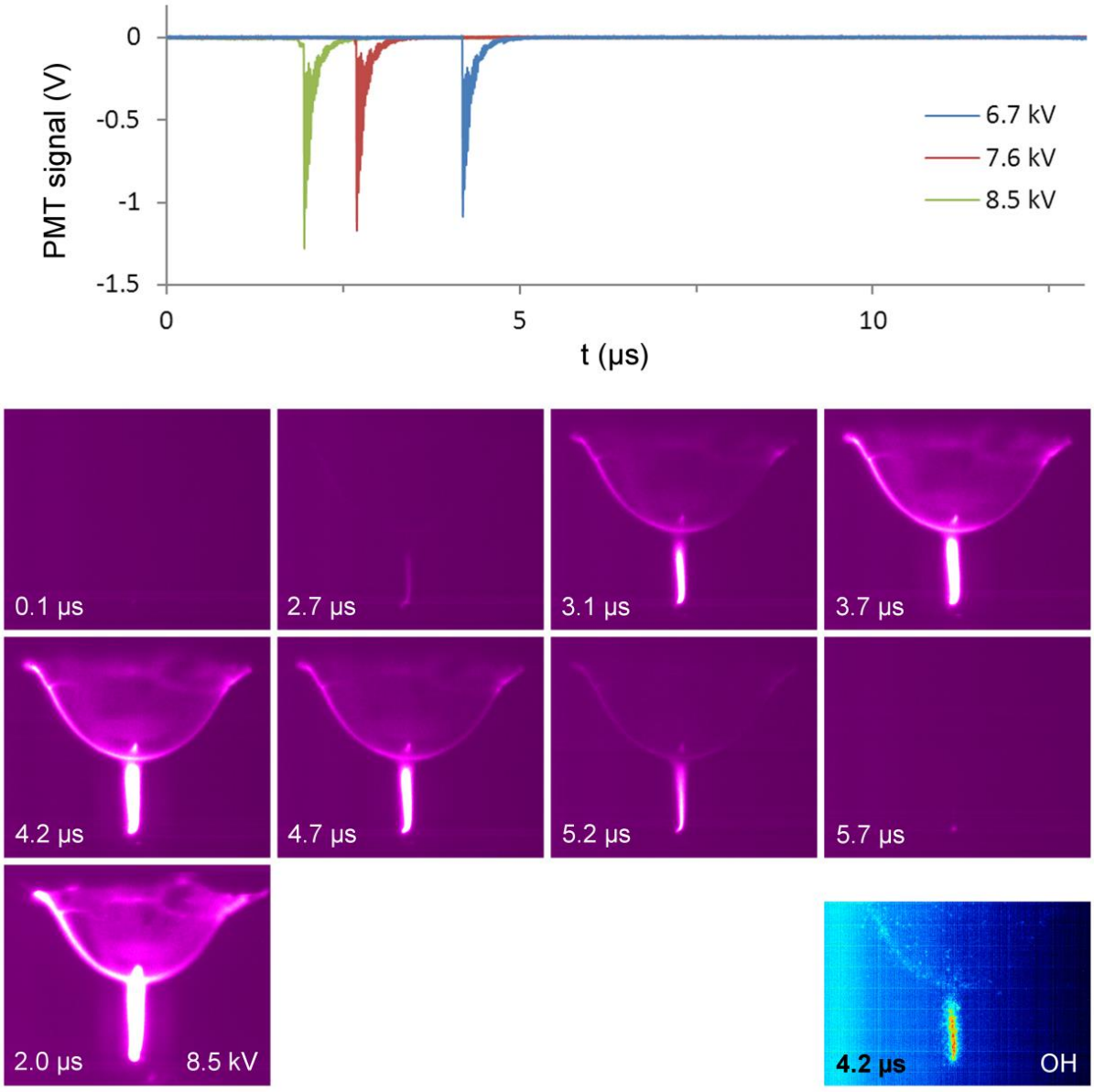

Figure 7.5 Evolution of plasma light emission during the negative voltage half cycle. (top) PMT output signal at a wavelength of 357.4 nm for different voltage. (bottom) Processed averaged ICCD images with 1.0 µs exposure time starting at the time indicated in the picture. Voltage amplitude for all images is 6.7 kV, unless indicated in the picture. The snapshot for 8.5 kV is to be compared with the one at 4.2 µs for 6.7 kV. The image with OH filter is found in the bottom right corner. The start of the negative half cycle is chosen as $t = 0$ µs.

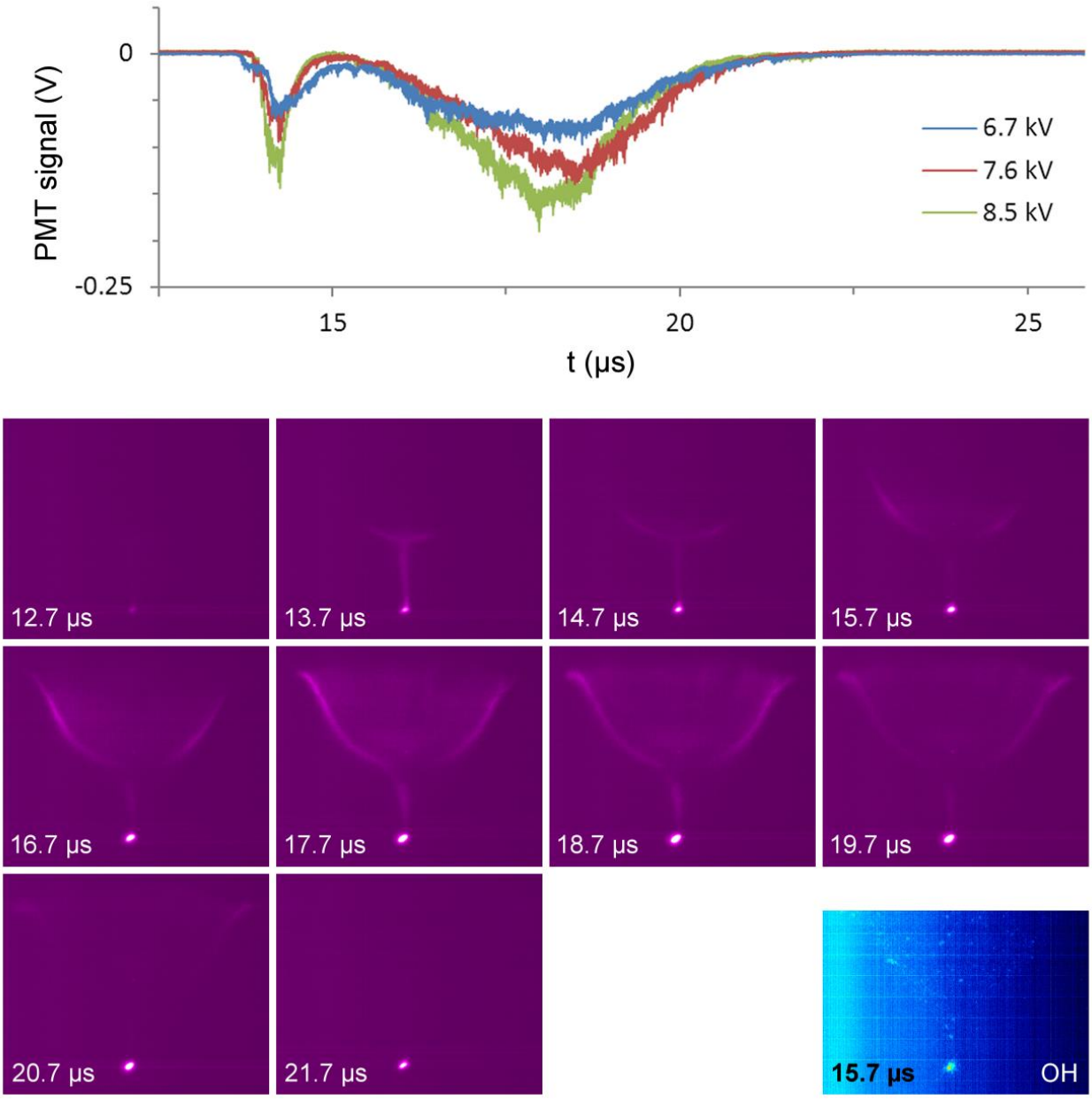

Figure 7.6 Evolution of plasma light emission during the positive voltage half cycle. (top) PMT output signal at a wavelength of 357.4 nm for different voltage. (bottom) Processed averaged ICCD images for a voltage amplitude of 6.7 kV starting at the time indicated in the picture. Exposure time for all images is 1.0 µs, unless for the image with OH filter, where it is 5.0 µs. The start of the negative half cycle is chosen as $t = 0$ µs.

When amplitude of applied voltage is increased, the bright stages become more intense, while their duration is unaffected. With amplitude increase from 6.7 kV to 8.5 kV, the onset voltage of the most intense stage during the negative voltage half cycle decreases from -4.3 kV to -2.7 kV, respectively. This change in breakdown voltage is caused by the higher amount of negative charge deposited on the dielectric during the positive half cycle, enhancing the electric field. In contrast, voltage amplitude has no significant effect on the

onset voltage of -0.7 kV of the short bright stage right before the positive half cycle (see dashed lines in Figure 7.4). This is a remarkable result, as the low negative voltage at breakdown implies that the critical electric field for breakdown is achieved by positive charge on the dielectric alone, which is deposited during the previous bright stage. This phenomenon is similar to the secondary breakdown during the voltage drop in DBD with square pulses. Nevertheless, it has, to our knowledge, not been reported and discussed before in literature for the case of AC powered DBD. Possibly, this is a phenomenon characteristic for DBD with a water electrode, where special conditions are met such as the continuous plasma discharge at the water surface.

7.6 Proposed mechanisms of glow discharge

In this section, different explanations are given for the glow-like discharge wave associated with the photocurrent hump during the positive voltage half cycle, as well as for the constant glow-like plasma at the water surface. Both phenomena are very interesting from the perspective of applications, since they indicate the continuous generation of reactive species in direct contact with the liquid. Therefore, it is useful to acquire a deeper understanding of the fundamental mechanisms behind them. Several properties of a water electrode can be responsible for the sustained generation of plasma species at the water interface, even with external electric fields that are too low for breakdown in atmospheric air:

1. Local electric field enhancement by water surface deformation;
2. Local electric field enhancement by micro- or nanosized droplets at the water interface;
3. Transfer of aqueous ions to the gas phase by ambient desorption ionization.

These three mechanisms can be important for both phenomena: the constant glow at the water and the glow-like discharge wave associated with the photocurrent hump. Since the latter only occurs during the positive voltage half cycle, when water acts as a cathode, two additional mechanisms are postulated:

4. Stabilization of the cathode fall region by increased local humidity;
5. Stabilization of the cathode fall region by effective secondary electron emission from the water cathode.

Each mechanism is explained in detail in the following subsections. Note that every one of them appeals to specific features of the water electrode. As a main argument, both discharge phenomena are most likely caused by the unique nature of a liquid electrode, since they have not been observed – or very rarely – in DBD with solid electrodes. They cannot be explained with the electrode geometry, because the electric field is higher at the dielectric barrier than at the water surface according to the COMSOL simulation results (see section 7.4).

Kozlov et al. reported a continuous glow on the solid dielectric surfaces of both electrodes in their reactor during the pre-breakdown stage for more than 500 ns. Nevertheless, this glow discharge was 5 orders of magnitude lower in intensity than the micro-discharge channel [21]. In contrast, the glow discharge in our experiments is only observed at the water electrode and has a similar intensity as the channel. To our knowledge, intensive continuous glow discharge localized at one electrode of a dielectric barrier discharge in air has never been reported in scientific literature for the case of solid electrodes. A photocurrent hump during only one voltage half cycle, on the other hand, has been observed by Miralaï et al. and by Li et al. in unusual DBD configurations with solid electrodes [39, 40]. In section 7.6.6 will be explained that this type of discharge is characteristic for resistive barrier discharge, which also occurs in our reactor due to the resistive character of the water cathode.

7.6.1 Local electric field enhancement by water surface deformation

Surface deformation of a water electrode can result from a combination of local disturbances, such as strong attraction of the local electric field, the impact of accelerated plasma species and the elevated gas temperature during breakdown to several hundreds of degrees above water's boiling point. Such deformations do not only allow a decrease in interelectrode distance, they can also significantly enhance the local electric field by formation of sharp electrode points with small radius of curvature. For example, Lu and Laroussi observed the formation of ripples on a water cathode under influence of a glow-like discharge due to the high voltage drop over the cathode fall region [41]. They suggested that the ripples offer sharp curvature points with high electric fields, which can initiate several discharges. Interestingly, ripples did not occur when water acted as anode. However, the formation of these ripples is relatively slow, as it was observed at larger timescales (100 μs and higher). In our experiments, on the other hand, the stable glow discharge in the course of 1 to 10 μs can only be explained with surface deformation if this deformation has a relatively static nature and can be reproduced in every voltage cycle. This could be the case for a static Taylor cone. The typical timescales for Taylor cone formation on a mercury surface is 0.85 μs according to the model of Suvorov [42]. Experimental investigation of Taylor cone formation on a water drop and on water surfaces shows that the instability develops on a timescale of typically 1 to 10 μs [43, 44]. The exact characteristic formation time is suggested to depend on electric stress, initial surface shape, and liquid properties such as surface tension, viscosity, density and conductivity [45]. Further investigation is required to determine whether Taylor cone formation plays an important role in our setup and DBD discharge with water electrode in general, since it was not observed within the accuracy of our measurements. As an additional advantage of a liquid electrode, a sharp surface deformation can maintain its curvature and surface properties over long periods in time, in contrast to solid electrodes that can be eroded and oxidized. This can also explain why a similar glow-like regime is not observed in DBD with solid electrodes.

7.6.2 Local electric field enhancement by micro- or nanosized droplets

Similarly to electrode surface deformation, micro- or nanosized droplets can be created at the water interface under influence of an external electric field and plasma processes. Since the local electric field is significantly enhanced at a droplet interface, a lower external field is required for ionization of the surrounding gas and acceleration of charged species up to dissociative energy levels. Such plasma-induced droplet formation is in agreement with some observations on electrolyte cathode atmospheric glow discharge, which is mostly investigated as a promising technique for monitoring toxic heavy metal content of water. In this technique, glow discharge is generated between a metal anode and an electrolyte cathode and its optical emission spectrum is investigated for spectral lines of dissolved metals. The appearance of emitted metal lines is attributed by many authors to sputtering of the water cathode as a dominant process. Cserfalvi, Mezei and co-workers have proposed a model where metal vapor is introduced into the gas phase as a consequence of water bombardment by positive gas ions and metastable atoms coming from the cathode dark space and the negative glow [46, 47]. Yagov et al., on the other hand, proposed an electrothermal sputtering model where the introduction of small aerosol particles into the plasma is the limiting step in the analytical signal. Their model is based on the observation that the analytical signal is enhanced with increasing temperature and decreasing flow rate of the solution, which both improve thermal sputtering [48]. Nevertheless, these models have been disputed by other authors, such as Marcus and Davis who cited volatilization of the analyte species due to Joule heating caused by current flow across the liquid–plasma interface as the key mechanism [49, 50]. Either way, sputtering of a water anode has never been suggested in literature and is expected to be less likely, as the electric field of a glow discharge near the anode is significantly lower than at the cathode. The electronegative nature of water vapor and thus the relatively high concentration of negative ions in the discharge gap renders, however, anode sputtering possible, especially for small interelectrode distance, as in our experiments. This can also explain why the continuous glow discharge in our measurements is dimmer during the long dark stages when water is acting as anode in comparison to the bright stages and short dark stage of the positive half cycle, when water is the cathode.

7.6.3 Ambient desorption ionization

Local enhancement of the electric field at the water surface during the dark stages can lead to so-called ambient desorption ionization, where ions are transferred from the liquid to the gas phase by means of highly charged droplet ejection. To understand the underlying mechanism, insights can be taken from recent fundamental research on electrospray ionization, as in [51]. Here, intermediate droplets are dispersed into the gas phase as an aerosol under influence of Coulomb repulsion. Subsequently, they decrease in size through a combination of evaporation and fission processes. The final production of gas-phase ions has

been explained with several competing models. In the charge residue model, a droplet decreases in size through evaporation until it reaches its Rayleigh limit, where it undergoes Coulomb fission. After the droplet has diverged into smaller droplets, the cycle continues until a charged solute residue is formed. In the ion evaporation model, on the other hand, direct desorption of solvated ions from the droplet is assumed when the field strength at the droplet surface reaches a threshold value for ion field evaporation. From theory and experiment, this value is calculated to be about 1 V/nm, which is 3 orders of magnitude higher than the field strength at the water interface according to our COMSOL simulation. Such high field strength is therefore expected only at the surface of droplets with a diameter smaller than 10 nm [51]. Electric field induced ion evaporation has been demonstrated for dielectric liquids in [52]. As molecular dynamics simulations have shown, ion field evaporation is also strongly dependent on temperature, in the range of 350 to 800 K [53]. A growing body of evidence suggests that ion field evaporation is mostly applicable for small ions, as in our experiments, while larger ions are more likely formed according to the charge residue model.

7.6.4 Cathode stabilization by increased local humidity

Under influence of the elevated temperature at the micro-discharge core during breakdown stages and of the continuous glow during dark stages, evaporation increases the local water vapor concentration at the water interface. Minor concentration variations or density fluctuations can lead to significant differences in plasma processes. In particular, humidity can strongly influence the formation of a cathode fall region, which is the most important criterion for glow discharge. If we assume that the glow-like discharge wave during the photocurrent hump can be modeled as a normal glow discharge, positive ions generated at the instantaneous anode travel towards the instantaneous cathode and collide with the cathode to produce secondary electrons. With the arrival of the ions, the net electric field is influenced by these space charges and most of the voltage is located over the cathode fall region, i.e. the gap between the cathode and the space charge layer. In the cathode fall region, ions can gain sufficient kinetic energy through acceleration to produce secondary electrons, while electrons can cause an electron avalanche even at relatively low applied voltage. In this way, the voltage required to maintain the discharge is lowered significantly. Consequently, the glow discharge's life time is prolonged until the voltage over the cathode fall region drops under a critical value. This manifests itself in the occurrence of the light hump. The higher the ion density at the cathode is, the easier the cathode fall region is to form. When the dielectric barrier acts as cathode, accumulation of wall charges can prevent the formation of a cathode fall region, with fast quenching of the discharge. At a water cathode, however, such charge accumulation is not expected.

In a normal glow discharge, the cathode fall length d can be expressed as [54]

$$d = \frac{1}{\alpha} \ln\left(1 + \frac{1}{\gamma}\right) \tag{7.5}$$

where α represents the first Townsend coefficient and γ is the secondary emission coefficient. A higher value of α leads to a smaller cathode fall region, which is beneficial for the stability of the glow discharge. For air ionization, α increases with relative humidity, as explained in more detail in [55]. Since the local relative humidity is higher at the water surface than at the dielectric barrier, so is α. Accordingly, cathode fall region formation is favored at the water electrode in our experiments due to the inhomogeneous humidity profile.

7.6.5 Cathode stabilization by effective secondary electron emission from the water cathode

Despite the above mentioned mechanisms, the low breakdown voltage at the start of the positive half cycle is most likely due to energy efficient secondary electron emission at the water cathode. Although the breakdown occurs at a slightly negative voltage of -0.7 kV, the water electrode acts as a cathode because of the positive surface charge deposited on the dielectric during the negative half cycle. In case of a water cathode, secondary electron emission occurs through an essentially different mechanism than in the case of solid electrodes. While direct photon induced electron emission from water requires 6.1 eV, only 1.56 eV of energy is spent per released electron through a chemical tunneling effect [47]. When positive ions are accelerated by the electric field in the cathode dark space and bombard the solution cathode, they collide with H_2O molecules at the liquid interface. Those energetic collisions produce solvated electrons and H_2O^+ near the surface. Next, the aqueous electrons react very quickly with H_3O^+ ions, producing H atoms that diffuse through the liquid interface towards the gas phase. In the cathode dark space, the H atoms are ionized, resulting in secondary free electrons. The formed H^+ ion hydrates back into the water, closing the cycle. The quartz barrier has a work function around 5 eV [56, 57], which requires a significantly higher voltage for breakdown. As a side-note, desorption of accumulated electrons on the dielectric surface takes less energy, around 1 eV, but this process is probably too limited before the moment of breakdown due to the lack of initiating mechanisms such as interactions with vibrationally excited N_2 and thermodesorption [8]. Because of the low surface density of adsorbed electrons, such desorption processes are more likely during the following bright microdischarge stage, when excited N_2 density and local temperature of the dielectric increase.

From Formula 7.5, it can easily be seen that a higher value of γ leads to a shorter cathode fall region, which is beneficial for the stability of the glow discharge. The value of γ depends on the cathode material. In [58], γ is estimated to be 0.01 for a quartz glass dielectric barrier, based on theory and simulation results. For a water cathode, on the other hand, γ depends on pH. According to the chemical tunneling model of Cserfalvi and Mezei, γ decreases from 0.18 at pH = 0.3 and 0.07 at pH = 1.71 to a constant value $\gamma = 0.02$ for pH = 2.5 or higher [47, 59]. In our system, the local pH at the glow discharge can be very low, as DBD plasma

discharge in air is known to decrease overall solution acidity to values below pH = 3, but an exact value for γ is unknown. In any case, these calculations suggest a shorter and more stable cathode fall region at a water cathode than at the dielectric barrier.

7.6.6 Resistive nature of the water electrode

Although the chemical tunneling process at the water cathode (section 7.6.5) is energetically more efficient than the photon or field induced alternative, it is obviously slower and depends on solution pH. Additionally, the mobility of aqueous ions limits the rate at which the corresponding loss of negative charge at the water cathode is compensated. As a result, the water cathode is expected to act as a resistive layer for time scales larger than the Maxwellian relaxation time of the solution, as given by Formula 7.1. This leads to the observed 7.0 μs long hump in the PMT signal. Note that the 7.0 μs corresponds to a quarter of the voltage period and ends at the voltage maximum. This is in good agreement with the observations of other authors. Miralaï et al. generated an AC dielectric barrier discharge in pure helium in a plate-to-plate configuration between a quartz barrier and a stainless steel electrode [39]. When the stainless steel electrode was coated with a resistive Al_2O_3 + 13% TiO_2 layer with thickness of 500 μm, similar humps were observed in the photocurrent during both negative and positive voltage half cycles, each following a bright discharge peak. Without the resistive coating, the peaks only occurred without any hump. This comparison seems to indicate that in our reactor a water cathode acts as a resistive layer, while a water anode behaves more like a metal. In contrast, Bruggeman et al. attributed a resistive character to a water anode, based on stabilization of a DC glow discharge and pattern formation of the anode layer, two phenomena which are observed as well in resistive barrier discharge with solid electrodes [60].

A 1 μs pulse followed by a long hump of several microseconds in the photocurrent has also been reported for filamentary argon plasma in an electrode configuration with a metal pin pointed towards a dielectric plate in contact with a water electrode [40]. For low voltage amplitude range, the hump is only observed during the voltage half cycle where the pin acts as cathode, while for higher amplitude it occurs during the other half cycle as well. The authors explain the hump with the formation of a cathode fall region, which prolongs the discharge's life time and leads to the light hump as in our experiments. As mentioned in section 7.6.4, the higher the ion density at the cathode is, the easier the cathode fall region is to form. When the dielectric barrier acts as cathode, accumulation of wall charges can prevent the formation of a cathode fall region, with fast quenching of the discharge. At a cathode pin, on the other hand, the electric field and the ion density are higher. This explains why for low voltage the photocurrent hump is only observed when the pin acts as cathode in the experiments of Li et al. It should be noted that also in their setup, the dielectric barrier in contact with the water electrode can be considered as a resistive barrier due to the relatively low mobility of aqueous ions. We therefore conclude that the occurrence of the photocurrent

hump is characteristic for a resistive barrier discharge, while its dependence on voltage polarity indicates that the cathode fall formation is favored at one of the electrodes.

Future research is required to determine the importance and dominance of the mechanisms mentioned above, in the formation of the cathode fall region as well as in the sustainment of the continuous glow discharge. As should be kept in mind, their effect can be significantly different for a water cathode than for a water anode. Apart from the dimmer glow discharge in our experiments for an instantaneous water anode, such asymmetric behavior can also partly explain the difference in plasma evolution during the negative and positive voltage half cycles. Especially mechanisms that favor field enhancement at a water cathode in comparison to a water anode are interesting from this point of view, as they can be responsible for the low breakdown voltage at the start of the positive half cycle. However, the continuous presence of glow discharge at the water anode seems to imply a slightly different breakdown mechanism than the one described in section 7.1 for solid electrodes. We believe that the bright glow discharge at the water electrode during the dark stages is always accompanied by a very dim glow-like column extended over the electrode gap. Whereas negative charge accumulation in front of the anode during the pre-breakdown stage is provided by a Townsend mechanism in the case of solid DBD electrode, in our experiments it can be achieved by the glow discharge.

7.7 Current density and electron density

The size of the current peak ΔI during the most intense stage, i.e. the difference between the current with plasma and the displacement current without plasma, represents the current through the filamentary channel at the corresponding discharge stage and has a value of 60 ± 2 mA. This value has no clear dependence on voltage amplitude in our experiments. As deduced from ICCD images for a voltage of 8.5 kV, the channel at the corresponding discharge stage has a diameter D which increases from 140 μm at the mesh electrode to 200 μm at the dielectric, with an average value of 173 ± 11 μm. This gives a current density of j = 2.55 ± 0.18 10^6 A m^{-2}. As shown in Figure 7.5, micro-discharge channel diameter increases with applied voltage and is found to be 143 ± 9 μm at 6.7 kV. Values at 7.5 and 9.5 kV are calculated with linear interpolation. The resulting values of channel diameter and current density j, as given in Table 7.2, are in good agreement with the range of 0.1 to 1.0 mm and 10^6 to 10^7 A m^{-2}, respectively, as mentioned in section 7.1.

Electron density during the most intense micro-discharge stage is determined from the current density j, electric field E and electron mobility μ_e as

$$n_e = \frac{\mathrm{j}}{\mathrm{E} \times \mu_e \times e} \tag{7.6}$$

As shown in Table 7.2, the calculated values in dry air and pure water vapor for voltage amplitude of 7.5, 8.5 and 9.5 kV are mostly of the order of $n_e \approx 10^{14}$ cm^{-3}. This is in good

agreement with the values around 10^{14} - 10^{15} cm^{-3} in the filament core of most DBDs with solid electrodes at breakdown (see section 7.1). For the pulsed DBD source with interchangeable opposite electrode described in section 7.3, a value of $n_e = 2 \times 10^{15}$ cm^{-3} was determined for an interelectrode distance of 1 mm over PBS solution. In comparison, diffuse atmospheric pressure DC glow discharge with water electrode usually has an electron density around $n_e \approx 10^{13}$ cm^{-3}, as explained in [61]. Therefore, the values in Table 7.2 have a realistic order of magnitude, despite the approximations used in the simulations, fittings and averaging for their determination.

7.8 Conclusion

In this study, an AC powered single DBD micro-discharge filament is investigated by means of electrical, spectroscopical and time- and space-resolved plasma diagnostics in combination with simulation software. The filament is generated between a hemispherical quartz barrier and a water layer flowing over a metal grid, in order to mimic the plasma discharge of the water treatment reactor that will be discussed in the Chapter 8. Since a water electrode behaves like a dielectric barrier on small time scales in the range of nanoseconds, a literature overview is given, where the breakdown mechanism and properties of filamentary DBD micro-discharge with solid electrodes is discussed. While the early breakdown stages resemble the ones for discharge without dielectric barrier, a memory effect related to deposited charge on the dielectric surface needs to be taken into account.

For the micro-discharge filament under study, optical emission spectroscopy gives a rotational and vibrational temperature of T_{rot} = 750 ± 150 K and T_{vib} = 4200 ± 500 K for the second positive N_2 (C-B) system. By means of simulation with COMSOL, the reduced electric field E/N in the middle of the electrode gap is calculated to increase from 128 to 164 Td with voltage amplitude from 7.5 to 9.5 kV. Electron mobility μ_e is determined with BOLSIG+ and current density j is calculated from the current pulse and micro-discharge channel diameter during the brightest discharge stage. An electron density in the order of $n_e \approx 10^{14}$ cm^{-3} is deduced from the obtained values of j, μ_e and E. All these results are in good agreement with values reported in scientific literature on DBD microfilaments in atmospheric air in between solid electrodes.

Discharge evolution during the positive voltage half cycle is remarkably different from the one usually observed for DBD in between solid electrodes. While in the negative voltage half cycle, one intense light pulse is seen as in the solid electrode case, the positive half cycle starts with a less intense light pulse followed by a hump in the photocurrent. The hump is associated with an intense cathode spot at the water surface and a glow-like discharge wave that moves upwards along the dielectric surface, indicating gradual charge deposition on the barrier. Based on two other scientific reports of similar photocurrent humps in AC powered DBD, it is concluded that the phenomenon is characteristic for resistive barrier discharge, where one electrode acts as a resistive barrier. In our experiments, the water electrode

behaves as a resistive layer, an observation which has been reported as well by Bruggeman et al [60]. As cathode fall formation can be favored at one electrode in asymmetric electrode configurations, the photocurrent hump is for certain voltage range present in only one voltage half cycle while absent in the other. In our experiments, cathode fall formation only occurs at the water cathode during the positive voltage half cycle for the entire working range of the power source. This preference can have many causes, including local field enhancement by water surface deformation or droplet formation, local ionization enhancement by the inhomogeneous humidity profile and more effective secondary electron emission at the water electrode than at the dielectric barrier. Similar mechanisms can be the underlying cause of the glow-like discharge spot which is continuously observed at the water electrode during the entire voltage cycle. All of these mechanisms are in good agreement with observations and interpretations by other authors.

References

[1] Y. Yang, *et al.*, *Plasma discharge in liquid: water treatment and applications*: CRC Press, 2012.

[2] V. I. Gibalov and G. J. Pietsch, "The development of dielectric barrier discharges in gas gaps and on surfaces," *Journal of Physics D: Applied Physics,* vol. 33, p. 2618, 2000.

[3] H. E. Wagner, *et al.*, "The barrier discharge: basic properties and applications to surface treatment," *Vacuum,* vol. 71, pp. 417-436, 2003.

[4] M. A. Jani, *et al.*, "Streamer polarity dependence of NOx removal by dielectric barrier discharge with a multipoint-to-plane geometry," *Journal of Physics D: Applied Physics,* vol. 32, p. 2560, 1999.

[5] A. Kulikovsky, "The mechanism of positive streamer acceleration and expansion in air in a strong external field," *Journal of Physics D: Applied Physics,* vol. 30, p. 1515, 1997.

[6] A. Kulikovsky, "Positive streamer in a weak field in air: A moving avalanche-to-streamer transition," *Physical Review E,* vol. 57, p. 7066, 1998.

[7] U. Kogelschatz, "Filamentary, patterned, and diffuse barrier discharges," *Plasma Science, IEEE Transactions on,* vol. 30, pp. 1400-1408, 2002.

[8] Y. B. Golubovskii, *et al.*, "Influence of interaction between charged particles and dielectric surface over a homogeneous barrier discharge in nitrogen," *Journal of Physics D: Applied Physics,* vol. 35, p. 751, 2002.

[9] T. Nozaki, *et al.*, "Optical diagnostics for determining gas temperature of reactive microdischarges in a methane-fed dielectric barrier discharge," *Journal of Physics D: Applied Physics,* vol. 34, p. 2504, 2001.

[10] X. Xu, "Dielectric barrier discharge—properties and applications," *Thin Solid Films,* vol. 390, pp. 237-242, 2001.

[11] N. Jidenko, *et al.*, "Temperature profiles in filamentary dielectric barrier discharges at atmospheric pressure," *Journal of Physics D: Applied Physics,* vol. 43, p. 295203, 2010.

[12] J. P. Boeuf, *et al.*, "Generation, annihilation, dynamics and self-organized patterns of filaments in dielectric barrier discharge plasmas," *Applied Physics Letters,* vol. 100, p. 244108, 2012.

[13] L. Dong, *et al.*, "A simple dielectric barrier discharge device for generating slot homogeneous plasma in atmospheric pressure air," *Applied Physics Letters,* vol. 94, p. 091502, 2009.
[14] X.-C. Li, *et al.*, "Spatial-Temporal Patterns in a Dielectric Barrier Discharge under Narrow Boundary Conditions in Argon at Atmospheric Pressure," *Chinese Physics Letters,* vol. 28, p. 045203, 2011.
[15] L. Dong, *et al.*, "Honeycomb hexagon pattern in dielectric barrier discharge," *Physical Review E,* vol. 76, 2007.
[16] L. Dong, *et al.*, "Direct measurement of electron density in microdischarge at atmospheric pressure by Stark broadening," *Applied Physics Letters,* vol. 86, p. 161501, 2005.
[17] L. Dong, *et al.*, "Processing of Signals of Ring-Shaped Spots in Dielectric Barrier Discharge," in *Image and Signal Processing, 2009. CISP'09. 2nd International Congress on*, 2009, pp. 1-3.
[18] L. F. Dong, *et al.*, "Temporal symmetry of individual filaments in different spatial symmetry filaments pattern in a dielectric barrier discharge," *Physics of Plasmas,* vol. 17, p. 102314, 2010.
[19] P. Jia, *et al.*, "Signal process of light emission patterns in argon/air dielectric barrier discharge," in *Image and Signal Processing (CISP), 2010 3rd International Congress on*, 2010, pp. 3035-3038.
[20] K. Kozlov, *et al.*, "Cross-correlation spectroscopy in investigations of filamentory gas discharges at atmospheric pressure," in *Proc. SPIE*, 2002, pp. 165-176.
[21] K. Kozlov, *et al.*, "Spatio-temporally resolved spectroscopic diagnostics of the barrier discharge in air at atmospheric pressure," *Journal of Physics D: Applied Physics,* vol. 34, p. 3164, 2001.
[22] M. Bogaczyk, *et al.*, "Development of Barrier Discharges: Operation Modes and Structure Formation," *Contributions to Plasma Physics,* vol. 52, pp. 847-855, 2012.
[23] C. Heuser, "Zur Ozonerzeugung in elektrischen Gasentladungen," PhD Doctoral, Aachen, 1985.
[24] D. Braun, *et al.*, "Two-dimensional modelling of the dielectric barrier discharge in air," *Plasma Sources Science and Technology,* vol. 1, p. 166, 1992.
[25] J. Coogan and A. Sappey, "Distribution of OH within silent discharge plasma reactors," *Plasma Science, IEEE Transactions on,* vol. 24, pp. 91-92, 1996.
[26] R. Sankaranarayanan, *et al.*, "Laser-induced fluorescence of OH radicals in a dielectric barrier discharge," *Applied Physics Letters,* vol. 77, p. 2970, 2000.
[27] H. F. A. Verhaart and P. C. T. van der Laan, "The influence of water vapor on avalanches in air," *Journal of Applied Physics,* vol. 55, p. 3286, 1984.
[28] I. Gallimberti, "The mechanism of the long spark formation," *Le Journal de Physique Colloques,* vol. 40, pp. C7-193-C7-250, 1979.
[29] E. Brodskaya, *et al.*, "Molecular dynamics simulations of water clusters with ions at atmospheric conditions," *The Journal of Chemical Physics,* vol. 116, p. 7879, 2002.
[30] J. Kornev, *et al.*, "Generation of Active Oxidant Species by Pulsed Dielectric Barrier Discharge in Water-Air Mixtures," *Ozone: Science & Engineering,* vol. 28, pp. 207-215, 2006.
[31] R. Messaoudi, *et al.*, "Influence of humidity on current waveform and light emission of a low-frequency discharge controlled by a dielectric barrier," *Dielectrics and Electrical Insulation, IEEE Transactions on,* vol. 3, pp. 537-543, 1996.

[32] Z. Falkenstein and J. J. Coogan, "Microdischarge behaviour in the silent discharge of nitrogen-oxygen and water-air mixtures," *Journal of Physics D: Applied Physics,* vol. 30, p. 817, 1997.

[33] Z. Falkenstein, "Influence of ultraviolet illumination on microdischarge behavior in dry and humid N2, O2, air, and Ar/O2: The Joshi effect," *Journal of Applied Physics,* vol. 81, p. 5975, 1997.

[34] U. Kogelschatz and B. Eliasson, "Fundamentals and applications of dielectric barrier discharges," in *HAKONE VII Int. Symp. On High Pressure Low Temperature Plasma Chemistry, Greifswald*, 2000.

[35] I. A. Soloshenko, *et al.*, "Effect of water adding on kinetics of barrier discharge in air," *Plasma Sources Science and Technology,* vol. 18, p. 045019, 2009.

[36] Q. Tang, *et al.*, "Generation of Reactive Species by Gas-Phase Dielectric Barrier Discharges," *Industrial & Engineering Chemistry Research,* vol. 50, pp. 9839-9846, 2011.

[37] I. G. Koo, *et al.*, "Room-temperature slot microplasma in atmospheric pressure air between cylindrical electrodes with a nanoporous alumina dielectric," *Applied Physics Letters,* vol. 91, p. 041502, 2007.

[38] P. Rajasekaran, *et al.*, "Filamentary and Homogeneous Modes of Dielectric Barrier Discharge (DBD) in Air: Investigation through Plasma Characterization and Simulation of Surface Irradiation," *Plasma Processes and Polymers,* vol. 7, pp. 665-675, 2010.

[39] S. Miralai, *et al.*, "Electrical and optical diagnostics of dielectric barrier discharges (DBD) in He and N2 for polymer treatment," *Plasmas and Polymers,* vol. 5, pp. 63-77, 2000.

[40] X. Li, *et al.*, "Investigation on the Micro-Discharge Characteristics of Dielectric Barrier Discharge in a Needle-Plate Geometry," *Plasma Science and Technology,* vol. 13, p. 213, 2011.

[41] X. Lu and M. Laroussi, "Ignition phase and steady-state structures of a non-thermal air plasma," *Journal of Physics D: Applied Physics,* vol. 36, p. 661, 2003.

[42] V. Suvorov and E. Litvinov, "Dynamic Taylor cone formation on liquid metal surface: numerical modelling," *Journal of Physics D: Applied Physics,* vol. 33, p. 1245, 2000.

[43] P. Bruggeman, *et al.*, "DC electrical breakdown in a metal pin–water electrode system," *Plasma Science, IEEE Transactions on,* vol. 36, pp. 1138-1139, 2008.

[44] E. Giglio, *et al.*, "Shape deformations of surface-charged microdroplets," *Physical Review E,* vol. 77, 2008.

[45] J. Kim, *et al.*, "Electrohydrodynamic drop-on-demand patterning in pulsed cone-jet mode at various frequencies," *Journal of Aerosol Science,* vol. 39, pp. 819-825, 2008.

[46] T. Cserfalvi, *et al.*, "Emission studies on a glow discharge in atmospheric pressure air using water as a cathode," *Journal of Physics D: Applied Physics,* vol. 26, p. 2184, 1993.

[47] P. Mezei and T. Cserfalvi, "Electrolyte Cathode Atmospheric Glow Discharges for Direct Solution Analysis," *Applied Spectroscopy Reviews,* vol. 42, pp. 573-604, 2007.

[48] V. Yagov, *et al.*, "Use of electrolyte jet cathode glow discharges as sources of emission spectra for atomic emission detectors in flow-injection analysis," *Journal of Analytical Chemistry,* vol. 59, pp. 1037-1041, 2004.

[49] W. C. Davis and R. K. Marcus, "An atmospheric pressure glow discharge optical emission source for the direct sampling of liquid media," *Journal of Analytical Atomic Spectrometry,* vol. 16, pp. 931-937, 2001.

[50] R. K. Marcus and W. C. Davis, "An atmospheric pressure glow discharge optical emission source for the direct sampling of liquid media," *Analytical Chemistry,* vol. 73, pp. 2903-2910, 2001.

[51] W. Luedtke, *et al.*, "Nanojets, electrospray, and ion field evaporation: Molecular dynamics simulations and laboratory experiments," *The Journal of Physical Chemistry A,* vol. 112, pp. 9628-9649, 2008.

[52] M. Gamero-Castaño, "Electric-Field-Induced Ion Evaporation from Dielectric Liquid," *Physical Review Letters,* vol. 89, 2002.

[53] G. Longhi, *et al.*, "Molecular dynamics of electrosprayed water nanodroplets containing sodium bis(2-ethylhexyl)sulfosuccinate," *Journal of Mass Spectrometry,* vol. 48, pp. 478-486, 2013.

[54] K. H. Schoenbach, "High-Pressure Microcavity Discharges," in *Low temperature plasma technology: methods and applications*, P. K. Chu and X. Lu, Eds., ed: CRC Press, 2013.

[55] I. Dogu, "Fundamentals of Electrostatic Spinning Part IV:-Ionization of Atmospheric Air under Action of an Electric Field," *Textile Research Journal,* vol. 54, pp. 111-119, 1984.

[56] J. W. Quinn, *et al.*, "Evaluation of tribocharged electrostatic beneficiation of lunar simulant in lunar gravity," *Journal of Aerospace Engineering,* vol. 26, pp. 37-42, 2012.

[57] Q. Tang, *et al.*, "A laser-optical-sheet based technique for monitoring particle charge distributions," *KONA Powder and Particle Journal,* vol. 15, pp. 142-149, 1997.

[58] X.-J. Shao, *et al.*, "One-dimensional modeling of dielectric barrier discharge in xenon," *Plasma Science, IEEE Transactions on,* vol. 39, pp. 1165-1172, 2011.

[59] T. Cserfalvi and P. Mezei, "Operating mechanism of the electrolyte cathode atmospheric glow discharge," *Fresenius' journal of analytical chemistry,* vol. 355, pp. 813-819, 1996.

[60] P. Bruggeman, *et al.*, "Dc excited glow discharges in atmospheric pressure air in pin-to-water electrode systems," *Journal of Physics D: Applied Physics,* vol. 41, p. 215201, 2008.

[61] T. Verreycken, *et al.*, "Spectroscopic study of an atmospheric pressure dc glow discharge with a water electrode in atomic and molecular gases," *Plasma Sources Science and Technology,* vol. 19, p. 045004, 2010.

Whenever you find yourself on the side of the majority,
it is time to pause and reflect.
- Mark Twain

Chapter 8

Removal of 6 micropollutants in a falling water film DBD reactor with activated carbon textile

Building further on the insights of all previous chapters, we developed a new type of plasma reactor, which is described and characterized in this chapter of the dissertation. As discussed in Chapter 3, AC powered dielectric barrier discharge over moving water film has been found to be effective and sustainable for aqueous organic removal. Bubnov et al. introduced this reactor type for the first time, where the internal electrode was covered with catalytic fabric [1]. In Chapter 6, we have demonstrated that adding an adsorptive nanofiber membrane near the plasma-active region, atrazine mineralization and associated energy efficiency is enhanced. Adsorption allows reaching higher local micropollutant concentration close to the active plasma region. As a result, more collisions will take place between plasma species and micropollutants, explaining the increase in overall energy efficiency of the treatment process. This reactor concept is further optimized in this chapter by adding an activated carbon textile underneath the water surface, which is remarkably more sustainable than the nanofiber membrane described in Chapter 6. In Chapter 2, the conclusion was made that combining different advanced oxidation processes generally leads to synergetic effects. Such synergetic effect of plasma and ozone treatment has been described already by Malik [2]. For that reason, an ozonation chamber has been added to our setup, where the generated plasma gas is bubbled through the solution under treatment.

In the first following sections, the reactor is presented and the used materials and methods are described in detail. Next, the generation of oxidative species in the reactor is explained.

In the first part of the degradation experiments, atrazine is used as model compound, since it is the most frequently used pesticide in water purification studies with plasma reactors. This permits to compare our reactor in energy efficiency with other reactors reported in literature. Moreover, the contribution of the ozonation process is determined and atrazine by-products are identified by means of HPLC-TOF-MS. Subsequently, the Zorflex® textile is characterized by means of adsorption and desorption experiments, in order to determine its performance and sustainability, and to learn more about the oxidation of adsorbed molecules. Afterwards, the energy efficiency of the reactor is investigated for the removal of 5 other compounds with distinct features, as a function of several operational parameters. In the last part of this chapter, a by-product analysis is conducted in depth for three of the investigated compounds. Based on the obtained results, recommendations are made for future work on the topic of water purification with plasma discharge and advanced oxidation processes in general.

8.1 Experimental methods and materials

8.1.1 DBD water treatment reactor

Each micropollutant solution was treated with modulated AC dielectric barrier discharge (DBD) in contact with a falling water film and subsequent plasma gas bubbling in a closed water circuit (Figure 8.1a-b). The discharge is generated in a plasma reactor chamber with cylindrical geometry. A stainless steel tube with outer diameter of 28 mm is placed inside a quartz glass tube with thickness of 1.5 mm. The stainless steel tube serves as grounded inner electrode and is covered by 2 layers of Zorflex® active carbon textile for the experiments with atrazine and 1 layer for all other micropollutants. The solution under treatment is pumped upwards through the stainless steel tube and subsequently flows downwards along the carbon textile. Plasma is generated in dry air over the carbon textile by applying a pulsed AC high voltage on the outer mesh electrode that covers the quartz glass tube. Next, the solution is pumped to a second chamber where the plasma generated ozone is bubbled through the solution bulk. The modulated AC high voltage is generated by a custom-made AC high voltage power supply triggered by a pulse generator model TGP110 Thurlby Thandar instruments. By pulsing the AC high voltage, gas and liquid temperature can be kept sufficiently low, in order to avoid excessive energy loss and ozone decomposition due to Joule heating. Temperature of the quartz glass tube after 20 min of continuous operation was determined with an infrared temperature probe to be 70°C for AC voltage without modulation and 38°C for used duty cycle of 14.3% at 25 W. Main parameters of the system are presented in Table 8.1 and the electrical characteristics are described in more detail in section 8.1.3. As should be noted, the different amount of Zorflex® layers in the setup for atrazine as compared to the other micropollutants causes a change in inter-electrode distance and consequently a shift in power range.

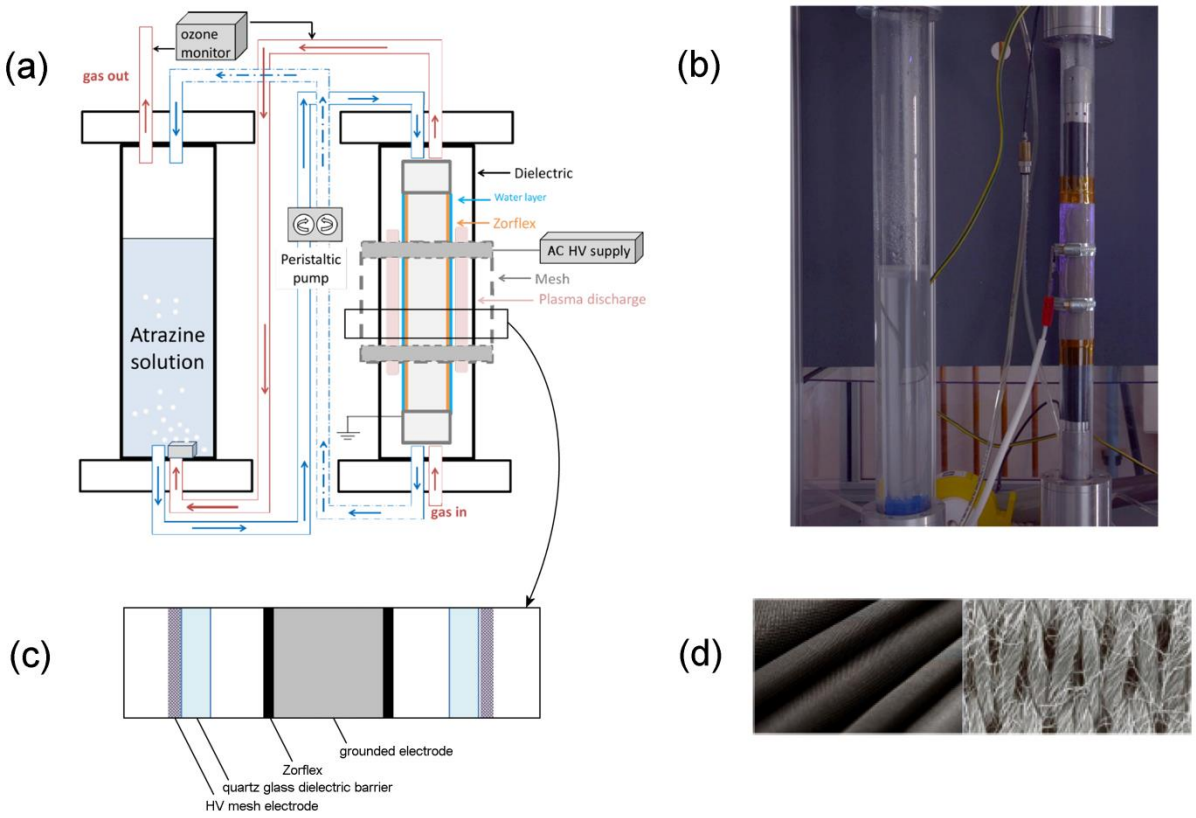

Figure 8.1 (a) Scheme of the setup with DBD reactor chamber (right) and ozonation chamber (left), (b) photograph of the setup during plasma generation, (c) electrode configuration scheme and (d) macroscopic (left) and microscopic photograph of Zorflex® active carbon textile, taken from [3].

Analytical standards of the six compounds are purchased from Sigma-Aldrich from the product line PESTANAL®. In our experiments with atrazine, initial conductivity was set at 350 µS/cm by addition of $NaH_2PO_4 \bullet 2H_2O$ to demineralized water, in order to simulate a drinking water matrix, while initial pH was measured to be 5.06. For all other micropollutants, no salt addition was used. The solution was pumped through the system in a closed circuit with peristaltic pumps at a flow rate of 85.6 mL/min. Solution samples up to 50 mL are taken during the experiments for analysis by means of GC-MS, HPLC-MS and to measure H_2O_2 production.

Zorflex® textile type FM50K was provided by Chemviron Carbon. The double jersey knit structure, as shown in Figure 1c, provides a stretchable elastic fabric that does not shed or fray, which allows its use in many possible geometries. The textile has a surface density of 130 g/m^2 and a thickness of 0.5 mm. Zorflex® consists of 100% activated carbon, with a carbon tetrachloride activity of 55 to 70 %ww. It is therefore fit for air and water filtration purposes. It has an extremely large surface area of more than 2000 m^2/g [3]. These features, in combination with the strong electrostatic forces within the cloth, make it highly efficient for pollutant adsorption.

Table 8.1 Reactor reference settings for the experiments in this work.

Experimental parameter	Atrazine	Other micropollutants
Voltage amplitude	6.0-7.5 kV	7.9-8.4 kV
Input power	20-25 W	See Table 8.13
AC frequency	47.8 kHz	47.8 kHz
Modulation frequency	35.7 Hz	33.3 Hz
Duty cycle	14.3%	15.0%
Treated volume	500 mL	500 mL
Water flow rate	85.6 mL/min	95.3 mL/min
Gas flow rate	0.33 SLM	1.00 SLM
Feed gas	air	air, Ar or O_2
Inter-electrode distance	1.75 mm	2.25 mm
Dielectric barrier thickness	1.5 mm	1.5 mm
Dielectric barrier material	Quartz	Quartz
Discharge zone length	15.0 cm	15.0 cm
Tube length for ozone transport	95 cm	95 cm
Tube diameter for ozone transport	4.0 mm	4.0 mm
Tube material for ozone transport	Teflon	Teflon
Ozonation chamber inner diameter	44.5 mm	44.5 mm
Solution height in ozonation chamber	25.7 cm	25.7 cm
Initial micropollutant concentration	30 µg/L	See Table 8.13
Salt addition	$NaH_2PO_4 \bullet 2H_2O$	none

8.1.2 Selected model micropollutants

In the first part of this chapter, only atrazine is used as model micropollutant. Since it is the most frequently investigated pesticide in studies on advanced oxidation with plasma treatment, this allows the comparison of several plasma reactors in their energy efficiency of atrazine removal. In the second experimental part of this chapter, five other persistent pesticides or pesticide-related compounds with significantly diverse properties are selected. Their variety permits to gain a more comprehensive view on the overall reactor performance and optimization. Ideally, the reactor should be able to remove as many types of micropollutants as possible, in order to be suitable for real-world applications. To this end,

the European Union has defined a limit of 0.1 μg/L for maximum concentration of all individual pesticides and by-products and 0.5 μg/L for total pesticide content in environmental water. The structural formulas of all compounds are depicted in Figure 8.2 and their most relevant physical and chemical properties are enlisted in Table 8.2. The Henry law constant and the reaction rate constants k_{O3} and k_{OH} are representative for the compound's removal rate by transfer towards the gas phase, oxidation by direct ozone attack and oxidation by OH radical attack, respectively. The water solubility and octanol water partition coefficient P_{OW}, on the other hand, indicate the extent of transfer from aqueous phase towards a more hydrophobic phase, such as activated carbon, soil or dichloromethane. Atrazine, alachlor, diuron and isoproturon are the four most investigated pesticides in water treatment by advanced oxidation processes from 2004 up to now [4], while advanced oxidation of α-HCH and PeCB has seldomly been reported before.

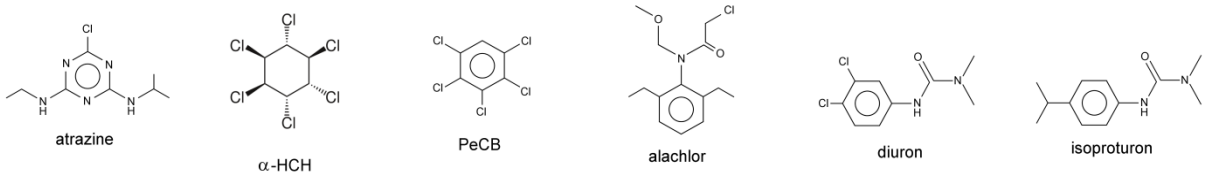

Figure 8.2 Structural formulas of the pesticides used in this work.

Atrazine is one of the most widely used herbicides in agriculture, with an estimated annual usage amount in the late 1980s of 70000 tons [5]. This pollutant exhibits low biodegradability and high persistence in the environment with half-life ranging from 21 days to over one year [6]. Due to its high mobility in soil, atrazine and its metabolites are commonly found in ground water, surface water and drinking water supplies [7]. Atrazine has endocrine disruptive properties at relatively small concentrations and is considered to be hazardous to humans, animals and aquatic life. As a consequence, it has been banned in the European Union (EU) in 2004 [8], while most countries, including U.S. and China, continue its use on large scales. Its removal by modern wastewater treatment plants is often incomplete.

α-Hexachlorocyclohexane (α-HCH) is the dominant isomer with an abundance of 60 to 70% in technical hexachlorocyclohexane, an isomeric insecticidal mixture which was introduced during World War II [9, 10]. It is also a by-product of lindane production, an improved pesticide mixture, which contains more than 90% of the gamma isomer [10]. The use of both mixtures has been banned or restricted in many countries and the alpha, beta and gamma isomers have been included in the Stockholm Convention persistent organic pollutants list in 2009 [11]. Although γ-HCH is the only isomer with significant insecticidal properties, α-HCH is notably more toxic [12, 13]. α-HCH is a volatile compound with very strong persistence in the environment. It can be easily transported over long distance by natural processes and is one of the most abundant organochlorine compounds in air and water of arctic and subarctic regions (see [9] and references therein). As a result, it is one of the most studied chemicals in arctic environmental research [10]. Despite its high volatility, its

condensation is favored in colder climates [9] and it is found worldwide in water and soil [12]. In studies on its removal percentage in wastewater treatment plants, α-HCH was found to be poorly biodegradable [14] and persistent even after tertiary treatment with additional ultrafiltration, reverse osmosis and UV disinfection [15].

Table 8.2 Henry law constant H, reaction rate for direct ozone attack k_{O3}, reaction rate for OH attack k_{OH}, water solubility, octanol water partition coefficient log P_{OW} and molar mass of all micropollutants used in this work.

	atrazine	α-HCH	PeCB	alachlor	diuron	isoproturon
H (atm/M)	2.63×10^{-6}	1.06×10^{-2}	6.91×10^{-1}	7.14×10^{-5}	5.10×10^{-7}	1.22×10^{-7}
k_{O3} (M^{-1} s^{-1})	5.65			3.40	16.5	141
k_{OH} (M^{-1} s^{-1})	1.70×10^{9}			5×10^{9}	7.10×10^{9}	5.70×10^{9}
Solubility (mg/L)	33	1.5	1.0	242	42	65.0
Log P_{OW}	2.61	3.89	4.94	2.92	2.85	2.46
Molar mass (g/mol)	216	291	250	270	233	206

Pentachlorobenzene (PeCB) was used in the past for many applications, including as a precursor and by-product in pentachloronitrobenzene production, but has been globally restricted by the Stockholm Convention on Persistent Organic Pollutants as of 2009. Like α-HCH, it is a recalcitrant volatile compound that has been detected worldwide. Although its atmospheric concentrations are mostly linked to current emissions, its presence in other media is more related to past emissions, with a half-life in soil of 194 to 345 days [16, 17]. PeCB displays bioaccumulative and carcinogenic activity [16, 18] and can be metabolized in mammals into pentachlorophenol, which is a probable human carcinogen included in the Stockholm Convention persistent organic pollutants list in 2015 [19]. PeCB was recently detected in the effluent of a Spanish secondary wastewater treatment plant in a concentration exceeding the European limit of 0.1 μg/L [20]. It was also found in the effluent of a tertiary wastewater treatment plant with additional ultrafiltration, reverse osmosis and UV disinfection [15].

Alachlor is one of the most frequently applied herbicides in the United States [21], while its use has been severely restricted or banned in other parts of the world such as Europe and Canada [22]. It is an endocrine disruptor, a possible carcinogen and generally toxic to mammals, as supported by many studies [23-25]. It has been frequently detected in natural water bodies in the United States [26]. In a review on micropollution in natural water bodies of Spain, alachlor was reported to be one of the most commonly encountered pesticides, with the highest maximum individual concentration [27]. However, many studies have shown that stable alachlor metabolites are often found in the environment in higher concentrations than their parent compound [26, 28, 29], which poses an additional ecological risk. Alachlor

has been frequently detected in the effluent of secondary wastewater treatment plants in concentrations surpassing the limit of 0.1 μg/L [20].

Diuron is one of the most commonly used herbicides in agricultural practices. It is considered to be an endocrine disruptor, a probable carcinogen and is classified as a hazardous substance under the US Comprehensive Environmental Response, Compensation, and Liability Act as well as under the European Union Water Framework Directives List [24, 30]. Despite its progressive suppression with Directive 200/60/CE, it is expected to remain persistently present in soil, surface water and ground water [31]. It has been frequently detected in natural water bodies around the world, sometimes exceeding limit values [15, 27, 31-35]. Its toxicity and detrimental effects on the ecosystem have been illustrated with vast amount of studies [30, 31]. Some of its biodegradation metabolites have even higher toxicity and increased risks for the environment [31], a topic that will be further discussed in the diuron oxidation by-product analysis of section 8.7.2. In wastewater treatment plants, diuron is in general insufficiently removed. It was detected with a frequency of 77 % in a recent EU-wide monitoring survey on emerging organic contaminants in the effluent of 90 wastewater treatment plants [36]. In [33], 60% of the total diuron load into the Swiss Lake Greifensee originated from wastewater treatment plants. Secondary treated rural and urban wastewater in Germany contained diuron concentration significantly higher than the limit of 0.1 μg/L [37]. This limit was also surpassed in the effluent of a Spanish tertiary wastewater treatment plant with additional ultrafiltration, reverse osmosis and UV disinfection [32]. Another Spanish tertiary treatment plant caused very little removal of the herbicide, as found from comparison of its influent and effluent [15]. In a review on water purification with natural wetlands, diuron was classified as one of the few pollutants recalcitrant to elimination [34].

Isoproturon is an herbicide whose use has been banned or restricted in several countries, while it is still intensively applied worldwide [38]. It is a suspected carcinogen and has harmful effects on the ecosystem, as supported by many investigations (see [38] and references therein). It is commonly found in natural water bodies in concentrations, often surpassing the 0.1 μg/L limit [37, 39-42]. It is relatively stable in several water matrices [43] and its half-life in soil can exceed 100 days [44]. Isoproturon is insufficiently removed by conventional wastewater treatment plants [33]. It was detected with a frequency of 51 % in a recent EU-wide monitoring survey on emerging organic contaminants in the effluent of 90 wastewater treatment plants, occasionally exceeding the 0.1 μg/L limit [36]. This limit was also extensively surpassed in the effluent of both a German urban and rural secondary wastewater treatment plant [37].

8.1.3 Power measurement method

Voltage was measured with a Tektronix P6015 HV probe and current was measured with a Pearson model 2877 current probe, both connected to a Tektronix S1200 oscilloscope. Voltage and current waveforms during reactor operation are presented in Figure 8.3. After every

time interval T_{on} of plasma generation, the input power is interrupted for a time T_{off}, giving a duty cycle DC = T_{on} / (T_{on} + T_{off}). The distorted current sine indicates the formation of plasma discharge. For atrazine, a value of DC = 14.3% is consistently used, while for all other micropollutants a value of DC = 15.0% is taken as reference setting. Total input power P is determined by multiplying the duty cycle with the power during one or more periods ΔT of the voltage sine:

$$P = \frac{DC}{\Delta T}\int_{\Delta T} IVdt \qquad (8.1)$$

where I is the current and V is the voltage during plasma generation. For atrazine, time averaged value of input power for one experiment is obtained from at least 8 voltage and current data acquisitions during 30 minutes treatment time. For all other micropollutants, the average of current and voltage over 128 waveforms is measured with the oscilloscope at different treatment times and subsequently the obtained power values are averaged. The latter method allowed us to gain a higher accuracy on the power value with less acquisitions. Due to the used AC power supply, the time averaged input power can deviate between experiments over a few Watt. This has to be taken into consideration mostly for the comparative experiments with atrazine at low power around 20 to 25 W.

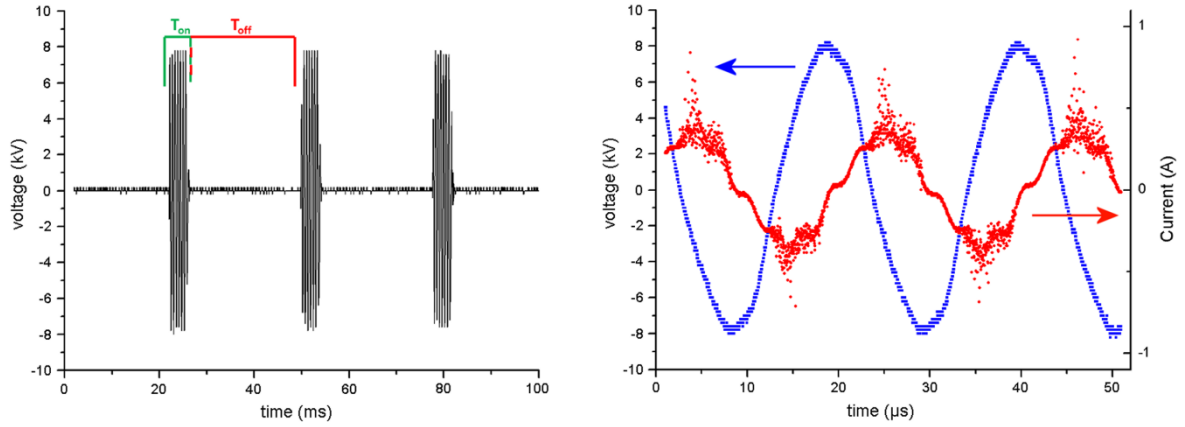

Figure 8.3 Voltage and current during reactor operation for the case of atrazine. The voltage sine is interrupted for a time T_{off} = 24 ms after every T_{on} = 4 ms of plasma generation, in order to prevent energy loss due to excessive Joule heating of gas and liquid.

8.1.4 Spectroscopical analysis method

In order to identify the main light emitting species generated in the dielectric barrier discharge, space- and time-integrated optical emission spectra are measured with an Ocean Optics spectrometer S1000 in the range of 250nm to 900nm. The device has an instrumental full-width at half maximum of 1.3 nm.

8.1.5 Ozone and H_2O_2 measurement method

Details on used ozone and hydrogen peroxide measurement methods can be found in section 6.2.3. Ozone measurement in gas phase with ozone monitor Envitec model 450 has 5% error with limit of detection of 2 ppm by volume (4.3 μg/L). For H_2O_2 measurement based on the method in [19], experimental error is estimated to be about 5% for H_2O_2 concentration higher than 5 mM and 10% in lower concentration range.

8.1.6 Micropollutant concentration measurement method

For atrazine, same GC-MS technique is used as in chapter 6. Total ion current (70 eV) was recorded in SIM mode for ions 173, 200, 202, 215 and 217, with an analysis time of 31.7 min. Alachlor and diuron concentration is measured by means of the same GC-MS device, but with a different cross-linked methyl silicone column (ZB-5MS, 30 m x 0.25 mm, 0.25 μm film thickness; Agilent Technology). Before extraction, alachlor was incubated for 5 minutes at 50 °C and diuron for 1 minute at 30 °C using agitation. Extraction of both dissolved compounds from the water matrix was performed with a different SPME fibre as compared to atrazine (75 μm Carboxen/Polydimethylsiloxane (CAR/PDMS), fused silica fibre core, Supelco, USA), for 45 minutes at 50°C in the case of alachlor and for 30 minutes at 30°C in the case for diuron. For alachlor, the temperature gradient was 60 °C (6 min) to 160 °C at 15 °C min^{-1}, held 11 minutes; then 7 °C/min to 205 °C for 0 min; then 25 °C/min to 250 °C for 5 min. For diuron, the gradient was 35 °C (6 min) to 160 °C at 15 °C min^{-1}, held 5 minutes; then 100 °C/min to 250 °C for 1 min. All other instrumental settings were the same as for atrazine. Both compounds are measured in Selected Ion Mode (SIM), alachlor at a retention time of 28.4 min and diuron at 16.3 min. Calibration of the detector was made with solutions of known concentration, from 1 to 100 μg/L. The integrated peak area in the obtained chromatogram was found to be linear with concentration in this range for each micropollutant.

Analysis of α-HCH, PeCB and isoproturon was carried out with Agilent GC-MS (6890 series GC system, 5973 MS) using Chemstation software. Before analysis, 20 mL water samples were extracted towards CH_2Cl_2 solvent by means of liquid-liquid extraction. α-HCH and PeCB extraction was executed with addition of 2 mL of CH_2Cl_2. The method was improved for isoproturon by using a CH_2Cl_2 volume of only 1 mL. The samples were shaken by hand for 5 min in 22.5 mL sized vials. Afterwards, 0.6 mL of the CH_2Cl_2 drop was separated by means of a micropipette. In the case of α-HCH and PeCB, 2 grains of dry $CaCl_2$ were added in order to absorb any water traces in the sample. Splitless injection of 1 μL sample occurred at temperature of 250°C and pressure of 78.4 kPa in HP-5 MS column (0.25 mm x 30 m x 0.25 μm) with constant He flow of 1 mL/min. α-HCH and PeCB were measured with an identical oven program. Oven temperature started at 125 °C, rising to 195 °C at 25 °C/min and further rising to 210 °C at 10 °C/min with a final hold of 1.5 min. Mass spectra were recorded in SIM mode with target ion 219 and qualifier ions 181 and 183 in the case of α-HCH and with target

ion 250 and qualifier ions 247 and 252 in the case of PeCB (MS source at 230°C, MS quad at 150 °C, solvent delay of 2 min). For isoproturon, splitless injection of 1 μL sample occurred at temperature of 270°C and pressure of 68.1 kPa. Oven temperature started at 90 °C held for 1 min, rising to 190 °C at 40 °C/min and further rising to 270 °C at 20 °C/min with a final hold of 2 min. Mass spectra were recorded in SIM mode with target ion 146 and qualifier ions 161 and 128 (solvent delay of 3 min). All other instrumental settings were kept the same. Peaks of α-HCH, PeCB and isoproturon were detected at retention time of 5.13 min, 4.03 min and 4.06 min, respectively. All three compounds were calibrated for the range of 0 to 1000 μg/L, where linear dependence on concentration was found. For α-HCH and PeCB, naphthalene was used as internal standard.

8.1.7 Oxidation by-product analysis method

The same HPLC-TOF system was used as in Chapter 6, but the HPLC column was longer (25 cm) than in previous experiments. For atrazine, the same extraction method was used as in Chapter 6. For all other investigated micropollutants, the extraction method was simplified and optimized to permit faster preparation and analysis of more samples with similar accuracy. A volume of 1.5 mL CH_2Cl_2 was added to 45 mL water samples in 130 mL sized bottles and the mixture was shaken by hand for 5 min. Afterwards, 0.45 mL of the CH_2Cl_2 drop was separated by means of a micropipette. TOF-MS detection was performed in the positive jetstream electrospray ionization mode and using the following parameters: capillary 4000 V, nebulizer 30 psi, drying gas 8 L/min, gas temperature 300 °C, sheath gas 8 L/min, sheath gas temperature 300°C, fragmentor 175 V, skimmer 66 V, OCT RF 750 V. The instrument was calibrated prior to each analysis using the solution and procedure recommended by the manufacturer. Spectra were acquired over the m/z 50 to 1700 range at a scan rate of 1.02 s/spectrum. All tests were carried out in duplicate with a regular blank solvent analysis to ensure absence of cross contamination. Due to the low concentration of the oxidation by-products in our samples, only a few by-products manifest themselves as clear peaks in the acquired chromatogram. Therefore, the chromatograms are manually scanned for ions present in treated samples and absent in the untreated sample by means of the open source software OpenChrom. Identification of the ions is conducted with the molecule formula generator included in the Agilent Masshunter software. If multiple formulas are generated, only the most probable one is presented. If the software, on the other hand, is not able to recognize a molecular formula, this is explicitly mentioned below.

8.1.8 Desorption analysis method

Adsorped compounds on activated carbon were investigated with a newly invented desorption analysis method. This analysis method was applied for four experiments, where each time new Zorflex® textile was installed in the reactor. All experiments were performed with atrazine as model micropollutant and are further described in sections 8.3.2 and 8.3.3. After each experiment, Zorflex® was carefully removed and left to dry in ambient air at

room temperature. 66 cm^2 of the textile was cut into 12 pieces equal in size and submerged in 60 mL dichloromethane with 5 mg/L of 1,4-dichlorobenzene. This compound is known to increase atrazine desorption without unwanted pore blockage [45]. The solution was mixed for 14 hours with magnetic stirrer bar at velocity of 120 rounds per minute. Afterwards, it was filtered, using Rotilabo® filter paper (type 601), to remove all Zorflex® fibers. In order to increase concentration of desorbed compounds, 47 mL of retrieved solution was slowly evaporated to 1.5 mL end volume. Samples were taken for analysis with GC-MS and HPLC-MS technique. GC-MS technique was different from the one explained in section 8.1.6, since atrazine analysis was carried out with the same GC-MS system as used for α-HCH, PeCB and isoproturon. Oven program and instrumental settings were the same as for isoproturon, with exception of a solvent delay time of 2.8 min, target ion 215 and qualifier ion 173. Atrazine peak was detected at retention time of 5.60 min and calibrated for range of 0 to 1000 µg/L, where linear dependence on concentration was measured. In the experiment without plasma treatment of the first desorption experiment, 31.3% of the initial atrazine mass in the water solution is desorbed from Zorflex®, indicating that the used extraction technique for desorption is highly effective.

8.2 Generation of oxidative species

In comparison with other advanced oxidation processes, plasma discharge is considerably more complex due to the wide spectrum of involved reactive species. Where the previous chapter focused on the physics behind AC powered micro-discharge filaments, the present chapter deals with the underlying chemistry. In order to preface the experimental characterization of our reactor, this section provides a chemical map that summarizes several insights found in scientific literature. Since we are dealing with a heterogeneous system, this map is subdivided in four regions of interest:

1. The plasma-chemistry inside the gas phase, where the active plasma is located;
2. The interface between the plasma phase and the liquid bulk or film, where transfer and transformation of reactive species occurs;
3. The liquid bulk or film, where the aqueous micropollutants and oxidants react;
4. The surface of the activated carbon, where micropollutants are adsorbed and reactive species can oxidize both the surface and the adsorbed compounds.

The map is further split into Figures 8.4, 8.5 and 8.6, representing mainly a few of the most important initiation, propagation and micropollutant oxidation reactions in the four regions, respectively. Termination reactions are not included, as the focus lies on the generation of reactive species and their oxidation processes. The initiation reactions take place in the plasma region and at the interface. They describe the excitation and dissociation of molecules in the gas phase and at the liquid surface by impact of energetic electrons and photons. The resulting metastables, ions and radicals can follow multiple propagation pathways, leading to the formation of other oxidants, as shown in Figure 8.5. In gas phase and water phase,

hydrogen peroxide is usually formed from collision of two hydroxyl radicals, while ozone from interaction of atomic oxygen with molecular oxygen. OH radicals are often formed during reactions of the oxidizing species with each other, such as in the photolysis of H_2O_2 or during interaction of O_3 and H_2O_2, which is also known as the peroxone process. Hydroxyl formation can also result from interactions of oxidizing species with other molecules, as for example by photolysis of water. Intermediate atomic oxygen can be formed as well through a wide set of initiation and propagation reactions in gas and water phase. Both OH and O are strong oxidants, able to decompose organic compounds through direct interaction. Other important oxidizing species include, but are not limited to, hydroperoxyl, superoxide anion, peroxynitrite, nitric dioxide, energetic electrons and UV photons [46]. Reaction rate constants of direct oxidation by most oxidants are largely unknown for even the most investigated pollutants. For instance, while experimental rate constants for direct oxidation of micropollutants by O_3 and by OH are often reported in literature, as illustrated in Table 8.2, rate constants for direct oxidation by H_2O_2, O and other oxidants are generally unexplored.

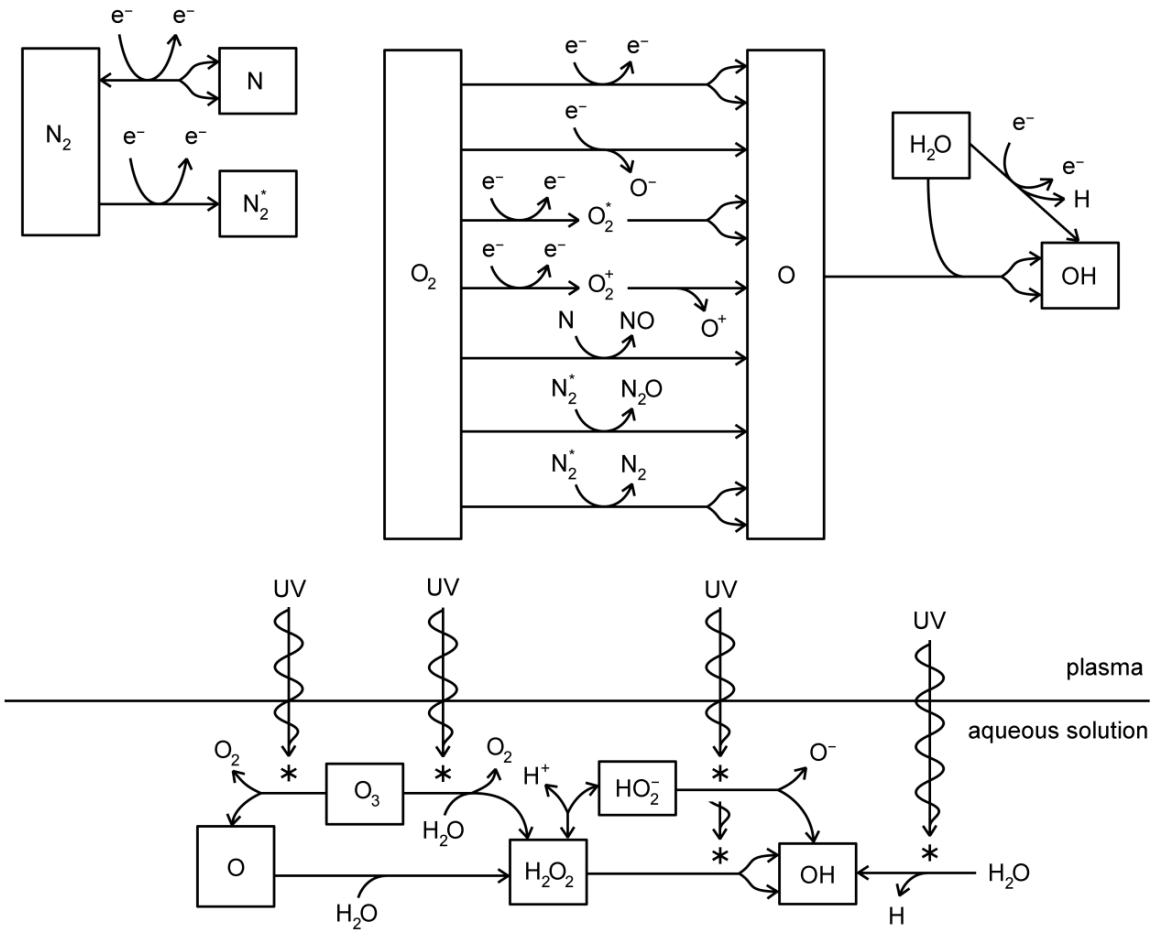

Figure 8.4 Simplified scheme of initiation reactions in the plasma phase and at the liquid surface.

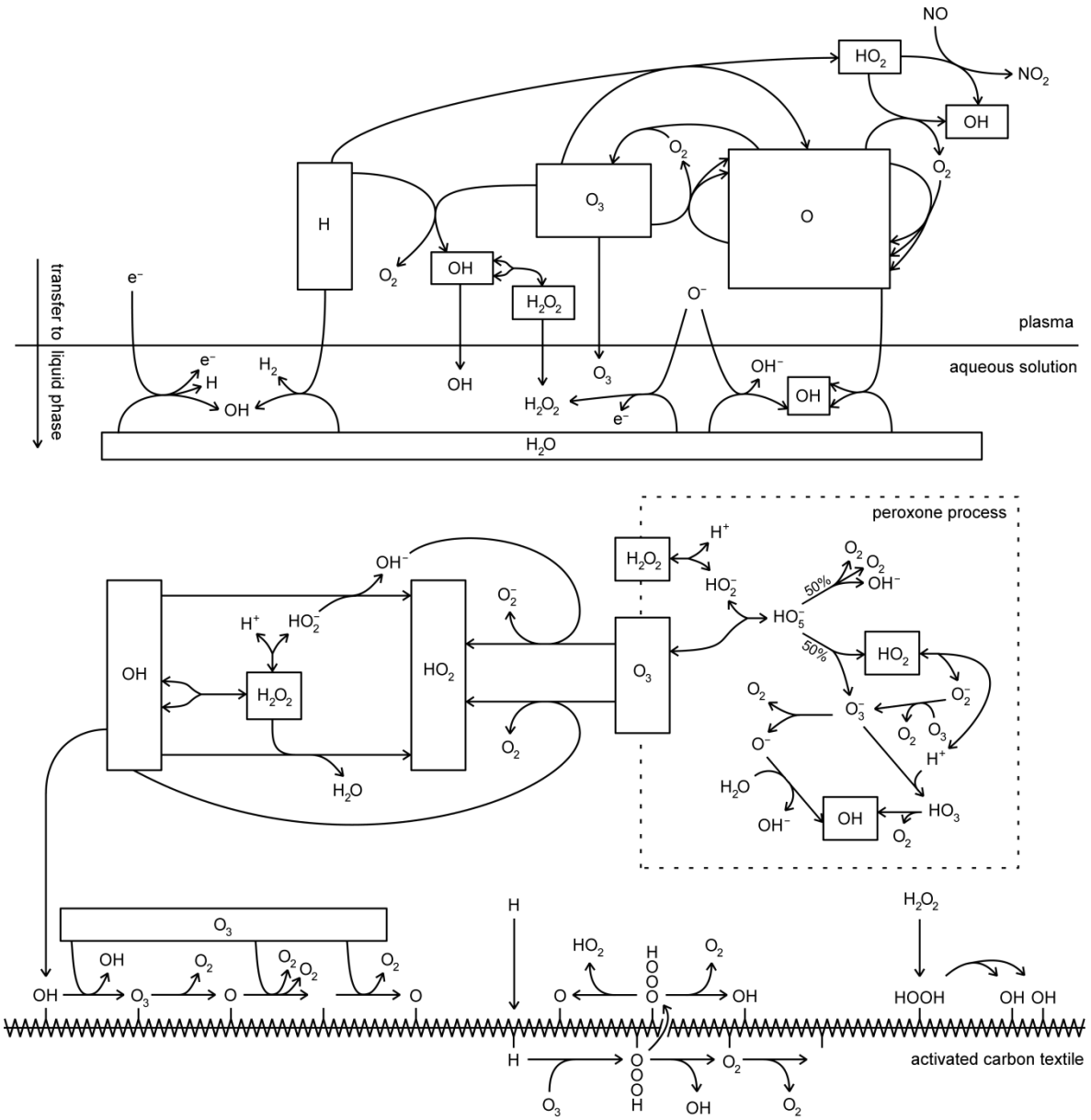

Figure 8.5 Simplified scheme of a few important propagation reactions in all considered phase regions. For reasons of simplicity, no distinction is made between species in excited and ground state.

In our reactor, atrazine can be oxidized while solved in the water bulk and while adsorbed on the activated carbon textile, where oxidizing species can be solved or adsorbed as well, as shown in figure 8.6. Accordingly, resulting by-products are supposedly found in the water bulk or on the activated carbon surface. As should be noted, aqueous oxidants can influence the adsorption capacity of activated carbon by decomposing adsorbed organics and by implementing new surface functional groups on the carbon surface. This set of hypotheses is experimentally tested for Zorflex® in section 8.5.

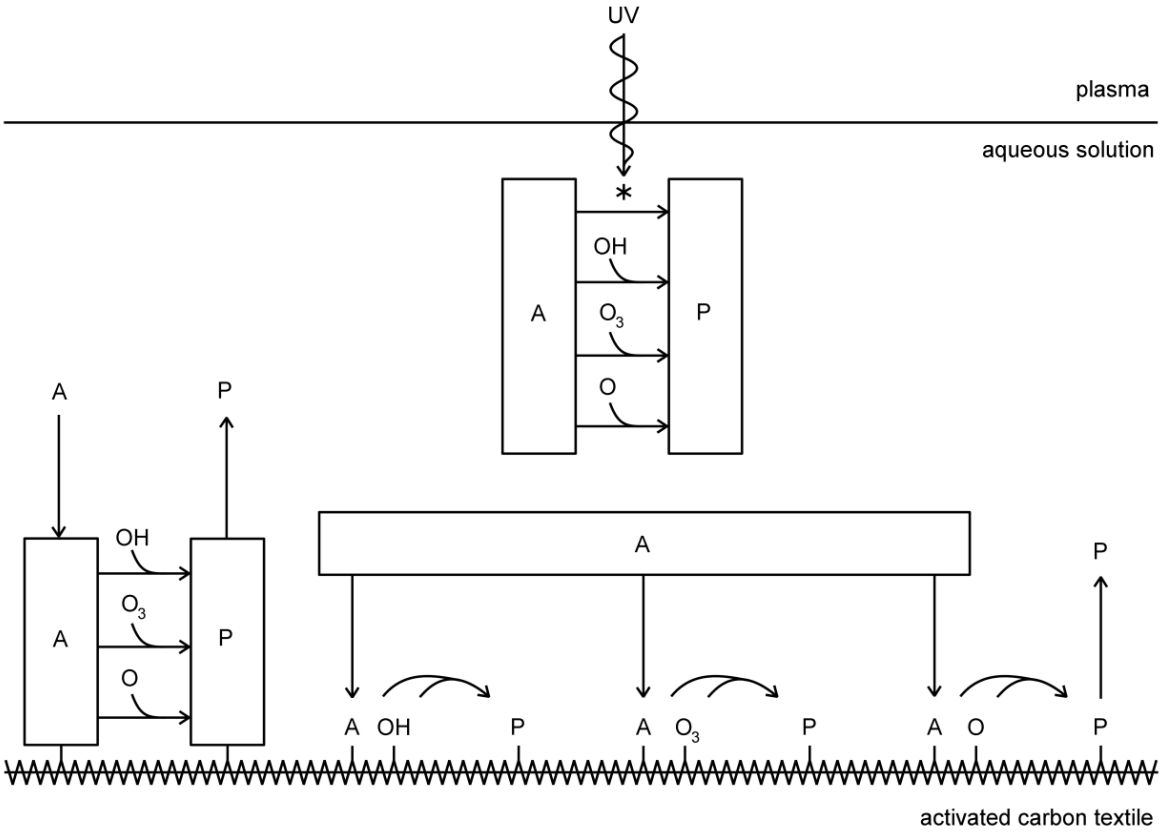

Figure 8.6 Simplified scheme of a few important micropollutant oxidation reactions. Here, A represents the organic target compound and P any of its oxidation by-products. The compound can be oxidized in the liquid bulk or while adsorbed on the activated carbon textile.

8.2.1 Spectral characterization

As discussed in Chapter 6, spectroscopic analysis of the plasma discharge can provide information on the formation of important oxidative species. Normalized emission spectra of the discharge for different input power are shown in Figure 8.7a. In the accuracy of measurement, the space-and-time averaged normalized emission spectrum is unchanged for increasing input power. Therefore, plasma characteristics which determine the normalized spectrum, such as average N_2 vibrational temperature should remain relatively unchanged as well. Emissivity, on the other hand, increases linearly with power P at a fixed duty cycle of DC = 0.15, as presented Figure 8.7b. In contrast to the isolated filament investigated in Chapter 7, where filament intensity rose with applied power, the emissivity increase in our cylindrical reactor is attributed to an expansion of the plasma volume by multiplication of the micro-discharges. Therefore, increase in power does not considerably change the local micro-discharge properties, but instead leads to an increase in number of micro-discharges, which is also observed by eye.

As argon and oxygen are also used in this work as feed gas, the normalized emission spectra for all three gases are compared in Figure 8.7c, for the wavelength interval from 250 to 550 nm. The clear similarities indicate presence of N_2^* molecules in all gases, although the overall intensity of oxygen plasma is significantly lower than for the other two gases. While the normalized spectrum of oxygen is in the accuracy of the measurement identical to the one of air, differences are seen for argon plasma. The higher intensity in the 280 - 300 nm region originates from metastable NO bands. Figure 8.7d presents the intense Ar(I) lines in the interval from 650 to 900 nm, which give the argon plasma its characteristic orange color.

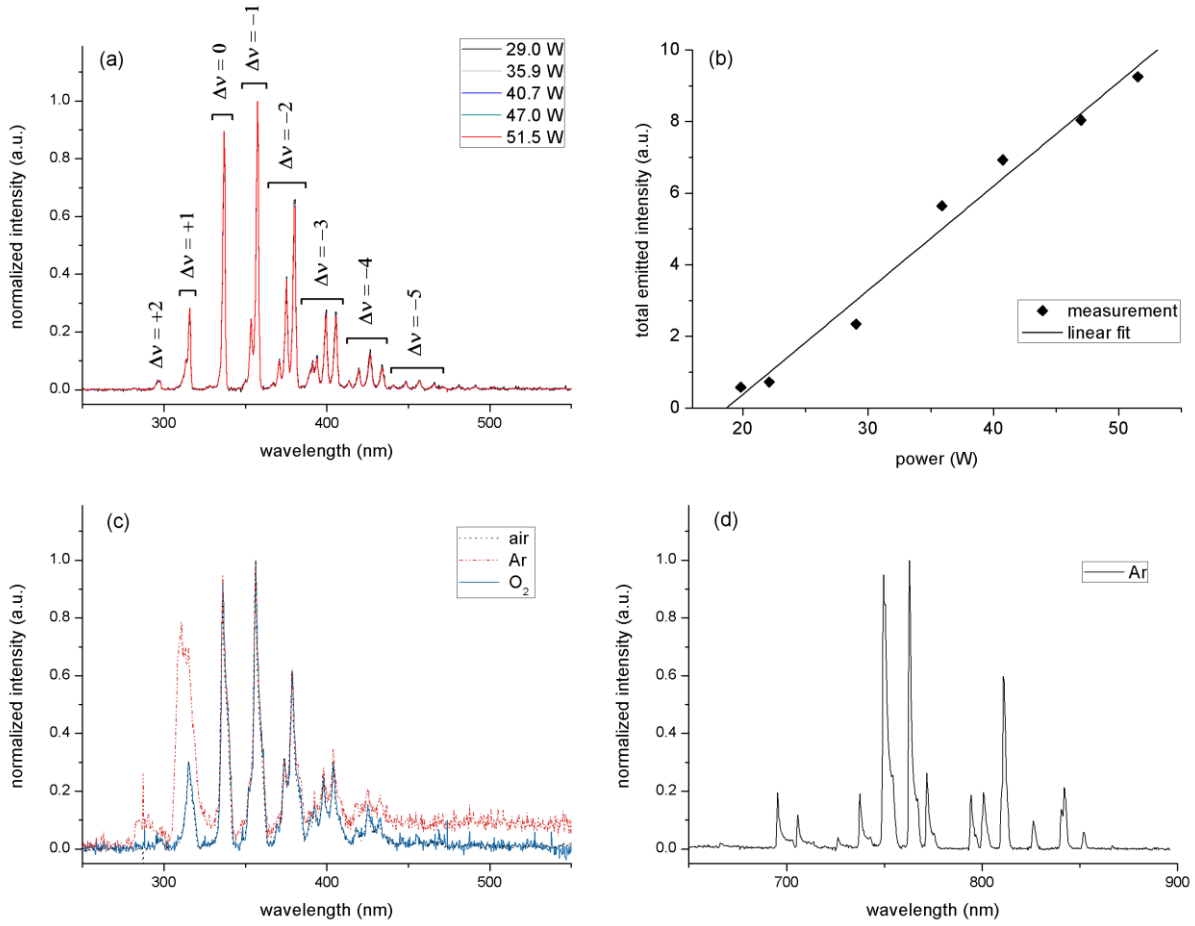

Figure 8.7 Normalized space-and-time averaged emission spectra of the discharge in the plasma chamber, measured with resolution of 1.3 nm. (a) Emission spectra of air plasma at different input power with reactor reference settings as defined for atrazine. Δν represents the change in quantum number ν of each radiative transition in the N_2(C-B) band system. (b) Emissivity in the wavelength interval 250 - 550 nm as a function of input power and linear fit to the data points. Emissivity is in good approximation directly proportional to $P - P_0$, with P_0 = 18.7 W the power threshold required for plasma formation with the reactor settings for atrazine. (c) Normalized emission spectra of air, Ar and O_2 plasma in the wavelength interval 250 - 550 nm with reactor reference settings as defined for all other micropollutants. (d) Emission lines of Ar(I) in the wavelength interval 650 - 900 nm.

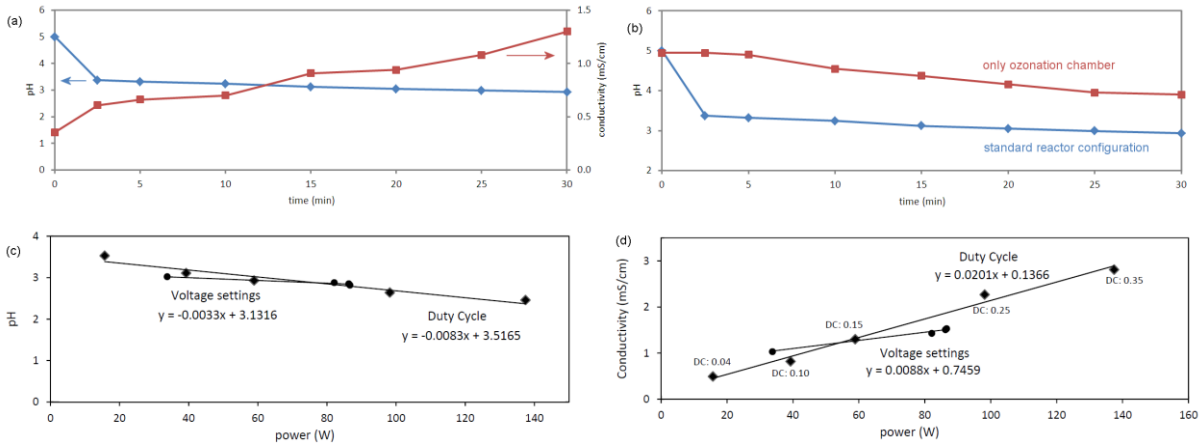

Figure 8.8 Measured pH and conductivity data during experiments with reactor settings as specified in Table 8.1 for all micropollutants except atrazine. Initial conductivity was set at 350 µS/cm by addition of $NaH_2PO_4 \bullet 2H_2O$ to demineralized water. (a) pH and conductivity as a function of treatment time for duty cycle DC = 0.15 and applied power of 59 W. (b) pH as a function of treatment time for the reactor in standard configuration compared to the solution subjected to plasma gas bubbling alone, with same operational settings as in (a). In the latter configuration, the investigated solution was not in direct contact with the active plasma zone, but another solution was recirculated through the plasma chamber in an isolated circuit, in order to have identical conditions as in the former configuration. (c) and (d) pH and conductivity after 30 min treatment time for different power at constant duty cycle of 0.15 and for different duty cycles.

8.2.2 Conductivity and pH

The formation of aqueous radicals and other species by plasma treatment induces a change in conductivity and pH during each experiment. Figure 8.8a gives an example of both solution parameters as a function of treatment time. As can be seen, conductivity grows gradually towards approximately 1.3 mS/cm during 30 min, while pH drops abruptly towards a value around 3 in the first 2.5 min of treatment time, followed by a slight further decrease. The end values of conductivity and pH after 30 min were found to be rather independent of initial conductivity and pH. When the solution is subject to plasma gas bubbling, but without direct contact to the active plasma region, the sharp pH drop at the start of the experiment does not occur, as shown in Figure 8.8b. This difference is explained with the formation of aqueous nitrites and nitrates in the plasma chamber through the dissolution of nitrogen oxides formed in the plasma by reactions of dissociated N_2 and O_2. During this process, H^+ ions are generated in the water phase, as described with the overall reactions [47]:

$$NO_2 + NO_2 + H_2O \longrightarrow NO_2^- + NO_3^- + 2H^+ \quad (8.2)$$

$$NO + NO_2 + H_2O \longrightarrow 2NO_2^- + 2H^+ \quad (8.3)$$

Other species can contribute to pH and conductivity change as well, including O_3 and H_2O_2. Figures 8.8c-d show the end values of both solution parameters for different power settings, where input power is varied for fixed duty cycle or where duty cycle is varied. Power at fixed duty cycle has a very limited effect on the final pH value. Increasing the duty cycle, on the other hand, has a slightly stronger effect, causing a reduction of the end pH with a value of approximately $\Delta pH = 1$ over the entire range of duty cycles used, due to more abundant formation of nitrites and nitrates. Accordingly, end conductivity is influenced stronger by duty cycle than by power at fixed duty cycle and is linearly proportional to both.

8.2.3 Aqueous H_2O_2 and gaseous O_3 generation in the reactor

As hydrogen peroxide and ozone play a prominent role in many advanced oxidation processes, they have received a lot of attention. Therefore, plasma reactors are often characterized in terms of H_2O_2 and O_3 production, in order to understand the contribution of both species to the overall degradation process. Table 4 summarizes data obtained from H_2O_2 and O_3 measurements in our reactor at operational settings as specified for atrazine (Table 8.1). At 73 W input power, H_2O_2 concentration remains constant at 182 ± 14 μM, after a rapid increase during first 5 minutes of treatment. Lack of further increase is caused by H_2O_2 decomposition in presence of activated carbon. This decomposition process by Zorflex® has been confirmed with experiments outside the reactor (results not shown here). Additionally, H_2O_2 scavenging by plasma produced nitrite ions leading to formation of peroxynitrous acid can also play an important role, which is in agreement with fast drop in pH to 3.3 in first 5 min of experiment. Average nett H_2O_2 production energy yield is estimated to be 0.51 g/kWh. This is in agreement with the literature study of Locke et al., where H_2O_2 production energy yield is investigated for reactors based on discharge over a liquid surface. According to this review, such reactors have reported H_2O_2 energy yields ranging from 0.04 to 5.0 g/kWh, with most data falling below 1 g/kWh [48].

Ozone production energy yield is 0.189 g/kWh at 24 W and halves when power is increased to 64 W. This yield reduction is probably due to higher plasma gas temperature at higher power, which results in faster ozone decomposition. Additionally, increased water content in the discharge with higher power can lower ozone production as well [49]. Quantitative measurement of aqueous ozone with the indigo method is generally assumed to be a very selective method. Application of this method on plasma-treated water samples from our reactor, however, resulted in aqueous ozone concentrations above the theoretically possible limit given by Henry's law. This is in agreement with the findings of Tarabová et al., who also detected more aqueous ozone than expected in plasma-treated solution by means of the indigo method [50]. The same authors measured indigo dye decomposition in peroxynitrite solution that had not been in contact with plasma and contributed this effect to oxidative attack of OH radicals formed by peroxynitrite decay.

Table 8.3 Measurements for determination of energy yield of H_2O_2 and O_3 production in the reactor.

Oxidant	Power (W)	Produced concentration	Production energy yield (g/kWh)
H_2O_2	73.3 ± 0.6	182 ± 14 μM [a]	0.51
O_3	23.7 ± 0.5	106 ppm [b]	0.189
	64.1 ± 1.3	136 ppm [b]	0.090

[a] After 5 min, concentration remains constant at this value.
[b] Measured at exhaust of the plasma chamber.

8.3 Kinetic analysis for atrazine removal

Since atrazine is the most investigated pesticide in water treatment research with plasma reactors, determining the energy efficiency for its removal in our reactor permits to make a comparison with other reactors in literature. Therefore, atrazine is treated separately from the other micropollutants in this chapter. Its removal is given as a function of treatment time for different experimental conditions in Figure 8.9. As expected from atrazine's low Henry's law constant of 2.664×10^{-4} Pa m^3 mol^{-1} [51], its evaporation by air bubbling alone is negligible. Adsorption by Zorflex® without plasma treatment causes linear atrazine concentration decrease of 1.08 μg L^{-1} min^{-1}, which is clearly slower than removal during plasma treatment. Decomposition kinetics can be described by an exponential decay which is in agreement with prior studies on atrazine decomposition with plasma without extra ozone bubbling and without adsorption [52]. Corresponding pseudo-first-order reaction rate constant k and energy yield G_{50} for 50% atrazine removal are presented in Table 8.4 for different experimental configurations. Value and error of reaction constant k are obtained with nonlinear least squares fitting based on the Levenberg-Marquardt algorithm. G_{50} (in g/kWh) is calculated by adapting the formula from [52],

$$G_x = -Ax\frac{kC_0V}{P\ln(1-x)} \tag{8.4}$$

where $A = 3.6 \times 10^6$ J/kWh is a unit conversion factor, x is the fraction of atrazine removal, k is reaction rate constant (in s^{-1}), C_0 is initial concentration (in g/L), V is treated water volume (in L) and P is applied power (in W). In convention with most literature, the index of G_x is expressed in percentage, thus G_{50} is defined for x = 0.5. As the results show, energy yield of atrazine removal is almost constant when input power is increased with a factor 3.5, which is interesting for application. Such negligible dependence of energy yield on input power is contradictory to some observations of other authors [53-55] which were done in different reactor configurations for much higher pollutant concentration where reaction kinetics starts to be concentration dependent. The effect of input power at constant duty cycle will be discussed further in section 8.6.4.

Table 8.4 Reaction rate constant k and energy yield G_{50} for 50% atrazine removal, with and without ozone bubbling and with ozonation alone.

Experimental parameter	Power (W)	k (10^{-3} s^{-1})	G_{50} (mg/kWh)
Plasma alone	27.0 ± 0.7	1.73 ± 0.10	2.25 ± 0.14
Ozone alone	25.7 ± 1.3	1.01 ± 0.01	1.53 ± 0.08
Plasma + ozone, low power	21.4 ± 0.8	2.02 ± 0.14	3.7 ± 0.3
Plasma + ozone, high power	70.0 ± 0.6	7.4 ± 1.7	4.1 ± 0.9

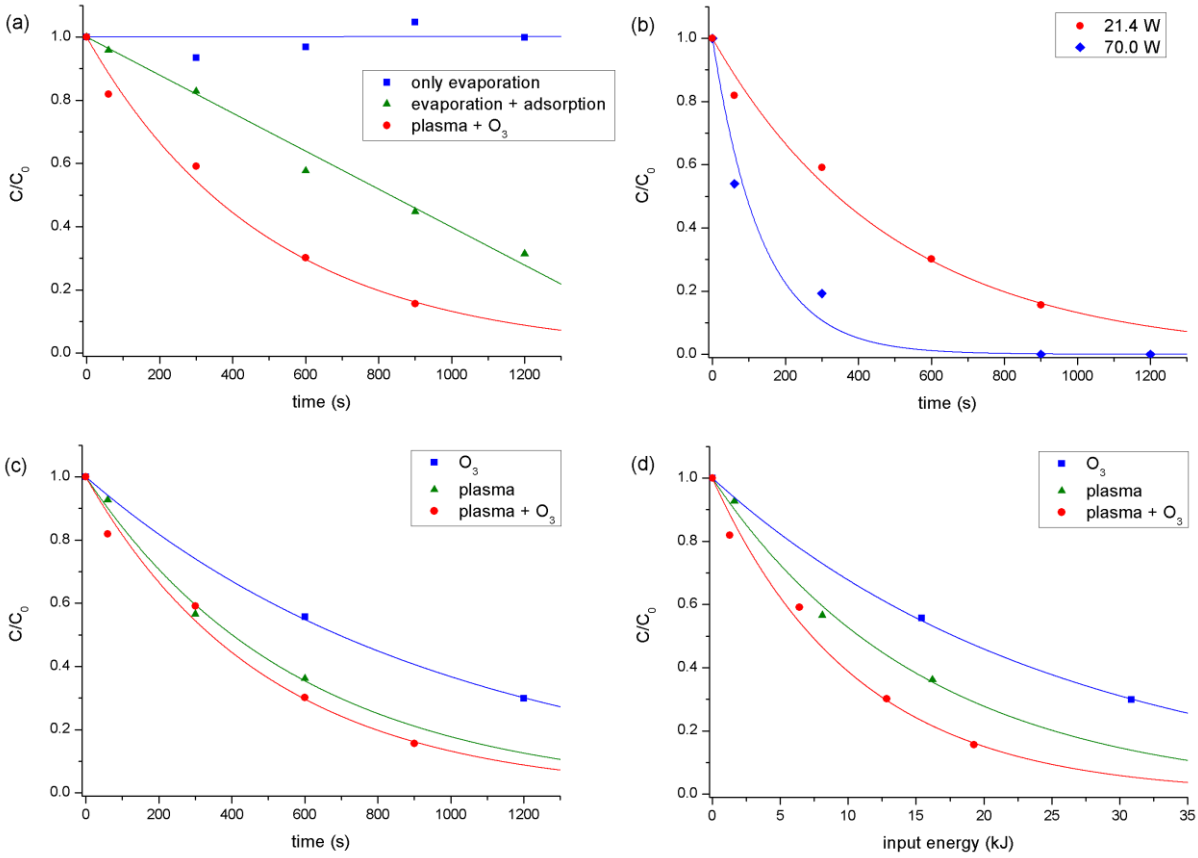

Figure 8.9 Kinetics of atrazine removal in the reactor. In all graphs, the red curve represents reference experiment with low input power of 21.4 W in normal reactor configuration (plasma + O_3). (a) Removal without plasma generation and in absence of Zorflex, but with air bubbling (only evaporation), without plasma generation, but with Zorflex and air bubbling (evaporation + adsorption). (b) Kinetics for different input power at fixed duty cycle in normal reactor configuration. (c-d) Kinetics for low power with only plasma gas bubbling (O_3) and only plasma treatment with adsorption without plasma gas bubbling (plasma). Initial atrazine concentration is always 30 μg/l. Error of measurement is 5% or less.

In order to investigate the contribution of ozone bubbling to the total atrazine removal, three experiments were performed for which the setup was adjusted accordingly:

- Atrazine decomposition by ozone bubbling alone. In this experiment, plasma gas was produced with the DBD reactor chamber and bubbled through the solution in the ozonation chamber. Another water solution with identical initial conductivity and volume was pumped along the discharge through the DBD reactor chamber in separate water circuit.
- Atrazine removal by adsorption combined with plasma, without ozone bubbling.
- Atrazine removal by adsorption, plasma and ozone bubbling.

The resulting atrazine removal kinetics is shown in Figure 8.9c and Table 8.4. In the accuracy of the measurement, energy yield G_{50} of the combined process of plasma treatment and ozonation equals the sum of the energy yields of each process apart, as can be easily deduced from Table 8.4. Based on the values of G_{50}, ozone bubbling contributes to 40.5% of total atrazine removal in the combined process. Plotting the kinetics as a function of input energy, as in Figure 8.9d, demonstrates that there is indeed a significant difference in energy efficiency between atrazine removal with the combined process and with plasma alone. Independence of the two separate mechanisms can be understood by means of very short life time of plasma produced active species (OH, HO_2, other radicals, N_2^* and metastables, O, and singlet oxygen). Therefore, these species will react immediately in the plasma chamber where they are produced, whereas O_3 will react slowly in the ozonation chamber, due to its low constant of reaction with atrazine $k_{A,O3} = 5.65\ M^{-1}s^{-1}$ (Table 8.2).

Table 8.5 summarizes the energy efficiency of all plasma reactors used for atrazine removal which we have found in literature, with exclusion of reactors that use gas discharge solely for UV production. Where G_x value was not explicitly given, we have calculated its value based on data found in the corresponding reports, such as treatment time t, treated solution volume V, applied power P, pseudo-first-order reaction rate constant k and atrazine removal percentage x. In case that a required value was not explicitly given, it was determined from the available graphs in the report, by means of a raster graphics editor. Special care was taken in unit conversion. Degradation energy yield G_x is not recommended for direct comparison of reactor energy efficiency, since it is strongly dependent on initial pollutant concentration C_0. Therefore, we used electrical energy per order EEO, as introduced for low contaminant concentration by Cater et al. [56]. This quantity is only slightly dependent on C_0. EEO is defined as the number of kilowatt hours of electrical energy required to reduce a pollutant's concentration by 1 order of magnitude (90%) in 1 m^3 of contaminated water. Accordingly, its formula is given by [57]

$$EEO = \frac{P \times t}{3600 \times V \times \log(C_0/C_f)} = \frac{\ln(10) \times P}{3600 \times V \times k} \tag{8.5}$$

where C_f is the final pollutant concentration after treatment time t and all other parameters are defined as in equation 2. EEO (in kWh/m^3) is related to G_{90} and G_x (in g/kWh) by

$$EEO = 0.9 \times 10^3 \frac{C_0}{G_{90}} = \frac{-x}{\ln(1-x)} \times \ln(10) \times 10^3 \frac{C_0}{G_x} \quad (8.6)$$

where C_0 is expressed in g/L. From the 13.6 kWh/m^3 consumption measured in our reactor and an electricity price of 0.15 euro/kWh, the treatment cost becomes 2.04 euro/m^3, which is comparable to conventional water treatment costs of 1 to 5 euro/m^3. Based on the value of EEO in Table 8.5, only two reactors have higher energy efficiency than ours. Mededovic and Locke have found high efficiency for plasma generation directly in the liquid phase [58]. They used a rather high initial atrazine concentration of 5 mg/L. Since EEO tends to decrease for lower initial concentration, their system is possibly the most energy efficient one of Table 8.5 for atrazine removal (see also section 8.6.2 for more information on the concentration effect). Gerrity et al. generated pulsed corona discharge in the gas phase over a moving water film for degradation of 6 pharmaceuticals and atrazine in spiked surface water [59]. In single-pass experiment, they found median EEO values ranging from 1.0 to 3.7 kWh/m^3 for the different micropollutants, where atrazine was the most persistent one. It should be noted that Gerrity et al. are the only authors in Table 8.5 who did not use distilled water as water matrix. Instead, they used spiked surface water containing humic acid, which can have a strong influence on the EEO value.

Table 8.5 Comparison of energy yield G_x and electrical energy per order EEO for atrazine degradation in different plasma reactors mentioned in literature.

Reactor type	C_0 (mg/L)	x (%)	G_x (mg/kWh)	EEO (kWh/m^3)	reference
Pulsed corona over water film	0.0011	90.0	0.272	3.7	[59]
Pulsed corona in liquid phase	5	90.0	910	4.9	[58]
AC DBD in air over falling water film	0.030	90.0	1.99	13.6	This Chapter, 21 W
on Zorflex®	1.0	90.0	29.5	30.5	This Chapter, 19 W
Pulsed DBD over nanofiber membrane	0.030	50.0	2.69	18.5	Chapter 6
Pulsed arc in liquid phase	0.11	86.5	5.44	19.7	[60]
AC DBD in He over falling water film	5.0	90.0	88.9	50.6	[52]
Pulsed corona over water surface	25.9	56.5	560	72.3	[61]
AC corona for ionized air bubbling	5.0	50.0	95.6	86.9	[57]
DBD for UV irradiation and ionized air bubbling	5.8	88.6	51.4	106.0	[62]

8.4 Atrazine by-product analysis

Additional attention is required to the atrazine oxidation pathway, since this is important for estimating toxicity of metabolites. By-product formation and degradation is investigated for low power (18.8 ± 0.3 W) and high power (70.2 ± 0.4 W) conditions after 15 and 30 min of

treatment. Four chlorine containing oxidation products have been found with lowest protonated monoisotopic mass 146.02 Da, 188.07 Da, 216.06 Da and 230.08 Da. They are identified respectively as didealkylatrazine (DIDEA), deethylatrazine (DEA), simazine amide (CDET) and atrazine amide (CDIT). Relative abundance of each by-product decreases in last 15 min of treatment time and decreases with increasing power, as shown in Figure 8.10. CDET and CDIT are mostly found amongst the first generation intermediates in several suggested atrazine degradation pathways by AOPs [63-65]. DEA, on the other hand, has been proposed in literature as both a first generation by-product by direct dealkylation and a second generation by-product through stable intermediates. Non-oxidative DEA formation by means of Mn-oxides is discussed in [66]. Pospíšil et al proposed DEA formation by two-electron reduction of atrazine in acidic media [67]. Several other authors see DEA as a degradation product of oxidized atrazine intermediates such as CDIT [65, 68-70]. Nevertheless, the selectivity of each pathway has not been reported in literature to our knowledge, for any AOP. DIDEA is one of the deep oxidation atrazine by-products, since its formation requires double dealkylation, where DEA is a possible intermediate.

To our knowledge, identified atrazine decomposition by-products from plasma treatment have only been reported before in [52, 58, 62]. Mededovic et al. used pulsed electrical discharge in liquid phase with a pin-to-plate electrode configuration. They identified the same by-products as we did, plus deisopropylatrazine and ammeline, which is formed from dehalogenation of DIDEA. Hijosa-Valsero et al. worked with an AC powered DBD reactor like ours, but with helium as feed gas and without extra ozonation chamber. They also identified DEA and CDIT, aside from deisopropylatrazine and one less common intermediate 4-chloro-6-(ethenylamino)-1,3,5-triazin-2-yl. Zhu et al. designed a novel wire-cylinder DBD plasma reactor with plasma generation in the gas phase for UV irradiation and plasma gas bubbling in the treated solution. According to their LC–TOF-MS analysis, CDIT and one isomere were formed during the degradation process, next to 4 dechlorinated compounds. De-chlorination of atrazine in advanced oxidation processes is mostly observed for processes that involve direct photolysis or sonolysis [71], which is in good agreement with these observations. In Mededovic et al., shock waves and intense UV radiation during discharge directly in liquid can explain the presence of ammeline. In Zhu et al., UV irradiation causes de-chlorination. Photolysis by plasma produced photons only plays a minor role in our reactor and the one of Hijosa-Valsero et al. In contrast, oxidation by direct, dark ozonation, hydroxyl radicals, singlet oxygen and Fenton's reagent has low de-chlorination rate and mainly occurs through effective attack on the alkyl groups [68, 72], which explains formation of chlorine-containing oxidation by-products.

Further, Zhu et al. found a strong initial increase of the treated solution's acute toxicity to Photobacterium phosphorem T3 during about the first 80% atrazine removal. However, the solution had become nearly non-toxic after adding 67% extra input energy. An initial acute toxicity increase of treated atrazine solution has been commonly found for other AOPs, such

as photocatalytic oxidation [73], photo-Fenton coupled with ozonation [74] and electrochemical treatment [71]. Although the main oxidation by-products of atrazine are found to be less toxic than their parent molecule, toxicity increase is attributed by most authors to atrazine intermediates. Unidentified oxidation by-products or interactive toxicity of by-products can underlie this phenomenon [73]. Nevertheless, higher toxicity does not necessarily indicate a lower biodegradability, as suggested by [75]. This keeps AOPs and plasma treatment in particular feasible as treatment step prior to biodegradation.

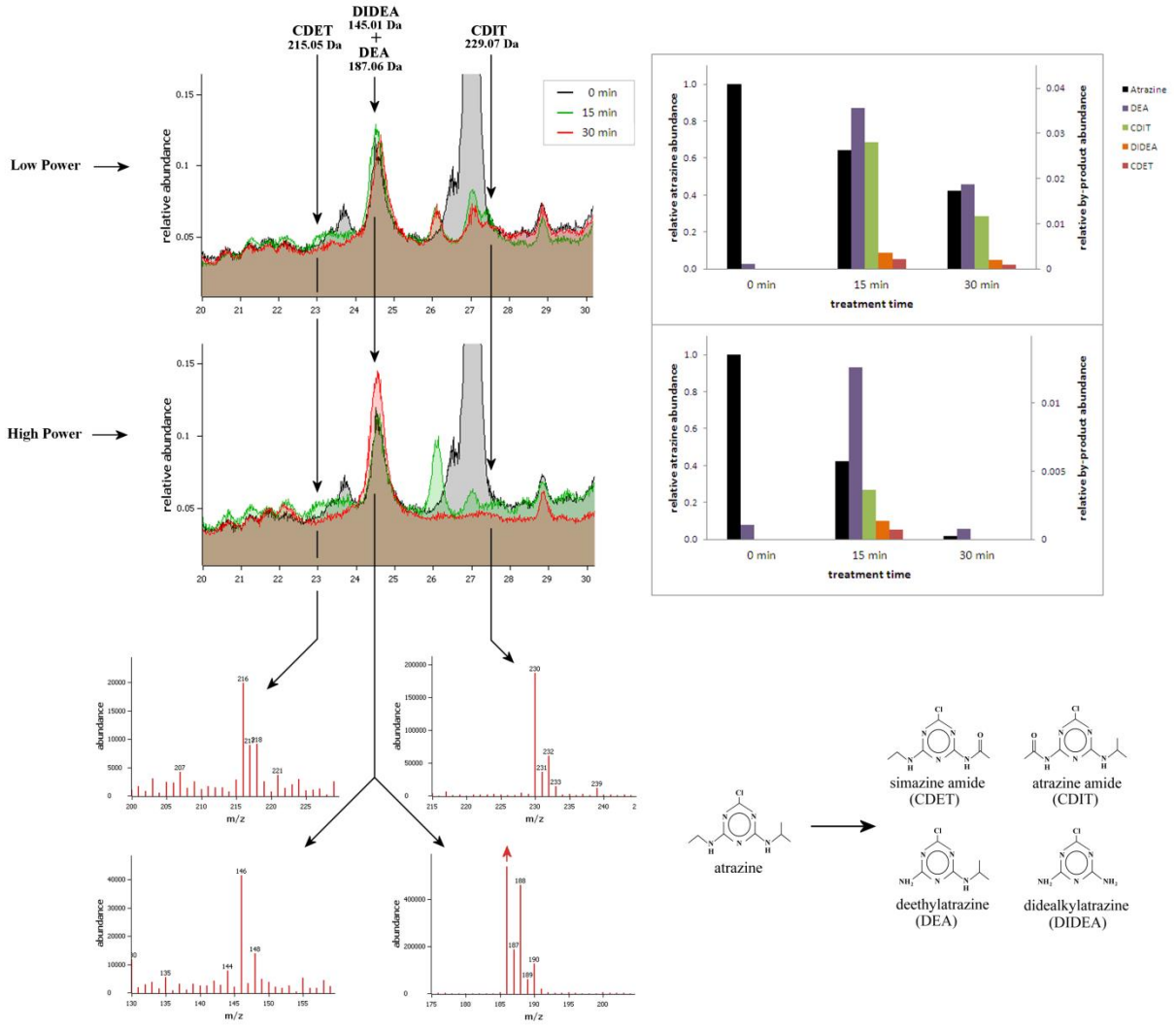

Figure 8.10 HPLC-MS analysis results of decomposition of 1 mg/L atrazine after 15 and 30 minutes of treatment for low power (18.8 ± 0.3 W) and high power (70.2 ± 0.4 W) conditions. In the chromatograms between retention time of 20 and 30 min (top left), abundance of every component is taken relative to the initial atrazine peak maximum. For every identified atrazine oxidation by-product, the mass spectrum is given (bottom left). The column diagrams present abundance of each by-product relative to the total initial atrazine abundance (top right). Structural formula of atrazine and its detected by-products are shown at the bottom right. Abundance of each compound is not calibrated and can only be used as indication of corresponding concentration.

8.5 Zorflex® characterization

Efficiency of an activated carbon material for organic compound adsorption mainly depends on its pore size distribution, surface chemistry and mineral matter content [76]. These features are strongly determined by the precursor material, preparation procedure and activation method used during the production process. Next to that, several external factors can modify the adsorptive properties over time. For instance, surface chemistry is expected to change by the interaction of the activated carbon surface with plasma-generated oxidants, as explained in section 8.2. On the other hand, accumulation of adsorbed aqueous matter will exhaust the activated carbon, diminishing further adsorption. Investigating the time-scale and magnitude of these influences in our reactor is important for at least two reasons. First of all, modifications of the Zorflex® textile can cause a decline in reactor efficiency over time, reducing its sustainability. Secondly, variation in Zorflex® performance hinders the reproducibility of experimental runs, complicating the comparison of different experiments. It is therefore important to characterize the Zorflex® textile by means of adsorption rate measurements in order to investigate how its functionality varies in time. This is the topic of following section. Afterwards, two desorption experiments with atrazine as model micropollutant are discussed, to reveal which compounds remain adsorbed on Zorflex® after plasma treatment.

8.5.1 Adsorption experiments

To determine the reproducibility of adsorption on Zorflex®, five identical experiments without plasma treatment are performed on different moments. During each experiment, 114 µg/L diuron solution is recirculated in the reactor under reference settings and samples are taken at different treatment times for GC-MS analysis. Figure 8.11a shows the results for one Zorflex® sample Z1 before it was in contact with plasma, after 1 hour of plasma contact and after multiple plasma treatment experiments equivalent to 27.5 hours of plasma contact. As can be seen, the adsorption rate is in good approximation constant for all three measurements, indicating an adequate comparability of plasma treatment experiments and a sustainable Zorflex® textile. A similar constancy of adsorption has been observed in a later study for 6 other compounds, including atrazine and alachlor (data not shown). Nonetheless, a significant increase in diuron and alachlor adsorption rate of an extensively used other Zorflex® sample Z2 is found in Figure 8.11b and 8.11c, after 10 hours of continuous plasma treatment with recirculation of demineralized water. Possibly, this dissimilarity is due to the absence of micropollutants during the 10 hours of plasma contact for sample Z2. This permits full mineralization of adsorbed contaminants by aqueous oxidants without the competitive process of pore blockage by newly adsorbed organics. A second possible mechanism behind the adsorption enhancement is an increase of micropore size and total pore volume of the activated carbon under influence of oxidative species. In a study by Chiang et al., for example, ozonation of activated carbon was shown to improve total pore

volume with 9.0 %, leading to enhanced adsorption of volatile methylethylketone and benzene [77]. As a third explanation, the improved adsorption rate can be caused by a change in surface chemistry of the activated carbon textile. Functional groups on activated carbon surface are predominantly oxygen complexes such as carbonyl groups. Such oxygen complexes can be generated via reaction with oxidizing gases (dry oxidation) and via reaction with oxidizing solutions (wet oxidation) [78]. For wet oxidation, aqueous solutions of HNO_3 and H_2O_2 are commonly applied, two oxidants that are also generated under plasma treatment (see sections 8.2 and 8.6.7). Formation of oxygen complexes, however, often leads to acidification of the activated carbon surface, which is generally assumed to impair organic uptake. Nonetheless, each functional group can change organic adsorption selectively, favoring the adoption of certain compounds, while obstructing the uptake of others [78].

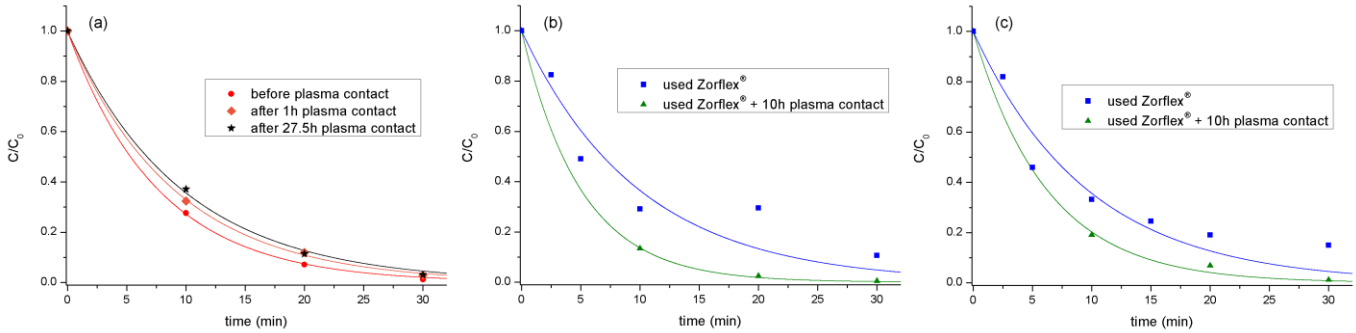

Figure 8.11 Normalized diuron concentration as a function of treatment time under reference settings (air flow rate of 1.00 SLM, water flow rate of 95.3 mL/min) without plasma generation for two different Zorflex® samples Z1 (a) and Z2 (b). (a) For Z1, the first experiment (before plasma contact) was conducted immediately after installing the new Zorflex® sample into the reactor. Afterwards, 500 mL of demineralized water was recirculated for 1 hour through the reactor under plasma treatment with reference settings and the next experiment (after 1 h plasma contact) was performed. The third experiment (after 27.5 h plasma contact) was carried out after several plasma treatment experiments with different micropollutants and settings, as described in 8.6, of which 6.5 hours with air plasma, 5.5 hours with argon plasma and 15.5 hours with oxygen plasma. (b) For Z2, the first experiment (used Zorflex®) was performed after more than 30 hours of similar plasma treatment experiments with air. Afterwards, 500 mL of demineralized water was recirculated for 10 hours through the reactor under continuous plasma treatment with air and the next experiment (used Zorflex® + 10 h plasma contact) was conducted. The exponential fitting of the last adsorption experiment of Z1 and the first adsorption experiment of Z2 are nearly indistinguishable. (c) Same experiment as (b), but for alachlor solution with initial concentration of 57 µg/L.

Regeneration of exhausted activated carbon by means of DBD discharge has been reported in several studies, under wet oxidation of activated carbon with about 15 % water content [79-81] up to 37.5 % water content [82]. In [83], granular activated carbon showed improved recovery and increased phenol decomposition for increasing water content up to 31 %. In these studies, decomposition of several adsorbed organic compounds was observed, as well as an increase of internal surface area and pore volume and formation of oxygen containing functional surface groups. Accordingly, all three processes were cited as underlying regeneration mechanisms. It is however unclear which one is the most dominant process.

8.5.2 Desorption experiment 1: treatment of aqueous atrazine

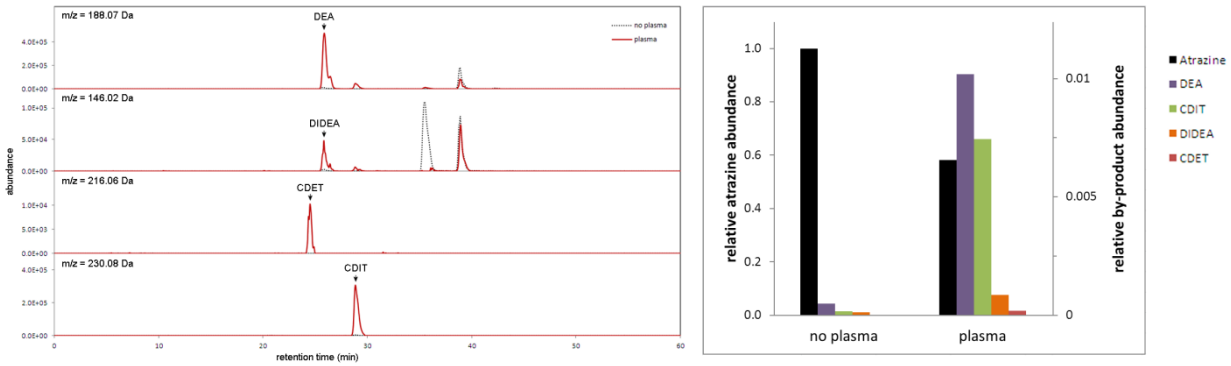

Figure 8.12 HPLC-MS analysis results of desorbed compounds from Zorflex® to dichloromethane solution after evaporation to 1.5 mL end volume. Chromatograms (left) and abundance of every identified by-product relative to total atrazine abundance (right) are shown for Zorflex textile in the experiment with only adsorption and air bubbling (no plasma) and for Zorflex textile in the experiment with plasma treatment and ozonation (plasma). Abundance of each compound as measured with HPLC-MS is not calibrated and can only be used as indication of corresponding concentration.

In order to investigate which compounds are adsorbed on Zorflex® after treatment of aqueous atrazine, two experiments were conducted with newly installed Zorflex® textile. In the first experiment, solution was pumped through the reactor without plasma discharge, but with air bubbling. The second experiment was analogue to the first one, but with plasma discharge at high power of 75.9 ± 1.2 W. Both experiments were performed with 200 µg/L initial atrazine concentration for 30 minutes and other experimental settings specified in Table 8.1. After each experiment, desorption analysis was performed as described in section 8.1.8. As shown in Figure 8.12, all 4 identified atrazine oxidation by-products in water phase are also detected as desorbed compounds from Zorflex®. Moreover, their relative abundance to atrazine and to each other after desorption is comparable to their relative abundance detected in water phase. Differences can be explained by different adsorption and desorption rates of each compound, different reaction rates while adsorbed and the lower initial atrazine concentration of 200 µg/L of the water solution used for desorption analysis. With calibrated GC-MS analysis, atrazine concentration in dichloromethane solution after desorption is

determined to be 522 μg/L and 304 μg/L for the experiment without plasma and the experiment with plasma, respectively. Therefore, Zorflex® contained 41.8% less atrazine at the end of the latter experiment. This is another confirmation that a significant amount of atrazine is decomposed by plasma and ozonation and that adsorption plays an additional role in its removal.

8.5.3 Desorption experiment 2: treatment of adsorbed atrazine

Based on observations by other authors, micropollutants can be oxidized in our reactor while solved in the water bulk and while adsorbed on the activated carbon textile, where oxidizing species can be solved or adsorbed as well, as shown in Figure 8.12 [84]. In order to test this hypothesis for our reactor, two additional experiments with newly installed Zorflex® were conducted for desorption analysis. Prior to both experiments, atrazine was adsorbed on Zorflex® textile by recirculating 500 mL of a 200 μg/L atrazine solution through the setup for one hour. As measured with GC-MS analysis of water samples before and after this adsorption process, 99.0 ± 0.2 % of atrazine content was adsorbed on Zorflex® in this manner. Afterwards, the reactor was rinsed with demineralized water. In the first experiment, 500 mL of demineralized water was pumped through the reactor without plasma discharge, but with air bubbling. The second experiment was analogue to the first one, but with plasma discharge at high power of 72.8 ± 1.2 W. Both experiments were performed for 30 minutes and other experimental settings specified in Table 8.1. The demineralized water solution was checked for traces of atrazine and its by-products before and after each experiment by means of GC-MS and HPLC-MS analysis. No aqueous by-products were found and aqueous atrazine concentration was below the limit of detection. Remarkably, adsorbed by-products were also not found on both Zorflex® textiles, as measured with desorption analysis described in section 8.1.8. With calibrated GC-MS analysis, atrazine concentration in dichloromethane solution after desorption is determined to be 563 μg/L and 281 μg/L for the experiment without plasma and the experiment with plasma, respectively. Therefore, Zorflex® contained 49.9% less atrazine in the latter experiment. This removal percentage is slightly higher than the 41.8% atrazine removal in desorption experiment 1 from previous section. The stronger removal and absence of detected by-products during oxidation of adsorbed atrazine suggests that atrazine is more energy efficiently and more deeply mineralized in the reactor when it is adsorbed on Zorflex® than when it is dissolved in the solution under treatment. This is in good agreement with the conclusion of Chapter 6 that higher local micropollutant concentration at the plasma-water interface leads to more energy efficient oxidation. This concentration effect will be discussed in more detail in section 8.6.2. Further investigation is required to confirm that this is also the case for different reactor settings, other micropollutants and different initial concentrations. Anyhow, the comparison of adsorbed and aqueous micropollutant decomposition by means of plasma discharge in general is an important research question that deserves additional attention.

8.6 Kinetic analysis for removal of 5 micropollutants

In this section, the reactor's performance is further investigated in more detail as a function of a few operational parameters and working conditions. To this end, removal experiments are performed in parallel for 5 selected micropollutants with diverse properties (see section 8.1.2 and Table 8.2), to gain a more comprehensive view and to uncover compound-related issues, if any. More statistical information of these experiments is found in Table 8.A in the Appendix.

8.6.1 Reference conditions

Figure 8.13 shows the removal of each micropollutant under the reference conditions of Table 8.1 in air atmosphere, with plasma generation, without plasma generation and in absence of both plasma and Zorflex®. As for atrazine, the corresponding nonlinear least squares exponential fitting is found by means of the Levenberg-Marquardt algorithm. Table 8.6 enlists the reciprocal time constant τ^{-1} or pseudo-first-order reaction rate constant k for each removal experiment, as deduced from the fitting, as well as the initial concentration of each micropollutant. As expected, the most volatile compounds, α-HCH and PeCB, decline fastest by air bubbling alone, while the most involatile compound, isoproturon, does not evaporate at all. Surprisingly, evaporation of diuron is relatively high, while its reported Henry law constant is lower than the one of atrazine (Table 8.2), which was not significantly removed by air bubbling (see Figure 8.9a). This can be partly explained with the three times lower air flow for atrazine and with direct oxidation of diuron by the introduced aqueous oxygen. However, another reason can be an inaccuracy in the reported Henry law constant H of diuron, as this value is solely based on calculations [31] and no experimental confirmation was found in literature. Apart from this deviation, the observed order of volatility PeCB > α-HCH > diuron > alachlor > isoproturon in our experiments agrees well with the literature values of the Henry law constant.

When Zorflex® is added in the reactor, stronger removal is observed for all micropollutants. Alachlor and isoproturon appear to be the most efficiently removed compounds by adsorption, followed by diuron. PeCB, on the other hand, is adsorbed least efficiently. According to Moreno-Castilla, four features of an organic compound regulate its rate of adsorption on activated carbon [85]:

1. molecular size;
2. acid dissociation constant pKa, in case it is an electrolyte;
3. solubility;
4. nature of substituents, in case it is aromatic.

The molecular size determines the compound's accessibility to the micro-pores of the carbon. The pKa value controls the dissociation of an electrolytic compound into ions, dependent on solution pH. Consequently, adsorption of the resulting organic ion is strongly regulated by

electrostatic interaction with the charges on the carbon surface. A molecule's water solubility is directly related to its hydrophobicity, which dictates how easily it is rejected by the aqueous solution and thus how readily it is accepted by another phase contacting the solution. Substituents on the aromatic ring can be electron-withdrawing or electron-donating, which is expected to affect the π-π dispersion interaction between the aromatic

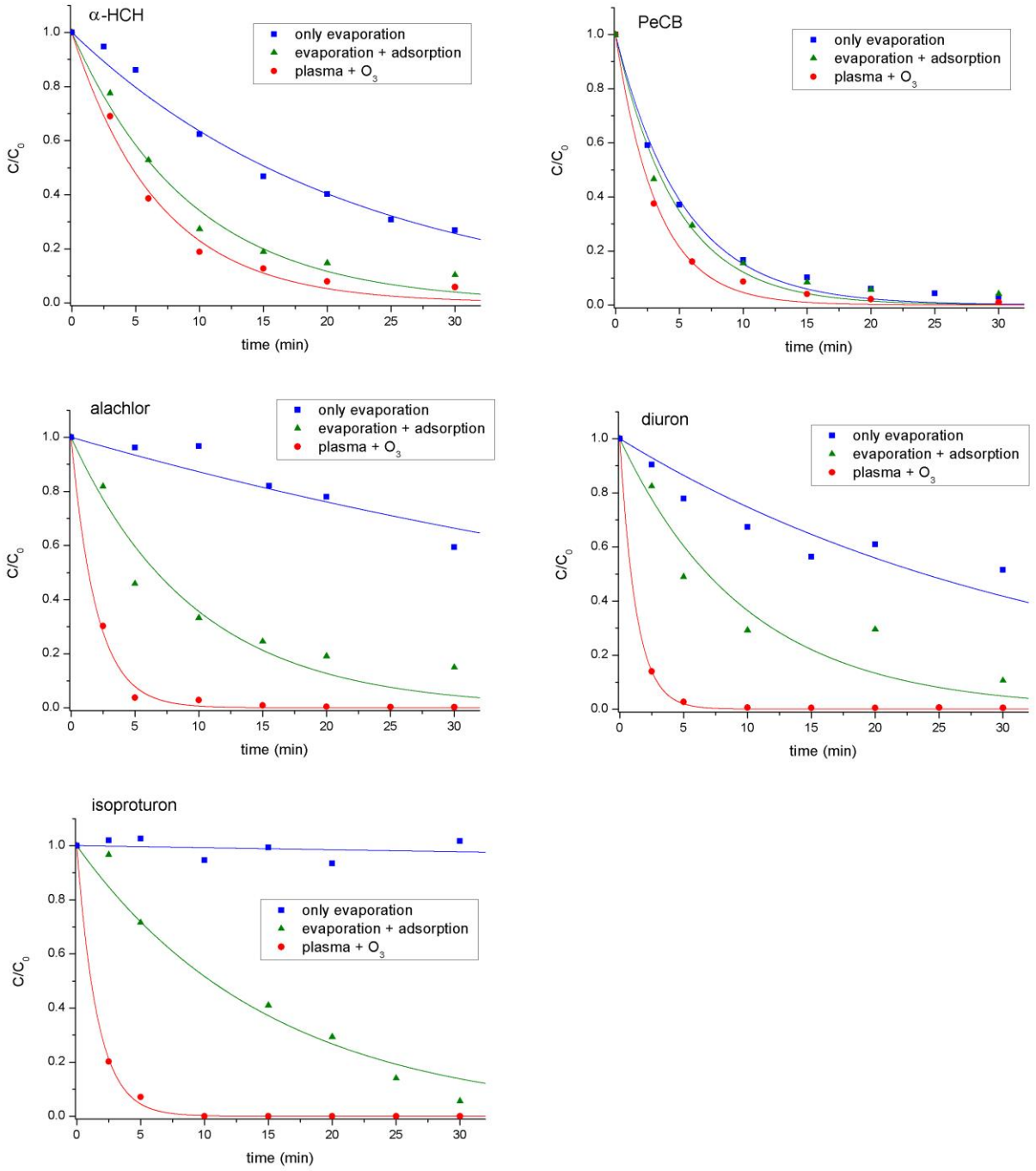

Figure 8.13 Removal kinetics for the 5 micropollutants in the reactor without plasma generation and in absence of Zorflex, but with air bubbling (only evaporation), without plasma generation, but with Zorflex and air bubbling (evaporation + adsorption) and with plasma generation in the reference settings (plasma + O_3).

Table 8.6 Initial concentration C_0, applied power, reciprocal of the time constant τ_e for only evaporation, reciprocal of the time constant τ_{e+a} for evaporation and adsorption, reaction rate k, energy yield G_{50} and electrical energy per order EEO for the reactor in reference settings.

	atrazine	α-HCH	PeCB	alachlor	diuron	isoproturon
C_0 (μg/L)	30.0 ± 1.5	215 ± 6	67 ± 2	57 ± 4	114 ± 6	101 ± 3
Power (W)	21.4 ± 0.8	49.9 ± 1.8	48.9 ± 1.7	40.3 ± 0.3	39.7 ± 0.5	41.0 ± 1.0
$1/\tau_e$ (10^{-5} s^{-1})	< 2.5	76 ± 3	314 ± 17	23 ± 3	49 ± 6	1.3 ± 1.5
$1/\tau_{e+a}$ (10^{-4} s^{-1})	8.9 ± 0.4	17.9 ± 1.2	35 ± 3	17 ± 2	17 ± 3	11.0 ± 1.0
k (10^{-3} s^{-1})	2.02 ± 0.14	2.45 ± 0.14	5.1 ± 0.3	8.5 ± 0.4	13.0 ± 0.2	10.3 ± 0.4
G_{50} (mg/kWh)	3.7 ± 0.3	13.7 ± 1.0	9.0 ± 0.6	15.5 ± 1.3	49 ± 3	33.0 ± 1.8
EEO (kWh/m^3)	13.6 ± 1.1	26.1 ± 1.7	12.2 ± 0.7	6.1 ± 0.3	3.90 ± 0.09	5.1 ± 0.2

ring of the compound and the aromatic structure of the graphene layers. Possibly, donor-acceptor interactions between the compound's aromatic ring or substituents and functional surface groups such as carbonyl can also play a role.

Since all selected micropollutants in our study are similar in size and nonionic, differences in their adsorption rate are supposed to be regulated predominantly by their solubility (see Table 8.2) and their substituents. Clearly, solubility is not the dominant factor, since the best soluble compounds, alachlor and isoproturon, are adsorbed more rapidly, while the most hydrophobic molecules, α-HCH and PeCB, are adsorbed worst. The amount of electron-withdrawing chlorine atoms on the aromatic ring of a micropollutant, on the other hand, seems to strongly regulate the adsorption rate. The five chlorine atoms present in PeCB strongly decrease the electron density in the ring, which explains its low adsorption on Zorflex®. Alachlor and isoproturon, in contrast, have an electron-rich aromatic cycle because of the absence of direct chlorine substitution. Diuron has a very similar molecular structure to isoproturon, but with two chlorines attached to the ring, corresponding to a lower adsorption rate. This is in good agreement with the observed results, suggesting that the above mentioned π-π dispersion or acceptor-donor interactions are the dominant mechanisms for adsorption in our experiments.

When plasma is turned on, all micropollutants are removed to higher extent. The additional removal process by plasma oxidation is strongest for isoproturon, diuron and alachlor, while α-HCH and PeCB appear most recalcitrant to oxidation by plasma-generated aqueous oxidants. It should be emphasized, nonetheless, that decomposition processes occur in the vapor phase as well, under influence of gaseous oxidants. In the active plasma region, such processes are expected to be relatively frequent, due to the high abundance of reactive species, including radicals, electrons and photons. Outside the active plasma region, for instance in the bubbling plasma gas, reactions with long-living oxidants such as ozone and

ions can take the upper hand. Investigation of these gaseous decomposition processes falls outside the scope of this work. However, a detailed study on this topic is made by Ognier et al., who used an AC powered coaxial DBD reactor similar to ours but without additional bubbling for treatment of 4 volatile compounds: acetic acid, phenol, ethanol and 1-heptanol [86]. When plasma was switched on in their reactor, an increase was observed in mass transfer of each pollutant from the liquid to the gas phase, proportional to the corresponding Henry law constant. This mass transfer increased was attributed to the intense mixing in the liquid film and the reaction of the pollutant with active species in the gaseous phase, in agreement with computational fluid dynamic modelling results. Interestingly, removal of the four volatile compounds was dominated by this mass transfer process, while aqueous oxidation reactions seemed to play only a subordinate role. The same authors also measured a minimum of 95 % decomposition of these compounds in the gas phase, by means of a calibrated solid phase microextraction fibre at the gas outlet of the reactor and subsequent analysis with gas chromatography coupled to a flame ionization detector. Accordingly, decomposition in the gas phase was found to be significantly more effective that decomposition in the liquid phase.

Table 8.6 gives the energy yield G_{50} and electrical energy per order EEO of the overall removal for each micropollutant in our reactor. The input energy required for 90% reduction increases in the order: diuron < isoproturon < alachlor < PeCB < α-HCH, where PeCB removal is approximately as energy intensive as atrazine removal, yet for different conditions. With the used reactor settings, it takes about 7 times as much energy to remove the same amount of α-HCH from the solution as compared to diuron, indicating that EEO values in our reactor for different compounds can vary over almost one order of magnitude. With the inclusion of more micropollutants, this range is likely to expand further. This expansion, however, is expected to be directed mostly towards lower EEO values, since the selected compounds are some of the most recalcitrant organic pollutants known to man (see section 8.1.2).

8.6.2 Effect of pH and salt addition

As this work mainly focusses on reactor characterization and optimization, the influence of the water matrix is illustrated only briefly for isoproturon. Figure 8.14a shows the decomposition of the pesticide for different initial pH. In the reference experiment of previous section, initial pH is 5.03. Reduction of pH to 4.2 with addition of H_2SO_4 has little effect on the oxidation rate, but further decrease to 2.08 leads to significant improvement of the degradation process. This is likely due to the formation of peroxymonosulfuric acid (H_2SO_5), also known as Caro's acid, via the reaction [87]

$$H_2SO_4 + H_2O_2 \longrightarrow H_2SO_5 + H_2O \tag{8.7}$$

Peroxymonosulfuric acid is one of the strongest oxidants known to man, which is able to decompose organics non-selectively with a redox potential comparable to the one of the

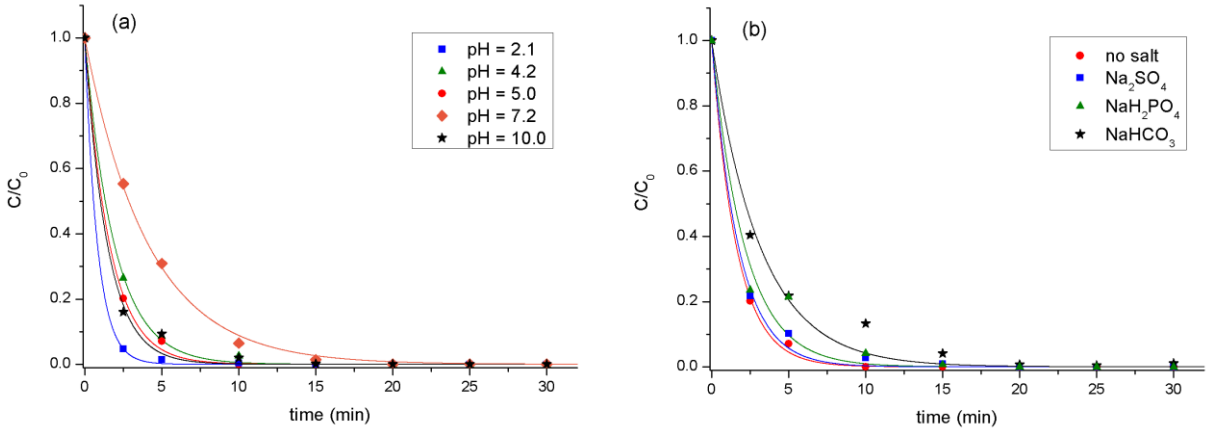

Figure 8.14 Kinetics for isoproturon removal (a) for different initial pH and (b) with initial salt addition. pH was lowered by addition of H_2SO_4 and raised by addition of NaOH. The salts were added in a concentration of 1.76 mM. For NaH_2PO_4, this resulted in an initial conductivity of 350 µs/cm.

hydroxyl radical [88]. Increase of pH to 7.2 with addition of NaOH quenches the oxidation of isoproturon, while further increase to a pH of 10 enhances the decomposition process again. Since isoproturon is relatively reactive to ozone, with reported values of k_{O3} from 141 to 2191 M^{-1} s^{-1} (Table 8.2), its degradation in our reactor is strongly influenced by the stability of aqueous O_3. Elevation of pH is known to gradually lower the stability of ozone, explaining the initial decrease. It is, however, less known that in highly alkaline solution, starting from addition of 5 M NaOH, ozone stability abruptly rises again [89, 90]. In the case that this stage of high O_3 stability has not been reached yet at pH = 10, the re-established of the decomposition rate can alternatively be explained with the peroxone process. Namely, the peroxone rate constant increases with pH and can take the upper hand in isoproturon decomposition above a certain pH value [91].

The influence of salt addition is shown in Figure 8.14b. In the accuracy of the measurements, addition of NaH_2PO_4 and Na_2SO_4 did not have any visible effect on isoproturon decomposition. $NaHCO_3$, however, significantly lowered the oxidation rate. Carbonate is an effective OH scavenger and can even reform ozone through the reactions [89]:

$$CO_3^{2-} + OH \longrightarrow CO_3^{-} + OH^{-} \quad (8.8)$$

$$CO_3^{-} + O_3^{-} \longrightarrow CO_3^{2-} + O_3 \quad (8.9)$$

Therefore, the reduction in the reaction rate is due to inhibition of OH radical attack, while O_3 is stabilized. As the above results indicate, direct attack by O_3 as well as by OH radicals play significant roles during the degradation of isoproturon at the reference conditions.

8.6.3 Effect of initial concentration

As suggested in section 8.3, EEO is a comparative parameter of preference for reactor energy efficiency in organic removal, whether it is between different reactors for the same compound or between different compounds for the same reactor. A priori, it is more advisable to carry out such comparison for a fixed initial pollutant concentration C_0, to exclude any concentration related effects. In practice, however, this is often not possible, as for instance is the case in Table 8.5. Therefore, it is useful to experimentally investigate the influence of the initial pollutant concentration on its removal rate and thus on the EEO value. As shown in Figure 8.15 and Table 8.7, this influence is relatively small for our reactor. With decreasing C_0, a drop in EEO is observed for α-HCH, alachlor, diuron and isoproturon. This is in good agreement with the observation of many other authors. Table 8.8 enlists all reported effects of a decreasing initial concentration of a water pollutant on its decomposition rate constant that have been found in literature on plasma reactors. For 25 cases dealing with different reactor types, decreasing C0 caused an increase in decomposition rate. Frequently, authors explain this concentration effect with a decrease in competition for OH radicals between the pollutant molecules as well as their by-products, assuming a constant concentration of OH radicals or other dominant oxidants. With the introduction of EEO as a physical quantity for energy efficiency, Cater et al. already stated this for advanced oxidation processes in general [56], as shortly reviewed for pharmaceutical compounds in [92]. The magnitude for this effect is, however, extremer for higher concentrations, while the concentration effect can become negligible for lower concentrations. A nearly constant decomposition rate has for instance been observed for the lower concentration ranges of 0.1 to 0.3 mg/L 17β-Estradiol in DBD over water in [93], 1.9 to 3.3 mg/L rhodamine B in the DBD spray reactor of [94], 5 to 10 mg/L acid blue 25 treated by DC glow discharge [95] and 5 to 10 mg/L paraquat under gliding arc [96]. This explains the relatively small deviations in our experiments. Accordingly, the strongest relative change of the oxidation rate and thus of EEO is observed for α-HCH, the compound with highest initial concentration (see Table 8.7). The threshold concentration under which the concentration effect is negligible should depend on the generated oxidant concentration and is therefore expected to be determined by the reactor type and operational settings. More experimental evidence and chemical modeling is required to confirm this statement and to estimate such threshold values.

It has to be noted that, despite the reduction in oxidation rate, energy yield G_{50} (or G_x for any fixed value of x, defined in Equation 8.4) is still larger for higher concentrations, as seen in Table 8.7 and measured for even higher ranges in many other reports, including [92-94, 97-99]. These insights lead to a few important conclusions:

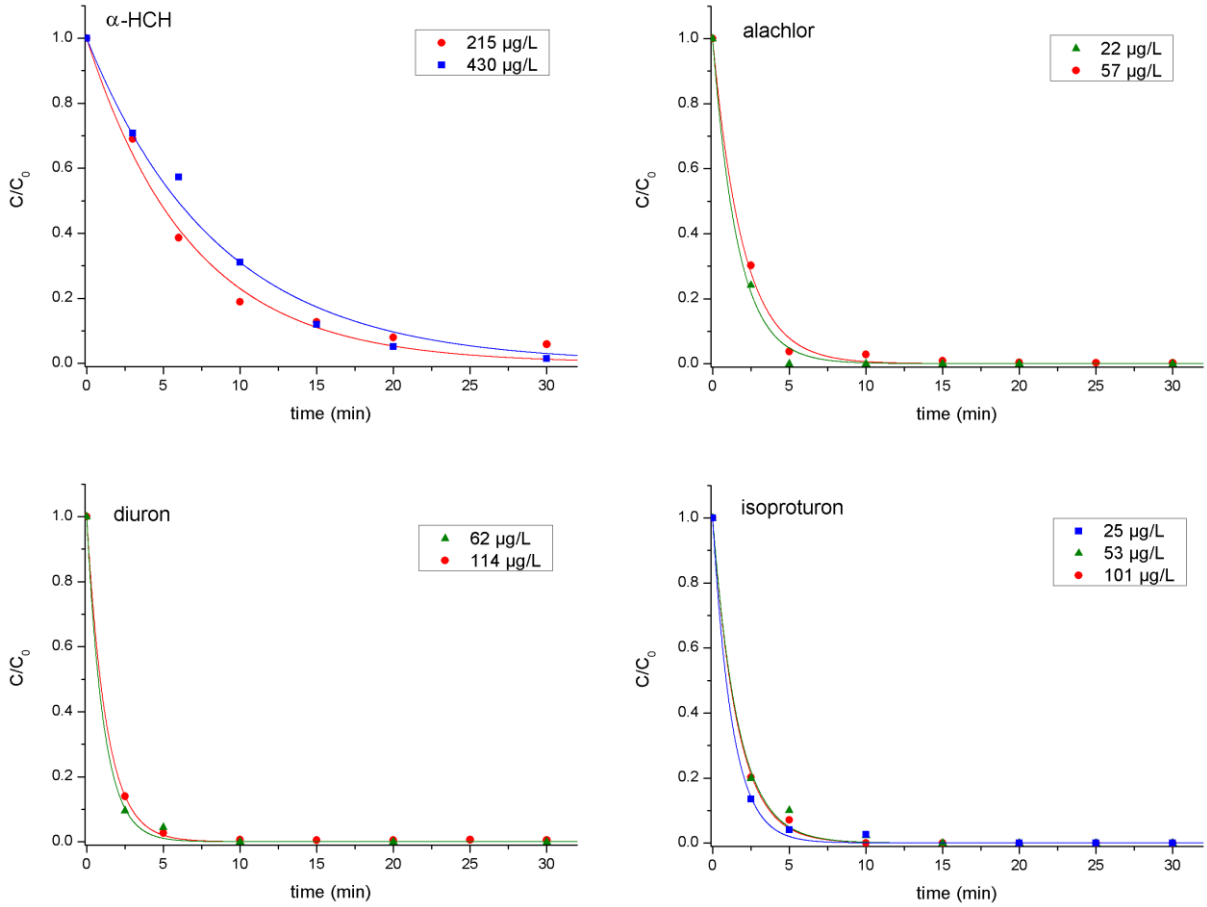

Figure 8.15 Removal kinetics in the reactor with reference settings for different initial concentrations.

Table 8.7 Energy yield G_{50} and electrical energy per order EEO for the reactor in reference settings with different initial concentrations. C_L represents the lowest concentration used, 2 × C_L represents the concentration that is approximately double as high and 4 × C_L is the highest concentration (if applicable).

		α-HCH	alachlor	diuron	isoproturon
G_{50} (mg/kWh)	C_L	13.7 ± 1.0	7.2 ± 0.7	30 ± 3	9.9 ± 0.7
G_{50} (mg/kWh)	2 × C_L	21.8 ± 1.7	15.5 ± 1.3	49 ± 3	16.6 ± 1.5
G_{50} (mg/kWh)	4 × C_L				33.0 ± 1.8
EEO (kWh/m³)	C_L	26.1 ± 1.7	5.0 ± 0.4	3.4 ± 0.3	4.1 ± 0.3
EEO (kWh/m³)	2 × C_L	33 ± 2	6.1 ± 0.3	3.90 ± 0.09	5.3 ± 0.4
EEO (kWh/m³)	4 × C_L				5.1 ± 0.2

- In applications that focus on decomposing as much pollutant mass as possible, plasma treatment and advanced oxidation processes in general are preferentially applied on the most condense state of the pollutant. This implies, for example, that plasma treatment will be more energy efficient before dilution than after. Note that this speaks in favor of the strategy proposed in Chapter 2 to treat water pollution with advanced oxidation at its source, such as effluents of hospitals and industry. From the other side, this concentration effect makes plasma discharge also more attractive for treatment of recalcitrant and hazardous concentrates after any advanced

Table 8.8 Reported influence of initial pollutant concentration C_0 on the decomposition rate constant for 25 different conditions.

Discharge type	Reactor description	Power type	Compound	C_0 range (mg/L)	reference
Increasing degradation rate constant with decreasing C0					
gas DBD	air DBD over mixed water bulk	+pulsed	17β-Estradiol	0.1-0.9	[93]
	O2 DBD coaxial falling water film reactor + plasma gas bubbling	-pulsed	methyl red	10-50	[99]
			pentoxifylline	25-150	[92]
	air coaxial whirlpool DBD reactor	HF ±pulsed	methyl orange	10-100	[97]
spray DBD	single-pass DBD coaxial spray + falling water film	+pulsed	rhodamine B	2.6-22	[94]
bubble DBD	air DBD bubble discharge reactor + plasma gas bubbling	AC	crystal violet	50-100	[55]
			methylene blue	50-100	[100]
			phenol	50-100	[101]
			methyl orange	50-100	[102]
			endosulfan	5-15	[54]
gas corona	multi-needle over streaming water	+pulsed	methyl orange	40-80	[103]
	corona wetted wall reactor with inner rod	pulsed	sulfadiazine	10-80	[104]
spray corona	single-pass corona multi-wire-to-plate spray + falling film reactor	+pulsed	salicylic acid	50-100	[105]
			lignin	80-600	
	single-pass air corona electrospray reactor	+pulsed	phenol	1-20	[106]
	corona spray in multi-wire-to-plate with TiO_2	+pulsed	cycloferon	100-300	[107]
glow	glow discharge above water bulk with mixing	+DC	acid blue 25	5-50	[95, 108]
	contact glow discharge electrolysis	+DC	brilliant red B	8-20	[109]
			acid flavine G	6-20	
gliding arc	non-thermal gliding arc over water bulk	unknown	paraquat	5-45	[96]
plasma gas bubbling	plasma gas bubbling reactors with UV irradiation through quartz barrier	AC	phenol	60-200	[110]
			coking waste	17-680	[111]
			Orange II	10-100	[112]
	100% relative humidity air DBD plasma gas bubbling	AC	acid red 88	10-50	[113]
Other observed influence of decreasing C0					
gas DBD	DBD over water bulk with radial flow	AC	nitenpyram	50-200	[98]
spray DBD	single-pass DBD coaxial spray + falling water film	+pulsed	rhodamine B	1.9-3.3	[94]
electrohydraulic	plasma electrolysis	DC	ionic liquids	$1\text{-}4 \times 10^4$	[114]

separation method for water treatment, such as electrochemical separation, nanofiltration, reverse osmosis and activated carbon (see also section 8.5), as well as any conventional separation method, such as activated sludge.

- In applications where dilution and separation do not play a role, plasma treatment or any other advanced oxidation process is more appealing in terms of energy consumption as an end-of-pipe process. One should not forget, however, that synergetic effects can occur when plasma is used as a preparation method for biological treatment. Yet, the problem with the latter strategy is that in every prior treatment step, water contains more scavengers and other competitors for oxidative attack.
- Caution should be used when comparing EEO values between reactors or organic pollutants if initial concentration is significantly different. For Table 8.6, the order of the micropollutants in their persistence to oxidation is not expected to change. For instance, the relative EEO change by doubling the initial α-HCH concentration is 26 ± 12%. Extrapolating this percentage for a 3 times lower concentration gives an EEO decrease of 44 ± 22%, i.e. 18 kWh/m^3, which is still above the EEO value for PeCB removal. Taking into consideration the concentration effect for Table 8.5, however, a few reactors might be more energy efficient relative to others than appears from the EEO values. The electrohydraulic reactor of Mededovic and Locke [58] is most likely shifted to the first place.

The above results and discussion imply that, generally, literature values of the oxidation rate constant for micropollutants in plasma reactors are underestimations for realistic situations in urban and rural wastewater treatment plants, where concentrations up to a few microgram per liter are usually measured (see section 8.1.2). Even in hospital wastewater, concentrations are in general only one order of magnitude higher [115]. Therefore, we want to accentuate the importance of experimental research with realistic or sufficiently low micropollutant concentrations as in the present work, in order to gather energy efficiency data that is more representative for real-world applications.

8.6.4 Effect of power at constant duty cycle

Applied power in our reactor can be changed in two ways: by varying the momentary power and by adjusting the duty cycle. Figure 8.16 and Table 8.9 present the results for variation of the momentary power at a fixed duty cycle DC = 0.15. As expected, increasing power leads in general to a higher oxidation rate, in agreement with other DBD reactors (see Table 8.10). For α-HCH, PeCB and isoproturon, G_{50} drops and EEO rises slightly for higher power. For alachlor, energy efficiency remains constant in the accuracy of the measurements, as in the case of atrazine reported in section 8.3. For diuron, there is a slight rise in energy efficiency when power is increased. Table 8.10 shows energy efficiency data as a function of applied power for four AC powered DBD reactors with discharge in air. G_{50} and EEO are calculated

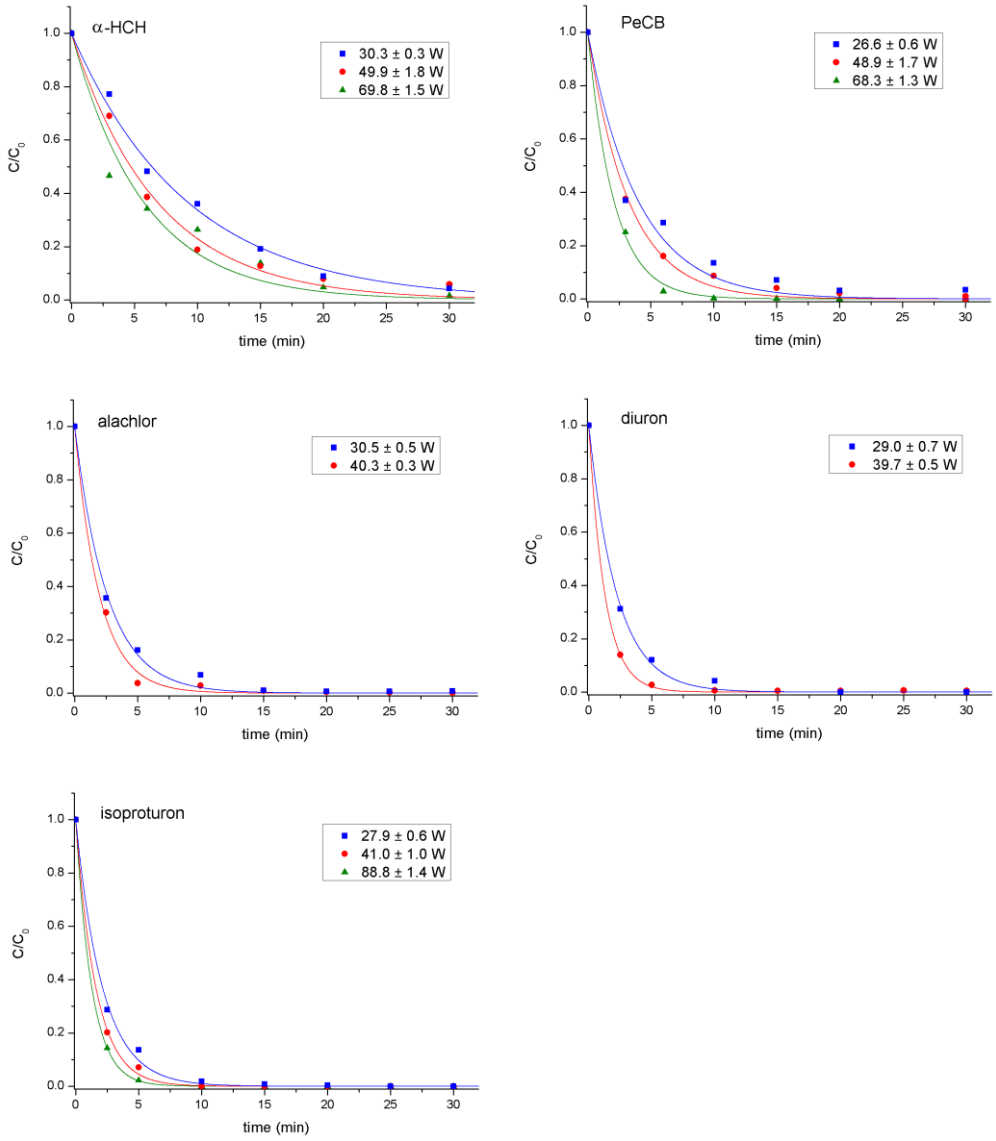

Figure 8.16 Removal kinetics in the reactor with reference settings for different power at a fixed duty cycle of DC = 0.15.

Table 8.9 Energy yield G_{50} and electrical energy per order EEO for the reactor in reference settings with different applied power at a fixed duty cycle of DC = 0.15. ~ 30 W, ~ 40 W and ~70 W represent the minimal, reference and maximal applied power, respectively.

		α-HCH	PeCB	alachlor	diuron	isoproturon
G_{50} (mg/kWh)	~ 30 W	16.7 ± 0.9	13.0 ± 1.5	15.6 ± 1.3	38 ± 2	36 ± 2
G_{50} (mg/kWh)	~ 40 W	13.7 ± 1.0	9.0 ± 0.6	15.5 ± 1.3	49 ± 3	33.0 ± 1.8
G_{50} (mg/kWh)	~ 70 W	11.7 ± 1.4	10.1 ± 0.5			19.1 ± 0.6
EEO (kWh/m^3)	~ 30 W	21.4 ± 0.9	8.5 ± 1.0	6.1 ± 0.3	5.0 ± 0.2	4.6 ± 0.2
EEO (kWh/m^3)	~ 40 W	26.1 ± 1.7	12.2 ± 0.7	6.1 ± 0.3	3.90 ± 0.09	5.1 ± 0.2
EEO (kWh/m^3)	~ 70 W	31 ± 4	10.9 ± 0.4			8.79 ± 0.14

Table 8.10 Energy yield G_{50} and electrical energy per order EEO as a function of applied power for four studies reported in literature. G_{50} and EEO are calculated based on the available data in the corresponding report. Initial concentration is given in the first column.

micropollutant	Power (W)	G_{50} (mg/kWh)	EEO (kWh/m^3)	reference
23 mg/L	100	225	170	
diuron	120	218	175	[116]
	150	249	154	
4.6 mg/L	90	25.4	301	
2,4-dinitrophenol	120	27.0	283	[117]
	150	23.5	325	
100 mg/L	80	259	641	
nitenpyram	140	187	889	[98]
	200	165	1008	
16.2 mg/L	120	269	100	
3,4-dichloroaniline	135	332	81	[118]
	150	327	82	

from the reported values of the reaction rate constant, power, initial concentration and solution volume. According to these data, there is no consistent trend of energy efficiency as a function of applied power. Since the four compounds in Table 8.10 are decomposed in very similar reactors, these results suggest that the effect of power might be specific for each compound. In our reactor, the influence of adsorption on Zorflex® is compound-specific and should be considered as well. In any case, the dependency of EEO on power seems to be rather limited, which is beneficial for applications where removal rate needs to be controlled as a function of the influent micropollutant concentrations.

8.6.5 Effect of duty cycle

Figure 8.17 and Table 8.11 present the effect of duty cycle on compound removal in our reactor. It should be noted that power is not directly proportional to the duty cycle, since variation of DC also affects the current amplitude. The rise in current with increasing duty cycle is possibly due to strong temperature elevation, which influences the humidity in the electrode gap. As seen from the measured data, an increase in duty cycle leads to a higher oxidation rate in general, except for diuron, for which removal rate remains constant in the accuracy of the measurement. Nonetheless, a higher duty cycle results in a significant decrease in energy efficiency. The same effect has been found with the gas phase DBD reactor of [119] with pulse-modulated AC power, where increasing the duty cycle from 25%

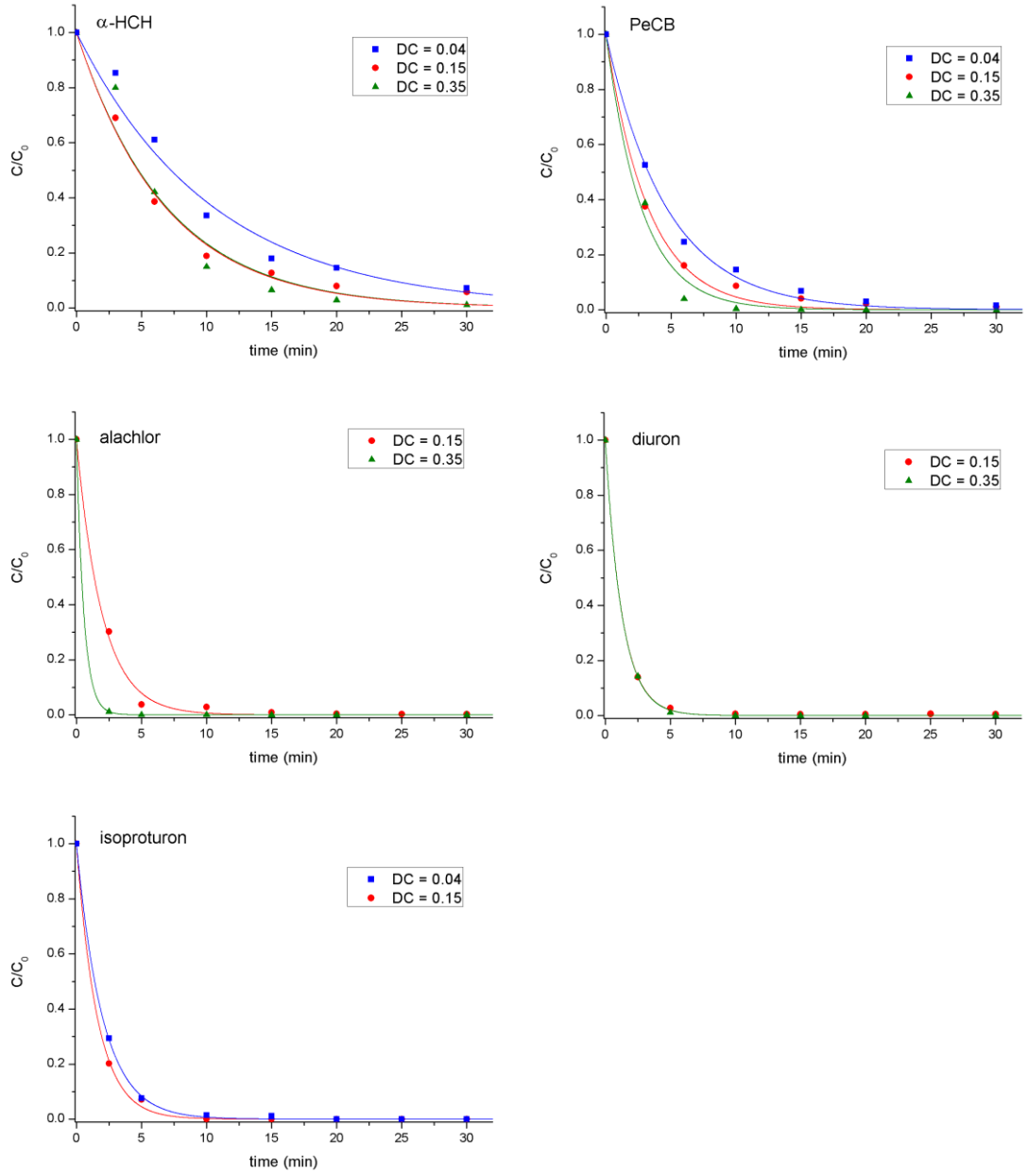

Figure 8.17 Removal kinetics in the reactor with reference settings for different duty cycles.

Table 8.11 Energy yield G_{50} and electrical energy per order EEO for the reactor in reference settings with different duty cycles.

		α-HCH	PeCB	alachlor	diuron	isoproturon
G_{50} (mg/kWh)	DC = 0.04	44 ± 5	33.3 ± 1.7			124 ± 10
G_{50} (mg/kWh)	DC = 0.15	13.7 ± 1.0	9.0 ± 0.6	15.5 ± 1.3	49 ± 3	33.0 ± 1.8
G_{50} (mg/kWh)	DC = 0.35	3.8 ± 0.5	4.2 ± 0.4	15.1 ± 1.1	13.4 ± 0.9	
EEO (kWh/m³)	DC = 0.04	8.1 ± 0.9	3.32 ± 0.13			1.35 ± 0.10
EEO (kWh/m³)	DC = 0.15	26.1 ± 1.7	12.2 ± 0.7	6.1 ± 0.3	3.90 ± 0.09	5.1 ± 0.2
EEO (kWh/m³)	DC = 0.35	94 ± 12	26 ± 2	6.29 ± 0.18	14.2 ± 0.5	

to 100% lowered energy efficiency 2.11 times. The authors explained the latter effect with additional organic degradation during plasma off time under influence of long living reactive species such as O_3 and H_2O_2. As seen in section 8.2.2, a higher duty cycle results in a lower pH due to stronger NO_2^- and NO_3^- formation. These anions and their conjugated acids can inhibit oxidation by O_3 and OH, which gives an alternative explanation for the reduction in energy efficiency at higher duty cycle. This effect will be discussed in more detail in section 8.6.7.

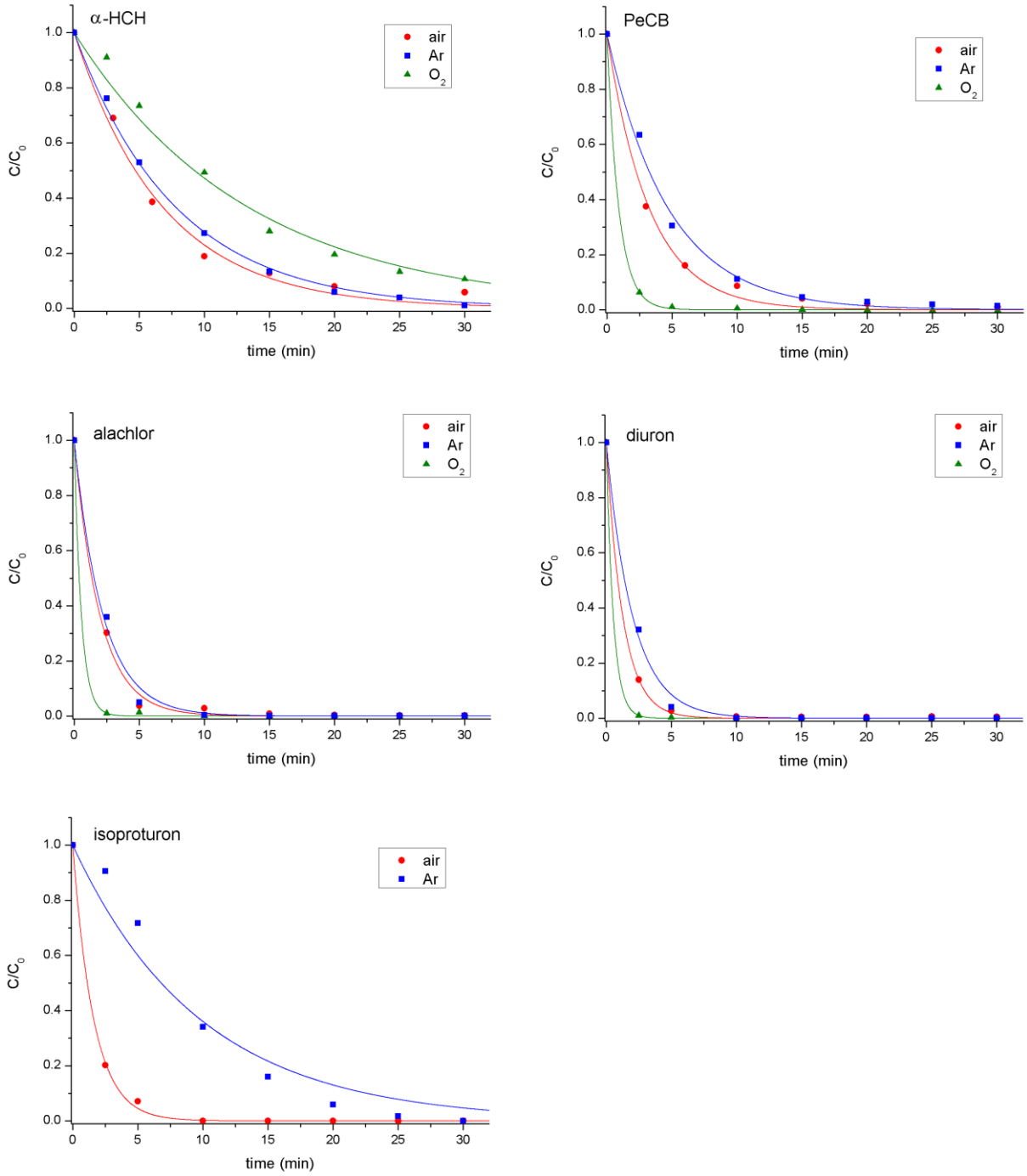

Figure 8.18 Removal kinetics in the reactor with reference settings for different feed gases.

8.6.6 Effect of feed gas

The removal of each micropollutant under air, argon and oxygen plasma is compared in Figure 8.18 and Table 8.12. Reactor performance is significantly enhanced with oxygen, except for α-HCH. Unfortunately, no data is available on the reaction rate constants k_{O3} and k_{OH} of α-HCH with ozone and OH radicals, respectively. However, the isomer γ-HCH is known to be very resistant to ozonation with $k_{O3} < 0.04\ M^{-1}\ s^{-1}$ [120, 121], while it is oxidized with OH radicals with reaction rate $k_{OH} = 7.5 \times 10^8\ M^{-1}\ s^{-1}$ [122]. According to Camel and Bermond, pesticides containing several chlorine atoms without unsaturations, such as α-HCH and γ-HCH, are generally unreactive to ozone, while presence of accessible unsaturated cycles as in PeCB leads to higher reactivity [123]. Since ozonation plays a more dominant role during plasma treatment with oxygen than with air, this partly explains the decrease in oxidation rate for α-HCH as opposed to the increase for PeCB when the feed gas is changed from air to oxygen. Argon plasma consistently performs worse than air plasma. Overall, the observed trends are in good agreement with the expectations, as discussed in Chapter 3, section 3.8. The better performance of O_2 in comparison to air can be explained with different effects, including:

- Less generation of aqueous O_3 and OH scavengers, such as HNO_3, NO_2^- and NO (see section 8.6.7 for more details).
- Higher O_3 production in the plasma chamber.
- A smaller pH drop and thus a better peroxone performance [47, 124].

Additional experiments are required to point out which of these mechanisms is the most dominant one.

Table 8.12 Energy yield G_{50} and electrical energy per order EEO for the reactor in reference settings for different feed gases.

		α-HCH	PeCB	alachlor	diuron	isoproturon
G_{50} (mg/kWh)	air	13.7 ± 1.0	9.0 ± 0.6	15.5 ± 1.3	49 ± 3	33.0 ± 1.8
G_{50} (mg/kWh)	Ar	14.2 ± 0.6	6.8 ± 0.4	13.8 ± 1.3	30 ± 2	5.6 ± 0.7
G_{50} (mg/kWh)	O_2	8.0 ± 0.4	34.3 ± 1.3	56 ± 8	114 ± 10	
EEO (kWh/m³)	air	26.1 ± 1.7	12.2 ± 0.7	6.1 ± 0.3	3.90 ± 0.09	5.1 ± 0.2
EEO (kWh/m³)	Ar	25.1 ± 0.7	16.2 ± 0.8	6.9 ± 0.4	6.3 ± 0.3	30 ± 3
EEO (kWh/m³)	O_2	44 ± 2	3.22 ± 0.08	1.7 ± 0.2	1.67 ± 0.12	

8.6.7 Single-pass experiments

Most plasma reactors described in literature operate in batch mode, where the solution under treatment is located inside the reactor during the complete treatment time. Often,

stirrer bars or a pumping circuit is added to the setup in order to enhance the diffusion of aqueous oxidants over the entire solution volume. Such reactor configurations are, however, unpractical for real-world applications where a large volume needs to be treated in a short time and where costs associated with implementation and operation of additional pumping or mixing installations should be avoided. In this line of though, it is more attractive to use a reactor in single-pass operation, where water is flowing through the system only once. Therefore, our reactor was modified to work in single-pass mode and micropollutant removal is investigated for three different configurations:

- a configuration where influent water exclusively flows through the plasma chamber (only plasma);
- a cascade configuration where influent water first flows through the plasma chamber and subsequently flows through the ozonation chamber (plasma before ozone);
- a cascade configuration where influent water first flows through the ozonation chamber and subsequently flows through the plasma chamber (ozone before plasma).

The latter is illustrated in Figure 8.19. To allow accurate comparison with the reactor in batch mode, all experiments were conducted with the same reference settings enlisted in Table 8.2. Before each experiment of the cascade configurations, the ozonation chamber was filled with the initial solution up to the same height of 25.7 cm as used in batch mode. In all experiments, one sample of the effluent solution was taken before plasma was switched on and without bubbling through the ozonation chamber, in order to measure the amount of pollutant removal by adsorption alone. During plasma treatment, samples of the effluent solution were taken after the same treatment times as in the batch mode experiments. All samples were analyzed with GC-MS to determine the average micropollutant concentration of the effluent. For both cascade configurations, this average was taken only over the samples in steady state conditions, i.e. after the treatment time where the solution in the ozonation chamber had reached a constant concentration.

The removal percentages and corresponding EEO values are given in Table 8.13. EEO (in kWh/m^3) is calculated with the formula introduced by Bolton et al. for reactors in flow-through operation [125]:

$$EEO = \frac{P}{A \times F \times \log(C_0/C_f)} \tag{8.10}$$

where P is applied power (in W), A = 3.6 × 10^6 J/kWh is a unit conversion factor, F is the water flow rate (m^3/s) in the flow-through system and C_0 and C_f are the initial and final concentration (in g/L), respectively. For all three flow-through mode configurations, operation without plasma resulted in the same removal percentage and is therefore given as one value. Surprisingly, removal without plasma is most effective for PeCB, while this compound was observed to be the most resistant to adsorption in batch mode (see section 8.6.1). As PeCB has very high volatility, this apparent contradiction can be explained with air stripping in the plasma chamber. Namely, air stripping of PeCB in the plasma chamber also

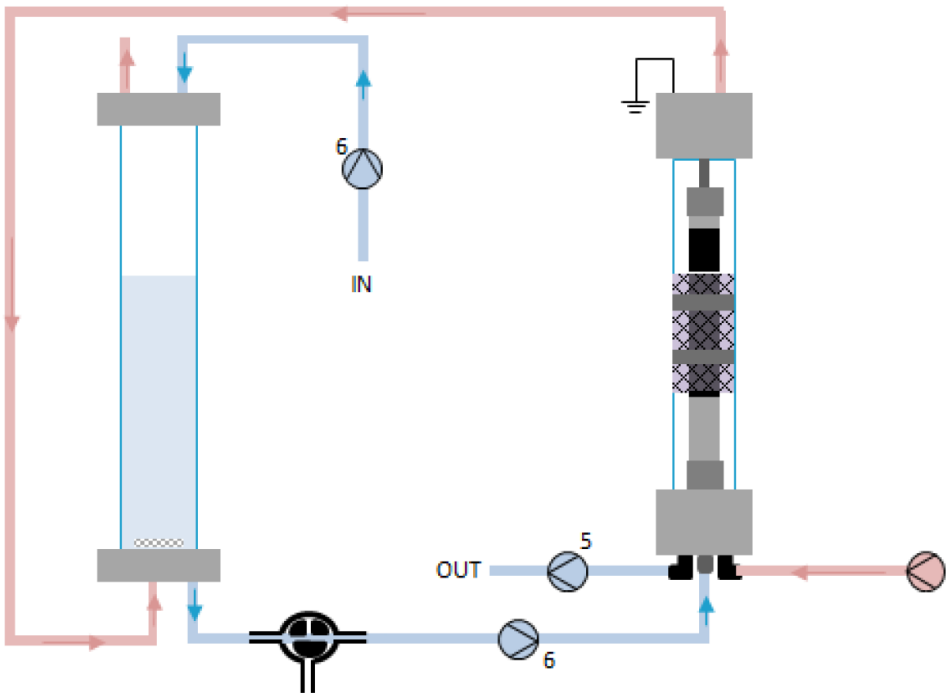

Figure 8.19 Cascade configuration of the reactor in single-pass mode where influent water first enters the ozonation chamber and subsequently passes through the plasma chamber.

Table 8.13 Removal percentage and electrical energy per order EEO for the reactor in single-pass mode for the different configurations. For comparison, also the removal percentage at the hydraulic retention time 4.20 min and the EEO value in batch mode are given, for the same reference settings.

		α-HCH	PeCB	alachlor	diuron	isoproturon
removal (%)	no plasma	31.7 ± 1.2	75.7 ± 0.6	44.6 ± 0.5	60.9 ± 0.9	37.6 ± 1.4
	only plasma	43.7 ± 1.5	79.0 ± 0.7	75.1 ± 0.4	79.3 ± 0.5	
	plasma before ozone	59 ± 2	82.6 ± 0.7	87 ± 2	90.5 ± 1.3	75.9 ± 0.4
	ozone before plasma	64.8 ± 1.0	94.5 ± 0.6	97.0 ± 0.6	96.9 ± 0.7	91.6 ± 1.0
	batch mode (4.20 min)	46.1 ± 1.9	72 ± 2	88.3 ± 1.2	96.2 ± 0.2	92.5 ± 0.8
EEO (kWh/m³)	only plasma	30.1 ± 1.5	11.4 ± 0.3	11.6 ± 0.2	9.9 ± 0.2	
	plasma before ozone	18.4 ± 1.1	9.9 ± 0.4	8.0 ± 0.7	6.7 ± 0.4	11.5 ± 0.3
	ozone before plasma	16.7 ± 0.7	6.2 ± 0.3	4.6 ± 0.3	4.6 ± 0.3	6.5 ± 0.3
	batch mode	26.1 ± 1.7	12.2 ± 0.8	6.1 ± 0.3	3.90 ± 0.09	5.1 ± 0.2

occurred in the experiment of Figure 8.13 without Zorflex®. As a result, it is not distinguishable in the batch mode experiments from air stripping in the ozonation chamber. In single-pass mode, however, air flow through the plasma chamber readily removes PeCB even without the bubbling process in the configuration without ozonation chamber.

Therefore, removal without plasma in single-pass mode includes both adsorption and volatilization.

Based on the water flow rate of 95.3 mL/min and solution volume of 400 mL in the ozonation chamber, hydraulic residence time in the ozonation chamber is calculated to be 4.20 min. Relative to this value, hydraulic residence time in the plasma chamber is negligible (0.86 ± 0.02 s). In these calculations, hydraulic residence time in the connecting tubes is not considered. Using the hydraulic residence time of 4.20 min and the reaction rate constants from Table 8.6 for reference settings in batch mode, the corresponding removal percentage in batch mode is calculated, as given in Table 8.13. According to the resulting removal percentages, single pass mode is performing as good as or better than batch mode for removal of the different compounds.

In Table 8.13, comparison of the reactor in absence of the ozonation chamber to the cascade configuration from Figure 8.19, where plasma gas bubbling precedes treatment in the plasma chamber, clearly shows that energy efficiency approximately doubles when the ozonation chamber is added to the reactor. As should be noted, this cascade configuration performs considerably better for removal of all micropollutants than the reverse cascade configuration. As the most likely reason, this is because of more efficient ozonation of untreated solution as compared to plasma-treated solution. In the plasma chamber, transfer of nitric oxides into the solution leads to the formation of NO_2^-, a known O_3 scavenger through the reaction

$$O_3 + NO_2^- \longrightarrow O_2 + NO_3^- \tag{8.11}$$

with reported reaction rate of k = 1.6 – 5.0 × 10^5 $M^{-1}s^{-1}$ [126-129]. When the solution enters the ozonation chamber afterwards, the aqueous NO_2^-, is mixed rapidly throughout the solution under influence of the bubbling, inhibiting the ozonation process. The transfer of nitric oxides into the solution by the bubbling process in the ozonation chamber is, on the other hand, relatively small, as confirmed by the limited decrease in pH (see Figure 8.8b). Therefore, ozonation has a stronger effect in the cascade configuration of Figure 8.19 than in the reverse setting. This scavenging mechanism has been reported before in water treatment processes with air plasma [47]. Additionally, aqueous OH radicals introduced by means of the bubbled plasma gas can be scavenged as well by reactive nitrogen species through the reactions

$$OH + NO \longrightarrow H^+ + NO_2^- \tag{8.12}$$

$$OH + HNO_3 \longrightarrow H_2O + NO_3 \tag{8.13}$$

$$OH + NO_2^- \longrightarrow OH^- + NO_2 \tag{8.14}$$

with reaction rates of k = 1.0 – 2 × 10^{10} $M^{-1}s^{-1}$ [130-132], k = 5.3 – 14 × 10^7 $M^{-1}s^{-1}$ [133, 134] and k = 6.0 – 14 × 10^5 $M^{-1}s^{-1}$ [132, 135-139], respectively. The NO_2 radical formed in Equation 8.14 has a redox potential of 1.04 V [140, 141] and is therefore significantly less reactive than the OH radical reagent with a redox potential of 2.80 V.

Energy efficiency for micropollutant removal in the cascade configuration of Figure 8.19 is in the same order of magnitude as in batch mode:

- As a negative effect, energy efficiency decreases in flow-through mode with 22 ± 5 % for isoproturon and 15 ± 6 % for diuron.
- As a positive effect, energy efficiency increases with 32 ± 10 % for alachlor, 56 ± 10 % for α-HCH and 96 ± 16 % for PeCB.

Since the most persistent compounds, α-HCH and PeCB, are removed significantly more effectively, while the EEO increase for isoproturon is relatively small, these results speak in favor of the flow-through system for general application. To our knowledge, this is the first time that a comparison in energy efficiency of organic decomposition has been made between batch mode and single-pass mode of the same reactor. These results seem to suggest that EEO values in batch mode are representative for the energy efficiency of an identical reactor in flow-through mode, at least in order of magnitude. Yet, it is uncertain whether this can be generalized for other reactor types as well. More experimental investigation on this topic is desirable, in order to gain more insight in possible restrictions on comparative studies.

8.7 By-product analysis for 3 micropollutants

HPLC-MS analysis is performed on water samples taken before and during plasma treatment under standard conditions in batch mode (power of 40 W, duty cycle of 0.15, gas flow of 1000 sccm). Since PCB and α-HCH were undetectable with the HPLC-MS technique due to their low polarity, results are presented only for alachlor, diuron and isoproturon. Initial concentration of the micropollutant was increased to 1.5 mg/L in order to improve detectability of oxidation by-products. Treatment times are selected in the same way as for GC-MS analysis.

Detected ions in HPLC-MS analysis are generated by means of electrospray ionization. In contrast to the dissociative processes occurring during electron impact ionization, as in the GC-MS technique, electrospray ionization usually keeps molecules intact and is therefore often called a soft ionization method. As explained in section 7.5 of the previous chapter, an electrospray is an example of ambient desorption ionization, where intermediate droplets are dispersed into the gas phase from a Taylor cone as an aerosol under influence of Coulomb repulsion. The charged droplets decrease in size through a combination of evaporation and fission processes, finally resulting in the formation of gas-phase ions. In positive ionization mode, mostly protonated molecular ions with the formula $(M+H)^+$ are detected, but also metallated species such as sodium adduct ions $(M+Na)^+$ are commonly found. It is generally assumed that solute molecules in the neutral droplet core remain unaffected by the harsh conditions at the droplet surface and in the surroundings beyond it until the last of the solvent molecules has been removed. Nevertheless, the exact processes inside the charged

droplets are yet far from being understood. For example, the acid-base equilibrium, the conformational states, and noncovalent bonding in the analyte can all be influenced by subtle variation in the composition and properties of the droplets during the electrospray. Banerjee et al. estimated the pH change caused by repeated solvent evaporation and Coulomb fission of the droplets with a simple calculation [142]. At low solution flow rate, droplets are being formed with a mean radius of 1.5 μm in a narrow distribution and a charge of about 10^{-14} C, corresponding to 60,000 singly charged ions. Assuming that all ions are protons in positive ion mode, this gives a pH of 5.2. Reduction of droplet size to a critical radius of about 10 nm at the Rayleigh limit, right before the formation of gas-phase ions, results in 125 H^+ ions in the droplet, giving a pH of 1.3. Decrease of pH in electrospray droplets is observed experimentally in [143]. Banerjee et al. also proved experimentally structure transformation of a highly stable intrinsically charged molecule inside electrospray droplets, due to the huge repulsive Coulomb force caused by the surface charge of the droplet [142]. After the possible chemical alterations in the electrospray droplets, the structure of the produced analyte ions can be changed drastically in the new gaseous environment. Often, such fragmentation during ionization in the HPLC-MS method occurs to a small extent. This results in the appearance of additional peaks with lower abundance in the mass spectrum at the same retention time as the undissociated ions. As an interesting advantage, the dissociation pattern observed in a molecule's mass spectrum reveals additional information on the molecule's structure [144], as will be shown below.

8.7.1 Alachlor oxidation by-products

Alachlor is an exceptional case, where fragmentation during electrospray ionization plays a major role at relatively low collision energy. In our measurements, the hydrogen adduct ion $(M+H)^+$ has an abundance that is about 2 times lower than its second daughter ion, 3 times lower than its first daughter ion and 7 times lower than the sodium adduct $(M+Na)^+$. Accurate mass, relative abundance and chemical formulas of the four most important ions of alachlor are given in Table 8.14 for the sample with highest abundance SHA = 0 min. The first daughter ion $C_{13}H_{16}ClNOH^+$ is formed from the hydrogen adduct by the loss of a neutral fragment with mass of 32 Da, which corresponds to the removal of CH_3OH. The second daughter ion is formed from the first daughter ion by a sequential loss of 76 Da, corresponding to the removal of C_2HClO. This dissociation pattern has been reported by other authors for both electron ionization in GC-MS analysis and electrospray ionization in HPLC-MS analysis. Bouchonnet et al. proposed a dissociation pathway based on isotope labeling and collision-induced dissociation experiments for the case of electron ionization. In this pathway, the first daughter ion is formed by α elimination of the $CH_3O\cdot$ radical group [145]. Volmer et al. suggested a similar dissociation pathway for the case of electrospray ionization [146], as depicted in Figure 8.20a. After protonation of the methoxy function, the hydrogen adduct dissociates through CH_3OH elimination to provide the first daughter ion. Next, proton rearrangement causes the elimination of C_2HClO, resulting in the second

daughter ion. Park et al. explained the observed daughter ions of alachlor in electrospray ionization mass spectrometry with a significantly different fragmentation mechanism, shown in Figure 8.20b [147]. This alternative mechanism involves one of the ethyl side chains of the

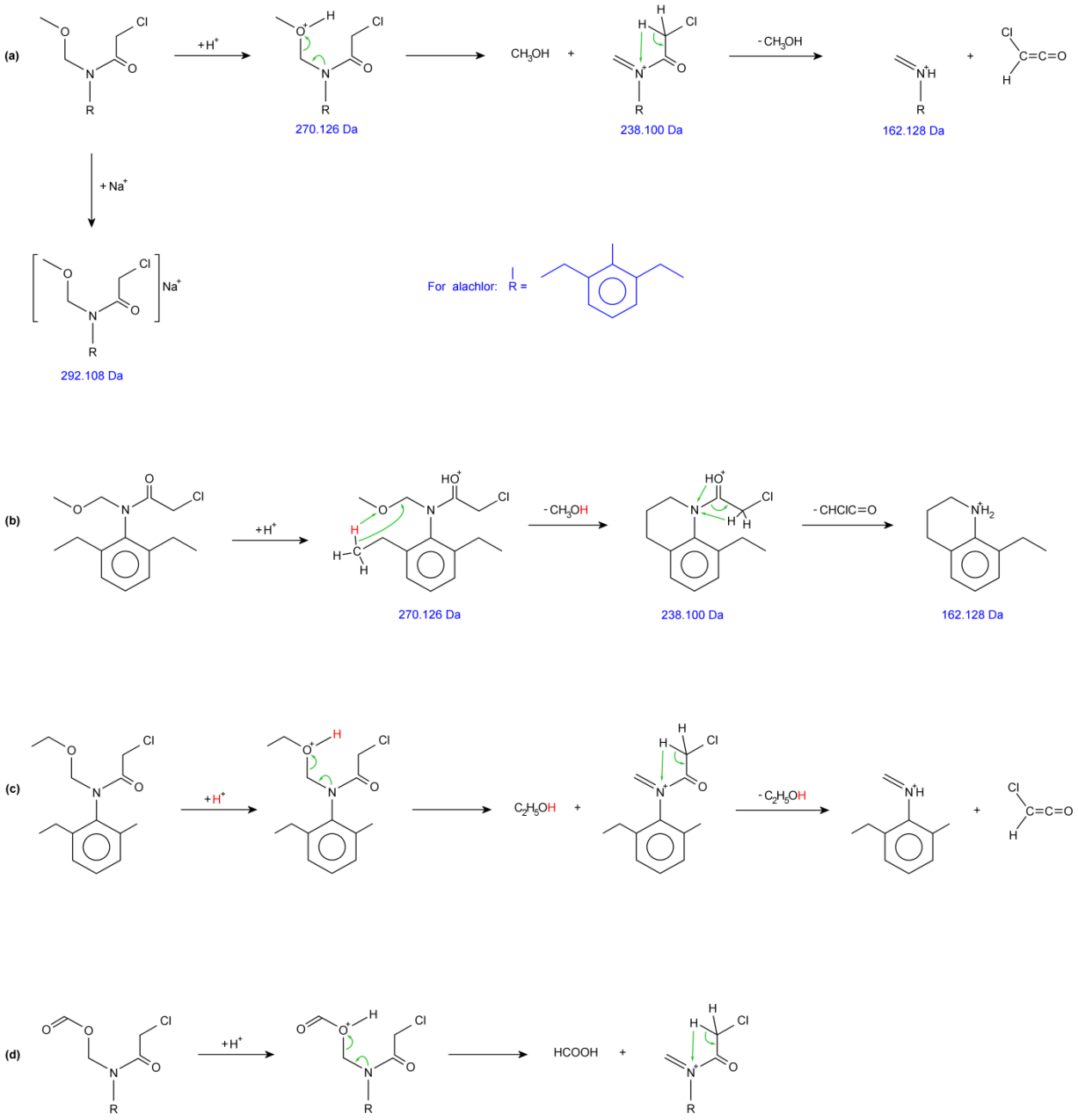

Figure 8.20 (a) Metallation, protonation and dissociation pathway into the first two daughter ions of alachlor and most of its oxidation by-products in HPLC-TOF-MS, adapted from [146] and proposed in this work. (b) Corresponding protonation and fragmentation mechanism of alachlor according to Park et al. [147], based on Electrospray ionization mass spectrometry without isotope labeling. (c) Corresponding protonation and fragmentation mechanism of acetochlor according to Bouchonnet et al. [148], as determined by means of HPLC/electrospray-QqTOF mass spectrometry and isotope labeling. (d) Proposed formation mechanism of the first daughter ion for by-products 3F and 3I.

Table 8.14 Proposed identification of alachlor and its by-products as deduced from the corresponding detected ions in HPLC-TOF-MS at retention time RT in the sample of highest abundance (SHA). For each ion, identification is based, amongst others, on Δppm as calculated from the measured mass m_{exp} and theoretical mass m_{cal}, confirmation by the molecular formula generator (CMFG) and its relative abundance RA to the associated Na adduct ion.

SHA	RT (min)	name	formula	detected ion	m_{exp} (Da)	m_{cal} (Da)	Δppm	CMFG	RA (%)
0 min	44.3	1A	$C_{14}H_{20}ClNO_2$	$C_{14}H_{20}ClNO_2\ Na^+$	292.107	292.108	-3.5	yes	100
				$C_{13}H_{16}ClNO\ H^+$	238.099	238.100	-3.6	yes	41
				$C_{11}H_{15}N\ H^+$	162.127	162.128	-7.9	yes	32
				$C_{14}H_{20}ClNO_2\ H^+$	270.125	270.126	-4.0	yes	14
5 min	28.3	3A	$C_{12}H_{16}ClNO_3$	$C_{12}H_{16}ClNO_3\ H^+$	258.087	258.090	-11.6	yes	100
	32.9	3B	$C_{14}H_{18}ClNO_4$	$C_{14}H_{18}ClNO_4\ Na^+$	322.088	322.082	18.6	no	100
				$C_{13}H_{14}ClNO_3\ H^+$	268.077	268.074	11.0	no	19
				$C_{11}H_{13}NO_2\ H^+$	192.105	192.102	13.3	no	17
	34.6	3C	$C_{13}H_{18}ClNO_2$	$C_{13}H_{18}ClNO_2\ Na^+$	278.096	278.092	14.4	no	100
				$C_{12}H_{14}ClNO\ H^+$	224.087	224.084	13.4	no	103
				$C_{10}H_{13}N\ H^+$	148.116	148.113	22.8	no	4
		3D	$C_{14}H_{20}ClNO_4$	$C_{14}H_{20}ClNO_4\ Na^+$	324.103	324.098	15.9	no	100
				$C_{13}H_{16}ClNO_3\ H^+$	270.093	270.090	12.2	no	33
				$C_{11}H_{15}NO_2\ H^+$	194.120	194.118	9.8	no	15
	35.5	3E	$C_{14}H_{20}ClNO_3$	$C_{14}H_{20}ClNO_3\ Na^+$	308.107	308.103	13.2	no	100
				$C_{13}H_{16}ClNO_2\ H^+$	254.098	254.095	12.7	no	22
				$C_{11}H_{15}NO\ H^+$	178.124	178.123	4.6	no	5
	35.8	3F	$C_{13}H_{16}ClNO_3$	$C_{13}H_{16}ClNO_3\ Na^+$	292.076	292.071	17.1	no	100
				$C_{12}H_{14}ClNO\ H^+$	224.087	224.084	12.4	no	44
		3G	$C_{12}H_{16}ClNO_4$	$C_{12}H_{16}ClNO_4\ Na^+$	296.070	296.066	13.5	no	100
				$C_{11}H_{12}ClNO_3\ H^+$	242.062	242.058	14.9	no	9
				$C_9H_{11}NO_2\ H^+$	166.091	166.087	25.3	no	51
	36.6	3H	$C_{14}H_{20}ClNO_3$	$C_{14}H_{20}ClNO_3\ Na^+$	308.107	308.103	13.2	no	100
				$C_{13}H_{16}ClNO_2\ H^+$	254.097	254.095	8.7	no	28
				$C_{11}H_{15}NO\ H^+$	178.125	178.123	10.2	no	16
				$C_{14}H_{20}ClNO_3\ H^+$	286.126	286.121	17.5	no	5
	37.3	3I	$C_{14}H_{16}ClNO_4$	$C_{14}H_{16}ClNO_4\ Na^+$	320.072	320.067	17.0	no	100
				$C_{13}H_{14}ClNO_2\ H^+$	252.082	252.079	11.4	no	39
				$C_{11}H_{13}NO\ H^+$	176.110	176.108	14.0	no	64
	38.1	3J	$C_{14}H_{20}ClNO_3$	$C_{14}H_{20}ClNO_3\ Na^+$	308.106	308.103	9.9	yes	100
				$C_{13}H_{16}ClNO_2\ H^+$	254.098	254.095	12.7	yes	32
				$C_{11}H_{15}NO\ H^+$	178.126	178.123	15.8	yes	11
				$C_{14}H_{20}ClNO_3\ H^+$	286.125	286.121	14.0	no	5
		3K	$C_{14}H_{18}ClNO_3$	$C_{14}H_{18}ClNO_3\ Na^+$	306.093	306.087	18.7	no	100
				$C_{13}H_{14}ClNO_2\ H^+$	252.083	252.079	15.3	no	14
				$C_{11}H_{13}NO\ H^+$	176.109	176.108	8.3	yes	33
	38.6	3L	$C_{14}H_{20}ClNO_6$	$C_{14}H_{20}ClNO_6\ Na^+$	356.092	356.088	12.1	no	100
				$C_{11}H_{15}NO_4\ H^+$	226.109	226.108	4.7	no	7
				$C_{14}H_{20}ClNO_6\ H^+$	334.109	334.106	9.8	no	6
	43.9	3M	$C_{14}H_{19}ClN_2O_5$	$C_{14}H_{19}ClN_2O_5\ Na^+$	353.088	353.088	0.0	yes	100
				$C_{13}H_{15}ClN_2O_4\ H^+$	299.082	299.080	7.2	no	6

aromatic ring, with formation of a new ring structure. The authors of both pathways, however, based their mechanism solely on collision-induced dissociation experiments without isotope labeling. Direct experimental confirmation of alachlor's dissociation pathway in electrospray ionization with isotope labeling has, to our knowledge, never been reported. Nevertheless, the experimental results of Bouchonnet et al. in a later publication contradict the mechanism of Figure 8.20b and speak in favor of the pathway we present in Figure 8.20a [148]. In their experiments, Bouchonnet et al. determined the dissociation pathway of acetochlor, a molecule with very similar structure to the one of alachlor, in electrospray of LC-MS/MS. By means of isotope labeling, they deduced that the ethyl side chain on the aromatic ring was not involved in the removal of ethanol from the acetochlor parent ion and therefore proposed the dissociation pathway presented in Figure 8.20c, with direct similarities to the pathway we propose in Figure 8.20a. In what follows, we will therefore refute the mechanism of Figure 8.20b and assume that only the N-substituted branches in the parent ion are involved in the two main fragmentation processes.

Table 8.14 enlists all detected ions that are associated to alachlor oxidation by-products. Unfortunately, HPLC-MS analysis of the sample taken after 2.5 min treatment time failed and new results are not known yet at the moment of writing. Based on the analysis results of the other samples, all by-products have highest abundance after treatment of 5 min. Based on the abundance of Na adducts, all oxidation products have an abundance of about 2 to 3 orders of magnitude lower than the initial abundance of alachlor. By-products with highest abundance are molecules 3K, 3J, 3E, 3C and 3H, with an abundance of, respectively, 3.0 %, 2.1 %, 0.9 %, 0.5 % and 0.4 % relative to the initial one of alachlor. Alachlor abundance has dropped after 5 min to 10.8 % of its initial value. Due to the low abundances, identification of most enlisted ions could not be confirmed by the molecular formula generator. Nevertheless, we used several other criteria to substantiate the likelihood of their identification:

1. Presence of the Cl atom is deduced for all ions from the characteristic isotope abundance pattern in the mass spectra. As only exception, chlorine is absent in the second daughter ions.
2. The deviation of the detected ion mass to the theoretical value from the proposed chemical formula is expressed as Δppm in Table 8.14. For most ions, a value around $\Delta\text{ppm} \approx 15$ is found. Such systematic deviation in measurement is usually not tolerated by the molecular formula generator, but it is common when abundance is either too high or too low.
3. When ions at a fixed retention time meet the requirements for the dissociation pattern of Figure 8.20a, this suggests they originate from a parent molecule which is an oxidation by-product from alachlor. The abundance of each ion relative to the corresponding Na adduct is given in Table 8.14 for comparison with alachlor. Such an approach based on group-specific fragmentation in LC-MS for the best confidence in

contaminant identification has been previously proposed by Niessen in his detailed review on pesticide dissociation patterns [144].

4. Suggestions for the structural formula of each identified parent molecule are given in Figure 8.21 in a proposed oxidation pathway of alachlor. As can be seen, every suggested structure resembles the one of alachlor. Moreover, each detected molecule can be linked as an oxidation by-product of another detected molecule. Only in two cases, expected intermediates are missing, namely for derivation of by-products 3A and 3L.
5. Where appropriate, references are given to identifications of the same and similar chemical or structural formulas in literature on advanced oxidation of alachlor.

With the exception of molecules 3A, 3F and 3I, the dissociation pattern observed for each proposed by-product is identical to the one presented in Figure 8.20a. As an implication, the N-substituted branches in the parent ion are identical to the ones of alachlor, in agreement with the proposed molecular structures in Figure 8.21. Due to the low abundances, the undissociated H adduct is only measured in a few cases, for intermediates 3H, 3J and 3L. Additionally, the second daughter ion is missing as well for 3M. Possibly, this is caused by a change in the Cl containing branch, but this could not be confirmed. Remarkably, the first daughter ion has not been detected for 3L, while the second daughter ion is present. This can be related to instability of the first daughter ion, as an influence of hydroxyl substitution on the ethyl side chains of the aromatic ring. Not all possible isomers are presented for each by-product in Figure 8.21. In particular, the exact position of hydroxyl groups on the aromatic ring or on the alkyl chains linked to the ring is unknown.

The first daughter ion of by-products 3F and 3I is formed from the H adduct by the loss of a neutral fragment with mass of 46 Da, which corresponds to the removal of formic acid (HCOOH), as shown in Figure 8.20d. Accordingly, the methoxy function has been oxidized into formate during one of the oxidation steps, to provide the molecular structures displayed in Figure 8.21. This is in excellent agreement with [145], where an identical oxidation mechanism is observed during ozonation of alachlor, as determined by means of collision-induced dissociation experiments. To our knowledge, Bouchonnet et al. were the first and only research group up to now to report this oxidation mechanism for alachlor. For 3I, the second daughter ion is formed by release of C_2HClO, i.e. in the same way as in Figure 8.20a. For 3F, however, the second daughter ion is not observed, probably due to its very low abundance. The formation of the second daughter ion is most likely hindered by the presence of the methyl group linked to the aromatic ring. This is also observed for by-product 3C, where the second daughter ion has abundance as low as 4 % relative to the Na adduct. For 3I, on the other hand, the second daughter ion is more abundant than the first daughter ion, which is probably caused by the double bonded oxygen in one of the ethyl side chains linked to the aromatic ring, as this is also observed for molecule 3K.

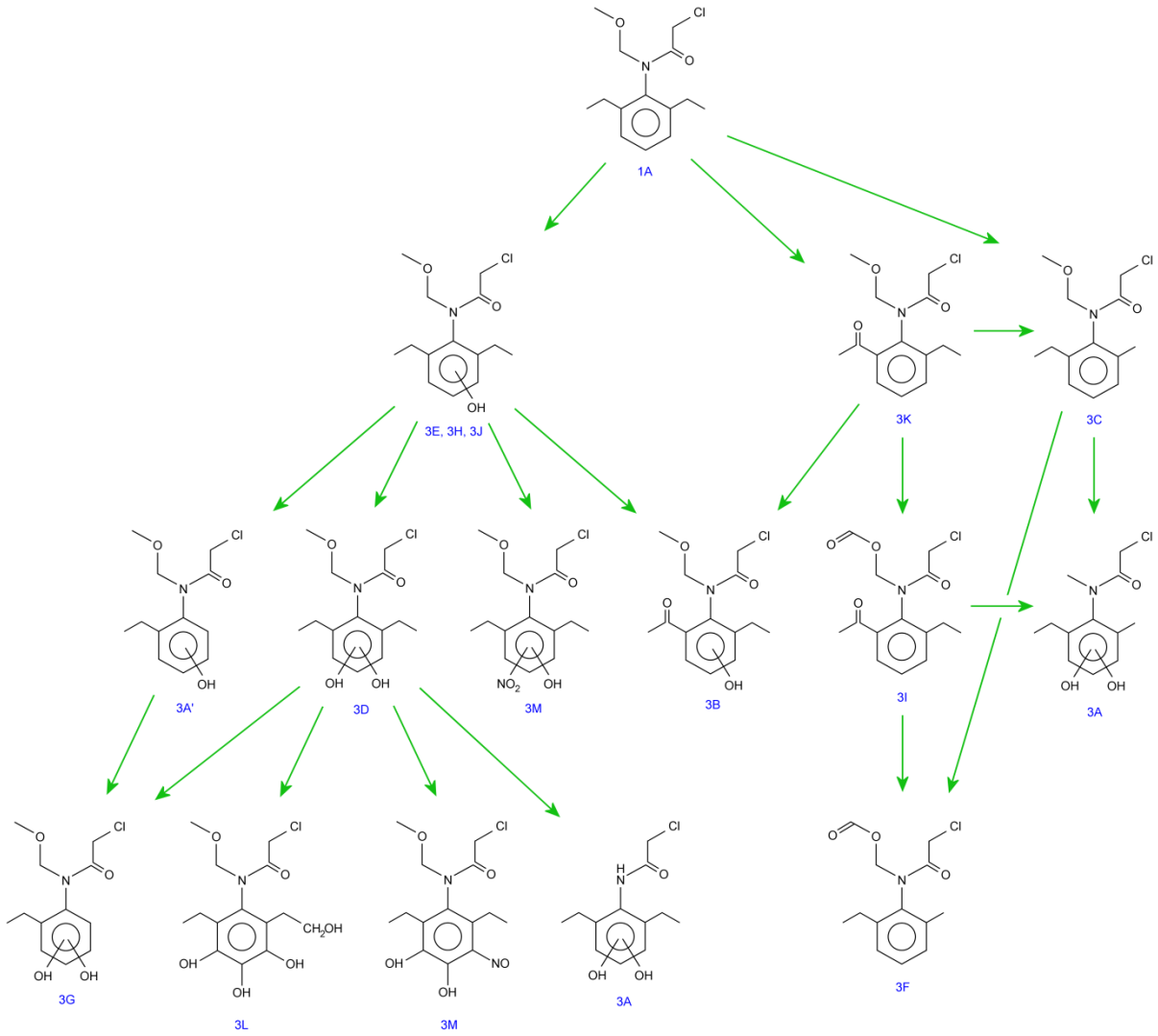

Figure 8.21 Proposed oxidation pathway of alachlor under DBD plasma treatment in air.

Molecule 3A is a particular case, since its chemical formula has been confirmed by the molecular formula generator, but a dissociation mechanism as well as its Na adduct are absent. It is therefore possible that formation of the Na adduct and dissociation of the H adduct are prevented by considerable changes in the methoxymethyl function, as for the two possibilities shown in Figure 8.21. The isomer with structural formula indicated as 3A' has been reported as an alachlor oxidation by-product in H_2O_2-assisted and unassisted photocatalytic degradation in [149, 150]. Its molecular structure was determined from the release of a methanol fragment in the corresponding dissociation pattern, which was measured by means of electrospray ionization coupled to a liquid chromatography system. Although this isomer could be an intermediate leading to the oxidation by-product 3G in our experiments, its structure contradicts the absence of a dissociation pattern and is therefore not attributed to molecule 3A. Scission or complete elimination of the methoxymethyl group in alachlor has been reported in many studies, including [151, 152] for ozonation, [153] for ultrasonication, [154] for hydrodynamic cavitation, [22] for electrochemical advanced oxidation, [155] for Fenton-like oxidation, [156] for sono-Fenton, [157] for photo-Fenton, [158-

160] for photodegradation and [149, 150, 159, 161, 162] for heterogeneous photocatalysis. In our experiments, however, 3A is the only by-product that might be formed through this degradation mechanism.

With the exception of molecule 3A, all proposed by-product structural formulas are derived from alachlor by a combination of four types of oxidation steps:

1. Hydroxylation by substitution of hydrogen with a hydroxyl group;
2. Oxidation by substitution of 2 hydrogen atoms with double bonded oxygen;
3. Dealkylation by substitution of an alkyl group with hydrogen;
4. Nitrification by substitution of hydrogen with a NO group (nitrosation) or NO_2 group (nitration).

The first 3 types are commonly encountered in ozonation and other advanced oxidation processes of organic compounds. Direct oxidation by ozone is, however, a very selective process, in comparison to hydroxyl radical attack. Aromatic compounds with higher electron delocalization are known to exhibit higher reactivity towards ozonation [163, 164]. This implies that O_3 attack is strongly electrophilic in nature and is preferably directed towards electron rich aromatic rings. Alterations of side-chains during ozonation, on the other hand, are mostly attributed to attack of OH radicals, which are produced from ozone hydrolysis. Proposed reaction pathways of hydroxylation of an aromatic ring by direct ozone attack and by OH radicals are, for example, described in detail in [165], along with pathways of hydroxylation and scission of an ester chain by OH attack.

Nitrification is uncommon in most advanced oxidation processes, as it requires the presence of reactive nitrogen species. Lukes et al. recently identified nitrified oxidation products of phenol after oxidation with plasma in air atmosphere [47]. They proposed several reaction pathways for both nitrosation and nitration. According to their model, nitrated by-products can be formed through attack of $NO_2\cdot$ or $NO\cdot$ radicals, nitrous and nitric acid in acidic conditions and decomposition of peroxynitrous acid in acid solution, while nitrosated by-products might result from $NO\cdot$ radical attack, reaction with nitrosonium NO^+ ion under acidic conditions or direct attack by peroxynitrite anion under alkaline conditions. To our knowledge, we are the first group to report experimental evidence on nitrification of non-phenolic micropollutants under plasma treatment. From our measurements on alachlor, however, it is unclear whether by-product 3M results from nitrosation or nitration.

The five intermediates with highest abundance are all found in the oxidation pathway of Figure 8.21 as first generation oxidation by-products. The most abundant intermediate, 3K, is supposedly formed by conversion of one of the ethyl side chains into an acetyl group. The exact same molecular structure was also identified with both GC-MS and HPLC-MS analysis as the main by-product in direct ozonation of alachlor [152, 166] as well as in the peroxone process [152]. It has also been reported as alachlor oxidation product in another ozonation study [151], hydrodynamic cavitation [154], permanganate-induced oxidation [152],

electrochemical advanced oxidation [22], photocatalysis [161], and enhanced sono-Fenton process [156]. As this implies, 3K can be formed in our experiments by several oxidation mechanisms, such as direct attack by molecular ozone, and attack by a hydroxyl radical. Attack by an oxygen radical has also been proposed in literature [154]. In only a few studies, an isomer of 3K is identified where the added double-bonded oxygen is positioned at a different location [145, 152]. This suggests that oxidation of the ethyl side chain into an acetyl group is favored over many other oxidation steps.

Hydroxylation of alachlor into isomers such as 3E, 3H and 3J is another commonly reported oxidation step. It has been observed in ozonation and peroxone process [152], ultrasonication [153], photo-Fenton [157], electrochemical advanced oxidation [22], Fenton-like oxidation [155] and unassisted or H_2O_2-assisted heterogeneous photocatalysis [149, 150]. Often, multiple isomers are detected in one study. For photocatalysis with TiO_2, the detected isomer is considered as one of the two main oxidation by-products [149]. In general, hydroxylation is commonly found to be one of the initial oxidation steps in advanced oxidation processes. Since an aromatic ring is electron-rich in nature, since OH attack is electrophilic and since hydroxyl radicals readily react with unsaturated carbons, hydroxyl addition most likely takes place directly to the aromatic ring [167]. In most research on alachlor oxidation, however, the exact location of the OH function is unknown and OH radical attack of the ethyl side chain is proposed as well. Next to that, also electrophilic attack of ozone on the benzene ring or on an ethyl group with formation of an OH function has been suggested [152].

An isomer of 3C, where the methyl group of the methoxy function is removed, has been reported as alachlor by-product of ozonation [151], electrochemical advanced oxidation [22], and Fenton-like oxidation [155]. In the latter study, a second isomer was identified as well, where the complete methoxy function has been detached. Similarly, an isomer of 3F with elimination of the same methyl group has been observed for alachlor oxidation with ozonation [151], electrochemical advanced oxidation [22], and hydrodynamic cavitation [154]. In all studies, molecular structure was deduced from the fragmentation pattern in electron ionization by matching the mass spectra obtained by GC-MS against those in the NIST mass spectra library. Additionally, an isomer of 3I has been detected in alachlor ozonation and peroxonation [152]. According to the fragmentation pattern of this isomer in both GC-MS and HPLC-MS, the methoxymethyl group was kept intact. Therefore, addition of the two double-bonded oxygen atoms was suggested to be located on the ethyl side chains. These isomer structures, however, are in contradiction with the dissociation patterns of 3C, 3F and 3I measured in our experiments. The structural formulas of 3C, 3F and 3I as proposed in Figure 8.21 are not found elsewhere in literature. To our knowledge, also the chemical formulas of 3B, 3D, 3G, 3L and 3M in Table 8.14 have never been identified before as advanced oxidation by-products of alachlor.

8.7.2 Diuron oxidation by-products

Diuron is more stable than alachlor during electrospray ionization. As given in Table 8.15, its mass spectrum (molecule 1A) is mostly characterized by its hydrogen adduct ion and its sodium adduct ion, in an abundance ratio of about 5 to 1. Draper proposed the dissociation pathway depicted in Figure 8.22a, based on collision-induced dissociation experiments with electrospray quadrupole ion trap liquid chromatography-mass spectrometry [168]. Niessen proposed a slightly different structure for the second daughter ion of 160 Da, where the positive charge is located on one of the Cl atoms [144]. The sequential loss of 45 Da and 28 Da is contributed to, respectively, dimethyl amine and carbon monoxide as neutral fragments. The corresponding daughter ions are detected in our measurements with relatively low abundance.

Table 8.15 Proposed identification of diuron and its by-products as deduced from the corresponding detected ions in HPLC-TOF-MS at retention time RT in the sample of highest abundance (SHA). For each ion, identification is based, amongst others, on Δppm as calculated from the measured mass m_{exp} and theoretical mass m_{cal}, confirmation by the molecular formula generator (CMFG) and its relative abundance RA to the associated ion of highest abundance.

SHA	RT (min)	name	formula	detected ion	m_{exp} (Da)	m_{cal} (Da)	Δppm	CMFG	RA (%)
0 min	36.9	1A	$C_9H_{10}Cl_2N_2O$	$C_9H_{10}Cl_2N_2O\ H^+$	233.024	233.025	-3.6	yes	100
				$C_9H_{10}Cl_2N_2O\ Na^+$	255.005	255.007	-7.0	yes	19
				$C_7H_3Cl_2NO\ H^+$	187.963	187.967	-21.2	no	0.3
				$C_6H_3Cl_2N\ H^+$	159.968	159.972	-25.5	no	0.2
2.5 min	35.3	2A	$C_8H_8Cl_2N_2O$	$C_8H_8Cl_2N_2O\ H^+$	219.006	219.009	-14.6	no	100
				$C_8H_8Cl_2N_2O\ Na^+$	240.988	240.991	-13.0	no	11
				$C_6H_5Cl_2N\ H^+$	161.985	161.988	-16.9	no	16
				$C_6H_5ClN\ H^+$	127.018	127.019	-6.9	no	13
	43.0	2B	$C_9H_9Cl_2N_3O_3$	$C_9H_9Cl_2N_3O_3\ H^+$	278.011	278.010	3.9	yes	100
				$C_9H_9Cl_2N_3O_3\ Na^+$	299.993	299.992	3.8	yes	53
5 min	36.6	3A	$C_9H_{10}Cl_2N_2O_2$	$C_9H_{10}Cl_2N_2O_2\ H^+$	249.014	249.020	-23.1	yes	100
				$C_9H_{10}Cl_2N_2O_2\ Na^+$	270.996	271.002	-21.0	yes	18
	36.9	3B	$C_9H_9Cl_2N_3O_3$	$C_9H_9Cl_2N_3O_3\ H^+$	278.007	278.010	-10.5	yes	100
				$C_9H_9Cl_2N_3O_3\ Na^+$	299.989	299.992	-9.5	yes	53
	40.1	3C	$C_8H_7Cl_2N_3O_3$	$C_8H_7Cl_2N_3O_3\ H^+$	263.993	263.994	-4.8	no	6
				$C_6H_4Cl_2N_2O_2\ H^+$	206.969	206.972	-14.5	yes	100
				$C_6H_2Cl_2N_2O\ H^+$	188.963	188.962	5.3	yes	31
10 min	36.7	4A	$C_8H_7Cl_2N_3O_3$	$C_8H_7Cl_2N_3O_3\ H^+$	263.995	263.994	2.8	no	27
				$C_8H_7Cl_2N_3O_3\ Na^+$	285.977	285.976	2.7	no	27
				$C_6H_4Cl_2N_2O_2\ H^+$	206.973	206.972	4.8	yes	100
				$C_6H_2Cl_2N_2O\ H^+$	188.963	188.962	5.3	yes	53

All detected ions that are associated to diuron oxidation by-products are enlisted in Table 8.15. In contrast to alachlor, maximal abundance of the by-products is observed for different treatment times, ranging from 2.5 min to 10 min. The maximal abundance of each

intermediate is 4 orders of magnitude lower than the initial abundance of diuron, except for molecule 2A, which appears to be the main oxidation by-product with maximal abundance that is only 3 orders of magnitude lower. Despite its relatively high abundance, 2A is the only intermediate of which none of the detected ions is confirmed by the molecular formula generator. Yet, its dissociation pattern is in very good agreement with the one commonly reported in literature for N-demethyldiuron, with a first daughter ion of 162 Da and a second daughter ion of 127 Da [169-173]. Nevertheless, a detailed fragmentation mechanism in electrospray ionization has never been reported before. Formation of the first daughter ion occurs through release of methyl isocyanate (CH_3NCO). This mechanism is also frequently observed for N-methyl carbamate pesticides, which possess a very similar group structure to N-demethyldiuron [174, 175]. Stamp et al. postulated a fragmentation mechanism for carbamate pesticides, which involves the formation of an intermediate protonated bound bimolecular complex [175], as shown in Figure 8.22b. In this complex, the proton originally linked to the N-methyl group is transferred to a location between the methyl isocyanate and the other neutral part of the ion. Before dissociation, the neutral molecules can rotate about the bound proton in the selection process of a suitable basic site for cation formation. Although the observed fragmentation of many carbamate pesticides can also be explained with alternative classical mechanisms, experiments with deuterated reagent gas have revealed the bimolecular complex formation as a more plausible, universal mechanism. As shown in Figure 8.22c, the same model can also tentatively be formulated for N-demethyldiuron (molecule 2A), where the ether group has been replaced by a secondary amine bond. This explains the hydride transfer during formation of the first daughter ion. The second daughter ion, with a mass of 127 Da, is formed by subsequent release of a chloride atom. This is confirmed in our measurements by the corresponding change in isotope abundance. Therefore, 2A is very likely equal to N-methyldiuron, the most frequently detected diuron by-product in advanced oxidation studies, including plasma treatment [116], ozonation [172, 176-179], peroxonation [178], photocatalytic ozonation [172], UV/H_2O_2 [177], photolysis [180, 181], TiO_2-based photocatalysis [170, 171, 182-184], heterogeneous photocatalysis with N-doped titania [172], photo-induced oxidation by nitrites and nitrates [185], photocatalysis with ZnO [170], photo-Fenton [171, 186, 187], electro-Fenton [188-190], ferrous-activated persulfate oxidation [173] and catalytic wet air oxidation [191]. It has been reported as one of the three main aromatic diuron intermediates in [170, 171, 178-180, 185, 187, 190]. Interestingly, N-demethylation is considered to be the main oxidation step of several substituted phenylurea herbicides, including isoproturon, linuron, fluometuron and metoxuron, which all possess a similar N-substituted branch as diuron [170].

For molecules 2B, 3A and 3B, identification of the hydrogen adduct as well as the sodium adduct has been confirmed by the molecular formula generator. As shown in Figure 8.23, their proposed structural formulas correspond to first generation oxidation products formed by hydroxylation or nitration. Since no demethylation has taken place, their dissociation

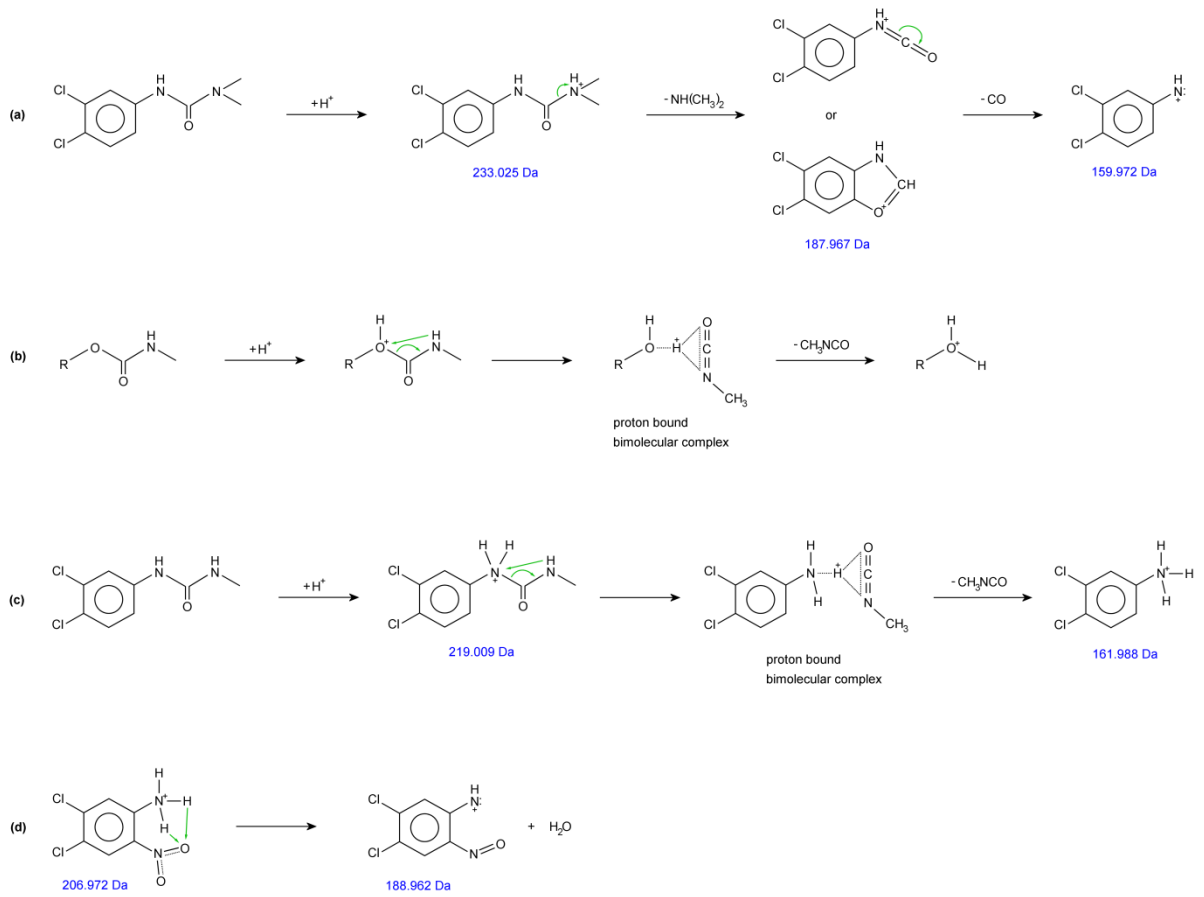

Figure 8.22 (a) Protonation and dissociation pathway into the first two daughter ions of diuron in HPLC-TOF-MS, as proposed by Draper et al. [168]. (b) Fragmentation mechanism of N-methyl carbamate pesticides according to Stamp et al. [175]. (c) Protonation and fragmentation mechanism of N-demethyldiuron into its first daughter ion, as proposed in this work. (d) Proposed formation mechanism of the second daughter ion for by-products 3C and 4A.

pattern is expected to be similar to the one of diuron. This is supported by the absence of any daughter ion, whose abundance presumably falls under the detection limit. Identification of the isomers 3C and 4A, however, requires more caution. Here, identity of the H adduct parent ion is not confirmed by the Agilent Masshunter software due to its low abundance. Nevertheless, its mass and isotope abundance agrees well with the ones of a second generation oxidation by-product of diuron after one demethylation step and one nitration step (Figure 8.23). For 4A, also the corresponding Na adduct is registered, but for 3C, abundance was too low for detection. Chemical formulas of the two most abundant ions of 207 Da and 189 Da are confirmed by the Agilent Masshunter software. They are identified as, respectively, the first and second daughter ion of the H adduct. Formation of the first daughter ion is in excellent agreement with the dissociation mechanism proposed for N-demethyldiuron (Figure 8.22c), indicating that the methyl isocyanate function is unaltered. Therefore, substitution of the NO_2 group during oxidation most likely occurred to the

aromatic ring. The relatively low abundance of the parent ion is possibly caused by high instability of the proton bound bimolecular complex before dissociation. Namely, due to the strong attraction between the dipolar nitro function and the proton, the aromatic neutral molecule in the complex quickly rotates to adopt the hydrogen ion. Sequentially, the second daughter ion is produced by loss of a H_2O molecule and formation of a nitroso function according to a fragmentation mechanism as proposed in Figure 8.22d. Since double hydride transfer towards one of the oxygen atoms is more likely when the NO_2 group is added to an alpha carbon, attachment to the beta carbon has not been depicted in Figure 8.23. H2O release by the first daughter ion of such isomer, however, should still be considered possible. This mechanism implies that NO_2 substitution occurred on the ring. In contrast, H_2O loss in the case of NO substitution is not expected, as it would require breaking of the strong π-bonding between the N and O atoms.

As depicted in Figure 8.23, the main oxidation steps in air plasma treatment of diuron according to our experiments are

- hydroxylation,
- demethylation and
- nitrification.

Unfortunately, the location of the added OH, NO and NO_2 groups in 2B, 3A and 3B is unknown, since no daughter ions were detected. If 3C and 4A are oxidation by-products of 2B and 3B, nitrification will occur on the aromatic ring. Shankar et al. investigated by-product formation during photo-induced oxidation of diuron in aqueous solution by nitrites and nitrates [185]. Interestingly, they also found two isomers with formula $C_9H_9Cl_2N_3O_3$ and two isomers with formula $C_8H_7Cl_2N_3O_3$. In all 4 cases, the fragmentation spectra in HPLC-analysis indicated nitrification of the aromatic ring, a process which was enhanced in NO_2^- conditions as opposed to NO_3^- conditions. The authors explained these observations with electrophilic attack of the ring by NO_2 radicals or the dimeric form N_2O_4. This hypothesis is strengthened in their later research, where aromatic nitration is shown to be significantly increased for compounds without electron-withdrawing halogens linked to the ring. Absence of halogens leads to electronic enrichment onto the ring, in favor of electrophilic NO_2 attack. NO_2 radical attack is also suggested in Lukes' model for nitration of phenol in air plasma treatment. If the dominant nitrification mechanism in our experiments is indeed electrophilic in nature, NO or NO_2 substitution will ideally occur on the aromatic cycle, at the positions in ortho of the C-N bond, leading to the structural formulas of 2B, 3B, 3C and 4A as shown in Figure 8.23. This is in agreement with the simulation results of Carrier et al., who calculated the location of preference for electrophilic attack on the diuron structure with different models [182].

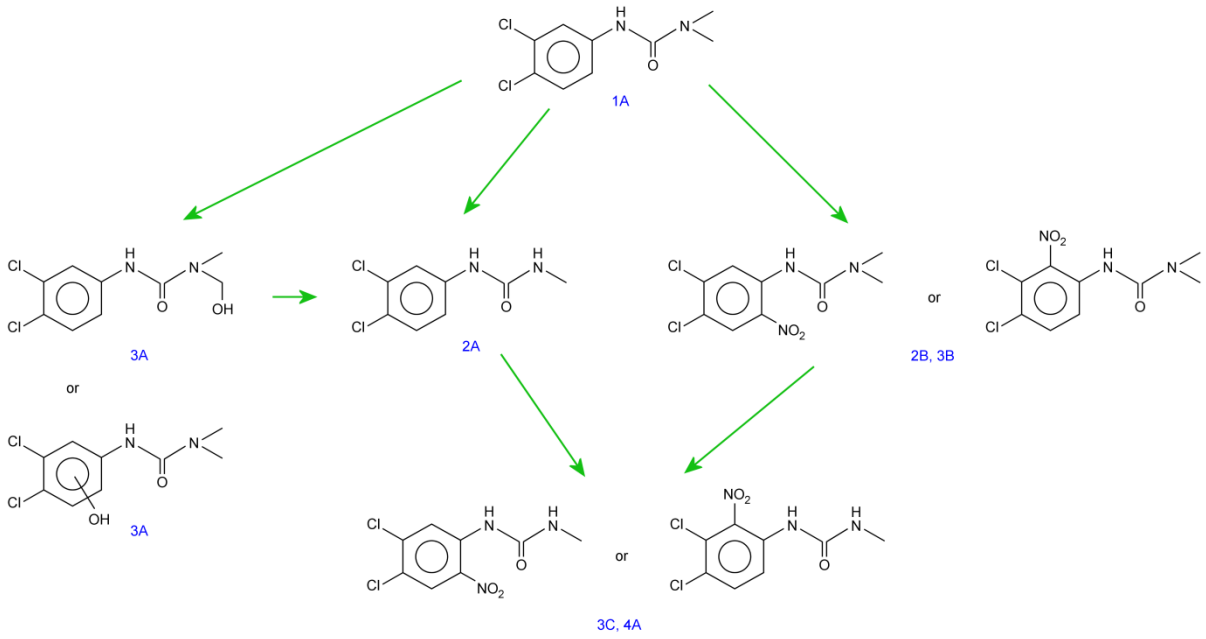

Figure 8.23 Proposed oxidation pathway of diuron under DBD plasma treatment in air atmosphere in this work.

Similarly, hydroxylation by electrophilic OH radical attack is expected to take place on the ring with higher possibility than on the methyl groups. Yet, such trend is not clearly observed experimentally. In advanced oxidation studies where monohydroxylated diuron (3A) is measured, for instance, ring hydroxylation is encountered in only about half of the cases, for ozonation and UV/H_2O_2 [177], TiO_2-based photocatalysis [171, 183], photo-Fenton [171], electro-Fenton [188-190] and oxidation by chlorine dioxide [192], while methyl hydroxylation is found in similar processes, i.e. for plasma treatment [116, 193], ozonation [176], photocatalytic ozonation [172], TiO_2-based photocatalysis [184], heterogeneous photocatalysis with N-doped titania [172] and photo-Fenton [194]. Either isomer has been reported as one of the three main diuron intermediates, e.g. in [171, 176, 184]. Carrier et al. performed TiO_2-based photocatalysis on diuron and found four monohydroxylated diuron isomers [182]. Three isomers were attributed to OH substitution on the ring and one isomer to hydroxylation of a methyl function. For photo-induced oxidation by nitrites and nitrates, both types of isomers have been detected simultaneously as well [185]. In the latter study, substitution of OH for H mainly occurred on the methyl groups. Hydroxylation on the ring without dechlorination was considered a minor process in NO_3^- conditions, while it was not observed for NO_2^- conditions.

Whereas OH attack of the aromatic cycle is a nucleophilic process, the methyl functions are assumed to be hydroxylated through hydrogen abstraction by many authors. Figure 8.24a shows the stepwise transformation of one of the methyl groups into a hydroxymethyl or formyl function. First, attack of the methyl group by an OH radical leads to abstraction of one of the hydrogen atoms. Subsequent dioxygen attack results in a peroxyl radical. Such radical is relatively stable and usually decays via bimolecular self-termination reactions to

form a transient tetroxide which on its turn decomposes into an alcohol or aldehyde. To our knowledge, Mazzelier et al. were the first to postulate this mechanism for formyl formation in diuron [187]. Later on, it was extended for OH addition by Macounová et al. [184]. The latter authors found the generated alcohol and aldehyde to be thermally unstable, especially in acidic solutions. They proposed the decay of both compounds by direct decomposition and hydrolysis, respectively, resulting in dealkylation and thus the formation of N-demethyldiuron. In good agreement with this model, Shankar et al. observed in their oxidation study increased yields of the alcohol, aldehyde and demethylated by-product under aeration, as opposed to nitrogen sparging, for both NO_2^- and NO_3^- conditions [185]. Demethylation of diuron by photolysis, on the other hand, is independent on oxygen and thus clearly occurs through a different mechanism. Jirkovsky et al. explained this with breaking of double bonded O under irradiation and the sequential intermediate formation of a methylenolate [180].

Feng et al. conducted two studies on plasma treatment of diuron, one with a AC powered DBD reactor without recirculation of the batch solution [116] and one with a pulsed bubble discharge reactor [193]. They reported several diuron intermediates in both studies with different alterations of the N-terminus. Accordingly, they proposed a stepwise mechanism for diuron demethylation, as presented in Figure 8.24b. In this line of thought, by-product 3A can be a precursor of 2A, on the condition that OH addition took place on one of the methyl groups. Next to such demethylation precursors, Feng et al. also detected one intermediate in their DBD reactor where one of the chlorine atoms had been substituted by a hydroxyl group. This has not been observed in our measurements, possibly because of its low abundance. New experiments are being performed with 20-fold higher initial diuron concentration, in order to detect more by-products with higher certainty and to gain more accurate information on their structure.

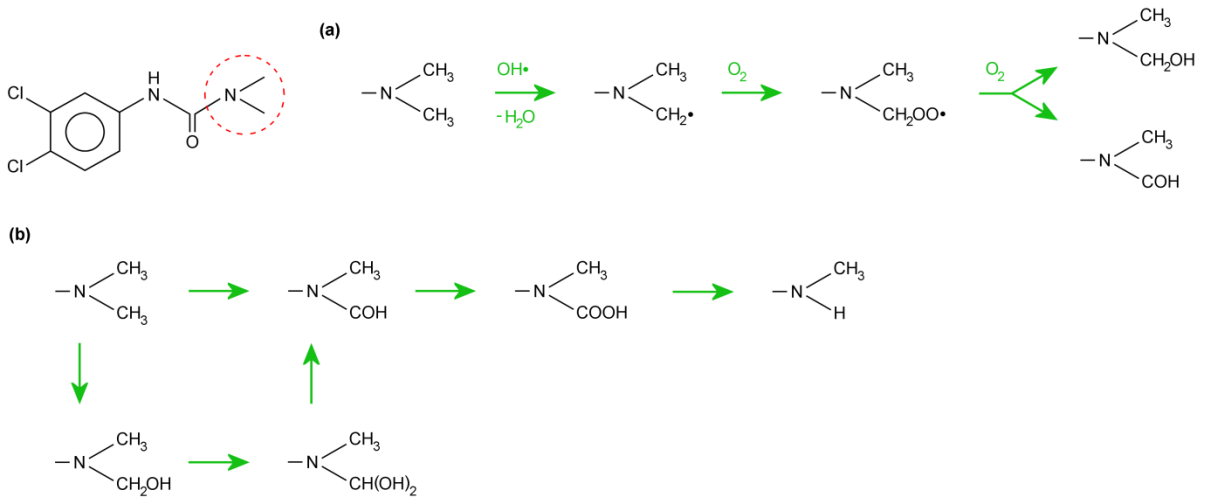

Figure 8.24 (a) Oxidation steps of the diuron N-terminus into an alcohol or aldehyde, as proposed in [184]. (b) Stepwise mechanism behind diuron demethylation by DBD treatment, as proposed in [116].

Especially for diuron, oxidation to the extent of full mineralization is recommended, since some of its by-products are known to be toxic. The by-product formed in electro-Fenton after elimination of the complete N-substituted branch was found to have a 90 times higher specific toxicity than diuron towards Vibrio fischeri [195]. The monodemethylated metabolite exhibits higher toxicity than diuron for Vibrio fischeri, Tetrahymena pyriformis and Spirostomum teres, which are all indicative for toxicity towards aquatic life [196]. Didemethylated diuron was found to have increased toxicity to all three species as well, although this depended for T. pyriformis on the type of test used. Interestingly, T. pyriformis is also proposed as a complement or alternative to animal and mammalian cell models in toxicological research [197], suggesting that the associated tests are representative for drinking water toxicity as well. Vibrio fischeri bacteria tests, on the other hand, have very good correlation with several tests based on other aquatic species, while they were found to have good correlation with mammalian toxicity only for intravenous LD_{50} data towards rat and mouse [198]. As V. fischeri is one of the most frequently used species in toxicity analysis, corresponding citations mostly refer to toxicity towards aquatic life, relevant for ecotoxic effects of effluent wastewater.

In our experiments, abundance of each by-product decreases after 10 min of treatment and no new by-products are detected. As for other advanced oxidation processes, opening of the aromatic ring is expected, with further decomposition into smaller organics such as oxalic acid, oxamic acid, acetic acid and formic acid [22, 171, 194]. After 30 minutes of treatment, only small traces of 3B, 3C and 4A are tentatively found. Quantitative analysis of these traces requires calibration of the analysis method and is outside the scope of this study. Nonetheless, this is without doubt an important issue for future research.

8.7.3 Isoproturon oxidation by-products

Isoproturon has an identical N-substituted side chain as diuron and accordingly has clear similarities in its mass spectrum, as can be seen in Table 8.16 (molecule 1A). As for diuron, the mass spectrum is dominated by the hydrogen adduct ion and the sodium adduct ion, in an abundance ratio of about 5 to 1. The second and third daughter ions of 162 Da and 132 Da are formed through the same fragmentation mechanism by release of dimethyl amine and carbonmonoxide respectively (see Figure 8.22a), in agreement with the group-specific dissociation of N-dimethyl phenylurea herbicides [144]. They are found in the same relative abundance as the first and second daughter ions of diuron (see Table 8.15 and 8.16). Isoproturon's more abundant first daughter ion of 165 Da results from propene loss of the H adduct ion. The underlying mechanism is explained by Baglio et al. with dislocation of the π-electrons of the aromatic ring under influence of the protonated secondary amine function [195]. Because of this dislocation, the ring has a partially positive charge at the bond with the isopropyl function, as shown in Figure 8.25. This charge attracts a hydride from the isopropyl function, generating a neutral propene fragment. A similar dissociation process has been proposed by Yinon and Vincze in their study on electron ionization in CID

processes of phenylurea pesticides using GC–ion-trap MS–MS [196]. Oxidation by-products of isoproturon containing the isopropyl and secondary amine functions are also expected to be subject to this fragmentation mechanism. Notwithstanding, electron-withdrawing substitution on the ring might interfere with the magnitude of electron dislocation, counteracting the propene detachment.

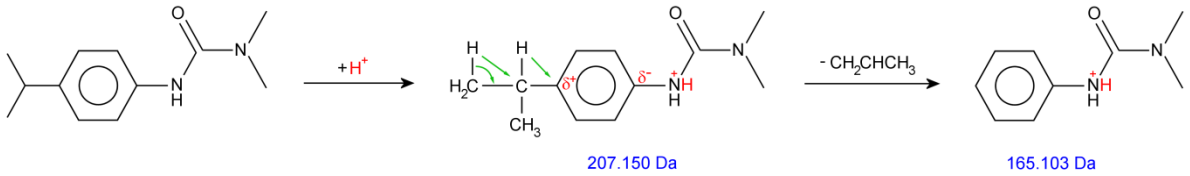

Figure 8.25 Mechanism of propene detachment from protonated isoproturon in HPLC-TOF-MS based on electron displacement, as proposed in [195].

Table 8.16 enlists all detected ions associated to isoproturon oxidation by-products. By-products with highest abundance are, in descending order, molecules 2G, 3F, 3G and 3H, two orders of magnitude lower in abundance relative to the initial one of isoproturon. All other by-products are found with relative abundance of three orders of magnitude lower. Since isoproturon does not contain chloride, it is more important to confirm a by-product's identification by means of its dissociation pattern, Δppm of each ion and by means of the molecular formula generator. Proposed molecular structures of the detected by-products are given in the reaction pathway of Figure 8.26. The daughter ion of 2D and 2G is formed through dimethyl amine release according to the mechanism of Figure 8.22a, indicating that their substituted groups can only be located on the aromatic ring or on the isopropyl group. Since propene release conforming to the mechanism of Figure 8.25 is not observed, the electron-withdrawing NO_2 function is probably substituted on the ring, decreasing the extent of electron dislocation. NO_2 substituted propene loss is observed in the mass spectrum of 2E, illustrating that NO_2 radical attack can also occur on the side-chains. Additionally, H_2O loss from the H adduct is measured, most likely resulting in the formation of a nitroso function and C=C double bond at the same location in the H adduct parent ion. Similarly, hydroxylated propene loss is detected for 3A, demonstrating OH substitution on the isopropyl group. On the other hand, the first daughter ion of 2C, 2F and 3F is formed by unsubstituted propene detachment, implying that the isopropyl function is not oxidized.

By-products formed by single demethylation of the dimethyl amide function are expected to dissociate in electrospray according to the mechanism of Figure 8.22c. This is in excellent agreement with the analysis results, where demethylated molecules 3F and 3H display the release of methyl isocyanate. Furthermore, H_2O loss is observed from the associated daughter ion of the NO_2 substituted variant 3H, with clear similarity to the NO_2 substituted diuron by-products 3C and 4A and conform to the dissociation mechanism depicted in Figure 8.22d. Propene detachment confirms that the NO_2 function is indeed attached to the aromatic ring and that H_2O loss by the mechanism working for 2E, with NO_2 substitution to

Table 8.16 Proposed identification of isoproturon and its by-products as deduced from the corresponding detected ions in HPLC-TOF-MS at retention time RT in the sample of highest abundance (SHA). For each ion, identification is based, amongst others, on Δppm as calculated from the measured mass m_{exp} and theoretical mass m_{cal}, confirmation by the molecular formula generator (CMFG) and its relative abundance RA to the associated ion of highest abundance.

SHA	RT (min)	name	formula	detected ion	m_{exp} (Da)	m_{cal} (Da)	Δppm	CMFG	RA (%)
0 min	36.3	1A	$C_{12}H_{18}N_2O$	$C_{12}H_{18}N_2O\ H^+$	207.151	207.150	6.1	yes	100
				$C_{12}H_{18}N_2O\ Na^+$	229.133	229.132	5.8	yes	20
				$C_9H_{12}N_2O\ H^+$	165.103	165.103	1.3	yes	5
				$C_{10}H_{11}NO\ H^+$	162.091	162.091	0.0	yes	0.2
				$C_9H_{11}N\ H^+$	134.095	134.097	-14.7	yes	0.2
2.5 min	27.7	2A	$C_{12}H_{18}N_2O_3$	$C_{12}H_{18}N_2O_3\ H^+$	239.143	239.140	14.4	no	100
				$C_{12}H_{18}N_2O_3\ Na^+$	261.126	261.122	17.2	yes (low)	41
	32.5	2B	$C_{12}H_{18}N_2O_2$	$C_{12}H_{18}N_2O_2\ H^+$	223.145	223.145	0.0	yes (low)	88
				$C_{12}H_{18}N_2O_2\ Na^+$	245.127	245.127	1.6	yes	100
	35.8	2C	$C_{12}H_{18}N_2O_2$	$C_{12}H_{18}N_2O_2\ H^+$	223.145	223.145	0.0	yes	100
				$C_{12}H_{18}N_2O_2\ Na^+$	245.127	245.127	1.6	yes	72
				$C_9H_{12}N_2O_2\ H^+$	181.097	181.098	-3.9	yes (low)	2
	38.1	2D	$C_{12}H_{17}N_3O_4$	$C_{12}H_{17}N_3O_4\ H^+$	268.128	268.129	-3.7	yes	100
				$C_{12}H_{17}N_3O_4\ Na^+$	290.111	290.111	0.0	yes	21
				$C_{10}H_{10}N_2O_4\ H^+$	223.071	223.072	-4.0	yes	4
	38.7	2E	$C_{12}H_{17}N_3O_4$	$C_{12}H_{17}N_3O_4\ H^+$	268.130	268.129	3.7	yes	100
				$C_{12}H_{17}N_3O_4\ Na^+$	290.111	290.111	0.0	yes	30
				$C_9H_{12}N_2O_2\ H^+$	181.097	181.098	-3.9	yes	13
				$C_{12}H_{15}N_3O_3\ H^+$	250.119	250.119	-0.7	yes	20
	40.2	2F	$C_{12}H_{16}N_2O_2$	$C_{12}H_{16}N_2O_2\ H^+$	221.128	221.129	-4.5	yes	100
				$C_{12}H_{16}N_2O_2\ Na^+$	243.109	243.110	-4.1	yes	27
				$C_9H_{10}N_2O_2\ H^+$	179.085	179.082	16.5	no	3
	42.4	2G	$C_{12}H_{17}N_3O_3$	$C_{12}H_{17}N_3O_3\ H^+$	252.134	252.134	0.0	yes	100
				$C_{12}H_{17}N_3O_3\ Na^+$	274.115	274.116	-3.6	yes	57
				$C_{10}H_{10}N_2O_3\ H^+$	207.077	207.077	0.2	yes	0.3
		2H	$C_{12}H_{15}N_3O_4$	$C_{12}H_{15}N_3O_4\ H^+$	266.112	266.114	-7.5	yes	100
				$C_{12}H_{15}N_3O_4\ Na^+$	288.095	288.096	-3.6	no	55
5 min	23.3	3A	$C_{12}H_{18}N_2O_2$	$C_{12}H_{18}N_2O_2\ H^+$	223.148	223.145	13.4	yes	100
				$C_{12}H_{18}N_2O_2\ Na^+$	245.131	245.127	18.0	yes	57
				$C_9H_{12}N_2O\ Na^+$	165.106	165.103	19.5	no	4
	26.2	3B	$C_{10}H_{14}N_2O_3$	$C_{10}H_{14}N_2O_3\ H^+$	211.112	211.108	18.9	no	100
				$C_{10}H_{14}N_2O_3\ Na^+$	233.094	233.090	17.2	no	53
	29.9	3C	$C_{11}H_{16}N_2O_3$	$C_{11}H_{16}N_2O_3\ H^+$	225.126	225.124	9.3	yes	20
				$C_{11}H_{16}N_2O_3\ Na^+$	247.108	247.105	12.1	yes	100
	31.2	3D	$C_{12}H_{17}N_3O_4$	$C_{12}H_{17}N_3O_4\ H^+$	268.133	268.129	14.9	no	100
				$C_{12}H_{17}N_3O_4\ Na^+$	290.115	290.111	13.8	no	89
	31.7	3E	$C_{12}H_{17}N_3O_4$	$C_{12}H_{17}N_3O_4\ H^+$	268.133	268.129	14.9	yes	99
				$C_{12}H_{17}N_3O_4\ Na^+$	290.115	290.111	13.8	yes	100
	34.6	3F	$C_{11}H_{16}N_2O$	$C_{11}H_{16}N_2O\ H^+$	193.136	193.134	9.9	yes	100
				$C_{11}H_{16}N_2O\ Na^+$	215.117	215.116	4.5	yes	58
				$C_8H_{10}N_2O\ H^+$	151.087	151.087	0.0	yes	10
				$C_9H_{13}N\ H^+$	136.112	136.113	-4.6	yes	3
	36.9	3G	$C_{12}H_{17}N_3O_4$	$C_{12}H_{17}N_3O_4\ H^+$	268.129	268.129	0.0	yes	74
				$C_{12}H_{17}N_3O_4\ Na^+$	290.111	290.111	0.0	yes	100
	39.4	3H	$C_{11}H_{15}N_3O_3$	$C_{11}H_{15}N_3O_3\ H^+$	238.117	238.119	-9.1	yes	10
				$C_{11}H_{15}N_3O_3\ Na^+$	260.100	260.101	-4.3	yes	16
				$C_9H_{12}N_2O_2\ H^+$	181.098	181.098	1.6	yes	100
				$C_9H_{10}N_2O\ H^+$	163.087	163.087	0.0	yes	18
				$C_6H_6N_2O_2\ H^+$	139.049	139.051	-12.6	yes	1
				$C_6H_4N_2O\ H^+$	121.039	121.040	-9.8	yes	2

the isopropyl group, can be ruled out. Propene loss in this case occurs preferably in the 181 Da and 163 Da daughter ions, presumably due to their higher stability than the H adduct parent ion. This propene loss can also be caused the stronger electron displacement by the protonated primary amide function as compared to the secondary amide function.

For 2A, 2B, 2H, 3B, 3C, 3D, 3E and 3G, no daughter ions were detected, in most cases due to their low abundance. Therefore, no information is available on the location of substituted groups and demethylation in their structure. The oxidation pathway proposed in Figure 8.26 is provisional, since not all possible isomeric structures are represented. Experiments with 20-fold higher initial isoproturon concentration are being performed at the moment, in order to gain more structural information on the by-products.

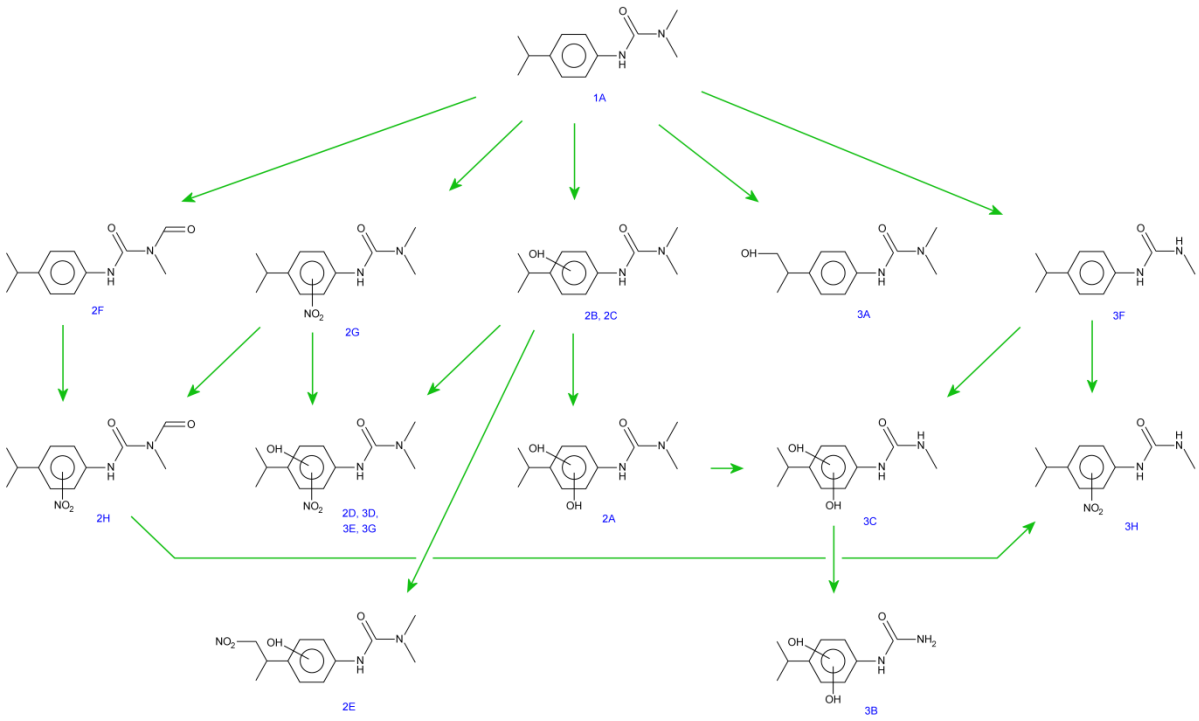

Figure 8.26 Proposed oxidation pathway of isoproturon under DBD plasma treatment in air atmosphere in this work.

Once again, the observed oxidation steps can be classified into

- hydroxylation,
- addition of a double bonded O,
- demethylation and
- nitrification.

Since no study is found on advanced oxidation of isoproturon in presence of nitrites or nitrates, the nitrificated intermediates have, to our knowledge, not been reported before. In our experiments, nitrificated by-products have the highest detected abundance in comparison to by-products formed by any other oxidation step. As this indicates,

nitrification is either the most frequent oxidation step or it produces the most recalcitrant intermediates. In other studies on advanced oxidation of isoproturon, on the other hand, hydroxylation clearly is the most frequent degradation mechanism. Singly hydroxylated isoproturon such as 2B, 2C and 3A, for instance, is the most commonly encountered by-product and has been reported for ozonation [197], oxidation with NaClO [198, 199], oxidation with ClO_2 [192, 198], electro-Fenton [200] and TiO_2-based photocatalysis [200-204]. As for diuron, the aromatic ring is theoretically expected to be the site of preference for O_3 and OH attack, but experiments show that hydroxylation occurs at many other locations as well. Three separate studies identified three isomers, of which two underwent OH substitution on the ring and one at the isopropyl group [197, 199, 203]. Amorisco et al., Losito et al. and López-Muñoz et al. made more profound by-product studies for TiO_2-based photocatalysis and found substitution of H with OH to occur at basically every possible location: on the ring, in the isopropyl and dimethyl amide groups and even at the secondary amide function [201, 202].

In contrast to diuron, transformation of methyl into formyl is observed in our experiments for isoproturon by-product 2F, in the dimethyl amide function. This by-product has only been reported before in a study on peroxonation [205] and presumably in a study on TiO_2-based photocatalysis [202]. Also here, formation of a hydroxymethyl or formyl function is postulated to proceed with H abstraction as depicted in Figure 8.24a. Besides, multiple authors support the demethylation mechanism of Figure 8.24b for isoproturon [201, 203]. Single demethylation in the dimethyl amide function as well as in the isopropyl function has only been reported up to now for TiO_2-based photocatalysis [201-204] and electro-Fenton [200]. Remarkably, dealkylation in the isopropyl function is often accompanied by replacement with OH, while in the dimethyl amide function, this is rather an exception.

In a UV/H_2O_2 reactor, toxicity towards Vibrio fischeri bacteria initially increased during isoproturon treatment, indicating that some oxidation products can be more hazardous than their precursor [206]. Nevertheless, the same study concluded that the oxidized effluent was compatible with biological treatment. It is yet unclear how nitrificated by-products add to the solution toxicity in our plasma reactor. As these by-products seem to be the most abundant ones, this is an essential question for future research. If nitrificated intermediates prove to be highly undesirable, research on water purification with plasma discharge should focus on how to avoid or eliminate them in the most economical and ecological way. Possibilities include the use of oxygen instead of air as working gas, optimizing the plasma parameters for minimal NO_x generation and increasing the energy efficiency for full mineralization.

8.8 Scalability of the reactor

As should be noted, the reactor technology described in this chapter can be scaled up for treatment of large amounts of influent water in at least 3 ways:

1. Reactor structure and size can be modified in order to enlarge the horizontal dimension of the plasma-liquid interface. By installing Zorflex® at the inner wall of the outer (grounded) electrode and by making the influent water flow over this wall, a higher water flow can be attained. The reactor can be further scaled up by increasing the radius of both electrodes. Alternatively, reactor geometry can be modified, for example by exchanging the axial DBD configuration with a planar (vertical) DBD geometry. This permits to tilt the falling water film, which can have additional practical advantages.
2. Reactors can be placed in parallel, while being powered by the same power source.
3. Only a part of the influent water can be treated in the plasma reactor and subsequently mixed again in the complementary water flow. In this manner, decomposition of micropollutants under influence of post-treatment effects can occur. This approach has already been proposed in studies on water sterilization, but is expected to be feasible for organic compound decomposition as well. In this case, plasma gas can still be bubbled through the total influent water volume in a preceding ozonation chamber.

8.9 Conclusion

In this work, we developed and characterized a new type of plasma reactor for water treatment, in which micropollutant decomposition by atmospheric dielectric barrier discharge (DBD) in dry air is combined with adsorption on activated carbon textile and with extra bubbling of generated ozone. In order to gain insight into the reactive species generated in the reactor, it is characterized by means of optical emission spectroscopy, pH and conductivity measurements and by determining its aqueous H_2O_2 and gaseous O_3 production. The emission spectra reveal the substantial presence of metastable N_2 in air, as well as in argon and oxygen plasma. Conductivity gradually rises during treatment time, while pH drops abruptly in the first minutes of treatment, to slowly decrease further afterwards. The end value of pH after 30 minutes of treatment is relatively independent of initial pH and conductivity and of applied power at constant duty cycle. The end pH changes, however, with a value of approximately 1 over the entire range of the duty cycle used in this work. At high power, average H_2O_2 production energy yield is 0.51 g/kWh. Ozone production energy yield halves from 0.189 g/kWh when input power is increased from 24 to 64 W, due to gas heating in the reactor.

Atrazine removal energy yield of the reactor remains relatively constant around 3.7 mg/kWh when power is increased with a factor 3.5. Up to 40.5% of total atrazine decomposition results from plasma gas bubbling, confirming an interesting synergy in terms of energy efficiency for applications. Comparison of our reactor with reactors described in literature indicates that combination of plasma discharge with pollutant adsorption and ozone recycling is more energy efficient than other plasma based water treatment technology. Detected by-products with HPLC-TOF-MS analysis are identified as the first or second

generation intermediates simazine amide, atrazine amide and deethylatrazine and the deeper oxidation product didealkylatrazine, in agreement with literature. These by-products are formed by substitution of 2 H atoms with double bonded oxygen or by dealkylation. Abundance of all by-products significantly dropped with increase in power. Desorption analysis revealed decreased concentration of atrazine and increased concentration of its by-products on activated carbon textile after plasma treatment in comparison to adsorption without plasma treatment.

The activated carbon textile in the reactor is characterized by means of adsorption and desorption experiments. Adsorption experiments performed over a period of several months, worth of 27.5 hours of plasma treatment, reveal a constant adsorption rate. After recirculating demineralized water through the reactor for 10 hours under plasma operation, however, adsorption rate is significantly increased. This effect can be caused by decomposition of adsorbed compounds, which unblocks the micropores of the activated carbon, by introduction of new surface functional groups on the textile or by increase or the micropore size and total pore volume, in agreement with other reports. As shown with the desorption analysis, initially adsorbed atrazine is removed without any detected by-products, indicating a different oxidation pathway or completer decomposition of attacked atrazine molecules. Moreover, treatment of adsorbed atrazine leads to a higher removal of 49.9% as compared to 41.8% removal after treatment of aqueous atrazine under identical experimental conditions. These results suggest that adsorption prior to plasma treatment is more energy efficient than adsorption during plasma treatment. Moreover, these experiments confirm that addition of activated carbon in a plasma reactor is a sustainable and energy efficient approach for reactor optimization.

For the other micropollutants, energy efficiency of their removal in reference conditions ranges over one order of magnitude, from 3.9 to 26 kWh/m^3, with increasing value in the order diuron < isoproturon < alachlor < PeCB < α-HCH. The contribution of evaporation as well as adsorption to the removal process is often significant, but strongly depends on compound properties. As shown for isoproturon, initial pH has a strong effect on the removal rate, which is explained with a change in oxidation rates of ozonation and the peroxone process. Addition of salt does not influence the removal rate, unless if ozone or OH radical scavengers are introduced into the solution this way. Investigation of the removal energy efficiency as a function of the initial micropollutant concentration showed a strongly increasing trend of G_{50} and a slight increase in EEO for higher concentrations, in agreement with results from other authors. Therefore, it is more advantageous to treat dense solutions or concentrates as opposed to dilute solutions if the aim is to decompose as much pollutant mass as possible. For water treatment applications where concentration cannot be controlled, however, this means that reducing the pollutant concentration with a factor 10 will require less energy at lower concentrations. Caution should be used when comparing energy efficiency for different reactors or for different compounds when initial concentrations are

significantly different. Energy efficiency displays limited changes and no clear trend under power variation at fixed duty cycle, indicating that removal rate can be increased with little loss in efficiency. Increasing duty cycle, on the other hand, results in a remarkably lower energy efficiency. Generally, the oxidation process is enhanced when oxygen is used as feed gas, except for α-HCH, most likely due to its strong resistance to ozonation. Argon, on the other hand, performs worse than air for removal of all compounds. Using the reactor in single-pass mode, where water flows through the treatment chambers only once, enhanced the removal process of the most persistent compounds α-HCH and PeCB, while it performed slightly worse for diuron and isoproturon removal. Comparison with single pass-mode experiments without the ozonation chamber proves that energy efficiency approximately doubles with the addition of ozonation chamber. Nonetheless, it is important to let the influent water flow through the ozonation chamber first and only afterwards through the plasma chamber, since the reverse cascade configuration gives consistently worse energy efficiency. This is explained with scavenging of ozone by NO_2^- ions, which are introduced into the solution during direct plasma contact in the plasma chamber.

In by-product analysis with HPLC-TOF-MS, alachlor, diuron and isoproturon display clear dissociation patterns in their mass spectra after electrospray ionization and subsequent acceleration, in good agreement with other scientific reports. Based on data found in literature, detailed dissociation pathways are proposed for each herbicide, in order to gain insight into the group-specific fragmentation mechanisms of their oxidation by-products. As the results show, several by-products are subject to identical dissociation processes. In a few cases, the dissociative behavior is similar, but the detached fragments are slightly altered. One example is by-products 3I of alachlor, where the fragment released from the first daughter ion contains double bonded oxygen. Other examples are isoproturon by-products 2E and 3A, where nitrification and hydroxylation are detected, respectively, on the propene fragment originating from the isopropyl function. These observations allow us to specify the location of substituted groups on the oxidation by-product. Accordingly, the preferable sites of ozone or radical attack on the initial compounds are determined. For diuron and isoproturon, single demethylation of the dimethyl amide function gives rise to a significantly different fragmentation mechanism, which is explained with an analogy to the known fragmentation of N-methyl carbamate pesticides.

Apart from by-product 3A from alachlor, all intermediates are explained with one or more oxidation steps that can be classified into 4 types: hydroxylation, substitution of 2 H atoms with double bonded oxygen, dealkylation and nitrification. Although the exact site of oxidation is unknown for the majority of by-products, the mass spectra often give clear indications of which part in the molecular structure is affected. While the aromatic ring is expected to be the oxidation site of preference, based on theoretical arguments, oxidation of the side chains is clearly detected as well, in good agreement with other studies on advanced oxidation. Hydroxylation of the ring occurs through electrophilic addition. In contrast,

hydroxylation and carbonyl formation on the side chains is initiated by hydrogen abstraction, as postulated by many authors. Additionally, hydroxyl and carbonyl functions are proposed as precursors of dealkylation. This is the first study, to our knowledge, where nitrification of non-phenolic micropollutants by means of plasma treatment is detected. Based on other research, the underlying mechanism is expected to be NO and NO_2 radical attack. Remarkably, it is one of the major oxidation steps for diuron and isoproturon, while only one minor nitrificated by-product of alachlor is tentatively identified. Toxicity analysis of nitrificated intermediates is an important topic for future research to understand the feasibility of air plasma for water purification.

Appendix

Table 8.A Welch's t-test with corresponding degrees of freedom ν and p-value for each couple of experiments of section 8.6, based on the reaction rate constants, their standard errors and their degrees of freedom. Experiment couples where the null-hypothesis cannot be rejected ($p > 0.05$) are marked in grey. Therefore, the kinetic curves of these experiment couples cannot be considered different in the accuracy of the measurements.

	experiment 1	experiment 2	α-HCH			PeCB			alachlor			diuron			isoproturon		
			ν	t	p	ν	t	p	ν	t	p	ν	t	p	ν	t	p
reference	evaporation	evap + ads	7.0	8.5	< 0.001	10.5	1.2	0.257	6.3	7.4	< 0.001	5.4	4.2	0.007	6.3	10.7	< 0.001
	evap + ads	plasma + O_3	11.7	3.7	0.003	12.0	4.4	0.001	10.0	14.8	< 0.001	10.8	30.9	< 0.001	7.8	22.0	< 0.001
	evaporation	plasma + O_3	6.8	12.0	< 0.001	10.6	6.4	< 0.001	7.1	20.0	< 0.001	7.8	51.4	< 0.001	7.0	25.4	< 0.001
initial concentration	C_L	$2 \times C_L$	11.8	-2.7	0.019				9.5	-1.9	0.083	5.5	-1.9	0.110	13.0	-2.7	0.020
	$2 \times C_L$	$4 \times C_L$													10.2	0.3	0.760
	C_L	$4 \times C_L$													9.2	-3.1	0.012
power	~ 30 W	~ 40 W	9.4	4.1	0.003	9.4	1.8	0.097	12.9	4.0	0.002	10.0	14.1	< 0.001	13.7	4.8	< 0.001
	~ 40 W	~ 70 W	8.0	1.3	0.233	12.0	7.7	< 0.001							7.2	6.4	< 0.001
	~ 30 W	~ 70 W	6.6	3.3	0.015	9.7	7.2	< 0.001							7.3	14.7	< 0.001
duty cycle	DC = 0.04	DC = 0.15	1.2	4.6	0.001	9.2	5.4	< 0.001							8.5	4.8	0.001
	DC = 0.15	DC = 0.35	8.7	-0.1	0.926	8.9	1.7	0.124	9.7	46.8	< 0.001	12.9	0.2	0.850			
	DC = 0.04	DC = 0.35	8.3	2.7	0.026	6.9	4.8	0.002									
feed gas	air	Ar	7.8	-2.1	0.070	10.2	-5.2	< 0.001	14.0	-1.6	0.134	11.5	-10.6	< 0.001	10.0	-19.2	< 0.001
	Ar	O_2	13.2	-10.3	< 0.001	9.2	34.6	< 0.001	7.2	6.4	< 0.001	7.4	9.8	< 0.001			
	air	O_2	8.8	-7.8	< 0.001	11.7	27.9	< 0.001	7.2	6.1	< 0.001	7.2	7.8	< 0.001			
pH	pH = 2.1	pH = 5.0													9.6	-9.7	< 0.001
	pH = 4.2	pH = 5.0													11.1	3.5	0.005
	pH = 5.0	pH = 7.2													7.7	-15.1	< 0.001
	pH = 5.0	pH = 10.0													9.6	1.0	0.342
salt	no salt	Na_2SO_4													12.6	-1.2	0.272
	no salt	NaH_2PO_4													9.0	-2.3	0.049
	no salt	$NaHCO_3$													13.9	-8.5	< 0.001

Acknowledgements

This research was partly funded by COST action TD1208 through STSM. The authors thank Carbon Cloth Division for Zorflex® samples and personally thank Jack Taylor for fruitful discussion of active carbon water treatment processes. We also kindly thank professor Karel De Schamphelaere from Environmental Toxicology Unit (GhEnToxLab) for advice and support on toxicity.

References

[1] A. Bubnov, *et al.*, "Plasma-catalytic decomposition of phenols in atmospheric pressure dielectric barrier discharge," *Plasma Chemistry and Plasma Processing,* vol. 26, pp. 19-30, 2006.

[2] M. A. Malik, "Synergistic effect of plasmacatalyst and ozone in a pulsed corona discharge reactor on the decomposition of organic pollutants in water," *Plasma Sources Science and Technology,* vol. 12, p. S26, 2003.

[3] (2015, 20 January). *Introduction to Zorflex Activated Carbon Cloth*. Available: http://www.chemvironcarbon.com/en/activated-carbon-cloth

[4] A. R. Ribeiro, *et al.*, "An overview on the advanced oxidation processes applied for the treatment of water pollutants defined in the recently launched Directive 2013/39/EU," *Environment International,* vol. 75, pp. 33-51, 2015.

[5] G. Premazzi and R. Stecchi, "Evaluation of the Impact of Atrazine on the Aquatic Environment," J. R. C. H. Collection, Ed., ed. Brussels, Belgium: Commission of the European Communities, 1989.

[6] Y. Zhang, *et al.*, "Metabolic ability and individual characteristics of an atrazine-degrading consortium DNC5," *Journal of Hazardous Materials,* vol. 237, pp. 376-381, 2012.

[7] N. D. Jablonowski, *et al.*, "Still present after all these years: persistence plus potential toxicity raise questions about the use of atrazine," *Environmental Science and Pollution Research,* vol. 18, pp. 328-331, 2011.

[8] J. Bethsass and A. Colangelo, "European Union bans atrazine, while the United States negotiates continued use," *International journal of occupational and environmental health,* vol. 12, pp. 260-267, 2006.

[9] L. M. Jantunen and T. Bidleman, "Air-water gas exchange of hexachlorocyclohexanes (HCHs) and the enantiomers of α-HCH in Arctic regions," *Journal of Geophysical Research: Atmospheres,* vol. 101, pp. 28837-28846, 1996.

[10] Y. Li and T. Bidleman, "Correlation between Global Emissions of alpha-hexachlorocyclohexane and its Concentrations in the Arctic Air," *Journal of Environmental Informatics,* vol. 1, pp. 52-57, 2003.

[11] J. Vijgen, *et al.*, "Hexachlorocyclohexane (HCH) as new Stockholm Convention POPs—a global perspective on the management of Lindane and its waste isomers," *Environmental Science and Pollution Research,* vol. 18, pp. 152-162, 2011.

[12] K. L. Willett, *et al.*, "Differential toxicity and environmental fates of hexachlorocyclohexane isomers," *Environmental Science & Technology,* vol. 32, pp. 2197-2207, 1998.

[13] "Toxicological profile for alpha-, beta-, gamma-, and delta-hexachlorocyclohexane," P. H. S. U.S. Department of Health and Human Services, Agency for Toxic Substances and Disease Registry, Ed., ed, 2005.

[14] A. Katsoyiannis, *et al.*, "Persistent organic pollutants (POPs) in the conventional activated sludge treatment process: Model predictions against experimental values," *Chemosphere,* vol. 65, pp. 1634-1641, 2006.

[15] G. Teijon, *et al.*, "Occurrence of emerging contaminants, priority substances (2008/105/CE) and heavy metals in treated wastewater and groundwater at Depurbaix facility (Barcelona, Spain)," *Science of The Total Environment,* vol. 408, pp. 3584-3595, 2010.

[16] E. J. Mrema, *et al.*, "Obsolete Pesticides – A Threat to Environment, Biodiversity and Human Health," pp. 1-21, 2013.

[17] Z. Xu, *et al.*, "Catalytic destruction of pentachlorobenzene in simulated flue gas by a V2O5–WO3/TiO2 catalyst," *Chemosphere,* vol. 87, pp. 1032-1038, 2012.

[18] R. Thomas, *et al.*, "Evidence for hepatocarcinogenic activity of pentachlorobenzene with intralobular variation in foci incidence," *Carcinogenesis,* vol. 19, pp. 1855-1862, 1998.

[19] E. O. Igbinosa, *et al.*, "Toxicological Profile of Chlorophenols and Their Derivatives in the Environment: The Public Health Perspective," *The Scientific World Journal,* vol. 2013, pp. 1-11, 2013.

[20] N. Barco-Bonilla, *et al.*, "Systematic study of the contamination of wastewater treatment plant effluents by organic priority compounds in Almeria province (SE Spain)," *Science of The Total Environment,* vol. 447, pp. 381-389, 2013.

[21] H. S. Kang, *et al.*, "Effects of Alachlor on Survival and Development of Bombina orientalis (Boulenger) Embryos," *Bulletin of Environmental Contamination and Toxicology,* vol. 74, pp. 1199-1206, 2005.

[22] A. R. Pipi, *et al.*, "Total removal of alachlor from water by electrochemical processes," *Separation and Purification Technology,* vol. 132, pp. 674-683, 2014.

[23] Y.-C. Lo, *et al.*, "Acute alachlor and butachlor herbicide poisoning," *Clinical Toxicology,* vol. 46, pp. 716-721, 2008.

[24] R. McKinlay, *et al.*, "Endocrine disrupting pesticides: Implications for risk assessment," *Environment International,* vol. 34, pp. 168-183, 2008.

[25] S. Weichenthal, *et al.*, "A Review of Pesticide Exposure and Cancer Incidence in the Agricultural Health Study Cohort," *Environmental Health Perspectives,* vol. 118, pp. 1117-1125, 2010.

[26] E. Thurman, *et al.*, "Occurrence of alachlor and its sulfonated metabolite in rivers and reservoirs of the Midwestern United States: the importance of sulfonation in the transport of chloroacetanilide herbicides," *Environmental Science & Technology,* vol. 30, pp. 569-574, 1996.

[27] A. Jurado, *et al.*, "Emerging organic contaminants in groundwater in Spain: A review of sources, recent occurrence and fate in a European context," *Science of The Total Environment,* vol. 440, pp. 82-94, 2012.

[28] D. W. Kolpin, *et al.*, "Degradates provide insight to spatial and temporal trends of herbicides in ground water," *Ground Water,* vol. 42, pp. 601-608, 2004.

[29] T. L. Potter and T. L. Carpenter, "Occurrence of alachlor environmental degradation products in groundwater," *Environmental Science & Technology,* vol. 29, pp. 1557-1563, 1995.

[30] K. Barrett and F. M. Jaward, "A review of endosulfan, dichlorvos, diazinon, and diuron – pesticides used in Jamaica," *International Journal of Environmental Health Research,* vol. 22, pp. 481-499, 2012.

[31] S. Giacomazzi and N. Cochet, "Environmental impact of diuron transformation: a review," *Chemosphere,* vol. 56, pp. 1021-1032, 2004.

[32] Y. Cabeza, *et al.*, "Monitoring the occurrence of emerging contaminants in treated wastewater and groundwater between 2008 and 2010. The Baix Llobregat (Barcelona, Spain)," *Journal of Hazardous Materials,* vol. 239-240, pp. 32-39, 2012.

[33] A. C. Gerecke, *et al.*, "Sources of pesticides in surface waters in Switzerland: pesticide load through waste water treatment plants—current situation and reduction potential," *Chemosphere,* vol. 48, pp. 307-315, 2002.

[34] K. Haarstad, *et al.*, "Organic and metallic pollutants in water treatment and natural wetlands: a review," *Water Science & Technology,* vol. 65, p. 76, 2012.

[35] S. Rodriguez-Mozaz, *et al.*, "Monitoring of estrogens, pesticides and bisphenol A in natural waters and drinking water treatment plants by solid-phase extraction–liquid chromatography–mass spectrometry," *Journal of Chromatography A,* vol. 1045, pp. 85-92, 2004.

[36] R. Loos, *et al.*, "EU-wide monitoring survey on emerging polar organic contaminants in wastewater treatment plant effluents," *Water Research,* vol. 47, pp. 6475-6487, 2013.

[37] L. Nitschke and W. Schüssler, "Surface water pollution by herbicides from effluents of waste water treatment plants," *Chemosphere,* vol. 36, pp. 35-41, 1998.

[38] S. Hussain, *et al.*, "Isolation and characterization of an isoproturon mineralizing Sphingomonas sp. strain SH from a French agricultural soil," *Biodegradation,* vol. 22, pp. 637-650, 2011.

[39] I. S. Fomsgaard, *et al.*, "Leaching of Pesticides Through Normal-Tillage and Low-Tillage Soil—A Lysimeter Study. I. Isoproturon," *Journal of Environmental Science and Health, Part B,* vol. 38, pp. 1-18, 2003.

[40] M. Legrand, *et al.*, "Occurrence of 38 pesticides in various French surface and ground waters," *Environmental Technology,* vol. 12, pp. 985-996, 1991.

[41] K. Müller, *et al.*, "Point-and nonpoint-source pesticide contamination in the Zwester Ohm catchment, Germany," *Journal of environmental quality,* vol. 31, pp. 309-318, 2002.

[42] N. H. Spliid and B. Køppen, "Occurrence of pesticides in Danish shallow ground water," *Chemosphere,* vol. 37, pp. 1307-1316, 1998.

[43] C. Mouvet, *et al.*, "Stability of isoproturon, bentazone, terbuthylazine and alachlor in natural groundwater, surface water and soil water samples stored under laboratory conditions," *Chemosphere,* vol. 35, pp. 1083-1097, 1997.

[44] L. Alletto, *et al.*, "Effects of temperature and water content on degradation of isoproturon in three soil profiles," *Chemosphere,* vol. 64, pp. 1053-1061, 2006.

[45] L. Ding, "Mechanisms of competitive adsorption between trace organic contaminants and natural organic matter on activated carbon," University of Illinois at Urbana-Champaign, 2010.

[46] P. Lukes, *et al.*, "Aqueous-phase chemistry of electricaldischarge plasma in water and in gas–liquid environments," in *Plasma chemistry and catalysis in gases and liquids*, V. I. Parvulescu, *et al.*, Eds., ed Weinheim, Germany: Wiley-VCH Verlag GmbH & Co., 2012.

[47] P. Lukes, *et al.*, "Aqueous-phase chemistry and bactericidal effects from an air discharge plasma in contact with water: evidence for the formation of peroxynitrite

through a pseudo-second-order post-discharge reaction of H2O2and HNO2," *Plasma Sources Science and Technology,* vol. 23, p. 015019, 2014.

[48] B. R. Locke and K.-Y. Shih, "Review of the methods to form hydrogen peroxide in electrical discharge plasma with liquid water," *Plasma Sources Science and Technology,* vol. 20, p. 034006, 2011.

[49] E. S. Bobkova, *et al.*, "Chemical composition of plasma of dielectric barrier discharge at atmospheric pressure with a liquid electrode," *High Temperature,* vol. 52, pp. 511-517, 2014.

[50] B. Tarabová, *et al.*, "Chemical and bactericidal effects induced in water treated by air transient spark," in *Hakone XIV*, Zinnowitz, Germany, 2014.

[51] H. Rogers, *et al.*, "Comparative predictions of Irgarol 1051 and atrazine fate and toxicity," *Environmental Technology,* vol. 17, pp. 553-556, 1996.

[52] M. Hijosa-Valsero, *et al.*, "Removal of priority pollutants from water by means of dielectric barrier discharge atmospheric plasma," *Journal of Hazardous Materials,* vol. 262, pp. 664-673, 2013.

[53] S. Machmudah and M. Goto, "Pulsed discharge plasma over a water surface induces decoloration of dyes," in *Journal of Physics: Conference Series*, 2013, p. 012008.

[54] P. M. K. Reddy, *et al.*, "Catalytic non-thermal plasma reactor for mineralization of endosulfan in aqueous medium: A green approach for the treatment of pesticide contaminated water," *Chemical Engineering Journal,* vol. 238, pp. 157-163, 2014.

[55] P. M. K. Reddy and C. Subrahmanyam, "Green Approach for Wastewater Treatment—Degradation and Mineralization of Aqueous Organic Pollutants by Discharge Plasma," *Industrial & Engineering Chemistry Research,* vol. 51, pp. 11097-11103, 2012.

[56] S. R. Cater, *et al.*, "UV/H2O2 treatment of methyl tert-butyl ether in contaminated waters," *Environmental Science & Technology,* vol. 34, pp. 659-662, 2000.

[57] J. Wohlers, *et al.*, "Application of an air ionization device using an atmospheric pressure corona discharge process for water purification," *Water, Air, and Soil Pollution,* vol. 196, pp. 101-113, 2009.

[58] S. Mededovic and B. R. Locke, "Side-chain degradation of atrazine by pulsed electrical discharge in water," *Industrial & Engineering Chemistry Research,* vol. 46, pp. 2702-2709, 2007.

[59] D. Gerrity, *et al.*, "An evaluation of a pilot-scale nonthermal plasma advanced oxidation process for trace organic compound degradation," *Water Research,* vol. 44, pp. 493-504, 2010.

[60] N. K. V. Leitner, *et al.*, "Generation of active entities by the pulsed arc electrohydraulic discharge system and application to removal of atrazine," *Water Research,* vol. 39, pp. 4705-4714, 2005.

[61] W. F. L. M. Hoeben, *Pulsed corona-iduced degradation of organic materials in water*: Technische Universiteit Eindhoven, 2000.

[62] D. Zhu, *et al.*, "Wire–cylinder dielectric barrier discharge induced degradation of aqueous atrazine," *Chemosphere,* vol. 117, pp. 506-514, 2014.

[63] J. L. Acero, *et al.*, "Degradation kinetics of atrazine and its degradation products with ozone and OH radicals: a predictive tool for drinking water treatment," *Environmental Science & Technology,* vol. 34, pp. 591-597, 2000.

[64] S. Nélieu, *et al.*, "Degradation of atrazine into ammeline by combined ozone/hydrogen peroxide treatment in water," *Environmental Science & Technology,* vol. 34, pp. 430-437, 2000.

[65] L. Xu, *et al.*, "Atrazine degradation using chemical-free process of USUV: Analysis of the micro-heterogeneous environments and the degradation mechanisms," *Journal of Hazardous Materials,* vol. 275, pp. 166-174, 2014.

[66] A. R. Adams, "The degredation of atrazine by soil minerals. Effects of drying mineral surfaces," ed: Master of Science in the Faculty of Agrisciences at Stellenbosch University. 177pp, 2014.

[67] L. Pospíšil, *et al.*, "Electrochemistry of s-triazine herbicides: reduction of atrazine and terbutylazine in aqueous solutions," *Journal of Electroanalytical Chemistry,* vol. 395, pp. 189-193, 1995.

[68] K. Chan and W. Chu, "Model applications and mechanism study on the degradation of atrazine by Fenton's system," *Journal of Hazardous Materials,* vol. 118, pp. 227-237, 2005.

[69] M. C. Guerreiro, *et al.*, "Aqueous atrazine removal by activated carbon/metal oxides composites," in *Int. Conf. Carbon Seattle*, 2007.

[70] A. Meyer, "Pathway dependent isotope fractionation in triazine degradation," Ph. D. Thesis, Technical University of Munich, München, 2010.

[71] G. R. Malpass, *et al.*, "Unexpected toxicity decrease during photoelectrochemical degradation of atrazine with NaCl," *Environmental chemistry letters,* vol. 10, pp. 177-182, 2012.

[72] C. L. Bianchi, *et al.*, "Mechanism and efficiency of atrazine degradation under combined oxidation processes," *Applied Catalysis B: Environmental,* vol. 64, pp. 131-138, 2006.

[73] C. Chan, *et al.*, "Treatment of atrazine by integrating photocatalytic and biological processes," *Environmental Pollution,* vol. 131, pp. 45-54, 2004.

[74] M. J. Farré, *et al.*, "Biodegradability of treated aqueous solutions of biorecalcitrant pesticides by means of photocatalytic ozonation," *Desalination,* vol. 211, pp. 22-33, 2007.

[75] L. Rizzo, "Bioassays as a tool for evaluating advanced oxidation processes in water and wastewater treatment," *Water Research,* vol. 45, pp. 4311-4340, 2011.

[76] J. M. Dias, *et al.*, "Waste materials for activated carbon preparation and its use in aqueous-phase treatment: a review," *Journal of Environmental Management,* vol. 85, pp. 833-846, 2007.

[77] H.-L. Chiang, *et al.*, "The surface characteristics of activated carbon as affected by ozone and alkaline treatment," *Chemosphere,* vol. 47, pp. 257-265, 2002.

[78] C. Y. Yin, *et al.*, "Review of modifications of activated carbon for enhancing contaminant uptakes from aqueous solutions," *Separation and Purification Technology,* vol. 52, pp. 403-415, 2007.

[79] N. Lu, *et al.*, "Application of double-dielectric barrier discharge plasma for removal of pentachlorophenol from wastewater coupling with activated carbon adsorption and simultaneous regeneration," *Plasma Chemistry and Plasma Processing,* vol. 32, pp. 109-121, 2012.

[80] G. Z. Qu, *et al.*, "DBD regeneration of GAC loaded with acid orange 7," *Asia-Pacific Journal of Chemical Engineering,* vol. 4, pp. 649-653, 2009.

[81] S. Tang, *et al.*, "Removal of bisphenol A in water using an integrated granular activated carbon preconcentration and dielectric barrier discharge degradation treatment," *Thin Solid Films,* vol. 521, pp. 257-260, 2012.
[82] G.-Z. Qu, *et al.*, "Simulataneous pentachlorophenol decomposition and granular activated carbon regeneration assisted by dielectric barrier discharge plasma," *Journal of Hazardous Materials,* vol. 172, pp. 472-478, 2009.
[83] S. Tang, *et al.*, "Design and application of an up-scaled dielectric barrier discharge plasma reactor for regeneration of phenol-saturated granular activated carbon," *Separation and Purification Technology,* vol. 95, pp. 73-79, 2012.
[84] P. Faria, *et al.*, "Activated carbon catalytic ozonation of oxamic and oxalic acids," *Applied Catalysis B: Environmental,* vol. 79, pp. 237-243, 2008.
[85] C. Moreno-Castilla, "Adsorption of organic molecules from aqueous solutions on carbon materials," *Carbon,* vol. 42, pp. 83-94, 2004.
[86] S. Ognier, *et al.*, "Analysis of Mechanisms at the Plasma–Liquid Interface in a Gas–Liquid Discharge Reactor Used for Treatment of Polluted Water," *Plasma Chemistry and Plasma Processing,* vol. 29, pp. 261-273, 2009.
[87] C. F. McDonogh and N. J. Sanders, "Peroxymonosulfuric acid formed by reaction of hydrogen peroxide and sulfuric acid," 1995.
[88] J. Spivey, *et al.*, *Catalysis*: Royal Society of Chemistry, 2015.
[89] M. Eriksson, "Ozone chemistry in aqueous solution: ozone decomposition and stabilisation," Department of Chemistry, Royal Institute of Technology, Stockholm, Sweden, 2005.
[90] L. J. Heidt and V. R. Landi, "Stabilization of ozone," 1967.
[91] E. C. Catalkaya and F. Kargi, "Dehalogenation, degradation and mineralization of diuron by peroxone (peroxide/ozone) treatment," *Journal of Environmental Science and Health, Part A,* vol. 44, pp. 630-638, 2009.
[92] M. Magureanu, *et al.*, "Degradation of pharmaceutical compound pentoxifylline in water by non-thermal plasma treatment," *Water Research,* vol. 44, pp. 3445-3453, 2010.
[93] L. Gao, *et al.*, "Degradation kinetics and mechanism of emerging contaminants in water by dielectric barrier discharge non-thermal plasma: The case of 17β-Estradiol," *Chemical Engineering Journal,* vol. 228, pp. 790-798, 2013.
[94] Y. Nakagawa, *et al.*, "Decolorization of Rhodamine B in Water by Pulsed High-Voltage Gas Discharge," *Japanese Journal of Applied Physics,* vol. 42, pp. 1422-1428, 2003.
[95] H. Ghodbane, *et al.*, "Non-thermal Plasma Degradation of Anthraquinonic Dye in Water: Oxidation Pathways and Effect of Natural Matrices," *Journal of Advanced Oxidation Technologies,* vol. 17, pp. 372-384, 2014.
[96] M. Fouodjouo, *et al.*, "Non-Thermal Plasma Coupled to TiO2 Applicable for the Removal of Paraquat from Aqueous Solutions," *International Journal of Research in Chemistry and Environment,* vol. 3, pp. 316-326, 2013.
[97] Y. Chen, *et al.*, "A Discharge Reactor with Water-Gas Mixing for Methyl Orange Removal," *International Journal of Plasma Environmental Science and Technology,* 2008.
[98] S. P. Li, *et al.*, "Degradation of nitenpyram pesticide in aqueous solution by low-temperature plasma," *Environmental Technology,* vol. 34, pp. 1609-1616, 2013.
[99] D. Piroi, *et al.*, "Pulsed dielectric barrier discharge generated at the gas-liquid interface for the degradation of the organic dye methyl red in aqueous solution," in

Optimization of Electrical and Electronic Equipment (OPTIM), 2010 12th International Conference on, 2010, pp. 1323-1328.

[100] P. M. K. Reddy, *et al.*, "Degradation and mineralization of methylene blue by dielectric barrier discharge non-thermal plasma reactor," *Chemical Engineering Journal,* vol. 217, pp. 41-47, 2013.

[101] P. M. K. Reddy, *et al.*, "Mineralization of Phenol in Water by Catalytic Non-Thermal Plasma Reactor - An Eco-Friendly Approach for Wastewater Treatment," *Plasma Processes and Polymers,* vol. 10, pp. 1010-1017, 2013.

[102] P. M. K. Reddy, *et al.*, "Mineralization of aqueous organic pollutants using a catalytic plasma reactor," *Indian Journal of Chemistry,* vol. 53, pp. 499-503, 2014.

[103] B. Jiang, *et al.*, "Degradation of azo dye using non-thermal plasma advanced oxidation process in a circulatory airtight reactor system," *Chemical Engineering Journal,* vol. 204-206, pp. 32-39, 2012.

[104] S. Rong and Y. Sun, "Wetted-wall corona discharge induced degradation of sulfadiazine antibiotics in aqueous solution," *Journal of Chemical Technology & Biotechnology,* vol. 89, pp. 1351-1359, 2013.

[105] I. C. Panorel, "Pulsed corona discharge as an advanced oxidation process for the degradation of organic compounds in water," Doctor Doctoral thesis, Acta Universitatis Lappeenrantaensis 535, Lappeenranta University of Technology, Lappeenranta, Finland, 2013.

[106] M. Elsawah, *et al.*, "Corona discharge with electrospraying system for phenol removal from water," *Plasma Science, IEEE Transactions on,* vol. 40, pp. 29-34, 2012.

[107] P. Ajo, "Combination of pulsed corona discharge with TiO2 photocatalysis: verification of hypothesis," Master, Faculty of Technology, Lappeenranta University of Technology, Lappeenranta, 2013.

[108] H. Ghodbane, *et al.*, "Degradation of AB25 dye in liquid medium by atmospheric pressure non-thermal plasma and plasma combination with photocatalyst TiO2," *Open Chemistry,* vol. 13, 2015.

[109] J. Gao, *et al.*, "Plasma degradation of dyes in water with contact glow discharge electrolysis," *Water Research,* vol. 37, pp. 267-272, 2003.

[110] L. Duan, *et al.*, "Study on the factors influencing phenol degradation in water by dielectric barrier discharge (DBD)," *Journal of Physics: Conference Series,* vol. 418, p. 012129, 2013.

[111] L. Duan, *et al.*, "Enhanced biodegradability of coking wastewater by gas phase dielectric barrier discharge plasma," *Separation and Purification Technology,* vol. 154, pp. 359-365, 2015.

[112] Y. S. Mok, *et al.*, "Degradation of an azo dye Orange II using a gas phase dielectric barrier discharge reactor submerged in water," *Chemical Engineering Journal,* vol. 142, pp. 56-64, 2008.

[113] Q. Tang, *et al.*, "Degradation of Azo Dye Acid Red 88 by Gas Phase Dielectric Barrier Discharges," *Plasma Chemistry and Plasma Processing,* vol. 29, pp. 291-305, 2009.

[114] J. Gao, *et al.*, "Degradation of imidazolium-based ionic liquids in aqueous solution using plasma electrolysis," *Journal of Hazardous Materials,* vol. 265, pp. 261-270, 2014.

[115] P. Verlicchi, *et al.*, "Hospital effluents as a source of emerging pollutants: an overview of micropollutants and sustainable treatment options," *Journal of Hydrology,* vol. 389, pp. 416-428, 2010.

[116] J. Feng, *et al.*, "Degradation of diuron in aqueous solution by dielectric barrier discharge," *Journal of Hazardous Materials,* vol. 154, pp. 1081-1089, 2008.
[117] J. Zhang, *et al.*, "Low-temperature plasma-induced degradation of aqueous 2, 4-dinitrophenol," *Journal of Hazardous Materials,* vol. 154, pp. 506-512, 2008.
[118] J. Feng, *et al.*, "Degradation of aqueous 3, 4-dichloroaniline by a novel dielectric barrier discharge plasma reactor," *Environmental Science and Pollution Research,* vol. 22, pp. 4447-4459, 2015.
[119] P. Olszewski, *et al.*, "Optimizing the electrical excitation of an atmospheric pressure plasma advanced oxidation process," *Journal of Hazardous Materials,* vol. 279, pp. 60-66, 2014.
[120] P. Roche and M. Prados, "Removal of pesticides by use of ozone or hydrogen peroxide/ozone," *Ozone: Science & Engineering,* vol. 17, pp. 657-672, 1995.
[121] C. D. Yao and W. R. Haag, "Rate constants for direct reactions of ozone with several drinking water contaminants," *Water Research,* vol. 25, pp. 761-773, 1991.
[122] W. R. Haag and C. D. Yao, "Rate constants for reaction of hydroxyl radicals with several drinking water contaminants," *Environmental Science & Technology,* vol. 26, pp. 1005-1013, 1992.
[123] V. Camel and A. Bermond, "The use of ozone and associated oxidation processes in drinking water treatment," *Water Research,* vol. 32, pp. 3208-3222, 1998.
[124] S. S. Kalra, *et al.*, "Advanced oxidation processes for treatment of textile and dye wastewater: a review," in *2nd International conference on environmental science and development*, 2011, pp. 271-5.
[125] J. R. Bolton, *et al.*, "Figures-of merit for the technical development and application of advanced oxidation processes," *Journal of Advanced Oxidation Technologies,* vol. 1, pp. 13-17, 1996.
[126] D. E. Damschen and L. R. Martin, "Aqueous aerosol oxidation of nitrous acid by O 2, O 3 and H 2 O 2," *Atmospheric Environment (1967),* vol. 17, pp. 2005-2011, 1983.
[127] J. A. Garland, *et al.*, "The mechanism for dry deposition of ozone to seawater surfaces," *Journal of Geophysical Research: Oceans,* vol. 85, pp. 7488-7492, 1980.
[128] J. Hoigné, *et al.*, "Rate constants of reactions of ozone with organic and inorganic compounds in water—III. Inorganic compounds and radicals," *Water Research,* vol. 19, pp. 993-1004, 1985.
[129] S. Penkett, "Oxidation of SO2 and other atmospheric gases by ozone in aqueous solution," *Nature,* vol. 240, pp. 105-106, 1972.
[130] W. Seddon, *et al.*, "Pulse radiolysis of nitric oxide in aqueous solution," *Canadian Journal of Chemistry,* vol. 51, pp. 1123-1130, 1973.
[131] H. Strehlow and I. Wagner, "Flash photolysis in aqueous nitrite solutions," *Zeitschrift für Physikalische Chemie,* vol. 132, pp. 151-160, 1982.
[132] A. Treinin and E. Hayon, "Absorption spectra and reaction kinetics of NO2, N2O3, and N2O4 in aqueous solution," *Journal of the American Chemical Society,* vol. 92, pp. 5821-5828, 1970.
[133] P. Y. Jiang, *et al.*, "Reduction potential of the nitrate radical in aqueous solution," *Inorganic Chemistry,* vol. 31, pp. 5135-5136, 1992.
[134] Y. Katsumura, *et al.*, "Pulse radiolysis study of aqueous nitric acid solutions: formation mechanism, yield, and reactivity of NO3 radical," *The Journal of Physical Chemistry,* vol. 95, pp. 4435-4439, 1991.

[135] G. Adams, *et al.*, "Reactions of the hydroxyl radical. Part 2.—Determination of absolute rate constants," *Transactions of the Faraday Society,* vol. 61, pp. 1417-1424, 1965.
[136] G. Adams, *et al.*, "Spectroscopic studies of reactions of the OH radical in aqueous solutions. Reaction of OH with the ferrocyanide ion," *Transactions of the Faraday Society,* vol. 61, pp. 492-505, 1965.
[137] G. Barker, *et al.*, "Pulse radiolytic induced transient electrical conductance in liquid solutions. Part 2.—Radiolysis of aqueous solutions of NO–3, NO–2 and Fe (CN) 3–6," *Transactions of the Faraday Society,* vol. 66, pp. 1509-1519, 1970.
[138] G. Buxton, "Pulse radiolysis of aqueous solutions. Some rates of reaction of OH and O–and pH dependence of the Yield of O–3," *Transactions of the Faraday Society,* vol. 65, pp. 2150-2158, 1969.
[139] T. Løgager and K. Sehested, "Formation and decay of peroxynitrous acid: a pulse radiolysis study," *The Journal of Physical Chemistry,* vol. 97, pp. 6664-6669, 1993.
[140] A. Moniczewski, *et al.*, "Oxidative stress as an etiological factor and a potential treatment target of psychiatric disorders. Part 1. Chemical aspects and biological sources of oxidative stress in the brain," *Pharmacological Reports,* vol. 67, pp. 560-568, 2015.
[141] G. L. Squadrito and W. A. Pryor, "Mapping the reaction of peroxynitrite with CO2: energetics, reactive species, and biological implications," *Chemical research in toxicology,* vol. 15, pp. 885-895, 2002.
[142] S. Banerjee and S. Mazumdar, "Electrospray Ionization Mass Spectrometry: A Technique to Access the Information beyond the Molecular Weight of the Analyte," *International Journal of Analytical Chemistry,* vol. 2012, pp. 1-40, 2012.
[143] C. L. Gatlin and F. Turecek, "Acidity determination in droplets formed by electrospraying methanol-water solutions," *Analytical Chemistry,* vol. 66, pp. 712-718, 1994.
[144] W. M. A. Niessen, "Group-specific fragmentation of pesticides and related compounds in liquid chromatography–tandem mass spectrometry," *Journal of Chromatography A,* vol. 1217, pp. 4061-4070, 2010.
[145] S. Bouchonnet, *et al.*, "Investigation of the dissociation pathways of metolachlor, acetochlor and alachlor under electron ionization–application to the identification of ozonation products," *Rapid Communications in Mass Spectrometry,* vol. 25, pp. 93-103, 2011.
[146] D. Volmer, *et al.*, "Thermospray mass spectral studies of pesticides: Temperature and salt concentration effects on the ion abundances in thermospray mass spectra," *Journal of Chromatography A,* vol. 647, pp. 235-259, 1993.
[147] S.-G. Park, *et al.*, "Structural characterization of alachlor complexes with transition metal ions by electrospray ionization tandem mass spectrometry," *Microchemical Journal,* vol. 86, pp. 248-256, 2007.
[148] S. Bouchonnet, *et al.*, "GC-MSn and LC-MS/MS couplings for the identification of degradation products resulting from the ozonation treatment of Acetochlor," *Journal of Mass Spectrometry,* vol. 47, pp. 439-452, 2012.
[149] W. Chu and C. Wong, "Study of herbicide alachlor removal in a photocatalytic process through the examination of the reaction mechanism," *Industrial & Engineering Chemistry Research,* vol. 43, pp. 5027-5031, 2004.

[150] C. Wong and W. Chu, "The hydrogen peroxide-assisted photocatalytic degradation of alachlor in TiO2 suspensions," *Environmental Science & Technology,* vol. 37, pp. 2310-2316, 2003.
[151] H.-y. Li, *et al.*, "Decomposition of alachlor by ozonation and its mechanism," *Journal of Environmental Sciences,* vol. 19, pp. 769-775, 2007.
[152] Z. Qiang, *et al.*, "Degradation mechanism of alachlor during direct ozonation and O3/H2O2 advanced oxidation process," *Chemosphere,* vol. 78, pp. 517-526, 2010.
[153] D. G. Wayment and D. J. Casadonte, "Frequency effect on the sonochemical remediation of alachlor," *Ultrasonics Sonochemistry,* vol. 9, pp. 251-257, 2002.
[154] X. Wang and Y. Zhang, "Degradation of alachlor in aqueous solution by using hydrodynamic cavitation," *Journal of Hazardous Materials,* vol. 161, pp. 202-207, 2009.
[155] J. Bolobajev, *et al.*, "Improvement in iron activation ability of alachlor Fenton-like oxidation by ascorbic acid," *Chemical Engineering Journal,* vol. 281, pp. 566-574, 2015.
[156] C. Wang and Z. Liu, "Degradation of alachlor using an enhanced sono-Fenton process with efficient Fenton's reagent dosages," *Journal of Environmental Science and Health, Part B,* vol. 50, pp. 504-513, 2015.
[157] H. Katsumata, *et al.*, "Photo-Fenton degradation of alachlor in the presence of citrate solution," *Journal of Photochemistry and Photobiology A: Chemistry,* vol. 180, pp. 38-45, 2006.
[158] A. Hogenboom, *et al.*, "Characterization of photodegradation products of alachlor in water by on-line solid-phase extraction liquid chromatography combined with tandem mass spectrometry and orthogonal-acceleration time-of-flight mass spectrometry," *Rapid Communications in Mass Spectrometry,* vol. 14, pp. 1914-1924, 2000.
[159] M.-S. Kim, *et al.*, "Effect of ferric ion added on photodegradation of alachlor in the presence of TiO2 and UV radiation," *Water Research,* vol. 39, pp. 525-532, 2005.
[160] G. A. Penuela and D. Barcelo, "Comparative degradation kinetics of alachlor in water by photocatalysis with FeCl 3, TiO 2 and photolysis, studied by solid-phase disk extraction followed by gas chromatographic techniques," *Journal of Chromatography A,* vol. 754, pp. 187-195, 1996.
[161] Y.-K. Chang, *et al.*, "Photodegradation of Alachlor Using BiVO4 Photocatalyst Under Visible Light Irradiation," *Water, Air, & Soil Pollution,* vol. 226, 2015.
[162] C. S. Ryu, *et al.*, "Photodegradation of alachlor with the TiO2 film immobilised on the glass tube in aqueous solution," *Chemosphere,* vol. 53, pp. 765-771, 2003.
[163] C. Decoret, *et al.*, "Experimental and theoretical studies of the mechanism of the initial attack of ozone on some aromatics in aqueous medium," *Environmental Technology,* vol. 5, pp. 207-218, 1984.
[164] J. Hoigné and H. Bader, "Rate constants of reactions of ozone with organic and inorganic compounds in water—I: non-dissociating organic compounds," *Water Research,* vol. 17, pp. 173-183, 1983.
[165] K. S. Tay, *et al.*, "Ozonation of parabens in aqueous solution: Kinetics and mechanism of degradation," *Chemosphere,* vol. 81, pp. 1446-1453, 2010.
[166] C. J. Hapeman-Somich, "Mineralization of Pesticide Degradation Products," vol. 459, pp. 133-147, 1991.
[167] W. M. Draper and D. G. Crosby, "Solar photooxidation of pesticides in dilute hydrogen peroxide," *Journal of agricultural and food chemistry,* vol. 32, pp. 231-237, 1984.

[168] W. M. Draper, "Electrospray liquid chromatography quadrupole ion trap mass spectrometry determination of phenyl urea herbicides in water," *Journal of agricultural and food chemistry,* vol. 49, pp. 2746-2755, 2001.
[169] K. Abass, *et al.*, "Characterization of Diuron N-Demethylation by Mammalian Hepatic Microsomes and cDNA-Expressed Human Cytochrome P450 Enzymes," *Drug Metabolism and Disposition,* vol. 35, pp. 1634-1641, 2007.
[170] J. Fenoll, *et al.*, "Photocatalytic transformation of sixteen substituted phenylurea herbicides in aqueous semiconductor suspensions: Intermediates and degradation pathways," *Journal of Hazardous Materials,* vol. 244-245, pp. 370-379, 2013.
[171] S. Malato, *et al.*, "Photocatalytic treatment of diuron by solar photocatalysis: evaluation of main intermediates and toxicity," *Environmental Science & Technology,* vol. 37, pp. 2516-2524, 2003.
[172] R. R. Solís, *et al.*, "Ozonation, photocatalysis and photocatalytic ozonation of diuron. Intermediates identification," *Chemical Engineering Journal,* vol. 292, pp. 72-81, 2016.
[173] L. Zhou, *et al.*, "Ferrous-activated persulfate oxidation of arsenic(III) and diuron in aquatic system," *Journal of Hazardous Materials,* vol. 263, pp. 422-430, 2013.
[174] K. S. Chiu, *et al.*, "High-performance liquid chromatographic/mass spectrometric and high-performance liquid chromatographic/tandem mass spectrometric analysis of carbamate pesticides," *Biomedical & environmental mass spectrometry,* vol. 18, pp. 200-206, 1989.
[175] J. J. Stamp, *et al.*, "Chemical ionization mass spectrometry of carbamate pesticides: a major dissociation pathway," *Analytical Chemistry,* vol. 58, pp. 873-881, 1986.
[176] J. Feng, *et al.*, "Degradation of diuron in aqueous solution by ozonation," *Journal of Environmental Science and Health, Part B,* vol. 43, pp. 576-587, 2008.
[177] H. Mestankova, *et al.*, "Evolution of algal toxicity during (photo)oxidative degradation of diuron," *Aquatic Toxicology,* vol. 101, pp. 466-473, 2011.
[178] R. M. Ramirez Zamora and R. Seux, "Oxydation du diuron et identification de quelques sous-produits de la réaction," *Revue des sciences de l'eau,* vol. 12, p. 545, 1999.
[179] L. A. Tahmasseb, *et al.*, "Ozonation of chlorophenylurea pesticides in water: reaction monitoring and degradation pathways," *Science of The Total Environment,* vol. 291, pp. 33-44, 2002.
[180] J. Jirkovský, *et al.*, "Photolysis of diuron," *Pesticide Science,* vol. 50, pp. 42-52, 1997.
[181] F. S. Tanaka, *et al.*, "Photolysis of 3-(3,4-dichlorophenyl)-1, 1 -Dimethylurea (Diuron) in dilute aqueous solution," *Toxicological & Environmental Chemistry,* vol. 11, pp. 261-269, 1986.
[182] M. Carrier, *et al.*, "Photocatalytic degradation of diuron: experimental analyses and simulation of HO radical attacks by density functional theory calculations," *The Journal of Physical Chemistry A,* vol. 113, pp. 6365-6374, 2009.
[183] H. Katsumata, *et al.*, "Photocatalytic degradation of diuron in aqueous solution by platinized TiO2," *Journal of Hazardous Materials,* vol. 171, pp. 1081-1087, 2009.
[184] K. Macounová, *et al.*, "Kinetics of photocatalytic degradation of diuron in aqueous colloidal solutions of Q-TiO2 particles," *Journal of Photochemistry and Photobiology A: Chemistry,* vol. 156, pp. 273-282, 2003.
[185] M. V. Shankar, *et al.*, "Photo-induced degradation of diuron in aqueous solution by nitrites and nitrates: Kinetics and pathways," *Chemosphere,* vol. 66, pp. 767-774, 2007.

[186] P. Mazellier and M. Bolte, "Photodegradation of Diuron Induced by Iron(III) in the Aquatic Environment," *International Journal of Environmental Analytical Chemistry,* vol. 70, pp. 163-176, 1998.
[187] P. Mazellier, *et al.*, "Degradation of diuron photoinduced by iron (III) in aqueous solution," *Pesticide Science,* vol. 49, pp. 259-267, 1997.
[188] M. C. Edelahi, *et al.*, "Degradation of diuron by the electro-Fenton process," *Environmental chemistry letters,* vol. 1, pp. 233-236, 2004.
[189] M. A. Oturan, *et al.*, "Kinetics of oxidative degradation/mineralization pathways of the phenylurea herbicides diuron, monuron and fenuron in water during application of the electro-Fenton process," *Applied Catalysis B: Environmental,* vol. 97, pp. 82-89, 2010.
[190] M. A. Oturan, *et al.*, "Oxidative degradation of herbicide diuron in aqueous medium by Fenton's reaction based advanced oxidation processes," *Chemical Engineering Journal,* vol. 171, pp. 127-135, 2011.
[191] M. Carrier, *et al.*, "Removal of herbicide diuron and thermal degradation products under Catalytic Wet Air Oxidation conditions," *Applied Catalysis B: Environmental,* vol. 91, pp. 275-283, 2009.
[192] F.-X. Tian, *et al.*, "Degradation of phenylurea herbicides by chlorine dioxide and formation of disinfection by-products during subsequent chlor(am)ination," *Chemical Engineering Journal,* vol. 258, pp. 210-217, 2014.
[193] J. Feng, *et al.*, "Gas–liquid hybrid discharge-induced degradation of diuron in aqueous solution," *Journal of Hazardous Materials,* vol. 164, pp. 838-846, 2009.
[194] M. J. Farré, *et al.*, "Evaluation of the intermediates generated during the degradation of Diuron and Linuron herbicides by the photo-Fenton reaction," *Journal of Photochemistry and Photobiology A: Chemistry,* vol. 189, pp. 364-373, 2007.
[195] D. Baglio, *et al.*, "Atmospheric pressure ionisation multiple mass spectrometric analysis of pesticides," *Journal of Chromatography A,* vol. 854, pp. 207-220, 1999.
[196] J. Yinon and A. Vincze, "Collision-induced dissociation (CID) processes in some carbamate and phenylurea pesticides studied by ion-trap MS/MS," *International journal of mass spectrometry and ion processes,* vol. 167, pp. 21-33, 1997.
[197] G. Mascolo, *et al.*, "By-products formation during degradation of isoproturon in aqueous solution. I: ozonation," *Water Research,* vol. 35, pp. 1695-1704, 2001.
[198] A. Lopez, *et al.*, "Degradation of herbicides (ametryn and isoproturon) during water disinfection by means of two oxidants (hypochlorite and chlorine dioxide)," *Water Science and Technology,* vol. 35, pp. 129-136, 1997.
[199] G. Mascolo, *et al.*, "By-products formation during degradation of isoproturon in aqueous solution. II: chlorination," *Water Research,* vol. 35, pp. 1705-1713, 2001.
[200] I. Losito, *et al.*, "Electro-Fenton and photocatalytic oxidation of phenyl-urea herbicides: An insight by liquid chromatography–electrospray ionization tandem mass spectrometry," *Applied Catalysis B: Environmental,* vol. 79, pp. 224-236, 2008.
[201] A. Amorisco, *et al.*, "Photocatalytic degradation of the herbicide isoproturon: characterisation of by-products by liquid chromatography with electrospray ionisation tandem mass spectrometry," *Rapid Communications in Mass Spectrometry,* vol. 19, pp. 1507-1516, 2005.
[202] M. J. López-Muñoz, *et al.*, "Heterogeneous photocatalytic degradation of isoproturon in aqueous solution: Experimental design and intermediate products analysis," *Catalysis Today,* vol. 209, pp. 99-107, 2013.

[203] M. V. P. Sharma, *et al.*, "Solar photocatalytic degradation of isoproturon over TiO2/H-MOR composite systems," *Journal of Hazardous Materials,* vol. 160, pp. 568-575, 2008.
[204] A. Verma, *et al.*, "Photocatalytic degradation of herbicide isoproturon in TiO2Aqueous Suspensions: Study of Reaction Intermediates and Degradation Pathways," *Environmental Progress & Sustainable Energy,* vol. 33, pp. 402-409, 2014.
[205] H. Allemane, *et al.*, "Recherche et identification des premiers sous-produits d'oxydation de l'isoproturon par le système ozone/peroxyde d'hydrogène," *Revue des sciences de l'eau,* vol. 8, p. 315, 1995.
[206] S. Parra, *et al.*, "Photochemical versus coupled photochemical–biological flow system for the treatment of two biorecalcitrant herbicides: metobromuron and isoproturon," *Applied Catalysis B: Environmental,* vol. 27, pp. 153-168, 2000.

Be water, my friend.
- Bruce Lee

Chapter 9

General conclusions and outlook

Advanced oxidation methods are attractive technology for water purification purposes, as they are able to effectively decompose persistent micropollutants. As a main drawback, their energy demand has been too high up to now for extensive real-world application. Therefore, research needs to focus on optimization of each method and comparison of different technologies as a function of energy efficiency. Low-temperature plasma discharge takes a particular place among the advanced oxidation processes due to the wide spectrum of generated oxidative species, its flexibility in design and the synergetic combination with other advanced water treatment methods. Its versatility, however, complicates optimization and intensifies the need for accurate comparative studies. The extensive overview on plasma reactors in Chapter 3 provides a map that can be used in this exploration. As the cited examples clearly illustrate, energy efficiency is not only a function of the plasma-water phase distribution, plasma regime, applied voltage waveform and operational parameters, but it also strongly depends on reactor design and materials. While the former four factors have been frequently considered in prior comparative studies, the importance of reactor design and materials needs to be emphasized more, as these factors can prove to play a key role in the further overall optimization of plasma technology. In this optimization process, mostly an experimental approach is taken by many research groups, where reactor performance is enhanced by trial and error. This experimental approach often includes analysis of the plasma-chemistry and aqueous chemistry in the reactor under study. Less frequently, a more fundamental approach is taken, where the underlying plasma-physics is scrutinized as well. Nonetheless, a deeper understanding of these underlying mechanisms is essential for faster progress in this field. With this motivation, the present work has studied different plasma reactors from both approaches.

As fundamental investigation of bubble discharge in Chapters 4 and 5 revealed, pulsed discharge in a submerged bubble commonly takes place with a certain delay time of typically several microseconds after application of the voltage pulse. For free rising bubbles in between a pin-to-plate electrode system, this delay time is explained with a bubble location that, at the moment of pulse application, is not readily reachable by the propagating streamer from the high voltage pin electrode. For a bubble in contact with a high voltage nozzle electrode, the delay time is explained with a significantly different mechanism, where the capacitive nature of the bubble plays a crucial role. As one of the main arguments for this distinct behavior, plasma light emission is observed during the delay time in the former case, while no plasma occurs during the delay time in the latter case. The difference is most likely caused by the dissimilar electrode configurations and bubble location, leading to either a delayed spark discharge in the former case or a delayed filamentary discharge in the latter case. Despite this difference, the free rising bubbles likely also display capacitive behavior during the delay time under influence of the strong external field. As suggested in Chapter 5, this capacitive behavior implies the strong attraction of aqueous ionic species towards the bubble during the initial delay time with a subsequent discharge that is most active at the bubble surface. This makes bubble discharge especially attractive for oxidation of ionic target compounds and surface-active agents. However, more research is required to confirm the proposed mechanisms of bubble discharge, to verify how valid they are in other bubble discharge reactors and to examine how important their role can be in reactor optimization. For now, reports that mention similar delay times in electrohydraulic discharge or bubble discharge are very scarce.

In the fundamental study in Chapter 7 on a single DBD micro-discharge filament with a liquid electrode, cathode fall formation was shown to occur only at the water cathode during the positive voltage half cycle. This preference, as well as the continuous glow at the water surface was suggested to have many possible causes, including local field enhancement by water surface deformation or droplet formation, local ionization enhancement by the inhomogeneous humidity profile and more effective secondary electron emission at the water electrode than at the dielectric barrier. Nevertheless, there is a clear need for deeper investigation to understand which mechanism is the most dominant one. The importance of chemical tunneling in secondary electron emission at the water cathode can be determined by variation of solution pH. The influence of water deformation and droplet formation can be revealed by modifying solution viscosity and surface tension. Conductivity is expected to reshape the photocurrent hump, but can also have an effect on surface deformation. Interpretation of these effects, however, needs to be performed with caution, since all solution parameters can significantly alter the overall plasma chemistry at the water interface by introduction of new species into the gas phase.

Although the fundamental study in Chapter 7 indicated several similarities with DBD between solid electrodes, the observed dissimilarities can be at least as interesting in the

context of water treatment. The most intense, but short plasma stage during the negative voltage half cycle will undoubtedly be responsible for a significant part of the generated aqueous oxidants. On the other hand, the uninterrupted presence of glow discharge at the water surface as well as the long duration of the cathode fall region at the liquid interface during the positive half cycle suggest continuous generation of oxidative species. Consequently, the new research questions are raised which of these three processes is most dominant in decomposition of aqueous pollutants, which one is most energy efficient and what is the difference in underlying chemistry. In light of reactor optimization, it is also interesting to investigate the effect of interelectrode distance, dielectric barrier material and thickness, working gas, and voltage waveform on the micro-discharge filament properties. For example, the question remains whether the conditions in a pulsed filament are identical to those of a filament initiated by a slowly rising voltage. Also, the possibilities to generate diffuse barrier discharges in contact with a water electrode need to be clarified, as they are expected to press energy consumption and increase plasma-liquid contact area. Such diffuse micro-discharges can be obtained, for instance, by replacing the dielectric barrier with a resistive coating. Up to now, the effect of such parameters on DBD reactor performance have mostly been investigated with a focus on oxidant production and chemistry as a whole, while very few attention has been directed to the role of temporal and spatial plasma features.

However, the reality in a volume DBD can be different from that of an isolated micro-discharge. For the case of solid electrodes, this is yet an open question as well. In particular, filaments of a volume DBD have the possibility to increase or decrease in number under influence of experimental parameters such as voltage amplitude or interelectrode distance, while this is not true for an isolated micro-discharge filament as in our reactor. Since such differences are still not well-known, the insights from Chapter 7 should be used with necessary caution for interpretation of results in any AC powered DBD reactor. Notwithstanding, they provide a helpful background for further discussion.

The micropollutant oxidation studies included in the present work clearly show the synergy between plasma discharge and micropollutant adsorption and the beneficial effect of bubbling the produced plasma gas additionally through the liquid under treatment. Not only do these synergies enhance reactor performance without increase of energy demand, they also result in a higher sustainability of the used activated carbon textile. Since plasma discharge is able to effectively regenerate activated carbon during water treatment and moreover as a post-process after adsorption, an important research question is which of both approaches has highest energy efficiency. Although the presented results from desorption analysis indicate that post-treatment is more likely to be a better approach, further detailed investigation is required to confirm this statement. Also, the sustainability of Zorflex® under plasma treatment needs to be substantiated with additional characterization by methods such as SEM and XPS, in order to investigate any structural damage and modifications in

functional surface groups. Since activated carbon is an expensive material, it is also useful to consider alternative adsorbents. When Zorflex® in our reactor was replaced with 100% cellulose filter paper, very fast removal of alachlor and diuron was recorded under reference conditions (see Figure 9.1), with maximal EEO values of 1.2 ± 0.2 kWh/m^3 and 1.5 ± 0.2 kWh/m^3, respectively. Possibly, this efficient removal is due a catalytic effect of the cellulose or due to increased adsorption of micropollutants on the filter paper as a result of surface oxidation. Improvement of compound adsorption on cellulosic fabrics has been reported before for dry plasma treatment [1], but, to our knowledge, never for wet treatment. Because these preliminary results were unexpected, they are mentioned here as a topic for future research. An alternative approach to purify water by means of plasma discharge is to pretreat fabrics in order to obtain increased adsorption afterwards, a method that has been proposed for dye wastewater reuse [2]. Another interesting research question concerns the effect of water vapor content in the feed gas. As mentioned in section 7.1, increased humidity leads to higher OH radical formation in the plasma and less nitrate in solution, while ozone production is quenched. Therefore, an experiment with humid air can reveal additional information on the relative importance of the different oxidants. Moreover, if relative humidity proves to result in overall enhanced energy efficiency, new doors are opened towards a higher oxidation rate of dissolved volatile compounds, by initially bubbling the feed gas through the solution under treatment.

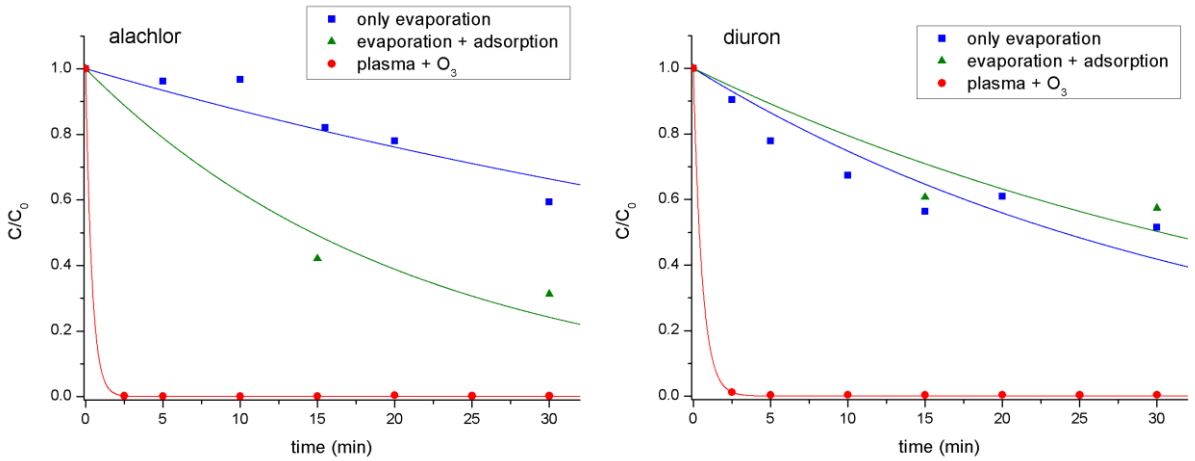

Figure 9.1 Removal kinetics for alachlor and diuron by air plasma under the same conditions as in Figure 8.13, but where Zorflex® is replaced with 5 layers of 0.1 mm thick filter paper (Rotilabo® type 601, 100% cellulose).

The main question, however, remains how this compares to all other synergetic combinations of advanced water treatment techniques. For real-world applications in water treatment, plasma discharge is a priori disfavored, as it is looked upon as a more complex technology than its competitors. Therefore, it needs to perform significantly better than any competitive technology, instead of as good, in order to be implemented on large scale. More comparative studies are required to gain a clear overview on the current state of affairs with

regard to energy efficiency of the different technologies. As shown in the present work for atrazine removal in plasma reactors, electrical energy per order EEO is a useful comparative parameter for this purpose. Notwithstanding, it is even more important that further oxidation studies are performed with characteristic micropollutants in low concentrations, in order to gather data that is representative for realistic situations to a greater extent.

Nevertheless, one should keep in mind that energy efficiency is not the only factor determining the applicability of advanced oxidation techniques. Since oxidation by-products can have higher toxicity than their parent compound, associated risks have to be taken into account as well. As shown in the present research, nitrification of a micropollutant can be a dominant oxidation process under plasma discharge in air. Therefore, toxicity analysis of nitrificated intermediates is an important topic for future research to understand the feasibility of air plasma for water purification. The same counts for the possible chlorination of compounds in presence of Cl^- ions. Chlorination has been reported for UV/TiO_2 [3], for UV/H_2O_2 [4] and for oxidation by peroxymonosulfate [5]. The authors of these studies propose the formation of aqueous chlorine radicals and dichloride anion radicals in presence of OH radicals through the reactions

$$OH + Cl^- \longrightarrow ClOH^- \tag{9.1}$$

$$ClOH^- + H^+ \longrightarrow Cl\cdot + H_2O \tag{9.2}$$

$$ClOH^- + Cl^- \longrightarrow Cl_2^- + OH^- \tag{9.3}$$

$$Cl\cdot + Cl^- \longrightarrow Cl_2^- \tag{9.4}$$

The formed radicals can add to C = C double bonds of organic compounds, generating chlorinated hydrocarbons. For the more specific case of aromatic molecules, Cl addition is expected directly on the aromatic ring, by a similar reaction mechanism as for OH attack as, for instance, proposed in [6].

Up to now, studies on water purification by means of advanced oxidation processes in general and plasma treatment in particular have mainly focused on reactor effectiveness and energy efficiency for degradation of single compounds. Although this approach allows us to compare different reactors and techniques, it gives insufficient information on the quality of the solution after treatment. In order to gain this information, detailed reports on reactor optimization in terms of effluent toxicity reduction are needed. However, such reports, if any, are sparse for most advanced oxidation techniques. Especially during plasma treatment, the complex mixture of oxidative species gives rise to several long-living aqueous species, such as hydrogen peroxide and peroxynitrite. The role of the latter in the disinfectant properties of so-called plasma-activated water has been discovered only in recent years. The generation of other long-living hazardous reactants by plasma treatment of water is still uncertain. As a direct implication, a new line of research is required with a stronger focus on

overall toxicity and post-treatment effects, if this young technology is to be brought closer towards real-world application.

References

[1] L. Fras Zemljič, *et al.*, "Improvement of chitosan adsorption onto cellulosic fabrics by plasma treatment," *Biomacromolecules,* vol. 10, pp. 1181-1187, 2009.

[2] F. R. Oliveira, *et al.*, "Reuse of effluent from dyeing process of polyamide fibers modified by double barrier discharge (DBD) plasma," *Desalination and Water Treatment,* vol. 57, pp. 2649-2656, 2016.

[3] R. Yuan, *et al.*, "Photocatalytic degradation and chlorination of azo dye in saline wastewater: Kinetics and AOX formation," *Chemical Engineering Journal,* vol. 192, pp. 171-178, 2012.

[4] N. Baycan, *et al.*, "Influence of chloride concentration on the formation of AOX in UV oxidative system," *Journal of Hazardous Materials,* vol. 143, pp. 171-176, 2007.

[5] R. Yuan, *et al.*, "Effects of chloride ion on degradation of Acid Orange 7 by sulfate radical-based advanced oxidation process: Implications for formation of chlorinated aromatic compounds," *Journal of Hazardous Materials,* vol. 196, pp. 173-179, 2011.

[6] K. S. Tay, *et al.*, "Ozonation of parabens in aqueous solution: Kinetics and mechanism of degradation," *Chemosphere,* vol. 81, pp. 1446-1453, 2010.

Every new beginning comes from
some other beginning's end.
- Seneca